www.dmu.ac.uk
DE MONTFORT UNIVERSITY

# MIMO-OFDM for Beyond 3G Systems


OMAR RAWHI DAOUD

**Wireless, Multimedia Communications and**

**Signal Processing Research Group**

**School of Engineering and Technology**

**Faculty of Computing Sciences and Engineering**

**De Montfort University**

**United Kingdom**


***A dissertation submitted in partial fulfilment of the requirements for the degree of Doctor of Philosophy***

OCTOBER 2006

# Declaration

No part of the material described in this thesis has been submitted for the award of any other degree or qualification in this or any other university or college of advanced education.

***Omar Daoud***

# Dedication

## To:

My parents with love…

Your support gives me determination for working harder…

Your belief gives me a hope …

Your love making me feels better…

I do really love you…

My sisters and brothers who deserve endless thanks…

My lovely and patient wife, AHLAM…

Your supports relief my stress and loneliness…

Your smile strengthens my determinations…

I am really lucky…

The gift of **ALLAH**, my "Al-Bara'a"

# Acknowledgements

First and foremost, my deepest gratefulness goes to GOD for all his blessings without which nothing of my work would have been done. I would also like to express my sincere gratitude to my supervisor Professor Marwan Al-Akaidi at De Montfort University, United Kingdom, for his guidance, ideas, invaluable directions and support throughout my research study. Without his contributions, this research would not have been possible. I am deeply indebted to him for his insights and suggestions to the thesis topic and for invaluable supervision at various stages of my work. He has helped me in many ways and has developed my academic thinking, problem solving and technical writing which will be very helpful in my future work and research. I feel extremely lucky to have him as my supervisor, who is always dedicated to the success of his students. Grateful acknowledgement is also made to my second supervisor Mr. Jon Ivins at De Montfort University, United Kingdom, for his ideas, encouragement, and support. His insightful assistance has greatly helped me to improve the quality of this work. I am grateful for the support and assistance from all members of the WMCSP (Wireless & Multimedia Communications & Signal processing) research group, who have given me a sense of belonging as a group. I am also thankful to my colleagues at the WMCSP Research group. I have benefited from many fruitful discussions and collaboration with them.

Also, I am pleased to thank Shawkat Ahmad, Mohammad Mahmoud and Hamza Malak for their support.

Last but not least, I would like to express my gratefulness to Dr. Ibrahim Badran for his help and support and my thankfulness to Philadelphia University for providing the scholarship to support my research study at De Montfort University.

***Omar Daoud***

***De Montfort University***

***Leicester, United Kingdom, October 2006***

# Abstract

The new generation of wireless and mobile communication systems have the ability to support multimedia applications as it is main feature. This quality has been achieved by the researchers who have turned their interest to the combination between two techniques, Orthogonal Frequency Division Multiplexing (OFDM) and Multiple – Input Multiple-Output (MIMO).

There are several significant advantages of OFDM, such as the ability to support a high data rate for wide area coverage, robustness to multipath fading and a greater simplification of channel equalisation. These advantages render the employment to OFDM attractive for different applications such as IEEE 802.11, Wireless Local Area Networks (WLAN), European Telecommunications Standards Institute (ETSI) and terrestrial video broadcasting. However, OFDM suffers from a high sensitivity to non-linear distortion caused by components in the transmitter section, such as Digital to Analogue Converters (DAC), mixers and High Power Amplifiers (HPA). The output signal will suffer from intermodulation distortion resulting in energy being generated at frequencies outside the allocated frequency band, resulting in costly filtering after the nonlinear devices. In some cases the transmission power is lowered at the expense of increasing the Bit Error Rate (BER).

The main advantages of the MIMO are increased system capacity (i.e. MIMO channel capacity scales linearly with respect to the minimum available transmitter and receiver antennas) and improved communication reliability. However, the maximum capacity that can be exploited in MIMO systems depends on a number of parameters observed at the receiver, such as the average received power of the desired signals and co-channel interference. Moreover, the multidimensional statistical behaviour of the MIMO fading channel is of utmost significance to system performance.

This research tackles some of the issues that are raised due to the combination between MIMO and OFDM technologies, such as the Peak-to-Average Power Ratio

(PAPR) problem, and investigates the effect of the correlation coefficients on the MIMO system capacity.

A competitive technique is proposed in order to tackle the PAPR. This technique gives significant results in reducing the PAPR compared with the conventional techniques, such as the clipping and Partial Transmit Sequence (PTS) techniques.

After deriving a MIMO channel capacitance formula, a simple channel model was proposed to help in understanding the effects of the correlation coefficients on the system capacitance. From this model, the determinant of the correlation coefficients matrices is mapped between zero and one. Respectively, the correlation values from the worst case to the best case are mapped between one to zero.

# Contents

# List of Figures

# List of Tables

# Nomenclature

| | |
|---|---|
| 2G | Second Generation |
| 3G | Third Generation |
| ASICs | Application-Specific Integrated Circuits |
| AWGN | Additive White Gaussian Noise |
| B3G | Beyond 3G |
| BER | Bit Error Rate |
| CDF | Cumulative Distribution Function |
| CCDF | Complementary CDF |
| DAC | Digital-to-Analogue Converters |
| D-BLAST | Diagonal Bell Labs Layered Space-Time |
| DSP | Digital Signal Processing |
| DVB-H | Digital Video Broadcasting-Handheld |
| ETSI | European Telecommunications Standards Institute |
| FDM | Frequency Division Multiplexing |
| FFT | Fast Fourier Transform |
| FPGA | Field Programmable Gate Array |
| HDL | Hardware Description Language |
| HPA | High Power Amplifiers |
| ICI | Inter Carrier Interference |
| IFFT | Inverse Fast Fourier Transform |
| i.i.d | identically independent distribution |
| ISE | Integrated Software Environment |
| ISI | Inter-Symbol Interference |
| JC | Joint Coding |
| MIMO | Multiple-Input Multiple-Output |
| MMSE | Minimum Mean Squared Error |
| MOM | Marwan Omar Model |
| M-PSK | M-ary phase shift keying |
| M-QAM | M-ary quadrature amplitude modulation |
| MRC | Maximum Ratio Combining |

| | |
|---|---|
| NTRPT | Novel Technique to Reduce the PAPR based on linear coding Techniques |
| OFDM | Orthogonal Frequency Division Multiplexing |
| PAC | Per-Antenna coding |
| PAPR | Peak-to-Average Power Ratio |
| PEP | Pairwise Error Probability |
| PDP | Power Delay Profile |
| pdf | probability density function |
| QoS | Quality of Service |
| RX | Receiving antenna |
| SDM | Space Division Multiplexing |
| SNR | Signal to Noise Ratio |
| STBCs | Space-Time Block Codes |
| STC | Space-Time Coding |
| STTC | Space-Time Trellis Codes |
| SVD | Singular Value Decomposition |
| TDM | Time Division Multiplexing |
| TDMA | Time Division Multiple Access |
| TX | Transmitting antenna |
| V-BLAST | Vertical-Bell Labs Layered Space-Time |
| WCDMA | Wideband Code Davison Multiple Access |
| WLAN | Wireless Local Area Network |
| X-OR | exclusive-OR |
| ZF | Zero Forcing |
| ZP-OFDM | Zero Padded-OFDM |

# Publications

- O. Daoud and M. Al-Akaidi, "**Improving the QoS for the 3rdG and beyond Systems**", London Communications Symposium (LCS2004), University College London, London, UK 2004.

- O. Daoud, M. Al-Akaidi and J. Ivins, "**Performance Analysis of OFDM by optimising PAPR**", 6th International Conference on 3G and Beyond (3G2005),The IEE, Savoy Place, London, UK 2005.

- O. Daoud, M. Al-Akaidi and J. Ivins, "**THE CAPABILITY OF REDUCING THE PAPR BY TURBO CODING**", The 7th International Middle Eastern Multiconference on Simulation and Modelling (MESM2005), the University of Porto, Portugal, October 2005.

- M. Al-Akaidi, O. Daoud and S. Linfoot, "**A NEW TURBO CODING APPROACH TO REDUCE THE PEAK-TO-AVERAGE POWER RATIO OF A MULTI-ANTENNA-OFDM SYSTEM**", *International Journal of Mobile Communications* (IJMC, ISSN: 1470-949X). (Accepted for publication on 26-04-06).

- M. Al-Akaidi and O. Daoud, "**REDUCING THE PEAK-TO-AVERAGE POWER RATIO USING TURBO CODING**", *IEE Proceeding Communications*. (Accepted for publication on 09-06-06).

- O. Daoud, M. Al-Akaidi and J. Ivins, "**MIMO-OFDM CHANNEL MODELLING AND PERFORMANCE**", The International Middle Eastern Multiconference on Simulation and Modelling (MESM2006), Mercure Romance Hotel, Alexandria, Egypt, August 2006.

- M. Al-Akaidi, O. Daoud and J. Gow, "**MIMO-OFDM-based DVB-H systems: A Hardware design for a PAPR reduction technique**", *IEEE Transaction on CE.* (Accepted for publication on 11-06).

# Chapter One

# 1. Introduction

## *1.1Background and Motivation*

Since the 19th century, communication technology has experienced revolutionary changes. Communication consists mainly of letters, telegraphs telephones and fax machines. The recent evolution of mobile phones has improved connectivity. The 21st century started with the revolution in wireless technology for Internet applications and other data communication applications, again in order to improve connectivity (i.e. to be available at anytime or anywhere), and to satisfy user demand.

The rapid growth in demand for mobile communication has led to an intensified interest in developing a new generation of wireless communication systems. These developments are aimed at increasing overall system throughput and improving network capacity to support high quality multimedia applications. Hence a larger bandwidth should be occupied, which will be limited by the equipment expense and by radio propagation at higher frequency ranges, and furthermore that the system's spectral efficiency should be improved to attain these aims.

To achieve this level of quality, researchers have turned their interest into the combination of two powerful techniques, MIMO and OFDM. The MIMO technique is used to improve the overall wireless communication system's capacity [1], while OFDM is used to increase its resistance to channel effects [2, 3].

In the early 1990s, research into information theory revealed that significant improvements in spectral efficiency can be accomplished by using multiple antenna technology at both ends. The functionality of the MIMO technique can basically be split into Space-Time Coding (STC) and Space Division Multiplexing (SDM). STC

improves the wireless communication system's robustness by sending the same data stream with different representations through the transmitter antennas. SDM increases the overall system's throughput by simultaneously sending different data streams on the different transmitting antennas. On the other hand, the main reason for selecting OFDM is its ability to deal with the multipath propagation present in the channel. Because of adding the multipath components together, a fading problem will appear which can severely distort the received signals. In OFDM, this problem can be mitigated, since the wideband fading channel is split up into multiple orthogonal narrowband flat fading channels. The ability to include a proper guard interval between subsequent OFDM symbols provides an effective mechanism to handle Inter-Symbol Interference (ISI) caused by severe multipath propagation. However, the major drawback of OFDM is its high Peak-to-Average Power Ratio (PAPR). If the added signals, in generating the OFDM symbol, are in phase with each other, then the Inverse Fast Fourier Transform (IFFT) will produce an OFDM symbol with high peak power. PAPR is defined by comparing the high peak power of the OFDM symbol to its average power. The following problems result in communication systems due to high PAPR

- significant spectral spreading and in-band distortion causing intermodulation among different subcarriers
- undesired out-of-band radiation
- quantisation noise, affecting the system's performance

The combination of MIMO and OFDM techniques will raise some issues which need addressing, such as the variety of trade-offs between capacity capabilities and BER which result from the selected MIMO functionality. A proper channel model should be proposed to cover the best and worst cases of MIMO channel performance.

OFDM is used to improve the system's robustness; but its main drawback limits the overall system throughput, since PAPR is linked with IFFT size (i.e. increasing the amount of data that will be transmitted as an OFDM symbol may cause higher PAPR). This deficiency can be mitigated by a number of techniques proposed for tackling PAPR problems. These techniques include amplitude clipping, clipping and

filtering, coding and multiple signal representation. As a general rule, these techniques achieve PAPR reduction at the expense of an increase in transmitted signal power, BER, data rate loss or computational complexity [4-7]. Therefore, a competitive technique should be developed to overcome the disadvantages of the conventional techniques and at the same time achieve very good PAPR reduction ratios.

## *1.2Aim and Objectives*

The research is aimed at improving the capability of supporting the next generation high quality multimedia applications; attained by increasing the overall system throughput and reducing the effects of the multipath channel on system performance.

The focal research questions that arise are:

(1) How effective is the combination of MIMO and OFDM techniques, and what are the advantages of adopting such a hybrid technique?
(2) How to address the effect of the MIMO channel components on MIMO systems overall capacity?
(3) How to propose an improved technique to tackle the PAPR problem?

The research objectives are;

(1) Understanding MIMO technique functionality
(2) Identifying the characteristics of the MIMO channel and the main effective parameters
(3) Identifying OFDM as a modulation technique
(4) Establishing a mathematical model for the proposed technique to tackle the PAPR problem
(5) Characterising the structure of the MIMO-OFDM system using the proposed technique, Novel Technique to Reduce PAPR based on linear coding Techniques (NTRPT)
(6) Demonstrating and validating the NTRPT-MIMO-OFDM system through a series of experiments, and evaluating the main concepts by conducting case studies into this system

## *1.3Scope of the Research*

The scope of the research is divided into two main areas, MIMO and OFDM. According to the research aim, MIMO technique functionality is determined by SDM, which is used to increase system capacity while in OFDM, the concern is with tackling the PAPR problem

Thus, the research scope for the MIMO area has been delimited to

i) deriving a MIMO channel capacity formula based on the correlation coefficients between the transmitted and received signals through different antennas
ii) proposing a distance based MIMO channel
iii) linking the BER with the SNR for some of the SDM algorithms, namely, Zero Forcing (ZF) and Minimum Mean Squared Error (MMSE)

The scope of the research is determined for the OFDM area by proposing and validating a new technique based on linear encoders to reduce the PAPR problem.

## *1.4Research Approach*

The adopted research approach consisted of the following main stages:

(1) Identification of research questions (via intensive literature reviews)
(2) Concept development
(3) Mathematical modelling
(4) Simulation and validation
(5) Case studies
(6) Future research

The research study was initiated with a theoretical literature review. This review was conducted for the identification of specific research problem(s) for both MIMO and

OFDM techniques. It also served the purpose of identifying potential solutions for the identified problem(s). The focus was on understanding MIMO technology and its main advantages and disadvantages. More specifically, the research focused on the following areas:

(1) concentrating on SDM techniques
(2) understanding the effect of correlation coefficients on system capacity

In OFDM, a new technique to tackle the PAPR problem is proposed. The technique is supported by a mathematical model and a simulation to be implemented in MIMO-OFDM systems. This stage was conducted continuously and in parallel with the other stages (from stage 2 to 5), throughout the period of this research. This was necessary in order to ensure that potential developments in related areas could be continuously fed back to the other activities throughout the research period.

For the concept development stage, a conceptual structure was formulated to breaking the MIMO-OFDM system down into sub-blocks. These sub-blocks were employed to develop an adaptive structure allowing the MIMO-OFDM system to be compatible with different applications. A mathematical model for the proposed technique (Novel Technique to Reduce PAPR based linear coding Technique (NTRPT)) was established to create NTRPT-MIMO-OFDM system.

In the fourth stage – simulation and validation, the mathematically achieved results have verified by performing a MATLAB based simulation. Firstly, the MATLAB results from this simulation were further validated by the Agilent signal generator and spectrum analyser (89600 Series Vector Signal Analysers). The verification process is based on the Signal Studio Toolkit. Secondly, the proposed technique was designed to be implemented to a Xilinx FPGA card for a demonstration and validation of the simulation results.

In the last stage, findings were documented and applied (by simulation) to two main systems namely, Digital Video Broadcasting-Handheld (DVB-H) and the WLAN IEEE 802.11n. A number of recommendations were made for future research and development.

## *1.5 Thesis Outline*

This section gives a general overview of the chapters in the thesis. The content of this thesis follows a logical order, starting from the theoretical analysis of MIMO-OFDM and ending with simulation and validation of the research. The outline of this work is as follows:

**Chapter 2** is divided into three parts: an overview about MIMO technology, its functionality, advantages and disadvantages; the structure of OFDM, advantages and disadvantages of this technique and its merits as a transmitter and receiver; and the PAPR problem, its effects on OFDM technique's performance and the conventional methods to overcome this drawback.

**Chapter 3** presents a derivation of a MIMO channel capacity formula based on the correlation coefficients matrices. the findings of which formulate a distance-based MIMO channel model proposed to cover best and worst capacity cases. There is a further discussion of the SDM receiving techniques for linking the BER with the SNR for the proposed model.

**Chapter 4** presents a detailed description of the proposed technique, NTRPT, the mathematical derivation, the structure, and the simulation to verify the result of the mathematical derivation.

**Chapter 5** establishes a design for the structure and the signal model for the overall NTRPT-MIMO-OFDM system, concurrently, and performs a MATLAB simulation to check the performance of the proposed technique in MIMO-OFDM systems.

**Chapter 6** presents the validation process of the achievements in Chapters 4 and 5. This validation is based on verifying the achieved simulation's results by using the Agilent signal generator, spectrum analyser and Signal Studio Toolkit. The proposed technique was designed to be implemented by a Xilinx Field Programmable Gate .

Array (FPGA) card in order to demonstrate and validate the results achieved from the simulation.

**Chapter 7** describes the results obtained from using the proposed technique in some real systems as case studies, such as DVB-H and IEEE 802.11n.

**Chapter 8** draws conclusions and outlines some recommendations for future research.

# Chapter Two

# 2. The MIMO-OFDM and the PAPR Problem

## *2.1Introduction*

This chapter is divided into five sections. Section 2.2 gives an overview of MIMO technology, Section 2.3, which covers OFDM technique, and Section 2.4, which describes PAPR, one of the main OFDM problems. The chapter is summarised in Section 2.5.

## *2.2Multiple-Input Multiple-Output*

The main advantages of using multiple antenna technology are an increase in system capacity and an improvement in the communication reliability as a result of the diversity gain. The capacity of MIMO channels scales linearly with respect to the minimum available transmitter and receiver antennas [8].

The MIMO channel model and the structure of the transmitted and received signals must both be taken into consideration when applying MIMO technology. The received signals vitally affect the maximum rate in a given bandwidth, whereas the transmitted signal structure strongly impacts on achievable system performance and capacity. Proposing a good MIMO channel model will therefore help in understanding the effects of channel components on system performance and capacity [9].

The effects of both the transmitted and received signals' structures have led to numerous developments of MIMO techniques. The proposed schemes can be divided into two groups, STC and SDM. These basic concepts have been fundamental to

various types of transmission schemes; respectively, they increase the robustness and performance of the communications system and improve the overall system data rate. An overview of channel modelling is given in Subsection 2.2.1, while Subsection 2.2.2 describes the functionality of MIMO systems.

### 2.2.1 The MIMO Channel

To construct a multidimensional channel matrix, consider a wireless communication system with $N$ transmitting (Tx) and $M$ receiving (Rx) antennas to transmit different streams of data on different transmitting antennas. When a transmission occurs, the transmitted signal from the $p$-th Tx antenna might find direct or indirect paths in order to arrive at $q$-th Rx antenna by a number of reflections. This principle is called multipath [10].

MIMO channel is delimited for indoor purposes. Some aspects must be taken into consideration in this case, such as the slow movement of the objects, the large number of reflecting surfaces, the propagation loss characteristics resulting in a neglected Doppler effect, multipath fading, and an exponential loss over time for the received power. Depending on these aspects, the multipath fading channel could be modelled in a simple manner as a tapped delay with a fixed number of channel taps denoted by '*TC*'. At the existence of either LOS or a specular component, the distribution of the channel will follow Ricean distribution, while it follows the Rayleigh distribution at the absence of both of them [9, 10]. It is assumed that an exponentially decaying Power Delay Profile (PDP)[1], with or without a specular component, is added to the first tap [11]. This results in a MIMO channel model as

$$\mathbf{y}(n) = P_{dn}\mathbf{G}(tc)\,\mathbf{x}(n\text{-}tc). \qquad (2.1)$$

where $\mathbf{x}$ is the transmitted data vector, $\mathbf{y}$ is the received data vector, $P_{dn}$ denotes a normalisation factor related to the discrete-time PDP, $n$ is the sampling index, $\mathbf{G}(.)$ is the channel transfer matrix and $tc$ is the number of the channel tap.

[1] The power of the channel impulse response as a function of the time-delay $\tau$.

The different representations of channel characteristics must be taken into consideration. Starting from (2.1), in order to model the channel transfer matrix, the existence or absence of the LOS or specular components must be checked. A lack of strong LOS or specular path in addition to a large number of reflectors within the indoor environment (i.e. rich-scattering environment) results in Rayleigh fading. Choosing a $\lambda/2$ antennas spacing (where $\lambda$ is the carrier wavelength) leads to the assumption of having an independent and identically distributed (i.i.d) channel coefficients. 2.1 $\mathbf{G}(tc)$ is then defined as $\mathbf{G}_{iid}(tc)$. The elements of this matrix are an i.i.d. *circularly-symmetric complex Gaussian variable*[2] with zero mean and unit variance, and an independent realisation of the entire channel taps *tc*, $tc = 0, 1 \ldots TC\text{-}1$. Each entry of $\mathbf{G}_{iid}$ $(tc)$ has uniformly distributed phase and Rayleigh distributed magnitude. After characterising $\mathbf{G}(tc)$, if the PDP is justified for the longer propagation delay paths, then these paths will arrive linearly later in time and will have a logarithmically-weaker energy. The PDP is characterised as an exponentially decaying function with equidistant delays by the following equation [11]

$$P_d(tc) = P_{cn} \exp(-\frac{tc}{\alpha_\tau}), \quad \text{for } \alpha_\tau > 0 \text{ and } tc = 0,1, \ldots, TC\text{-}1 \qquad (2.2)$$

where $\alpha_\tau$ denotes a factor related to the delay spread and the sampling frequency, and $P_{cn}$ represents a normalised channel gain with respect to the delays. From (2.2), it is apparent that if $\alpha_\tau$ equals to zero, the channel will have one tap at *tc* equal to zero, and consequently, the PDP will equal the total power.

On the other hand, in the presence of a strong, or at least a direct, path between transmitter and receiver (i.e., the specular or the LOS components, respectively), the channel characteristics will change. In this case the channel characteristics will be modelled as a part of the MIMO channel impulse response first tap, which is considered as a Ricean distribution. The modified version of (2.1) will be as in [11]

---

[2] say $z$, with zero mean and variance $\sigma^2$ is given by $z = x + jy$ with $x$ and $y$ being i.i.d zero mean real Gaussian variables with variance $\sigma^2/2$.

$$\mathbf{G}(tc) = \begin{cases} \alpha_n \beta_{K1} \mathbf{G}_{spec} + \beta_{K2} \mathbf{G}_{iid}(tc), & for \quad tc = 0 \\ \beta_{K2} \mathbf{G}_{iid}(tc), & for \quad tc = 1,...,TC-1 \end{cases} \tag{2.3}$$

where $\mathbf{G}_{spec}$ is the MIMO channel part related to the specular or the LOS component and can be defined as an *MxN* matrix, $\alpha_n$ is a normalisation factor for the $\mathbf{G}_{spec}$, and $\beta_{K1}$, $\beta_{K2}$ are factors related to the Ricean factor *K* which then equals to $\sqrt{\frac{K}{K+1}}$, and $\sqrt{\frac{1}{K+1}}$ respectively. The Ricean factor, *K*, is the energy ratio of the MIMO channel specular part to the MIMO channel scattering part.

The channel gain in this case will be modified to contain the part of the Ricean distribution for the first tap, as follows:

$$P_c = P_{dspec} + P_{dscatt} \tag{2.4}$$

From (2.3), if *K* equals to zero, the model will be reduced to the Rayleigh fading channel model, which means that the distribution of the first tap in the channel does not presence of either LOS or a specular component.

### 2.2.2 MIMO Systems Functionality

According to the main goal of the research (improving communication systems' capacity to support higher quality multimedia applications), in addition to highlighting the crucial effects of the transmitted and received signal structure on achievable system capacity and performance, this section will cover the main characteristics of MIMO techniques. A literature search reveals much research into achieving good MIMO techniques to reach the best balance between complexity and performance. The proposed techniques can be divided into two main groups: STC and SDM. STC increases the robustness and performance of the communication system by coding over different transmitter branches, while SDM achieves a higher data rate by transmitting independent data streams on the different transmitter branches

simultaneously and at the same carrier frequency. For the purposes of the present research, SDM is the most interesting technique [12].

A general MIMO structure is shown in Figure 2.1 with *N* representing the number of transmitting antennas and *M* the number of receiving antennas. This figure presents a block diagram of the main processing tasks on the input data stream. These are channel coding, serial to parallel processing, and constellation mapping.

The other part of the system is the receiver; whose complexity depends strongly on the Tx signal design. The detection process is performed over the spatial and temporal dimension. Without complexity reducing techniques, increasing the dimension size will exponentially increase the number of codewords.

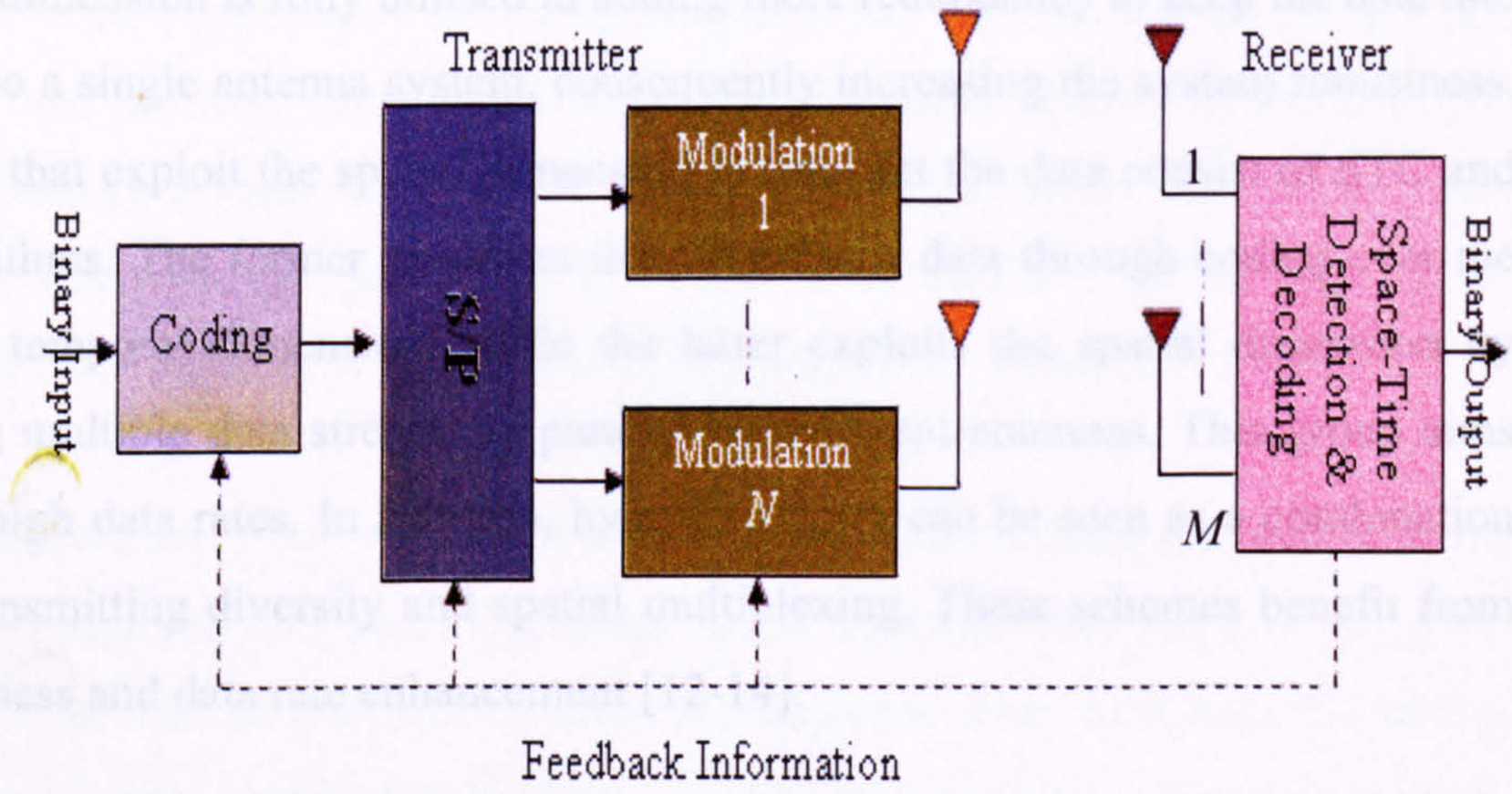


**Figure 2.1: General MIMO system structure**

The different MIMO algorithms that are mentioned in the literature could be classified as follows as in [13]:

(1) The system is either o*pen-loop* or *closed-loop*

(2) The transmitted signal is send over the temporal and spatial dimension

(3) The coding process is either joint coding or per-antenna coding

The first classification is made between two different types of systems:

(1) Systems that do not adhere to the channel response's information at the transmitter (open-loop systems)

(2) Systems that depend partly or fully on the channel information at the transmitter through the feedback mechanism (closed-loop systems).

As shown in Figure 2.1, the feedback loop mechanism provides information for all system stages such as the coding rate, the constellation size, and the type of modulation.

The second classification describes whether the transmission algorithms are applied over temporal or spatial dimensions. This can be determined by establishing which algorithm makes the best use of the diversity provided by a richly scattered channel. The spatial dimension is fully utilised in adding more redundancy to keep the data rate equivalent to a single antenna system, consequently increasing the system robustness. Techniques that exploit the spatial dimension to transmit the data consist of STC and SDM algorithms. The former generates the redundancy data through coding over the spatial and temporal dimension, while the latter exploits the spatial dimension by transmitting multiple data streams in parallel on different antennas. This group aims to achieve high data rates. In addition, hybrid schemes can be seen as a combination between transmitting diversity and spatial multiplexing. These schemes benefit from both robustness and data rate enhancement [12-14].

The classification process which depends on the coding stage can be categorised into two types:

(1) If the coding process commences before the serial to parallel stage as shown in Figure 2.4, it is referred as the Joint Coding (JC).

(2) Per-Antenna Coding (PAC) denotes the coding process that commences after the serial to parallel stage.

JC provides better performance than PAC, since the coding is performed over the spatial and temporal dimensions. While in PAC, the receiver architecture might be

less complex since the encoding process is separated over the temporal and the spatial dimensions [14].

#### 2.2.2.1 MIMO Transmitter structure

As mentioned earlier, the proposed techniques of MIMO transmitters can be divided into two main groups: STC and SDM. The following subsection discusses these two groups and identifies their differences.

##### *2.2.2.1.1 Space-Time Coding*

As mentioned before in Subsection 2.2.2, STC is performed over the spatial and temporal dimension to improve the system's robustness. In [15-17], the main concerns about the performance of coding criteria in two dimensions according to the analysis of the pairwise error probability are addressed. Rank, determinant and Euclidean distance criteria represent the basis of different space-time codes. These space-time codes could be split into Space-Time Block Codes (STBCs), Space-Time Trellis Codes (STTC), Space-Time Turbo Codes and Linear Dispersive Codes.

The rank criteria tries to improve the diversity order by maximising the rank, *r*, of the codeword difference matrix over all possible codeword pairs, since the diversity order is given by *rxM*. The determinant criterion is concerned with increasing the coding gain. This gain is achieved by the minimum product of the nonzero eigenvalues of the codeword difference matrix and its Hermitian matrix over all distinct pairs of codewords. In addition, the Euclidean criterion is based on maximising the minimum Euclidean distance between any pair of codewords [17].

***Space-Time Block Codes:***

The STBC encoder works on a block level. Assume that, an input symbol denoted by '$D_{sym}$', from a real or complex constellation. This type of encoder maps the $D_{sym}$ into codewords **C** in the dimension $NxN_{sym}$, where $N$ denotes the transmit antennas and $N_{sym}$ denotes the symbol time instant. The coding rate for this process could be

calculated as $R_{cod} = D_{sym}/N_{sym}$, Therefore increasing $D_{sym}$ per unit of time will improve the encoder rate. A STBC encoder's design must achieve two goals: to keep $R_{cod}$ as high as possible and to obtain a robust communication link. The codes should therefore be designed to achieve these targets. Different studies in the literature show, however, that they cannot always be met simultaneously [18-21]. Different architectures of orthogonal STBCs can be summarised as follows

(1) linear and non-linear complex design
(2) linear and non-linear real design
(3) suitability to the number of antennas
(4) the extent to which this technique will make use of the available transmit diversity

A special case from the efficiency point of view, the orthogonal STBC does not always make full use of available MIMO channel capacity. In addition, for the complex type, the coding rate drops below one in case of having more than two transmitting antennas [22-24]. Checking the functionality of the STBCs starts from [25], since the authors introduce a linear STBCs, which are called "Linear Dispersive Codes" in $N > M$ domain of interest. Many of the codes need assistance from outer one-dimensional codes because they act like space-time mappers or interleavers.

Alamouti and Jankiraman described one of the most popular orthogonal STBCs, which is called the "*Alamouti scheme*" for two transmit antennas [26, 27]. The functionality of this scheme is clearly described in Figure 2.2. The two symbols $s_1$ and $s_2$ are transmitted simultaneously on $Tx_1$ and $Tx_2$, while the processed versions of these two symbols $-s_2^*$ and $s_1^*$ are transmitted on $Tx_1$ and $Tx_2$ during the next symbol period. From the figure shown below, the signal at $Rx_q$ at time 1 and time 2 for both symbols can be expressed as shown in (2.5) [27].

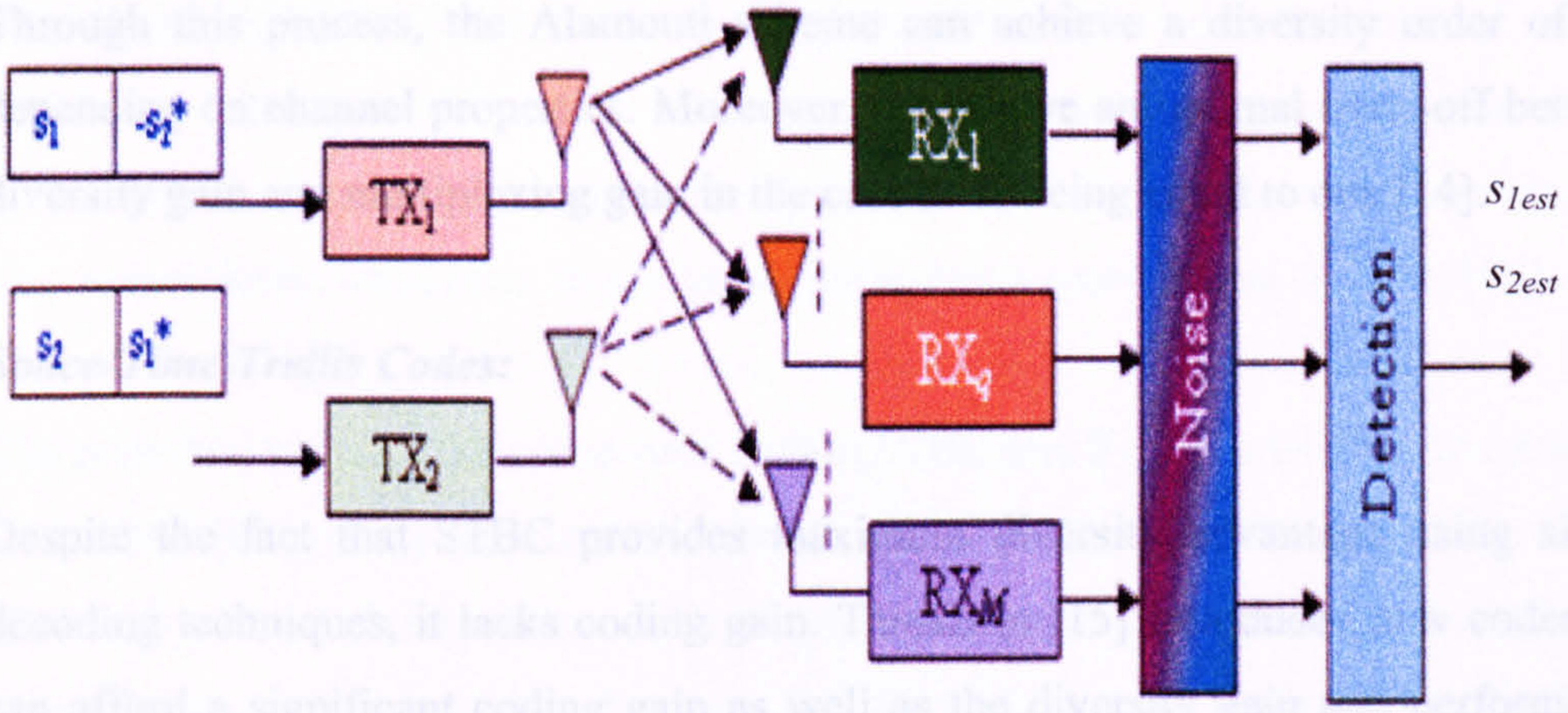


**Figure 2.2: The Alamouti STBC scheme**

$$\begin{pmatrix} x_q(1) \\ x_q(2) \end{pmatrix} = \begin{pmatrix} s_1 & s_2 \\ -s_2^* & s_1^* \end{pmatrix} \begin{pmatrix} h_{q1} \\ h_{q2} \end{pmatrix} + \begin{pmatrix} n_q(1) \\ n_q(2) \end{pmatrix} \tag{2.5}$$

where $n_q(t)$ represents the additive noise at symbol time $t$, and $h_{qp}$ denotes the response of a flat fading channel between $Tx_p$ and $Rx_q$. To produce the receive signals as a function of the channel matrix, (2.5) is analysed and multiplied by the left side Hermitian transpose of the channel gives:

$$\begin{pmatrix} h_{q1}^* & h_{q2} \\ h_{q2}^* & -h_{q1} \end{pmatrix} \begin{pmatrix} x_q(1) \\ x_q(2) \end{pmatrix} = \left( |h_{q1}|^2 + |h_{q2}|^2 \right) \begin{pmatrix} s_1 \\ s_2 \end{pmatrix} + \begin{pmatrix} h_{q1}^* n_q(1) + h_{q2} n_2^*(2) \\ h_{q2}^* n_q(1) - h_{q1} n_2^*(2) \end{pmatrix} \tag{2.6}$$

From (2.6), it is easy to estimate the received signals by using Maximum Ratio Combining (MRC)[3] principle to be

$$\sum_{q=1}^{M} \begin{pmatrix} h_{q1}^* & h_{q2} \\ h_{q2}^* & -h_{q1} \end{pmatrix} \begin{pmatrix} x_q(1) \\ x_q(2) \end{pmatrix} = \left( \sum_{q=1}^{M} \sum_{p=1}^{2} |h_{qp}|^2 \right) \begin{pmatrix} s_1 \\ s_2 \end{pmatrix} + \sum_{q=1}^{M} \begin{pmatrix} h_{q1}^* n_q(1) + h_{q2} n_2^*(2) \\ h_{q2}^* n_q(1) - h_{q1} n_2^*(2) \end{pmatrix} \tag{2.7}$$

[3] In telecommunications, maximal-ratio combining is a method of diversity combining in which (a) the signals from each channel are added together, (b) the gain of each channel is made proportional to the rms signal level and inversely proportional to the mean square noise level in that channel, and (c) the same proportionality constant is used for all channels. It is also known as ratio-squared combining, pre-detection combining and selective combining.

Through this process, the Alamouti scheme can achieve a diversity order of $2M$, depending on channel properties. Moreover, it can give an optimal trade-off between diversity gain and multiplexing gain in the case of $M$ being equal to one [14].

***Space-Time Trellis Codes:***

Despite the fact that STBC provides maximum diversity advantage using simple decoding techniques, it lacks coding gain. Tarokh in [15] introduced new codes that can afford a significant coding gain as well as the diversity gain and perform well both spatially and temporally. Nevertheless, this advantage comes at the expense of the receiver complexity, which limits these systems to two, three, or four transmitting antennas.

Figure 2.3 shows the trellis diagram of 8-state QPSK code and a possible design of the encoder to implement this code.

| Input State $D_2D_1D_0$ | Output State $D_2D_1D_0$ | Outputs ($RX_1$_$RX_2$) |
|---|---|---|
| 000 | 000 | 00, 01, 02, 03 |
| 001 | 001 | 10, 11, 12, 13 |
| 010 | 010 | 20, 21, 22, 23 |
| 011 | 011 | 30, 31, 32, 33 |
| 100 | 100 | 22, 23, 20, 21 |
| 101 | 101 | 32, 33, 30, 31 |
| 110 | 110 | 02, 03, 00, 01 |
| 111 | 111 | 12, 13, 10, 11 |

transition

(a)

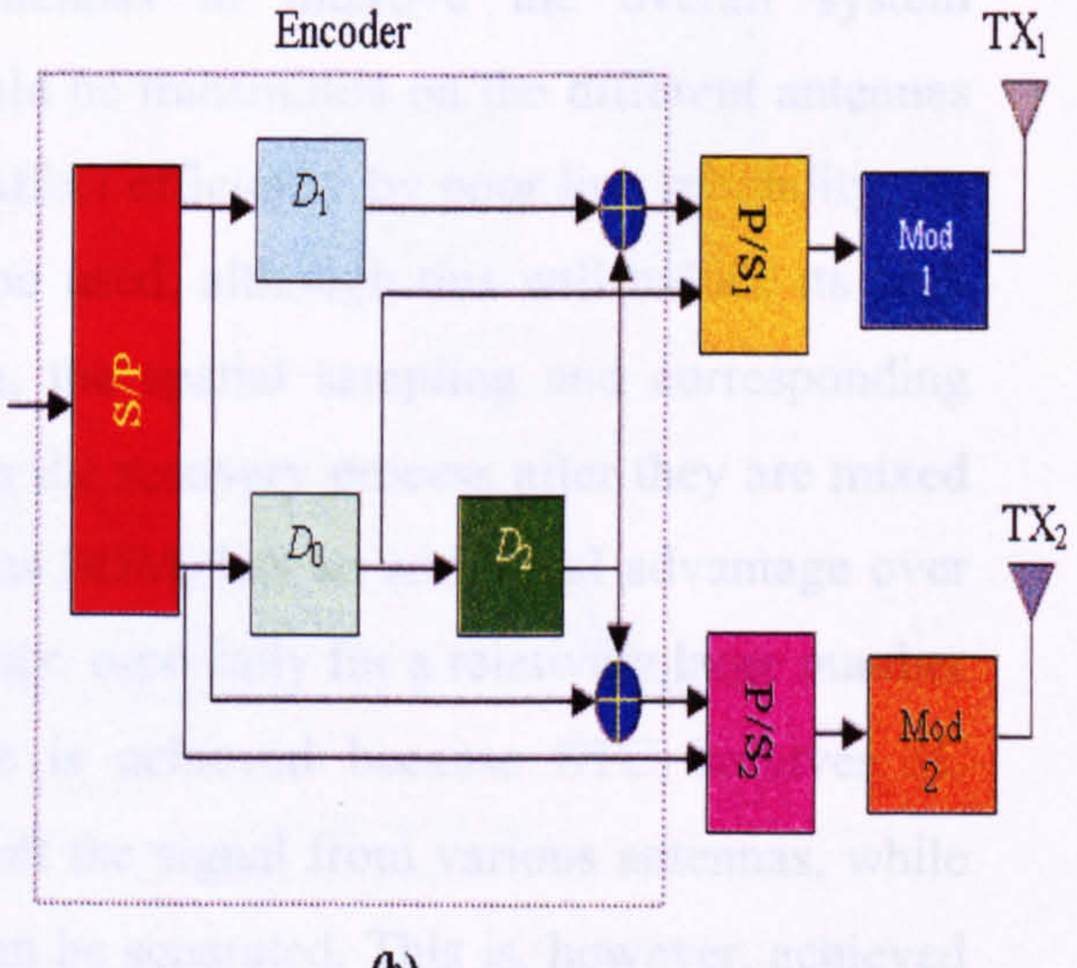


(b)

**Figure 2.3: (a) The Trellis of the 8-state QPSK STTC proposed in [15] and (b) Its mapping to the general block diagram**

Part (a) from this figure describes the 8-state QPSK code which is proposed by Tarokh. The input to the encoder consists of two bits at a time. The binary encoder

state is represented by $D_2D_1D_0$ and the two input bits results in four possible transitions per state. These four transitions result in four possible encoder outputs which are listed per input state. The outputs are denoted as a combination of two quaternary numbers that represent the QPSK symbol to be transmitted on $Tx_1$ and $Tx_2$, respectively. Moreover, this type of coding has a complicated receiver [15].

The main two types of the space-time codes (STBC and STTC) will now be compared to the MIMO general structure that is shown in Figure 2.1. Starting from STBC, Alamouti scheme clearly does not fit directly due to that it needs modulated symbols as an input to the encoder. Redesigning the encoder to work at bit level, the modulation can be performed after the encoding. The architecture of the second type (STTC) which is shown in Figure 2.3 (b) obviously matches the general model without modifications.

#### *2.2.2.1.2 Space Division Multiplexing*

As a result of exploiting multiple antennas to improve the overall system performance, different streams of data could be transmitted on the different antennas at the same carrier frequency, which will affect efficiency by poor link reliability. As a result, additional channel coding must be used, although this will reduce its high data rate advantage. At the receiver side, the spatial sampling and corresponding signal-processing algorithms can guarantee the recovery process after they are mixed in transmission. This process, referred to as SDM, has an additional advantage over STC in that it has lower decoding complexity, especially for a relatively large number of transmitting antennas. This advantage is achieved because STC involves JC spatially and temporally in order to transmit the signal from various antennas, while the spatial and temporal coding in SDM can be separated. This is, however, achieved at the expense of performance degradation [28, 29].

The coding stage in SDM consists of two procedures, JC and PAC. PAC, which is also called layered architecture coding introduced by [12], incurs a capacity penalty, since it uses different propagation channels for the various antennas used. Thus, a

diagonally layered architecture was proposed (Diagonal Bell Labs Layered Space-Time (D-BLAST)) [22].

In D-BLAST, a stream of encoded symbols is sent on different Tx antennas by cyclically selecting another Tx antenna per symbol period as shown in Figure 2.4. This will guarantee that each stream of data will be sent through a different propagation channel within the MIMO channel. Despite the fact that eliminating the capacity penalty is the main advantage of this technique over those that do not use cycling, this technique incurs different decoding complexity. To simplify the decoding process, diagonal spatial mapping must be dropped. In this case, D-BLAST is converted to be Vertical-Bell Labs Layered Space-Time (V-BLAST). In V-BLAST, spatial mapping is changed from diagonal mapping into vertical mapping (*i.e.* per spatial vector) [22].

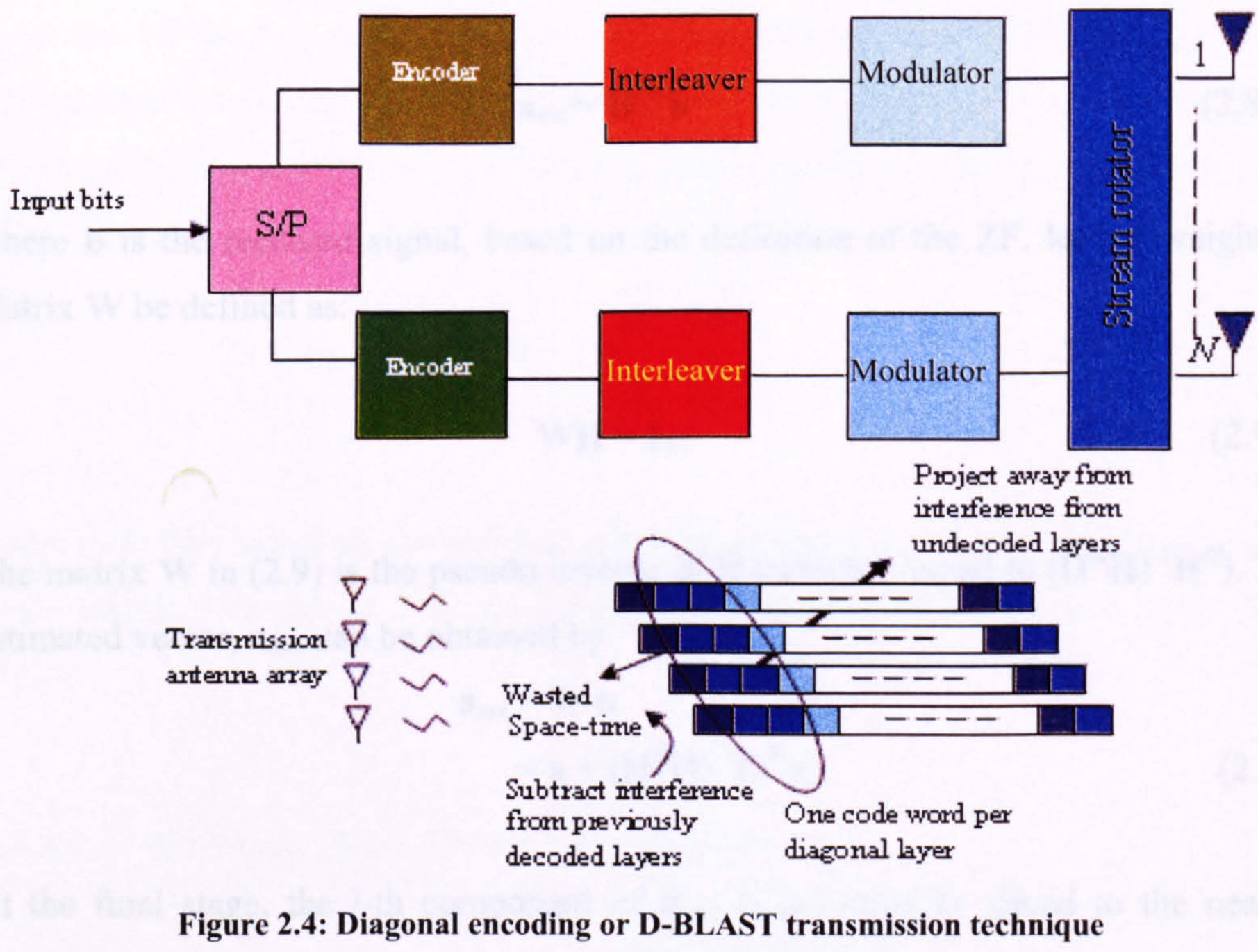


**Figure 2.4: Diagonal encoding or D-BLAST transmission technique**

### 2.2.2.2 MIMO Receiver Structure

At the receiver stage, both linear and non-linear processing can be used, since the algorithm PAC (as defined in Subsection 2.2.2) adopts detectors that operate in the

spatial domain. ZF and MMSE algorithms are considered as linear processes, while Maximum Likelihood Detection is an example of a non-linear detector [27]. This subsection concentrates on giving a brief insight into linear processing techniques.

#### *2.2.2.2.1 Zero-Forcing Technique*

The ZF technique is a linear MIMO technique based on linear combinational nulling technique uses a linear weighting process to cancel interfering terms from the received vector. It assigns each stream in turn as a desirable signal, while the remaining signal is assigned to be as an interfering one. To make use of ZF in the receiving process of a MIMO signal, the transfer matrix of the channel, **H**, must be assumed to be invertible. Thus, the estimated version of the transmitted MIMO vector **a** is given by [27]

$$\mathbf{a}_{est} = \mathbf{H}^{-1}\,\mathbf{b} \tag{2.8}$$

where **b** is the received signal, based on the definition of the ZF, let the weighting matrix **W** be defined as:

$$\mathbf{WH} = \mathbf{I}_N, \tag{2.9}$$

The matrix **W** in (2.9) is the pseudo inverse of **H** (which is equal to $(\mathbf{H}^H\mathbf{H})^{-1}\mathbf{H}^H$). The estimated vector, $\mathbf{a}_{est}$, can be obtained by

$$\begin{aligned}\mathbf{a}_{est} &= \mathbf{W}\,\mathbf{b} \\ &= \mathbf{a} + (\mathbf{H}^H\mathbf{H})^{-1}\mathbf{H}^H\,\mathbf{n}.\end{aligned} \tag{2.10}$$

At the final stage, the $j$-th component of $\mathbf{a}_{est}$, $(\mathbf{a}_{est})_j$, must be sliced to the nearest constellation point in order to decode the elements of **a** at the receiver.

The next step is to calculate the performance of the technique by expressing the probability of an erroneous decision between two different vectors. Starting with a definition of the conditional probability density function (pdf) for a given **H**, and

assuming that a multivariate complex Gaussian distributed data is used, the pdf is shown as [27, 28]

$$p(\mathbf{a}_{est}|\mathbf{a}, \mathbf{H}) = \det(\pi\mathbf{Q})^{-1}\exp(-(\mathbf{a}_{est}-\mathbf{a})\mathbf{H}\mathbf{Q}^{-1}(\mathbf{a}_{est}-\mathbf{a})) \qquad (2.11)$$

where **Q** is the covariance matrix of the estimation error with a multivariate complex Gaussian distribution, $\boldsymbol{\varepsilon} = \mathbf{a}_{ets} - \mathbf{a}$, which is given by

$$\begin{aligned}\mathbf{Q} &= E[\boldsymbol{\varepsilon} \cdot \boldsymbol{\varepsilon}^H] \\ &= \sigma_n^2 (\mathbf{H}^H\mathbf{H})^{-1}\end{aligned} \qquad (2.12)$$

Proakis in [30] shows that the upperbound of the performance can be calculated starting from Pairwise Error Probability (PEP). Besides, assume that the modulation technique for the two different vectors that are mentioned early is the BPSK, besides having equal interfering areas (i.e., area under the tail of the pdf). Then the probability for which the receiver decides speciously is the $k$-th element of $\mathbf{a}_j$, $(\mathbf{a}_j)_k$, while $(\mathbf{a}_i)_k$ ($i \neq j$) has been sent is given by [27]

$$\Pr((\mathbf{a}_i)_k \rightarrow (\mathbf{a}_j)_k|\ \mathbf{H}) = Q\left(\sqrt{\frac{d_{ij}^2}{2\sigma_{BPSK}^2}}\right) \qquad (2.13)$$

where $d_{ij}$ is the Euclidean distance between $(\mathbf{a}_i)_k$ and $(\mathbf{a}_j)_k$ is equal to $|(\mathbf{a}_i)_k-(\mathbf{a}_j)_k|^2$. $\sigma_{BPSK}$ is the standard deviation and can be given by the element-by-element basis from (2.12).

#### *2.2.2.2.2 Minimum Mean Square Error Technique*

The MMSE technique is another example of a linear MIMO technique. It is based on choosing an appropriate function that will minimise the mean square error (MSE) between the transmitted signal and the estimated one, thus the MMSE can be achieved as a result of substituting the function **f(b)** instead of the estimated received signal [31]. This process is clearly can be shown as follows

$$\varepsilon^2 = E\,[(\mathbf{a}\text{-}\mathbf{a}_{est})^H(\mathbf{a}\text{-}\mathbf{a}_{est})]$$
$$= E\,[(\mathbf{a}\text{-}\mathbf{f}(\mathbf{b}))^H(\mathbf{a}\text{-}\mathbf{f}(\mathbf{b}))] \qquad (2.14)$$

Since the MMSE is an example of a linear MIMO technique and an exact function **f(b)** is hard to obtain, by choosing the **f(b)** as a linear processing of the received signal, and simultaneously minimising (2.14) this equation can be written as

$$\varepsilon^2 = E\,[(\mathbf{a}\text{-}\mathbf{a}_{est})^H(\mathbf{a}\text{-}\mathbf{a}_{est})]$$
$$= E\,[(\mathbf{a}\text{-}\mathbf{W}\mathbf{b})^H(\mathbf{a}\text{-}\mathbf{W}\mathbf{b})] \qquad (2.15)$$

In order to find suitable linear processing **W** to minimise (2.15), this equation can be rewritten by making use of $\mathbf{c}^H\mathbf{c} = \mathrm{tr}^4(\mathbf{c}\mathbf{c}^H)$ and observing that the $\mathbf{Q}_b$ is Hermitian[5] and nonnegative as follows

$$\varepsilon^2 = \mathrm{tr}(E\,[(\mathbf{a}\text{-}\mathbf{W}\mathbf{b})(\mathbf{a}\text{-}\mathbf{W}\mathbf{b})^H])$$
$$= \mathrm{tr}(\mathbf{Q}_a\text{-}\mathbf{Q}_{ab}\mathbf{W}^H\text{-}\mathbf{W}\mathbf{Q}_{ba}+\mathbf{W}\mathbf{Q}_b\mathbf{W}^H) \qquad (2.16)$$
$$= \mathrm{tr}(\mathbf{Q}_a - \mathbf{Q}_{ab}\mathbf{A}^{-1}\mathbf{A}\,\mathbf{W}^H - \mathbf{W}\,\mathbf{A}^H(\mathbf{A}^H)^{-1}\mathbf{Q}_{ba} + \mathbf{W}\,\mathbf{A}^H\mathbf{A}\,\mathbf{W}^H)$$
$$= \mathrm{tr}(\mathbf{Q}_a - \mathbf{Q}_{ab}\mathbf{A}^{-1}(\mathbf{A}^H)^{-1}\mathbf{Q}_{ba} + (\mathbf{W}\,\mathbf{A}^H - \mathbf{Q}_{ab}\mathbf{A}^{-1})(\mathbf{W}\,\mathbf{A}^H - \mathbf{Q}_{ab}\mathbf{A}^{-1})^H)$$

where matrix **A** can be defined as the square root of the covariance matrix $\mathbf{Q}_b$. It is obvious that to minimise (2.16),
$\mathbf{W}\,\mathbf{A}^H - \mathbf{Q}_{ab}\mathbf{A}^{-1} = 0$. Then

$$\mathbf{W} = \mathbf{Q}_{ba}\,\mathbf{A}^{-1}(\mathbf{A}^H)^{-1} = \mathbf{Q}_{ba}\,(\mathbf{Q}_b)^{-1} \qquad (2.17)$$

From (2.17), the function that will minimise the MSE between the transmitted and the estimated signal depends on $\mathbf{Q}_{ba}$ and $\mathbf{Q}_b$. where $\mathbf{Q}_{ba}$ is equal to $\mathbf{Q}_a\mathbf{H}^H$ and $\mathbf{Q}_b$ is equal to $\mathbf{H}\mathbf{Q}_a\mathbf{H}^H + \mathbf{Q}_n$ for the general MIMO model in Subsection 2.2.2.

---

[4] tr (.) stands for the trace of a matrix, i.e., the summation of the diagonal elements of the matrix.
[5] The Hermitian transpose is the conjugate transpose of a matrix.

## *2.3Orthogonal Frequency Division Multiplexing*

This section provides an introduction to OFDM transmission, providing all the necessary material to fully understand the proposed technique. Harada and van Nee in [2, 3] give a comprehensive study on multicarrier and OFDM systems.

Historically, OFDM was introduced in 1966 by Chang [32] but was originally hardly considered. Then due to its resistance to slow fading compared to Time Division Multiple Access (TDMA), and also to its simplicity of implementation, it has recently attracted growing interest. Its use was further increased due to the rapid growth in demand for wireless communication services such as live video transmission; mobile games; and various location-based services. These services require higher data rates compared to the data services (short message services) in the second generation (2G). In existing systems, data rates in excess of 1 Mbps are becoming available in the countries that use cdma2000, while Wideband Code Division Multiple Access (WCDMA) promises to provide up to 10 Mbps [33].

To satisfy the requirement for high data rates, various wireless technologies have been introduced to develop the existing 2G and third Generation (3G) cellular systems, and WLAN, which introduces future wireless communication systems such as beyond 3G (B3G) and includes 4G cellular systems. One of the main theoretical challenges is *the bandwidth efficiency*, which has a direct relationship to both the network and physical layers. Beside it *could include powerful coding and modulation techniques, transmission adoption methods and antenna configurations* [8, 34].

For B3G, researchers have increasingly attempted to extend the services available through wired communication systems to mobile wireless systems. These attempts have raised expectations that the development of broadband mobile communications is increasingly likely. For broadband multimedia mobile communication systems, it is necessary to use high bit rate transmissions of at least several megabits per second. The challenge is now to find novel solutions to counter the effects of transmitting

such a huge bit rate through a fading channel with considerable scattering. In addition, if digital data is transmitted at a rate of several megabits per second, the delay time of the delayed waves may exceed one symbol period. Delayed signals interfere with others, which negatively affect the signal. There are several ways to overcome this drawback. For example, using adaptive equalisation techniques at the receiver is one of the ways to equalise the received signal. However, in practice, achieving this equalisation at several megabits per second with compact and low cost hardware is quite difficult. One of the main effects of a mobile radio channel that is characterised by a multipath fading environment is the ISI. This outcome results from the delayed signals generated by the reflection, refraction or diffraction of the signal from terrain features such as trees, hills, mountains, vehicles, or buildings. The ISI causes a significant degradation of network performance. A wireless network must be designed in such a way as to minimise these adverse effects [1, 2].

To overcome such environmental multipath fading effects and achieve a wireless broadband multimedia communication system, it is possible to use a scheme based on OFDM. An OFDM system consists of a parallel data transmission scheme that reduces the effects of multipath fading and renders the need for complex equalisers unnecessary. This technique is essential to future mobile communication systems and WLAN systems such as ETSI BRAN in Europe, IEEE 802.11 in the United States, and ARIB MMAC in Japan [8, 34]. This is the reason behind choosing the OFDM modulation technique over single carrier modulation. The orthogonality in this technique is maintained by adding a cyclic prefix with length greater than the expected delay spread that can be easily implemented by using IFFT [35].

### 2.3.1 OFDM Historical Background

Chang in [32] expressed the basis for contemporary OFDM technique, initially by checking the possibility of transmitting a number of amplitude modulated signals through a band limited channel. The experiments concluded that main problem is to increase system throughput in order to reach the Nyquist rate (the theoretical maximum rate for any channel [36]).

The signals used in orthogonal-multiplexed systems, such as ***sinc*** [6] signals, are characterised by a wide frequency spectrum. However, these signals will cause an information distortion as a result of the filtering process, which occurs due to the transmission process through a band limited channel. To overcome these problems, Chang described a new type of signal - *i.e.*, the band limited signals - without any distortion caused by transmission through such channels. Consequently, the ISI problem can be mitigated if the signals are correctly filtered. Also, depending on the number of symbols, he displayed whether or not the Nyquist rate can be achieved. This can be shown clearly from the following equation of overall throughput as [32]:

$$R = \frac{2N_s BW}{N_s + 1} \tag{2.18}$$

where R is the overall data rate, $N_s$ is the number of symbols used, and BW is the overall baseband bandwidth.

Saltzberg in [37] tried to generalise the proposed work of Chang in [32] by considering the importance of the transmission channel effects on the orthogonal multiplexed system's performance. He also analysed the effects of various channel deteriorations (such as the effect of phase offset, the introduction of delay distortion, and the results of adding amplitude distortion) on Chang's mathematical model. The result of this analysis was compared to the unimpaired model to be the first step towards the realisation of a practical, efficient and parallel channel digital communications system [37].

Two types of division multiplexing technique can be implemented in a parallel system: Frequency Division Multiplexing (FDM) and Time Division Multiplexing (TDM) system. As a comparison in accordance to the sensitivity toward wide-band impulse noise, the FDM system has an advantage over the TDM system [37]. Moreover, parallel transmission (FDM) avoids the dropping of the corrupted signal

---

[6] In digital signal processing and communication theory, the normalised sinc function is commonly defined by **sinc** $(x) = \frac{\sin(\pi x)}{\pi x}$

since it adaptively drops out the corrupted signals. In serial transmission (TDM), if the stream is corrupted, it might disable the whole system. These advantages led researchers into an interesting area, that of the parallel transmission system. Chang and Gibby performed a realisation of parallel systems by analysing the performance of a parallel transmission system under selected channel impairments (jointly considering practical design factors such as timing error, subcarrier phase offset and non ideal filter characteristics) [38].

Generating a parallel data signal can be achieved by arrays of oscillators (sinusoidal generators). In order to achieve the Nyquist rate, Chang in [32] increased the number of parallel channels (2.18) provided. Therefore, in order to satisfy the criteria set down by Chang; a receiver would not be commercially viable.

In 1969, this research area was reinvestigated with the discovery of the production of parallel data by using a Fourier transform. In [39] it was proved that the parallel data signal is similar to the passed serial data stream through a Fourier transform.

Chang's work on this area was patented in 1970. He patented his theoretical model (due to technological constraints) as OFDM [40].

Following the work carried out in 1969 by J. Salz and S. Weinstein, a solution for the ease of generating a large number of subcarriers problems was suggested. This suggestion was based on a fact that parallel data signal is perfectly generated by applying the inverse of the Fourier transform on the original serial data. Concurrently, the demodulation process is attained efficiently by the Fourier transform process. Thus, the function of the modulation and demodulation process can be performed on a computer dedicated to performing the Fast Fourier Transform (FFT) and its inverse [41].

In [41], a modified version of the previous models [32, 37, 38] indicated that the sinusoidal components of the parallel data signal are truncated in the time domain. Due to this truncation process, the power density spectrum of the sinusoids consists of the squared sinc shaped spectra as depicted in Figure 2.5. It should be remembered

that the discrete Fourier transform is still efficient in extracting the data. The figure also shows a negligible overlapping of the spectra, and the peak of the $(sinc(x))^2$ signal occurs at the null of the other $(sinc(x))^2$ signals. This characteristic ensures that no corruption will arise while orthogonality is attained by the correct adjustment of the tracing process.

Furthermore, Weinstein and Ebert in [41] continued to analyse the proposed system under the effects of various channel distortions. The results of this work showed that linear distortion delayed each carrier differently. Consequently, the signal must be analysed when all of the subcarriers are present to overcome the effects of linear distortion. Also, it was concluded that their proposed method did not maintain the orthogonality as in Chang's system as well as only the real part of the Fourier transform was transmitted.

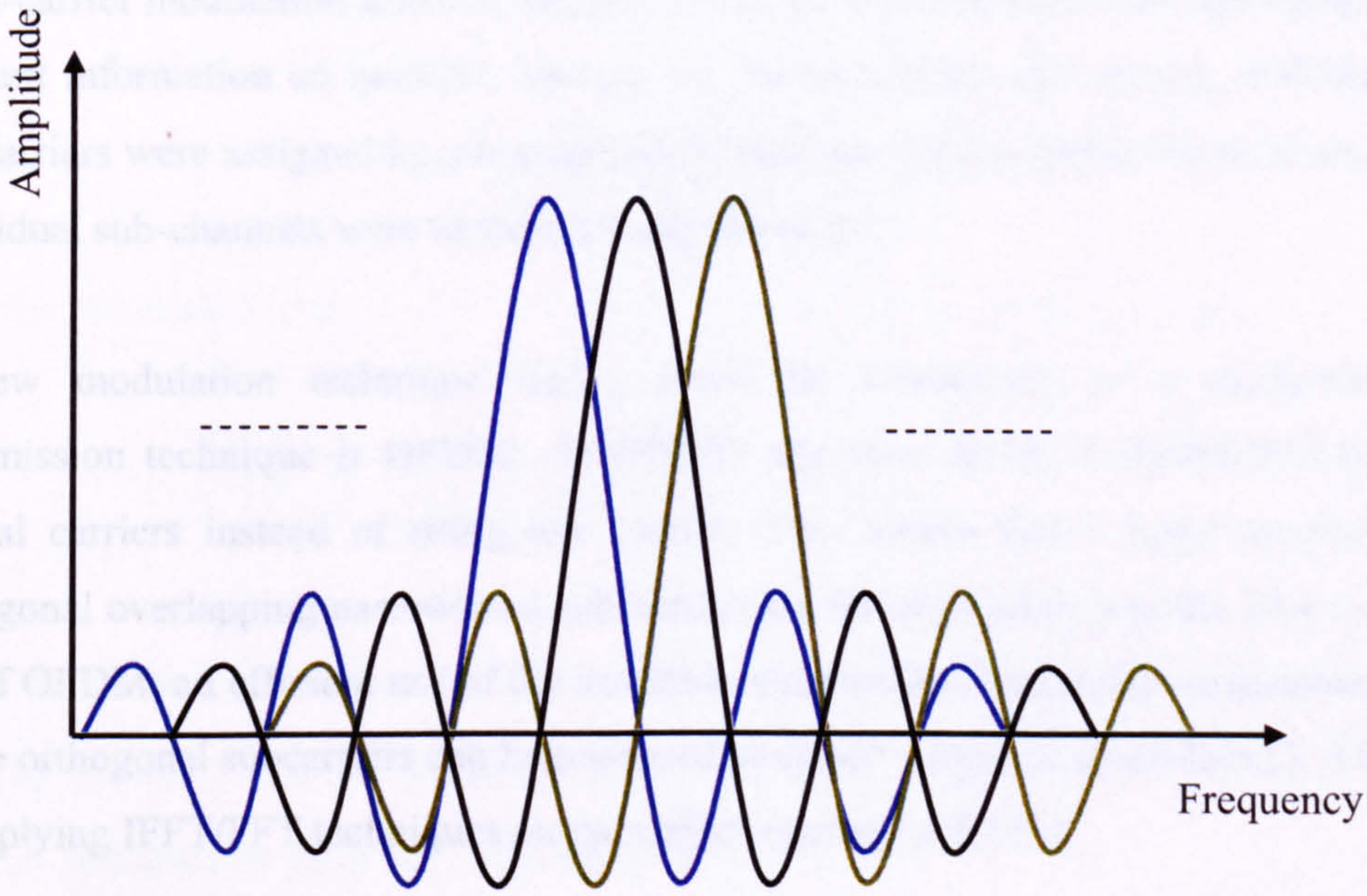


**Figure 2.5: Overlapping the sinc(x) function spectra**

Based on the experiments performed in [42] it was concluded that the theoretical models proposed in [32, 37, 38] could possibly be transformed into a practical solution useful for commercial applications. Besides, the Digital Signal Processing (DSP) methods were being used to implement the *N*-point Fast Fourier Transform (FFT) where *N* is the number of subcarriers.

## 2.3.2 OFDM Basics

Contrary to single-carrier modulation schemes, multi-carrier modulation ones support high data rate applications. A high-rate serial data is divided into low-rate parallel data which modulates a set of subcarriers. Another advantage over single-carrier systems is that signalling intervals are much larger than that of an equivalent single-carrier system, and consequently the time-dispersive effects of a multi-path fading channel can be easily and efficiently reduced without requiring complex time-domain equalisation techniques.

### 2.3.2.1 OFDM Implementation

Multi-carrier modulation schemes initially relied on conventional FDM technology to transmit information on multiple carriers. At the transmitter, the spectra of different sub-carriers were assigned to non-overlapping frequency slots, and at the receiver, the individual sub-channels were retrieved using filters [37].

A new modulation technique which could be considered as a multi-carrier transmission technique is OFDM. In OFDM, the data stream is transmitted using several carriers instead of using one carrier. This means that a large number of orthogonal overlapping narrowband subcarriers are transmitted in parallel. Due to the use of OFDM, an efficient use of the available transmission bandwidth is maintained. These orthogonal subcarriers can be produced by either a bank of oscillators [2, 43] or by applying IFFT/FFT techniques on the transmitter/receiver [41].

#### *2.3.2.1.1 Oscillator-Based*

The structure of an oscillator-based OFDM transmitter is shown in Figure 2.6. $N$ consecutive complex data symbol modulates $N$ complex orthogonal subcarriers which are then added and transmitted. The frequency separation between adjacent subcarriers is equal to the inverse of the signalling interval $T$, which is the minimum frequency separation required to achieve orthogonality between two complex

subcarriers over a signalling interval of length $T$ [30]. For this frequency separation, there is a considerable overlapping between the spectra of the different subcarriers but the information can still be reliably recovered. An OFDM symbol is then given by the following figure [2]

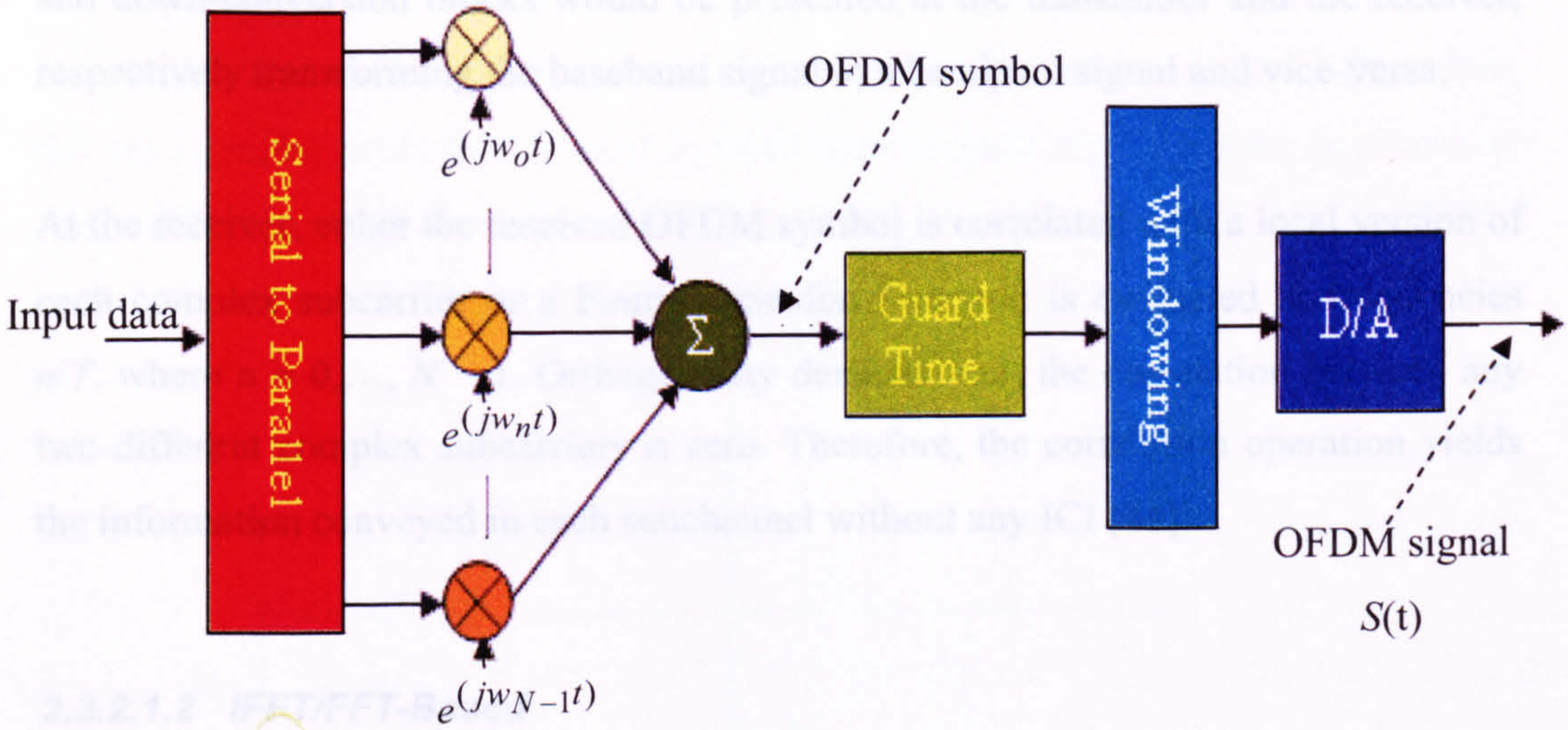


**Figure 2.6: OFDM signal generation**

After the summation stage and D/A converter, the output of the transmitter is

$$S(t) = \sum_{k=-\infty}^{\infty} \sum_{i=0}^{N-1} d_i(k) \exp(j2\pi f_i(t+\beta_i)) \tag{2.19}$$

where $d_i$ is $i$-th input data, $f_i$ ( i = 0, 1, …. ) is the frequency of the $i_{th}$ subcarrier given by $f_i$, and $\beta$ is initial phase on the subcarrier. For simplicity, let $\beta = 0$ and $f_i = i/(N\,T_d)$. The discrete form of (2.19) is then

$$s^m[kT_d] = \sum_{i=0}^{N-1} d_i^m \exp(j2\pi \frac{i}{NT_d} kT_d)$$

$$s^m[k] = IFFT(d^m) \tag{2.20}$$

where $T_d$ is the time duration of the $i$-th input data from the $m$-th data block, $d_i^m$ . It is well known that OFDM is very sensitive to frequency offset and phase noise that

causes Inter Carrier Interference (ICI). Accordingly, the orthogonality of subchannels in OFDM must therefore be guaranteed. This can be maintained by different methods such as by using time domain windowing [44]. The guard time and the windowing blocks are described later in Subsections 2.3.2.1 and 2.3.2.2. In a typical system, up- and down-conversion blocks would be presented at the transmitter and the receiver, respectively transforming the baseband signal to a bandpass signal and vice-versa.

At the receiver, either the received OFDM symbol is correlated with a local version of each complex subcarrier or a Fourier transform version is evaluated at frequencies $n/T$, where $n = 0,\ldots, N-1$. Orthogonality demands that the correlation between any two different complex subcarriers is zero. Therefore, the correlation operation yields the information conveyed in each subchannel without any ICI [44].

#### *2.3.2.1.2 IFFT/FFT-Based*

In [41], the authors have indicated that OFDM generation and detection can be achieved by employing an IFFT and a FFT at the transmitter and the receiver respectively. An oscillator-based OFDM system includes a bank of oscillators both at the transmitter and the receiver, and hence is hardware intensive. Thus the IFFT/FFT based implementation is highly preferable [41].

Referring to (2.20), the OFDM signal generation is shown in Figure 2.7. The OFDM symbol can be generated by conveying the IFFT of the input data in each subcarrier.

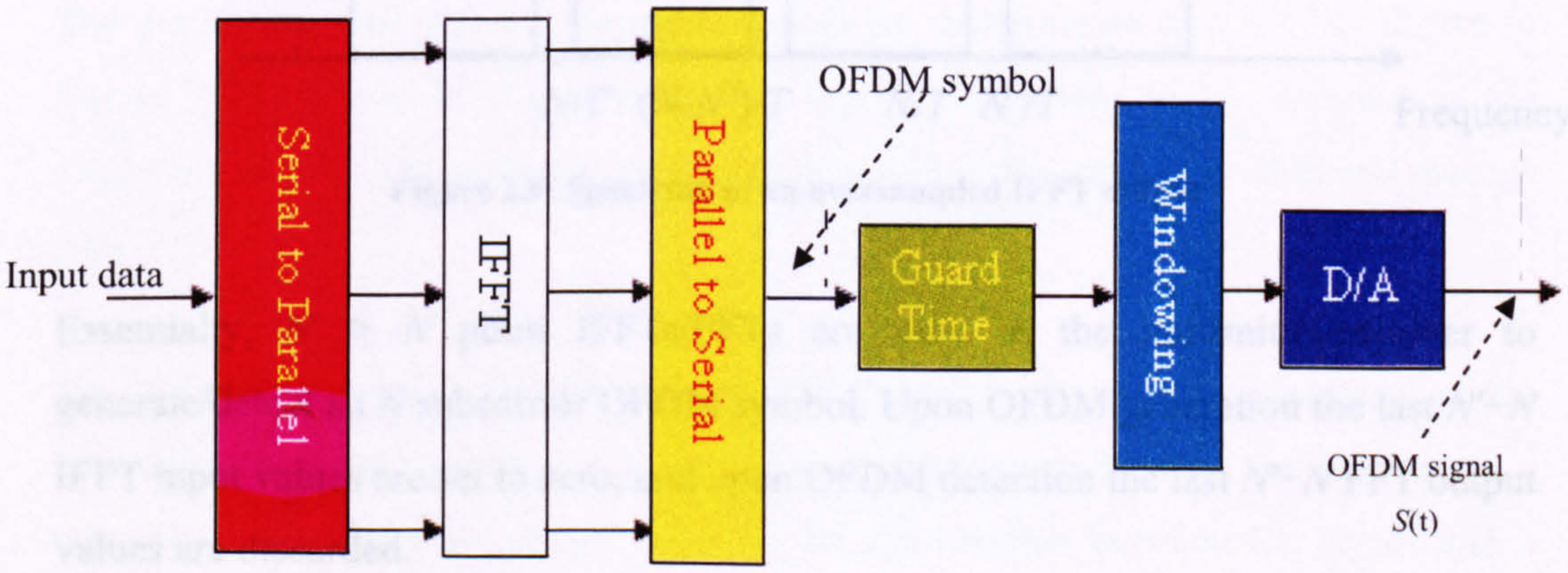


**Figure 2.7: IFFT based OFDM signal generation**

In order to yield the continuous-time signal from the discrete-time signal, the required oversampling cannot be practically achieved by taking $N$ samples per OFDM symbol. Figure 2.8 shows the spectrum of a nonoversampled IFFT output. It is obvious that a filter with a realistic passband-to-stopband transition region cannot be used to recover the continuous-time OFDM symbol from its samples. The solution is to increase the sampling rate to the m-Nyquist rate, where m is a positive integer number. Therefore, the zero padding technique is used to fulfil the required sampling rate, as shown in Figure 2.9 [2]

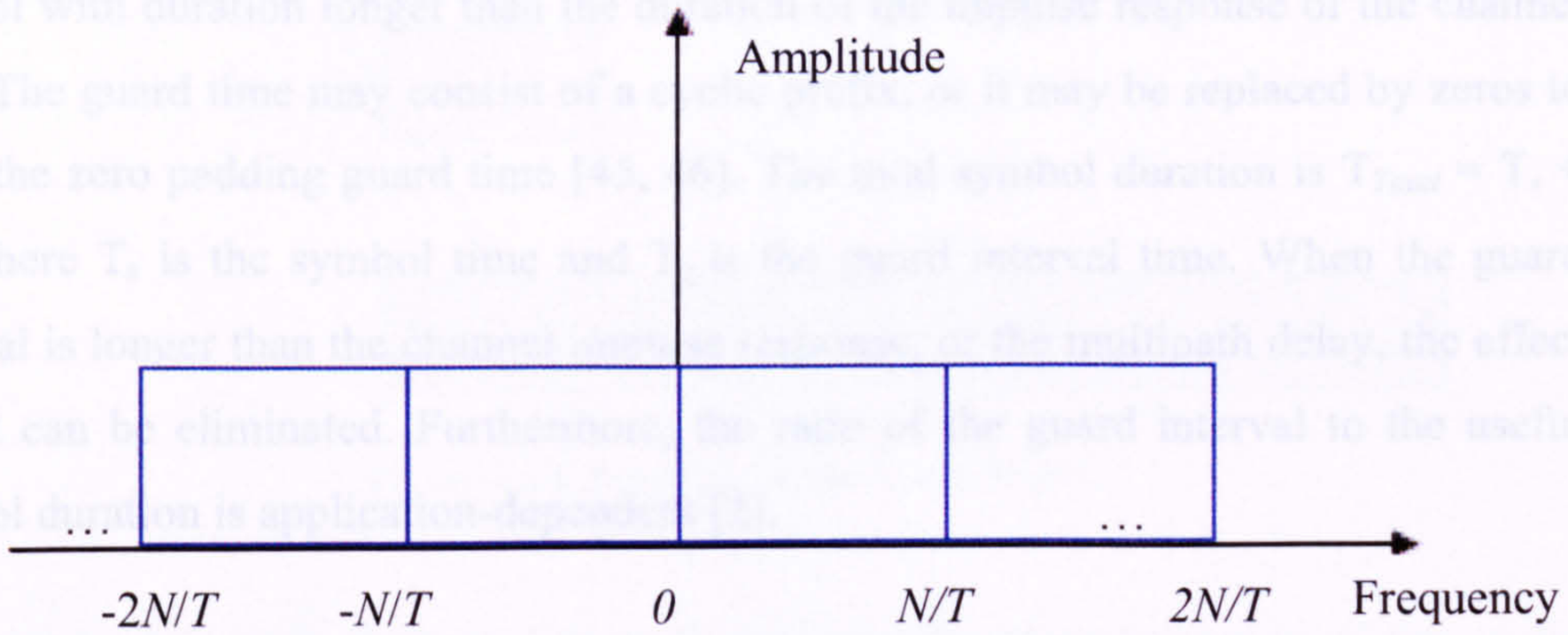


**Figure 2.8: Spectrum of a non-oversampled IFFT output**

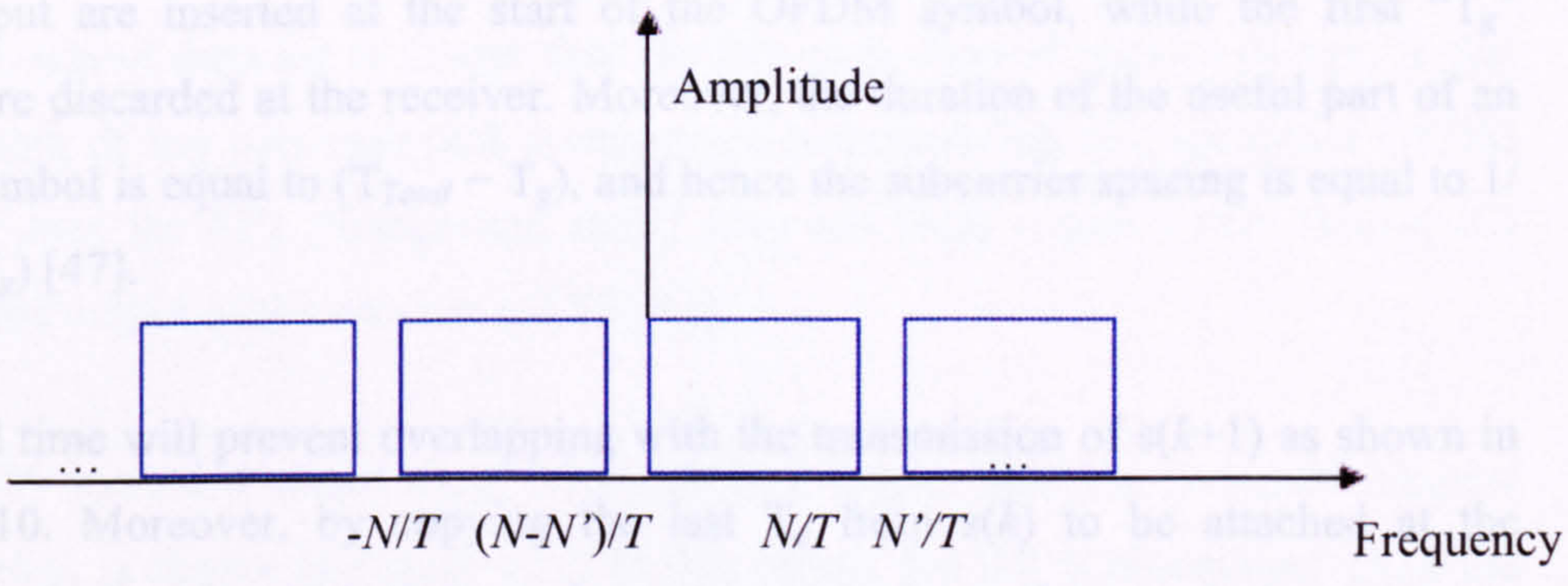


**Figure 2.9: Spectrum of an oversampled IFFT output**

Essentially, $N' > N$ point IFFTs/FFTs are used at the transmitter/receiver to generate/detect an $N$ subcarrier OFDM symbol. Upon OFDM generation the last $N'-N$ IFFT input values are set to zero, and upon OFDM detection the last $N'-N$ FFT output values are discarded.

### 2.3.2.2 Guard Time (Cyclic Prefix and Zero Padding)

OFDM has an advantage over single carrier modulation in handling multipath delay. Dividing the input data stream into *N* subcarriers reduces the symbol duration. By transmitting information on *N* subcarriers, the symbol duration of an OFDM signal becomes *N* times longer than the symbol duration of an equivalent single carrier signal. Accordingly, ISI effects induced by linear time dispersive channels are minimised. To eliminate ISI completely, a guard time is introduced for each OFDM symbol with duration longer than the duration of the impulse response of the channel [41]. The guard time may consist of a cyclic prefix, or it may be replaced by zeros to form the zero padding guard time [45, 46]. The total symbol duration is $T_{Total} = T_s + T_g$, where $T_s$ is the symbol time and $T_g$ is the guard interval time. When the guard interval is longer than the channel impulse response, or the multipath delay, the effect of ISI can be eliminated. Furthermore, the ratio of the guard interval to the useful symbol duration is application-dependent [2].

Cyclic extension of an OFDM symbol is shown in Figure 2.10. Note that in the presence of linear time dispersive channels, an appropriate guard time avoids ISI but not ICI unless it is cyclically extended. At the transmitter, the last "$T_g$" samples of the IFFT output are inserted at the start of the OFDM symbol, while the first "$T_g$" samples are discarded at the receiver. Moreover, the duration of the useful part of an OFDM symbol is equal to ($T_{Total} - T_g$), and hence the subcarrier spacing is equal to 1/ ($T_{Total} - T_g$) [47].

The guard time will prevent overlapping with the transmission of s($k$+1) as shown in Figure 2.10. Moreover, by copying the last $T_g$ from s($k$) to be attached at the beginning of s($k$), r($k$) will be independent of s($k$-1) in the cycle convolutional process [48].

The frequencies used in OFDM are regularly spaced in the spectrum required, so the time domain signal s'($k$) has to be limited in the frequency domain. For this reason a spectrum limitation must be provided by the convolution between the signal and a

window function that has a spectrum bounded exactly on the required one [48]. As example, windowing each OFDM symbol by a raised cosine window [2].

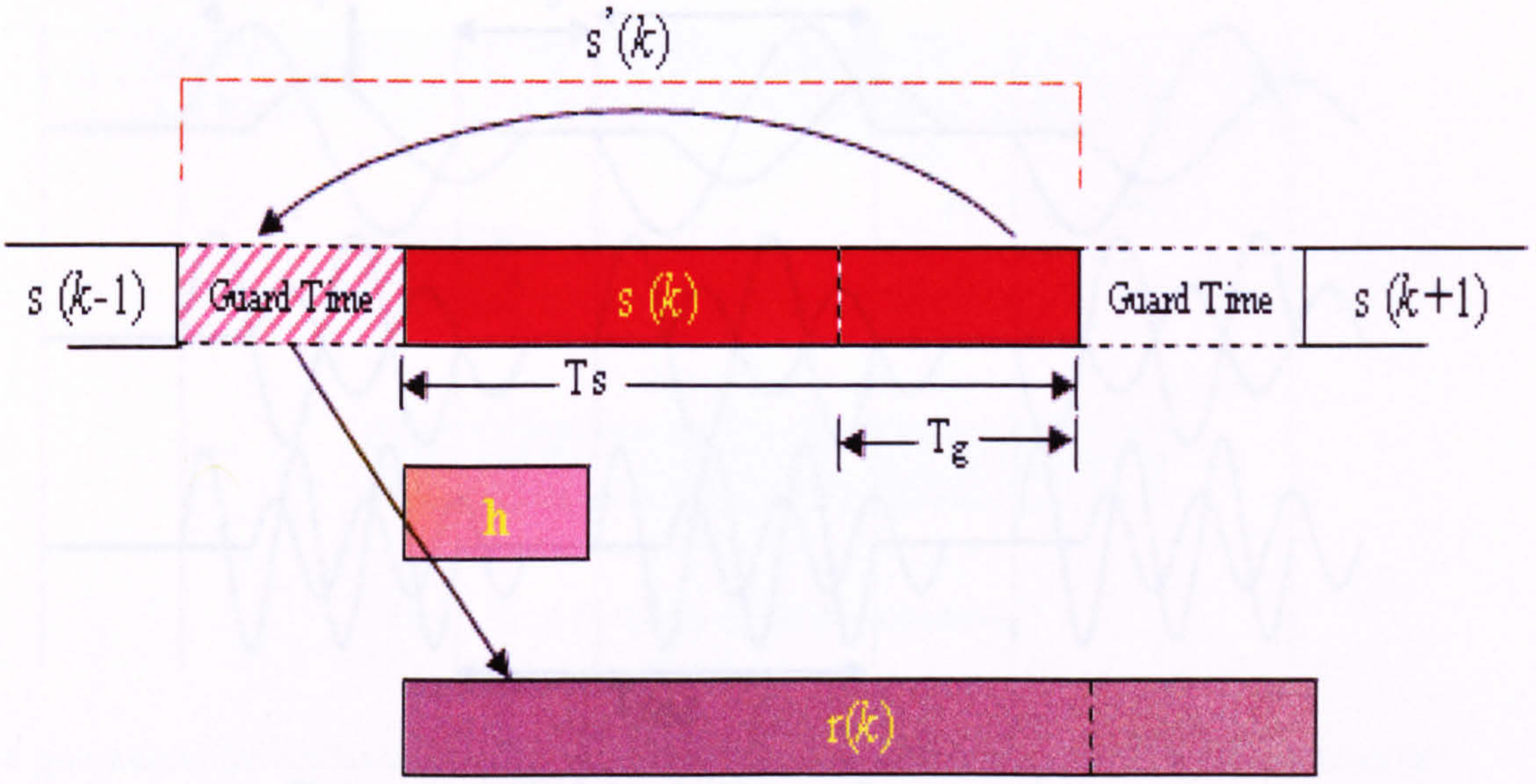


**Figure 2.10: Principle of the Cyclic Prefix.**

Assuming a two-path channel, this is to evaluate the basic operation of the cyclic prefix. Two replicas of the transmitted OFDM signal are combined to form the received signal. As a channel effect, the received OFDM signal possibly attenuated and delayed with respect to itself. Figure 2.11 shows the principle of an ordinary guard time whose duration is longer than the two-path channel relative delays. In this case, the sum of any two multipath components corresponding to a particular OFDM subcarrier over the FFT "integration time" does not yield a sine wave. Hence, ICI occurs at the output of the receiver's FFT [41].

A cyclically extended guard time, with duration longer than the two-path channel relative delay, is shown in Figure 2.12. In this figure, the ICI is eliminated. Over the $T_{Total}$ the sum of any two multipath components corresponding to a particular OFDM subcarrier yields an attenuated/phase rotated version of the same subcarrier [48].

Specifically, the amplitude/phase rotation of the *n*-th complex data symbol corresponds to the amplitude/phase of the frequency response of the two-path channel evaluated at the n-*th* subcarrier frequency.

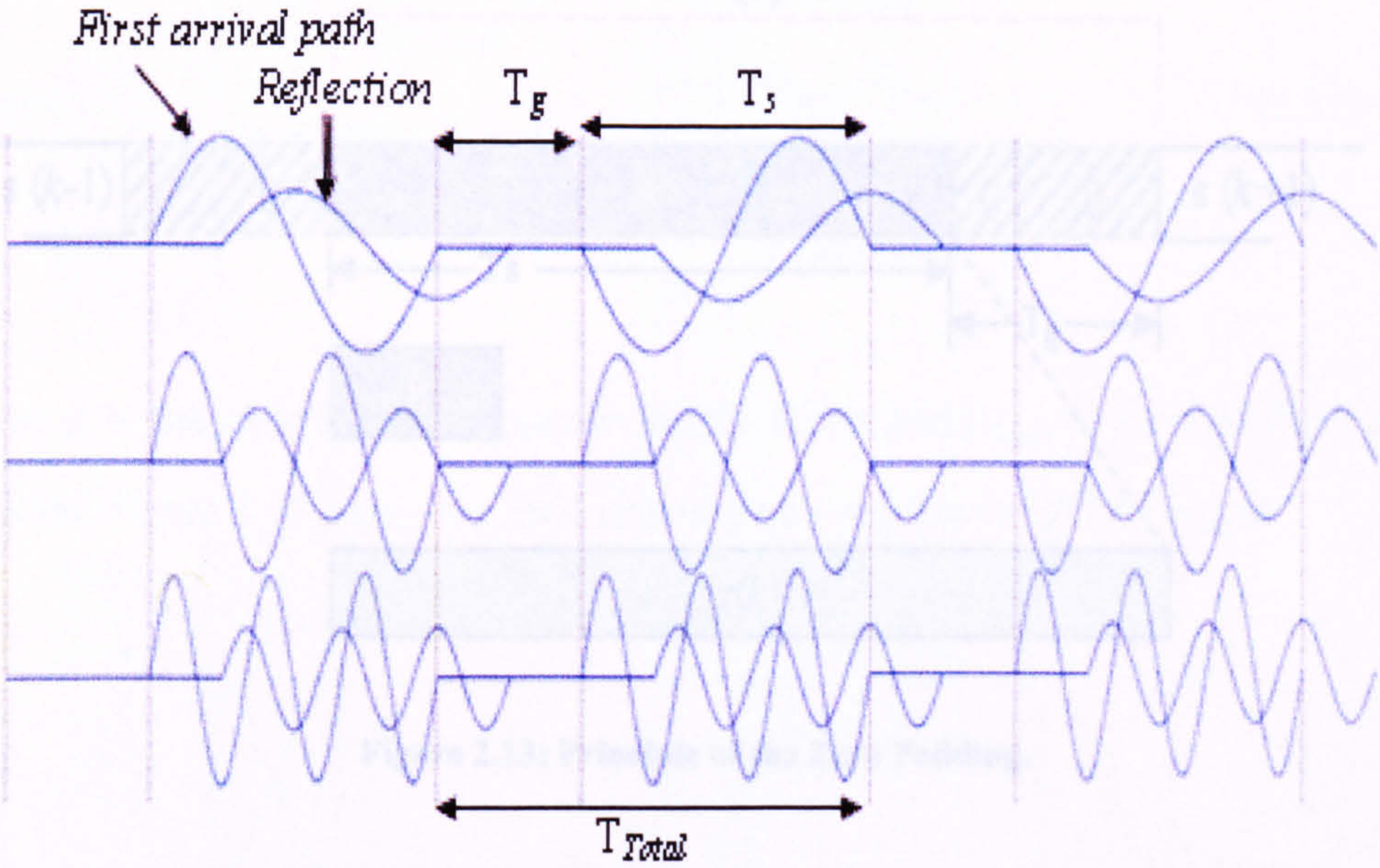


**Figure 2.11: OFDM signal with an ordinary guard time.**

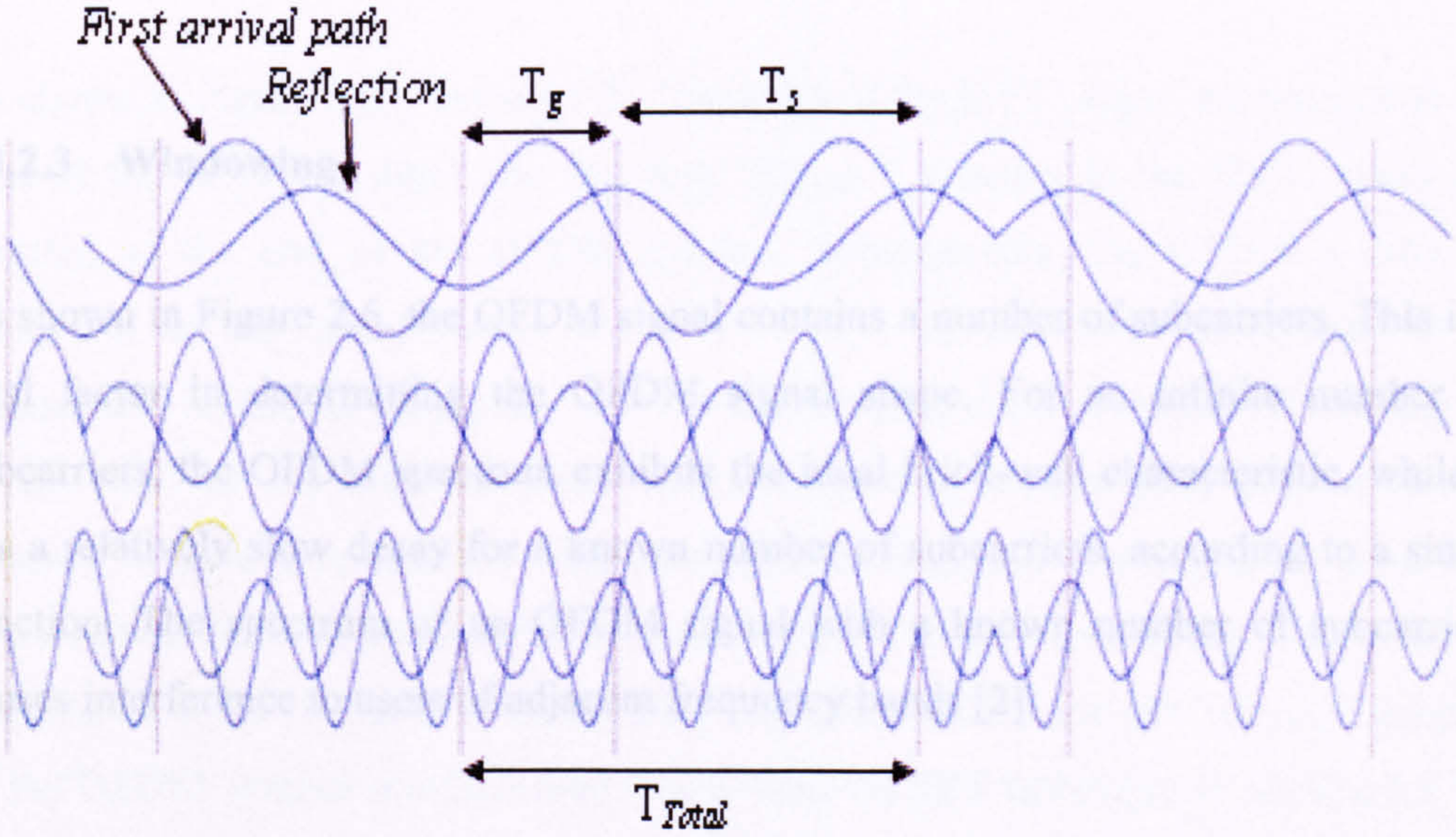


**Figure 2.12: OFDM signal with a cyclic prefix guard time.**

An obvious problem of the cyclic prefix OFDM system is that the transmitted symbols cannot be recovered, even in absence of noise, when some channel zeros are located on subcarriers. Thus, it has been recently proposed to replace the cyclic prefix by the padding of zeros. As shown in Figure 2.13 [46, 49]

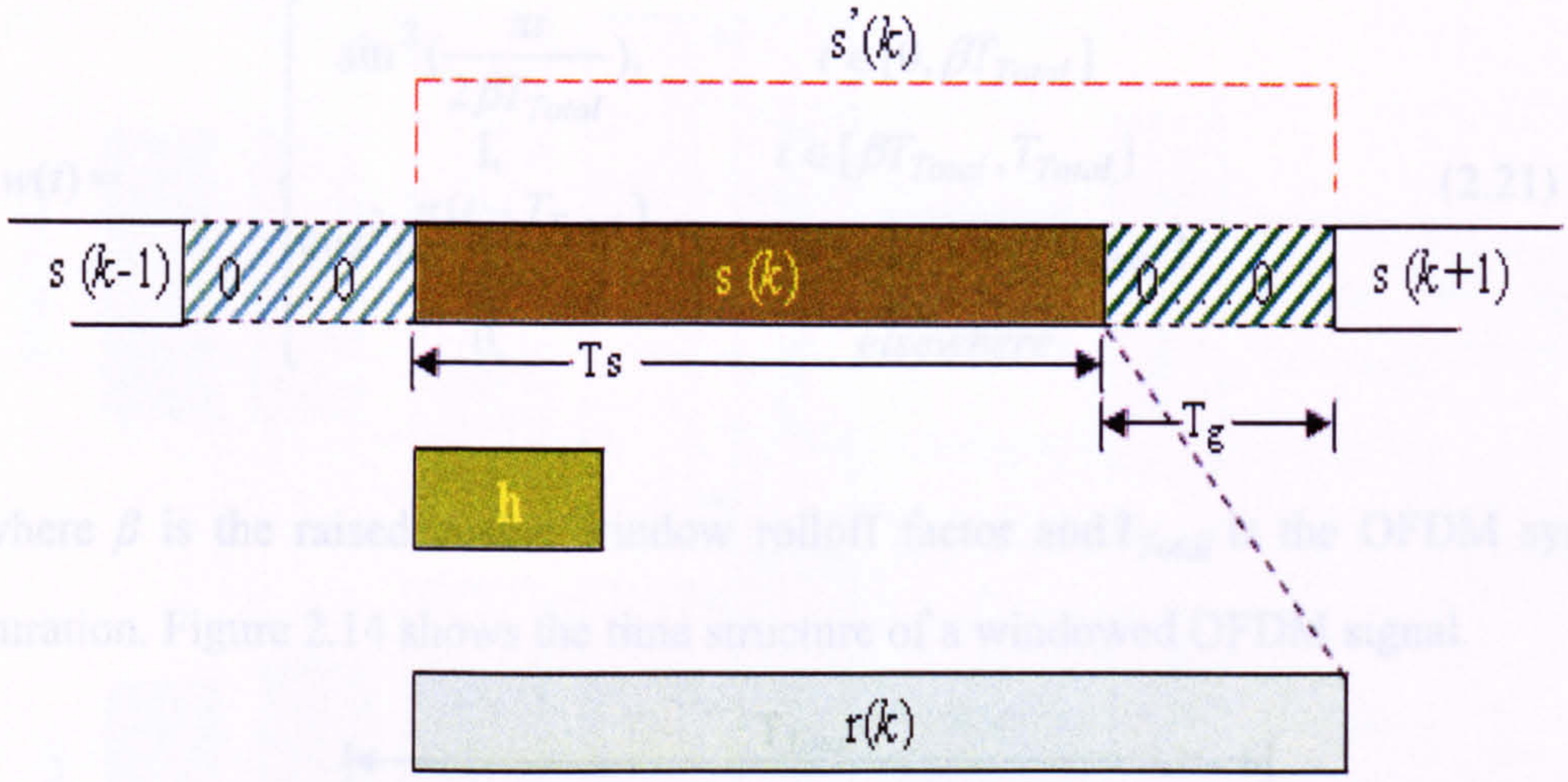


**Figure 2.13: Principle of the Zero Padding.**

To guarantee the retrieval process of s($k$), the zeros at the end of s($k$) leads to a larger number of observations of r($k$) than the number of s($k$). In Figure 2.10, s'($k$) denotes the new symbol after the insertion of the guard time [49].

### 2.3.2.3 Windowing

As shown in Figure 2.6, the OFDM signal contains a number of subcarriers. This is a vital factor in determining the OFDM signal shape. For an infinite number of subcarriers, the OFDM spectrum exhibits the ideal brick-wall characteristic, while it has a relatively slow decay for a known number of subcarriers, according to a sinc() function. The spectrum of an OFDM signal with a known number of subcarriers causes interference to users of adjacent frequency bands [2].

According to [2, 41], a raised cosine window is often used to allow the amplitude of an OFDM symbol to go smoothly to zero at the symbol boundaries. The raised cosine window is given by

$$w(t) = \begin{cases} \sin^2(\dfrac{\pi t}{2\beta T_{Total}}), & t \in [0, \beta T_{Total}] \\ 1, & t \in [\beta T_{Total}, T_{Total}] \\ \cos^2(\dfrac{\pi(t - T_{Total})}{2\beta T_{Total}}), & t \in [T_{Total}, (1+\beta)T_{Total}] \\ 0, & elsewhere \end{cases} \quad (2.21)$$

where $\beta$ is the raised cosine window rolloff factor and $T_{Total}$ is the OFDM symbol duration. Figure 2.14 shows the time structure of a windowed OFDM signal.

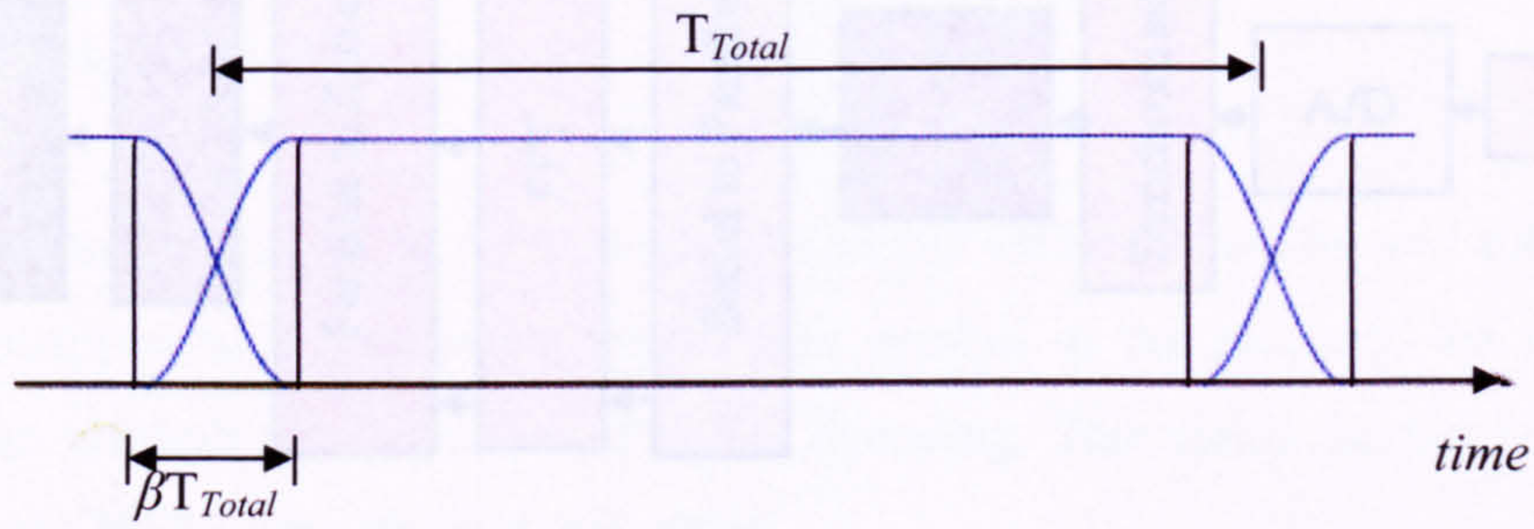


**Figure 2.14: Time structure of a windowed OFDM signal.**

As shown in Figure 2.14, the last " $T_g$ " samples of the IFFT output are inserted at the start of the OFDM symbol and the first "$\beta T_{Total}$ " samples of the IFFT output are inserted at the end of the OFDM symbol. Subsequently, the OFDM symbol is multiplied by the raised cosine window. Finally, the signal is upconverted to be transmitted. Multipath fading and AWGN contaminate the transmitted OFDM signal. At the receiver, the received signal r($k$) is filtered by a band pass filter, which is assumed to have a sufficiently wide pass band to introduce only negligible distortion in the signal. An orthogonal detector is then applied to the signal at the point of down conversion to the IF band. Then, the first "$T_g$" samples and the last "$\beta T_{Total}$" samples of the OFDM symbol are discarded. After that, the FFT technique is applied for the received signal. This process will obtain the Fourier coefficients of the signal in observation periods [2].

### 2.3.3 OFDM Communications Systems Elements

Figure 2.15 depicts the principal elements of the conventional OFDM communication system. It is meant that the OFDM system is without multiple antenna technology.

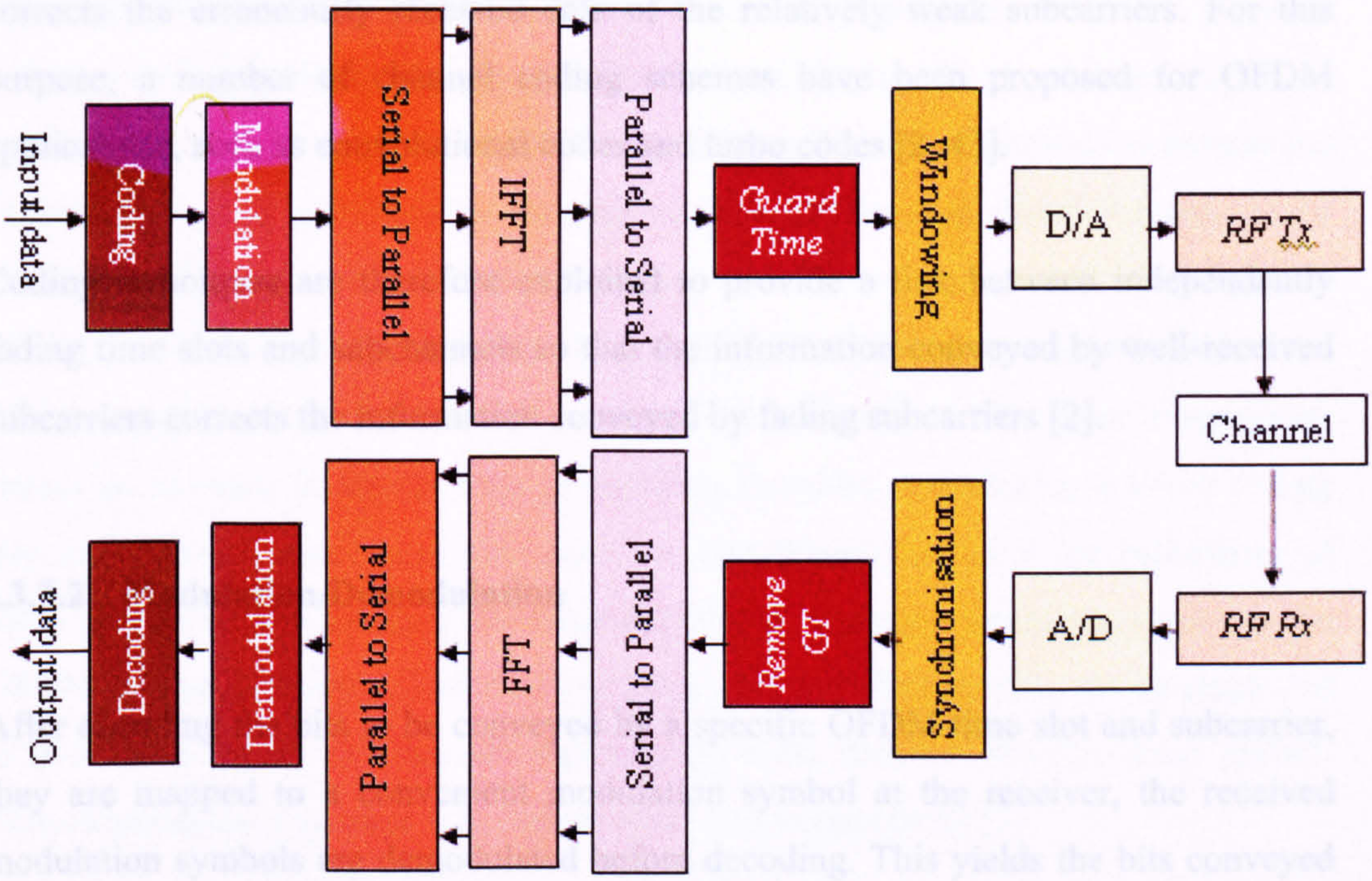


**Figure 2.15: OFDM communication system**

Subsection 2.3.2.1 introduces the role of OFDM implementation, guard time and windowing. In this section, the other elements of the OFDM communication system: encoders/decoders, and modulator/demodulator techniques are considered.

### 2.3.3.1 Coding/Decoding

During the transmission and reception process, the received symbol is an attenuated and phase shifted version of the transmitted symbol, where the attenuation and phase shift are given by the frequency response of the channel evaluated at the subcarrier frequency assigned for this symbol. According to a Rayleigh distributed channel, some subcarriers will be amplified whereas and others attenuated, resulting in high and low SNR based decisions at the receiver. In the presence of Rayleigh fading, the error rate decreases inversely with SNR whereas in the absence of this fading, the error rate decreases exponentially with the SNR [30].

Channel coding techniques are used to correct errors in the received data. In OFDM with channel coding, the correctly received data of the relatively strong subcarriers

corrects the erroneously received data of the relatively weak subcarriers. For this purpose, a number of channel coding schemes have been proposed for OFDM applications, such as convolutional codes and turbo codes [2, 43].

Coding techniques are therefore exploited to provide a link between independently fading time slots and subchannels so that the information conveyed by well-received subcarriers corrects the information conveyed by fading subcarriers [2].

### 2.3.3.2 Modulation/Demodulation

After encoding the bits to be conveyed by a specific OFDM time slot and subcarrier, they are mapped to a convenient modulation symbol at the receiver, the received modulation symbols are demodulated before decoding. This yields the bits conveyed in their own OFDM time slot and subcarrier.

Examples of this modulation technique include M-ary phase shift keying (M-PSK) or M-ary quadrature amplitude modulation (M-QAM), where groups of $\log_2 M$ bits are mapped to a particular point in an M-PSK or an M-QAM signal constellation. As an example, Figure 2.16 illustrates Gray coded 16-PSK and 16-QAM signal constellations. In this figure, binary digit words assigned to adjacent symbol states differ by one binary digit only [2].

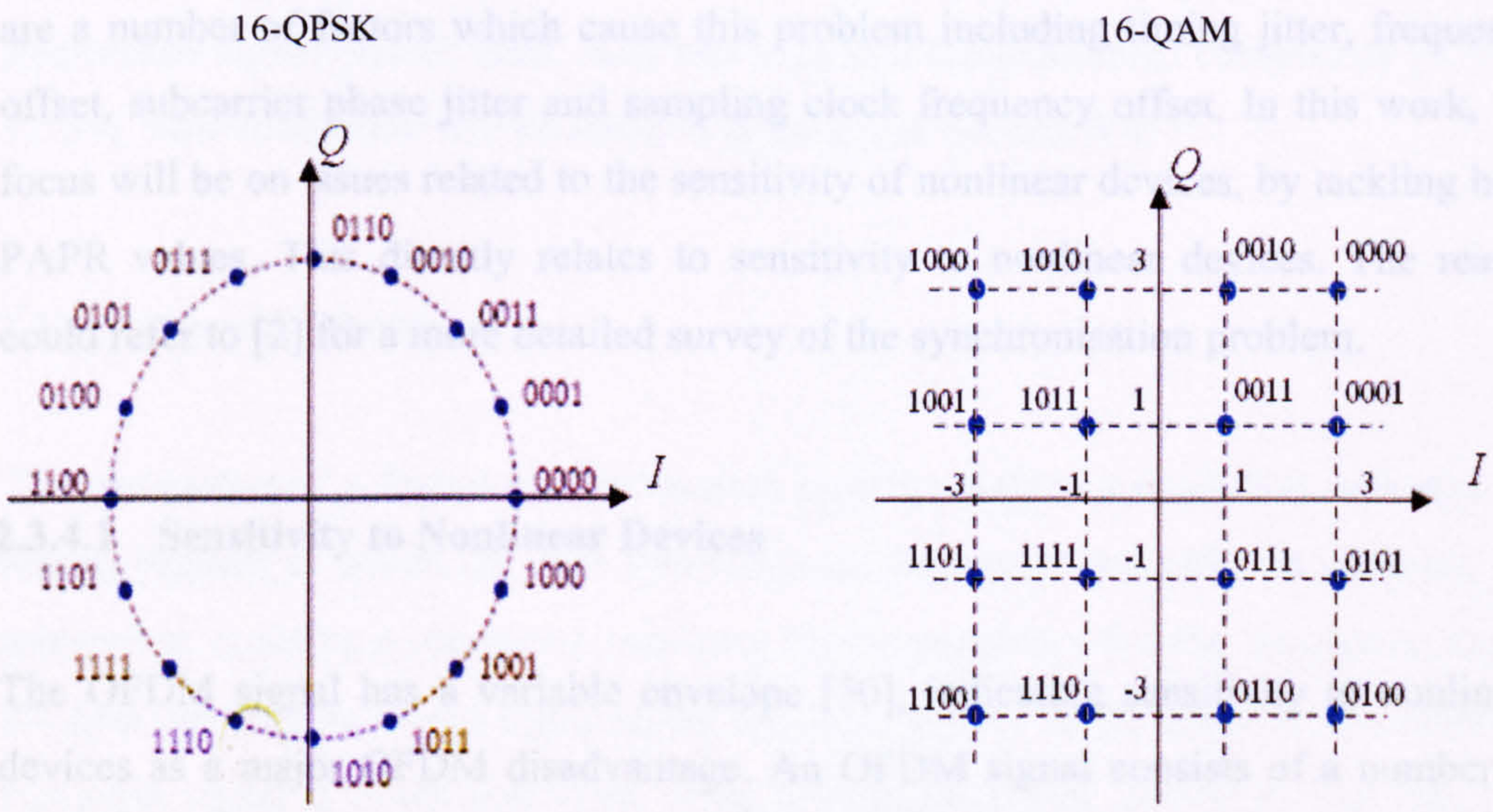


**Figure 2.16: Gray coded 16-PSK and 16-QAM signal constellations.**

The constellation level of the modulation technique plays a vital role in some communication systems. In any modulation technique, the modulated signal is quantised in both its in-phase and 90° components. The set of possible combinations of different values is defined by the constellation. Different modulation types can be used in accordance with the relationship between the constellation size and the power. For single carrier systems with equalisers, the performance degrades abruptly if the delay spread exceeds the threshold value of the equaliser. The error propagation causes an increase in the bit error probability; therefore, introducing a lower coding rate or a lower constellation size does not significantly improve the robustness of delay spread. On the contrary, the nonlinear effects of error propagation vanish in the OFDM system. Moreover, lower coding rates and constellation sizes can be employed to provide fallback rates that are significantly more resistant towards delay spread. This enhances the coverage area and prevents non-connectivity [2].

### 2.3.4 OFDM Drawbacks

Sensitivity to nonlinear devices and synchronisation are the two major problems being faced by OFDM transmission. The nonlinear devices such as HPA clip the amplitudes of OFDM signals containing greater power levels than its own range, causing the adjacent channel interference problem. In the OFDM link, orthogonality must be maintained amongst the subcarriers in order to avoid synchronisation problems. There are a number of factors which cause this problem including timing jitter, frequency offset, subcarrier phase jitter and sampling clock frequency offset. In this work, the focus will be on issues related to the sensitivity of nonlinear devices, by tackling high PAPR values. This directly relates to sensitivity to nonlinear devices. The reader could refer to [2] for a more detailed survey of the synchronisation problem.

#### 2.3.4.1 Sensitivity to Nonlinear Devices

The OFDM signal has a variable envelope [50], indicating sensitivity to nonlinear devices as a major OFDM disadvantage. An OFDM signal consists of a number of independently modulated subcarriers, which can produce a high PAPR when added up

coherently with the same phase, sometimes reaching up to $N$ times the average power where $N$ is the total number of subcarriers. The PAPR value can be very high in certain input sets of samples and can cause the system to enter a non-linear mode of operation [51].

The signal with high PAPR values will suffer from different problems if it passes through nonlinear devices, such as converters, mixers, and power amplifiers [48]. These problems are:

- significant spectral spreading and in-band distortion causing intermodulation among different subcarriers
- undesired out-of-band radiation
- quantisation noise, affecting the system's performance

These problems result in increased system complexity and reduced power amplifier efficiency. This deficiency can be mitigated by a number of techniques proposed for tackling the PAPR problem. These include amplitude clipping; clipping and filtering; coding; and multiple signal representation techniques. It has been shown [6] that amplitude clipping leads to an increase in the BER, while coding schemes decrease the net bit rate.

Generally, these techniques achieve PAPR reduction at the expense of an increase in transmitted signal power, BER, data rate loss, and computational complexity [4, 5, 7, 52-58]. This subsection will be covered in details in Section 2.4.

#### 2.3.4.2 Synchronisation

The transmitter of a digital communication system contains a clock that indicates the timing instants at which the data symbols must be transmitted [48]. In addition, the transmitter contains a subcarrier oscillator that is necessary for the up conversion of the data carrying baseband signal to the bandpass signal. At the receiver, the received bandpass signal is down converted using a local subcarrier oscillator. The resulting signal is sampled at timing instants determined by the receiver clock [59]. Therefore,

at the receiver, the sampling process must be carried out in order for the correct sequence to recover the received data on the subcarriers. This problem is caused by various factors, such as frequency offset and phase noise. An increased guard interval between OFDM subcarriers could reduce this problem as shown by [2]. Moreover, different techniques are proposed in the literature to tackle synchronisation deficiency, such as timing recovery [60], blind equalisation, and tone reservation [61, 62].

Differences between the transmitter and receiver local oscillators will result in frequency offset, causing ICI and degrading the orthogonality of subcarriers. For more details, the reader could refer to [2, 63, 64].

A local oscillator in a receiver introduces phase noise. It can be interpreted as a parasitic phase modulation in the oscillator's signal, especially when the oscillator line width is much smaller than the OFDM symbol rate. The phase noise could have two effects; a Common Phase Error (CPE) due to the rotation of the signal constellation, and ICI [2]. The CPE can be rectified by using reference information within the same symbol. Unfortunately, ICI is more difficult to overcome due to the additive noise, which is different for all subcarriers. This difference can be interpreted as a loss of orthogonality [48].

A general model capable of making accurate, quantitative predictions about phase noise is introduced in [58]. For different types of electrical oscillators, this model acknowledges the true periodically time-varying nature of all oscillators.

## *2.4 The PAPR Problem*

As has been described earlier in this chapter, multi-carrier signal large envelope fluctuations cited as a major drawback of OFDM since all practical transmissions systems are peak-power limited. Therefore, designing any system to operate in a linear region often implies operating at average power levels below the maximum power available.

Additional nonlinear distortion must be allowed in order to avoid operating the amplifiers (nonlinear devices) with extremely large back-offs occasional saturation of the power amplifiers or clipping in the DAC. This will create inter-modulation distortion that increases the bit error rate in standard linear receivers, also causing spectral widening of the transmit signal that increases adjacent-channel interference to other users. The focus of this section is to introduce the problem of PAPR and provide most of the necessary background information for understanding the subsequent chapters [2].

The next subsection elaborates on the fluctuating envelope phenomenon. The statistical properties of PAPR are covered in section 2.4.2, while Section 2.4.3 will cover the effect of this phenomenon on system performance. Section 2.4.4 will review some of the conventional techniques to tackle PAPR that have been proposed in the literature.

### 2.4.1 PAPR Concepts

Typically, PAPR quantifies the signal's fluctuating envelope. The PAPR of a signal $s_\tau$, where $\tau$ represents time index shown in (2.19) is defined in [2] as:

$$\mathrm{PAPR}\{s_\tau\} = \frac{\max_{\tau \in T} |s_\tau|^2}{E\{|s_\tau|^2\}} \tag{2.22}$$

where $\max_{\tau} |s_\tau|^2$ denotes maximum instantaneous power (i.e., the instantaneous power is defined by the maximum of squared absolute value of the sample at each time index), $E\{|s_\tau|^2\}$ denotes the average power of the signal and $\tau \in T$ is the interval over which the PAPR is evaluated. Moreover, $s_\tau$ can be replaced by the full definition of an OFDM symbol, (i.e. OFDM symbol with cyclic prefix, and zero padding, or the over-sampled OFDM symbol). Throughout this thesis, 'PAPR' will refer to baseband

PAPR. For the passband transmission, the transmitted multi-carrier signal denoted by $S(t)$ which is modulated onto a carrier frequency $f_c$,

$$\begin{aligned} S_{PB}(t) &= \mathrm{Re}\{S(t)e^{j2\pi f_c t}\} \\ &= \mathrm{Re}\{S(t)\}\cos(2\pi f_c t)\} - \mathrm{jIm}\{S(t)\}\sin(2\pi f_c t)\} \\ &= S_I(t)\cos(2\pi f_c t) \pm S_Q(t)\sin(2\pi f_c t) \end{aligned} \tag{2.23}$$

Since the carrier frequency is usually much higher than the signal bandwidth, the maximum of the modulated signal is the same as the maximum of the baseband signal. As an example for a QAM modulated signal $x(t)$, the average power of the imaginary and the real parts are defined as $E\{|x_I(t)|^2\} = E\{|x_Q(t)|^2\} = \frac{1}{2}E\{|x(t)|^2\}$.

From (2.23) the average power can be written as

$$E\{|S_{PB}(t)|^2\} = \frac{1}{2}E\{|S_I(t)|^2\} + \frac{1}{2}E\{|S_Q(t)|^2\} = \frac{1}{2}E\{|S(t)|^2\} \tag{2.24}$$

Thus, passband PAPR is roughly twice the baseband PAPR. Moreover, since the cyclic prefix is just a replica of the last samples from the OFDM symbol, it does not change the average or peak power, therefore, (2.24) will remain the same with or without the cyclic prefix [2].

### 2.4.2 Statistical Properties for PAPR

For simplicity, assuming the input data to the OFDM modulator is i.i.d with zero mean and unit variance. From (2.19), the resultant OFDM symbol samples with large values of $N$ are i.i.d Gaussian random variables with zero mean and unit variance as each sample is a linear combination of Gaussian random variables [65]. The Cumulative Distribution Function (CDF) of random variable PAPR $\{s^m[k]\}$ has a simple closed form distribution as follows [66]

$$\Pr\{\text{PAPR}\{s^m[k]\}<\rho^2\}=\Pr\{\frac{\left|s^m[0]\right|^2}{E\{\left|s^m[k]\right|^2\}}<\rho^2,\ldots,\frac{\left|s^m[N-1]\right|^2}{E\{\left|s^m[k]\right|^2\}}<\rho^2\}$$

$$=[\Pr\{\frac{\left|s^m[k]\right|^2}{E\{\left|s^m[k]\right|^2\}}<\rho^2\}]^N \tag{2.25}$$

where, $s^m$ is the $m$-th OFDM symbol as defined by (2.19), $\rho$ is a PAPR threshold. For real multi-carrier case, the symbol CDF of $\text{PAPR}\{s^m[k]\}$ is

$$\Pr\{\text{PAPR}\{s^m[k]\}<\rho^2\}=(1\text{-}2Q(\rho))^N \tag{2.26}$$

The Complementary CDF (CCDF) is

$$\Pr\{\text{PAPR}\{s^m[k]\}>\rho^2\}=1\text{-}(1\text{-}2Q(\rho))^N \tag{2.27}$$

where $Q()$ is the error function, where the standard normal cdf can be expressed in terms of it.

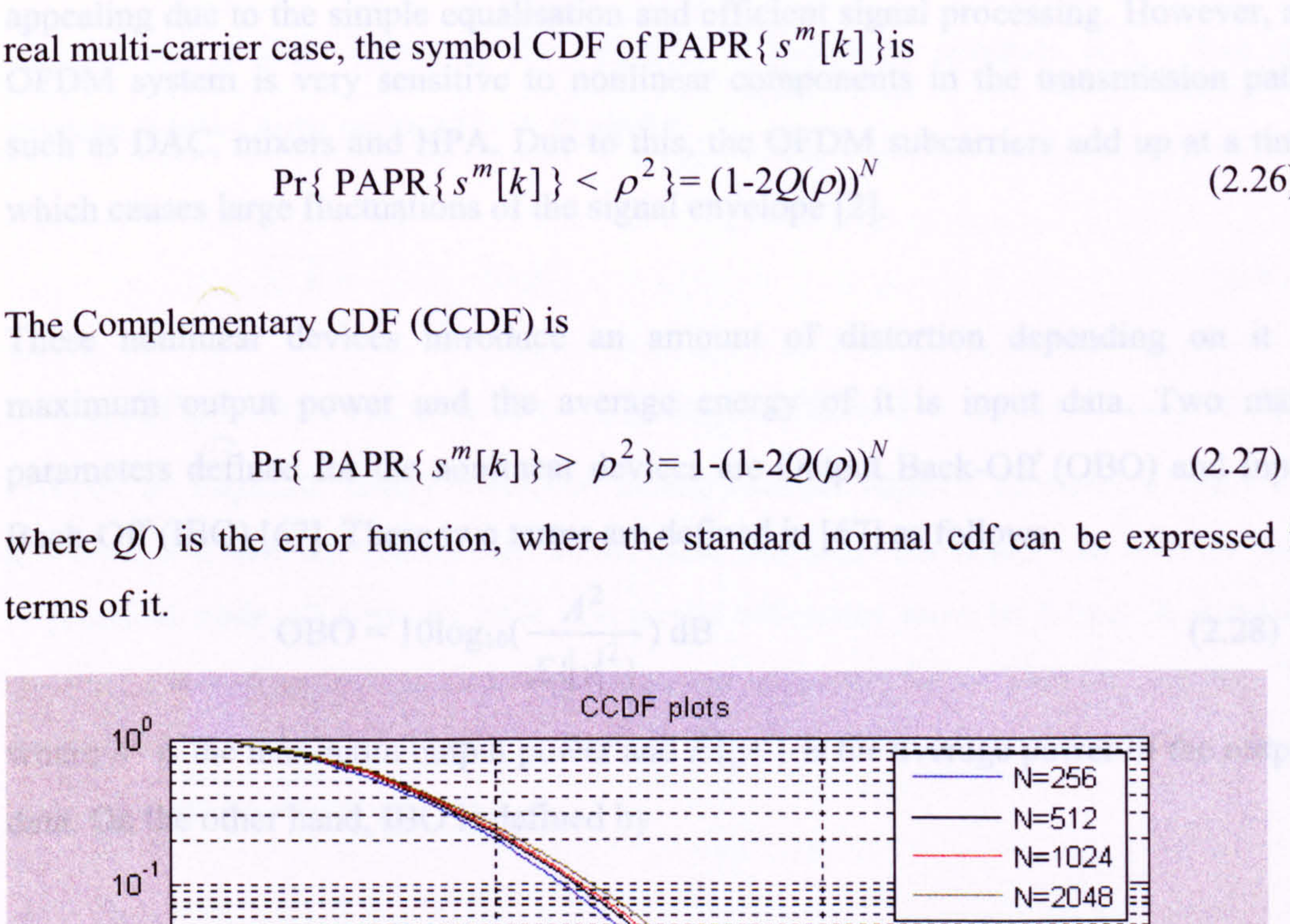


**Figure 2.17: CCDF of OFDM symbol for N= 256, 512, 1024, and 2048.**

It can be inferred from Figure 2.17 that most of the symbols have a PAPR less than 15 dB, and that statistical PAPR does not increase significantly with increased symbol size.

### 2.4.3 The Power Problem Effect on the System Performance

As mentioned earlier in Section 2.3, the OFDM system concept appears to be rather appealing due to the simple equalisation and efficient signal processing. However, an OFDM system is very sensitive to nonlinear components in the transmission path, such as DAC, mixers and HPA. Due to this, the OFDM subcarriers add up at a time which causes large fluctuations of the signal envelope [2].

These nonlinear devices introduce an amount of distortion depending on it is maximum output power and the average energy of it is input data. Two main parameters defined for the nonlinear devices are Output Back-Off (OBO) and Input Back-Off (IBO) [67]. These two terms are defined in [67] as follows

$$\text{OBO} = 10\log_{10}\left(\frac{A^2}{E\{|y|^2\}}\right) \text{dB} \tag{2.28}$$

where $A^2$ is the maximum output power and $E\{|y|^2\}$ is the average power of the output data. On the other hand, IBO is defined by

$$\text{IBO} = 10\log_{10}\left(\frac{A^2}{E\{|x|^2\}}\right) \text{dB} \tag{2.29}$$

where $E\{|x|^2\}$ is the average power of the input data. These two powers are considered equal values if the multi-carrier signal operates in the linear region of the device [67].

Two main problems, the PSD degradation and increment of Symbol Error Rate (SER) are experienced by the system when the transceiver signal suffers from nonlinear distortion.

The impact on PSD is described as the spectral regrowth phenomenon. The output of nonlinear devices will suffer from intermodulation distortion resulting in energy being generated at frequencies outside the allocated bandwidth. It is known that users in different applications share the spectra among them, requiring a large clip level value (IBO) or alternatively a filter after the nonlinear device. However, the transmit power is usually lowered at the expense of increasing BER [68].

The SER is one of the common performance measures used to assess the communication link. Denoting the estimated information symbols as $\hat{c}_i$ , then the average symbol error probability is given by

$$\overline{\text{SER}} = \frac{1}{N} \sum_{i=0}^{N-1} \text{SER}_i \tag{2.30}$$

where $\text{SER}_i$, = $\Pr(c_i \neq \hat{c}_i)$, is the $i$-th subcarrier SER. For standard channels like AWGN or Rayleigh fading multipath fading channel explicit formulas of SER are known. For a detailed information about these formulas, the reader can refer to [68]. A practical trade off between SER and power efficiency must be found. A common measure for trading SER to clipping and power efficiency is the total degradation. To meet a certain target of SER, the sum of the energy per bit and the OBO due to clipping must be minimised [69].

A transmission, which is free from any distortion, requires linear operation over a range of $N$ times the average power, which prevents power efficient operation of the high power amplifiers and reduces the system efficiency [2]. Thus, some techniques of peak power reduction are desirable.

### 2.4.4 PAPR Reduction Techniques

PAPR concept, its statistical properties and its effect on system performance were defined in the previous subsections. This subsection describes some of the most interesting techniques proposed for PAPR reduction.

The use of OFDM began more than two decades ago. However, techniques for PAPR reduction were not proposed until the mid 90's, and they have been extremely prolific [70].

The classification of work since the mid 90's is difficult to summarise in a few pages without leaving some interesting areas out of the picture. The following outline of all these efforts covers the major methods. These methods are classified into PAPR reduction with and without distortion.

In the former classification, the transmitted symbols are distorted and the transmitter is not designed for the maximum PAPR range although the decoded BER is degraded. This set of techniques will be described in more detail in Subsection 2.4.4.1. The latter classification reduces the symbol PAPR prior to the nonlinear device without increasing the BER. These methods will be described in Subsection 2.4.4.2 and typically achieve lower PAPR at the expense of a reduced data rate.

### 2.4.4.1 PAPR Reduction with Distortion

Clipping is a simple technique applied to the affected OFDM symbol by PAPR. It clips the affected signal at the transmitter to the desired power level. The operation is implemented on discrete samples prior to DAC or by designing the DAC and/or amplifiers with saturation levels that are lower than the signal dynamic range. This approach is widely used, although it is known to degrade the received SER and to increase out-of-band radiation [71].

Multi-carrier signal degradation, due to nonlinearities, has been detailed in a number of publications. Some of these explanations apply to real signals and others to complex ones. As an example, in [71, 72] Mestdagh and Gross were proposed a work to reduce PAPR for real multi-carrier signals, while O'Neill and Lopes in [73] were quantified the PAPR problem for passband multi-carriers signals.

The main assumption for all works (either for real or complex signals), is that, nonlinearity is an ideal soft limiter, after the SNR degradation and the PSD of the

clipped/limited signal is computed. Due to the clipping process, the out of band radiation increases; this is reduced by applying filtering after the clipping technique. Unfortunately, filtering after HPA can be very costly. In practice, clipping and filtering is done prior to HPA, but in this case, the PAPR can significantly increase after filtration [74].

This can be overcome by the alternative method of peak windowing [75, 76]. The clipping operation will reduce out-of-band radiation at the expense of increasing BER.

Chow in [77] proposed a new technique to help in reducing BER which is denoted by shaped clipping. This technique is applicable for some special applications specifically when the channel exhibits a known structure. In this case, the clip noise can be shaped to reduce BER.

Unfortunately, in a general channel, the determinant effects on BER can not be mitigated. For this purpose error correction codes are used. Data rate reduction and complexity at both ends as well as increased overall delay of the system are the by-products of a general channel structure.

### 2.4.4.2 Distortionless PAR Reduction

This subsection details methods that reduce the symbol PAPR prior to the nonlinear device without increasing BER. These techniques are classified into two main categories; coding, and optimisation.

#### *2.4.4.2.1 Coding*

In the early 90s Popvic [69] showed that a low PAPR, 3dB, can be achieved for baseband complex symbols generated by Golay complementary sequences[7]. After

[7] Complementary sequences were introduced by Marcel Golay in 1949 in the context of infrared spectrometry.

that, in [78,79] van Nee and Davis have done a further studies of the coding methods revealed that these codes can only be applied to M-ary PSK data and are not applicable for $N > 32$, where $N$ is the total number of subcarriers, however, this coding methods provide error correction capability.

Further studies in [70, 80, 81] were performed to study these coding techniques. These methods yield large PAPR reductions at the expense of minimal data rate loss, and an increase in system complexity. The authors discovered an exponential relationship between finding suitable codewords and the number of subcarriers. As an example, if there are 32 subcarriers with a 16-QAM modulation technique, then there are $10^{18}$ stored symbols, a discovery which leads to other possible ways to tackle effect of the PAPR on the system performance.

#### *2.4.4.2.2 The Signal Optimisation*

The reduction techniques include two types of methods: discrete and continuous signal representations. In discrete signal representations, a limited number of possible transformations of the symbol can describe PAPR reduction techniques. In this type of techniques two main conditions must be maintained to guarantee its practical implementation; the representation process must be reversible, and the error rate must be allocated within acceptable limits. The main drawback for this kind of technique is that the transformation chosen at the transmitter must be communicated to the receiver. Thus, the overhead data problem appears and needs to be tackled [77].

As an example, most of these techniques attenuate the symbol with a high envelope greater than a determined threshold [77, 82]. These kinds of techniques are the simplest but, as a compromise, the SER increases due to scaling the SNR at the receiver. In order to combat this problem, the researchers have proposed a pseudo-random transformation process based on the phase shifts of the data symbols, such as selective scrambling techniques [83]. The limitation of these techniques is that IFFT must be recalculated for each phase transformation. This will increase transmitter complexity proportional to the total number of transformations, forcing researchers to

propose a structured phase transformations to avoid this large complexity, such as selected mapping and partial transmit sequence techniques [57, 84, 85].

Because of using these structured phase transformations, mathematical properties of the IFFT are exploited, leading to savings in recomputing IFFT for each transformation of the OFDM symbol are made. Moreover, the complexity decreases at the expense of PAPR reduction since the transformed symbols are dependent on the original symbol. This saving in complexity could vanish by using a larger set of transformations to achieve the same PAPR reduction [85].

For continuous signal representations, reduction techniques can be described by a set of parameters that must be optimised. A simple optimisation scheme is that of trying each possible combination of optimisation parameters and selection of the parameter leading to the smallest PAPR. The drawback of this simple scheme is that its computational complexity is of the order $e^N$, rendering it unfeasible for large $N$ [86].

In conclusion, the techniques already used to tackle the PAPR problem are divided into two groups, one of which suffers from a high degree of computational complexity, while the other does form an increase in BER. In Chapter 4 the new technique (NTRPT) is described, which yields significant PAPR reduction with a computational complexity formula of the first order.

## *2.5Summary*

This chapter provided the reader with the needed material to understand the remaining chapters. It is divided into three subsections to cover the three main parts of the proposed system; NTRPT-MIMO-OFDM.

Section 2.2 introduced the MIMO technique to cover the MIMO channel, and the MIMO system's basic components with different MIMO techniques. To summarise the optimum performance could be achieved with full diversity, but only at the expense of decoding complexity. The complexity of such a receiver grows exponentially with the size of the spatial and temporal dimension.

Section 2.3 presented the principal ideas behind OFDM used throughout this thesis. The section began with a discussion of the basic principles of OFDM, including the implementation of OFDM communication system elements (such as the FFT-based implementation of an OFDM transceiver), the guard time (cyclic prefix or zero padding) and a review of windowing. The drawbacks of OFDM then reviewed, particularly, introducing the effects of synchronisation errors and non-linear distortion on an OFDM signal.

Section 2.4 overviewed one of the major drawbacks of the OFDM systems (PAPR). The section also covered the main conventional techniques in the literature. For simplicity, the techniques were further divided into two main groups: distortion and distortionless techniques.

# Chapter Three

# 3. MIMO: Channel Modelling

## *3.1Introduction*

Section 2 of the previous chapter covered the main schemes proposed for MIMO technology, which they offer variety trade-offs between capacity capabilities and the BER (when they combined with corresponding receiver techniques). In Section 3.1, the capacity of MIMO channels is determined. The BER for the ZF and the MMSE is linked with the SNR in Section 3.2.

As mentioned in the previous chapter, it is important to have a good MIMO channel model, which should cover a range between the best and worst cases, such as the effect of spatial fading correlation. In Section 3.3, a simple MIMO channel is proposed to study the effect of spatial correlation on channel capacity.

## *3.2 The MIMO Systems Capacity*

A main factor that makes MIMO systems preferable over SISO systems is capacity, defined here as the maximum rate of information without any changes at the receiver. An important issue that must be mentioned here is that MIMO systems' capacities are based not only on the fading statistics (as for SISO systems) but also on the spatial correlation coefficient. Nevertheless, both of them can approach maximum capacity boundaries obtained from information theory by a proper design of both of the coding and decoding techniques.

Starting from the channel transfer matrix proposed in [87], its impact can be written based on the Singular Value Decomposition (SVD) as

$$\mathbf{x} = \mathbf{U}\mathbf{D}\mathbf{V}^{H}\mathbf{a} + \mathbf{n} \tag{3.1}$$

where **x** is the received signal; from the definition of SVD; with the $\mathbf{UDV}^{H}$ equal to the channel transfer matrix, **H; D** is an *MxN* dimensional matrix having the square root of the nonzero eigenvalues of $\mathbf{HH}^{H}$ or $\mathbf{H}^{H}\mathbf{H}$ [88] on its diagonal; and **U** and **V** are the unitary matrices with dimensions *MxM* and *NxN*; **a** denotes the transmitted signal; and **n** is the added noise. The nonzero eigenvalues must be less or equal to a minimum number between *N* and *M*.

In order to simplify (3.1), multiply the overall received signal by $\mathbf{U}^{H}$ and sending **a'** instead of **a**, where **a'**= **V a.** The received signal, **b**, will be written as

$$\mathbf{b} = \mathbf{U}^{H}\mathbf{x} = \mathbf{U}^{H}\mathbf{U}\mathbf{D}\mathbf{V}^{H}\mathbf{V}\mathbf{a} + \mathbf{U}^{H}\mathbf{n} = \mathbf{D}\mathbf{a} + \mathbf{n}' \tag{3.2}$$

This achievement is based on the fact that the unitary matrices, whose rows and vectors have an orthonormal basis while keeping in mind that a space rotation results in the multiplication of any matrix by a unitary matrix. In [89], the equivalence of **H** consists of $N_k$ parallel spatial subchannels with the *k*-th eigenvalue, $\lambda_k$, as a gain for the *k*-th subchannel. This can be derived from (3.2) for the *k* component notations as

$$b_k = \lambda_k^{1/2} a_k + n_k' \tag{3.3}$$

Figure 3.1 shows the equivalence representation of (3.3).

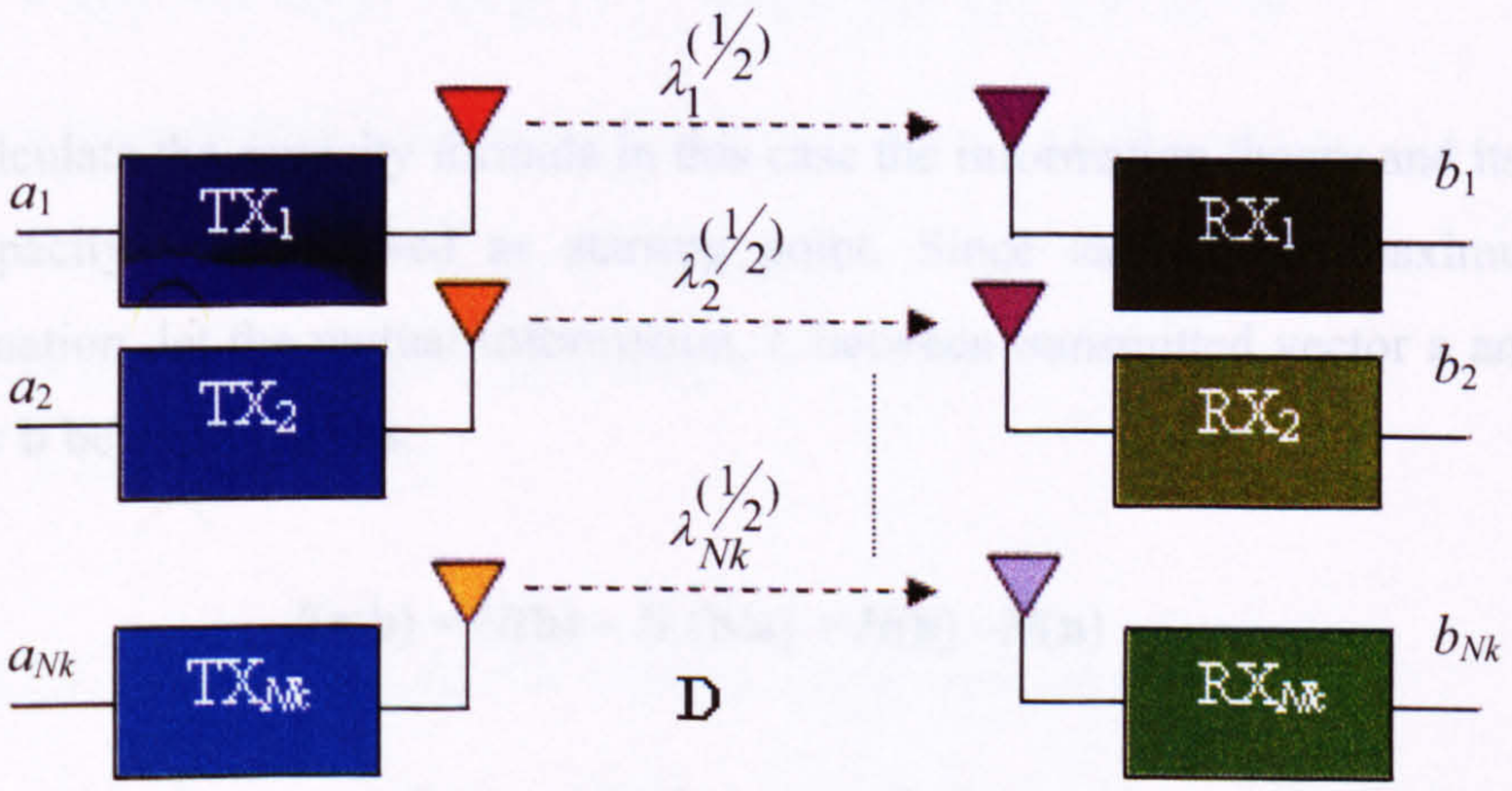


**Figure 3.1: Equivalence of the physical model of a MIMO system.**

From the figure shown above, the capacity can measured according to the spatial subchannels, since they are the parallel paths that are allocated to send the data in the same allocated bandwidth. Making use of Shannon's capacity formula [90], the capacity, *C*, can be defined as [89]

$$C = \sum_{k=1}^{N_k} \log_2(1 + \rho_k |h_k|^2) = \sum_{k=1}^{N_k} \log_2(1 + \lambda_k \frac{\sigma_k^2}{\sigma_n^2}), \text{ bits/ s/ Hz} \qquad (3.4)$$

where $\rho_k$ is the average SNR at the $k$-th logical Rx antenna, the transfer function of the $k$-th subchannel is $h_k$, and $\sigma_k^2$ is the power allocated to the $k$-th subchannel. Thus, capacity depends on the power allocated per channel. Moreover, the capacity increases linearly with $N_k$ when there are equal values for gains $\lambda_k$ and a uniform power allocation.

From (3.4) and the consequence that the capacity depends on the power allocated per channel, the two common types of capacities, *open-loop* and *closed-loop*, can be defined.

The closed-loop scenario exists when the transmitter has the knowledge of the CSI. An optimal feedback with zero delay is assumed. Perfect knowledge of the channel matrix at the transmitter gives the choice of optimal distribution of the total available power $P_t$ among $N$ transmitting antennas [87, 91].

To calculate the capacity formula in this case the information theory and its definition of capacity will be used as starting point. Since capacity is maximum mutual information, let the mutual information, $I$, between transmitted vector **a** and received vector **b** be expressed as:

$$I(\mathbf{a};\mathbf{b}) = H(\mathbf{b}) - H(\mathbf{b}/\mathbf{a}) = H(\mathbf{b}) - H(\mathbf{n}) \qquad (3.5)$$

where $H(.)$ denotes entropy. Maximising (3.5) is related to maximising $H(\mathbf{b})$, according to [87], the Gaussian distribution of a complex multivariate **y** has the

largest entropy. The entropy of this complex multivariate normal distribution is given by:

$$H(\mathbf{y}) = -\int p(\mathbf{y}) \log_2 (p(\mathbf{y}))\, d\mathbf{y} \tag{3.6}$$

where $p(\mathbf{y})$ is the pdf of a complex multivariate normal distribution $\mathbf{y}$ with covariance matrix $\mathbf{Q}_y$ and mean $\mu_y$. This pdf is given in [92] by

$$p(z) = \det(\pi \mathbf{Q}_z)^{-1} e^{(-(z-\mu_z))^H \mathbf{Q}_z^{-1} (z-\mu_z))} \tag{3.7}$$

Thus, the capacity can be expressed as

$$C = \max(I(\mathbf{a};\mathbf{b})) = \max(H(\mathbf{b})-H(\mathbf{n})) \tag{3.8}$$

From (3.6) and (3.7), and making use of the fact that $\mathbf{a}^H\mathbf{b} = \mathrm{tr}(\mathbf{b}\mathbf{a}^H)$ (where tr (.) stands for the *trace* of a matrix - *i.e.*, the sum of diagonal elements of the matrix), the entropy of $\mathbf{y}$ is calculated as

$$\begin{aligned}
H(\mathbf{y}) &= -\int p(\mathbf{y}) \log_2 (\det(\pi \mathbf{Q}_y)^{-1} e^{(-(y-\mu_y)^H \mathbf{Q}_y^{-1} (y-\mu_y))})\, d\mathbf{y} \\
&= -\int p(\mathbf{y}) \log_2 (\det(\pi \mathbf{Q}_y)^{-1})\, d\mathbf{y} - \int p(\mathbf{y}) \log_2 (e^{(-(y-\mu_y)^H \mathbf{Q}_y^{-1} (y-\mu_y))})\, d\mathbf{y} \\
&= -\int p(\mathbf{y}) \log_2 (\det(\pi \mathbf{Q}_y)^{-1})\, d\mathbf{y} - \int p(\mathbf{y}) ((-(\mathbf{y}-\mu_y)^H \mathbf{Q}_y^{-1} (\mathbf{y}-\mu_y)))\log_2 (e)\, d\mathbf{y} \\
&= \log_2 (\det(\pi \mathbf{Q}_y)) + (\log_2 e) \int p(\mathbf{y})(\mathbf{y}-\mu_y)^H \mathbf{Q}_y^{-1} (\mathbf{y}-\mu_y)\, d\mathbf{y} \qquad (3.9) \\
&= \log_2 (\det(\pi \mathbf{Q}_y)) + (\log_2 e)\, E[(\mathbf{y}-\mu_y)^H \mathbf{Q}_y^{-1} (\mathbf{y}-\mu_y)] \\
&= \log_2 (\det(\pi \mathbf{Q}_y)) + (\log_2 e)\, \mathrm{tr}(E[\mathbf{Q}_y \mathbf{Q}_y^{-1}]) \\
&= \log_2 (\det(\pi \mathbf{Q}_y)) + (\log_2 e)\, \mathrm{tr}(\mathbf{I}). \\
&= \log_2 (\det(\pi e \mathbf{Q}_y))
\end{aligned}$$

From (3.9) and $\mathbf{Q}_n = \sigma_n^2 \mathbf{I}_M$, the capacity can be denoted as

$$\begin{aligned}
C &= \log_2 (\det(\pi e \mathbf{Q}_b)) - \log_2 (\det(\pi e \mathbf{Q}_n)) \\
&= \log_2 (\det(\pi e(\mathbf{Q}_n + \mathbf{H}\mathbf{Q}_a\mathbf{H}^H))) + \log_2 (\det(\pi e \mathbf{Q}_n)^{-1}) \qquad (3.10)
\end{aligned}$$

$$= \log_2 (\det( \mathbf{I}_M + \frac{1}{\sigma_n^2} \mathbf{H}\mathbf{Q}_a\mathbf{H}^H)) \text{ bits/s/Hz}$$

Foschini and Goldsmith in [13, 93] also derived a capacity formula similar to that achieved in (3.10). To achieve the closed-loop capacity from (3.10), tr($\mathbf{Q}_a$) must be smaller or equal to $P_t$ [87]. Thus,

$$C_{cl} = \log_2 (\det( \mathbf{I}_M + \frac{1}{\sigma_n^2} \mathbf{H}\mathbf{Q}_a\mathbf{H}^H))$$

$$= \log_2 (\det( \mathbf{U}\,\mathbf{U}^H + \frac{1}{\sigma_n^2} \mathbf{U}\,\mathbf{D}\,\mathbf{V}^H\mathbf{Q}_a\mathbf{V}\,\mathbf{D}^H\,\mathbf{U}^H)) \qquad (3.11)$$

$$= \log_2 (\det(\mathbf{I}_M + \frac{1}{\sigma_n^2} \mathbf{D}\,\mathbf{V}^H\mathbf{Q}_a\mathbf{V}\,\mathbf{D}^H)) \text{ bits/s/Hz}$$

If CSI is not known at the transmitter, (3.11) can be re-written to express the second type (*i.e.*, the open-loop), providing [13] that the optimal transmit strategy is to distribute the available power uniformly over the transmit antennas. Thus, $\mathbf{Q}_a = \frac{P_t}{N}$ $\mathbf{I}_N$, which leads to

$$C_{ol} = \log_2 (\det( \mathbf{I}_M + \frac{P_t}{N \cdot \sigma_n^2} \mathbf{H}\mathbf{H}^H)) \text{ bits/s/Hz} \qquad (3.12)$$

Figures 3.2-3.5 depict the ergodic capacity as a function of SNR. The ergodic capacity is determined for 10,000 realisations of **H** to cover most examples cases of a real life channel. The realisations of **H** are assumed to be i.i.d. circularly-symmetric complex Gaussian distributed. The number of nonzero eigenvalues of $\mathbf{H}\mathbf{H}^H$ or $\mathbf{H}^H\mathbf{H}$ for this type of channels equal $N_k = \min(N,M)$.

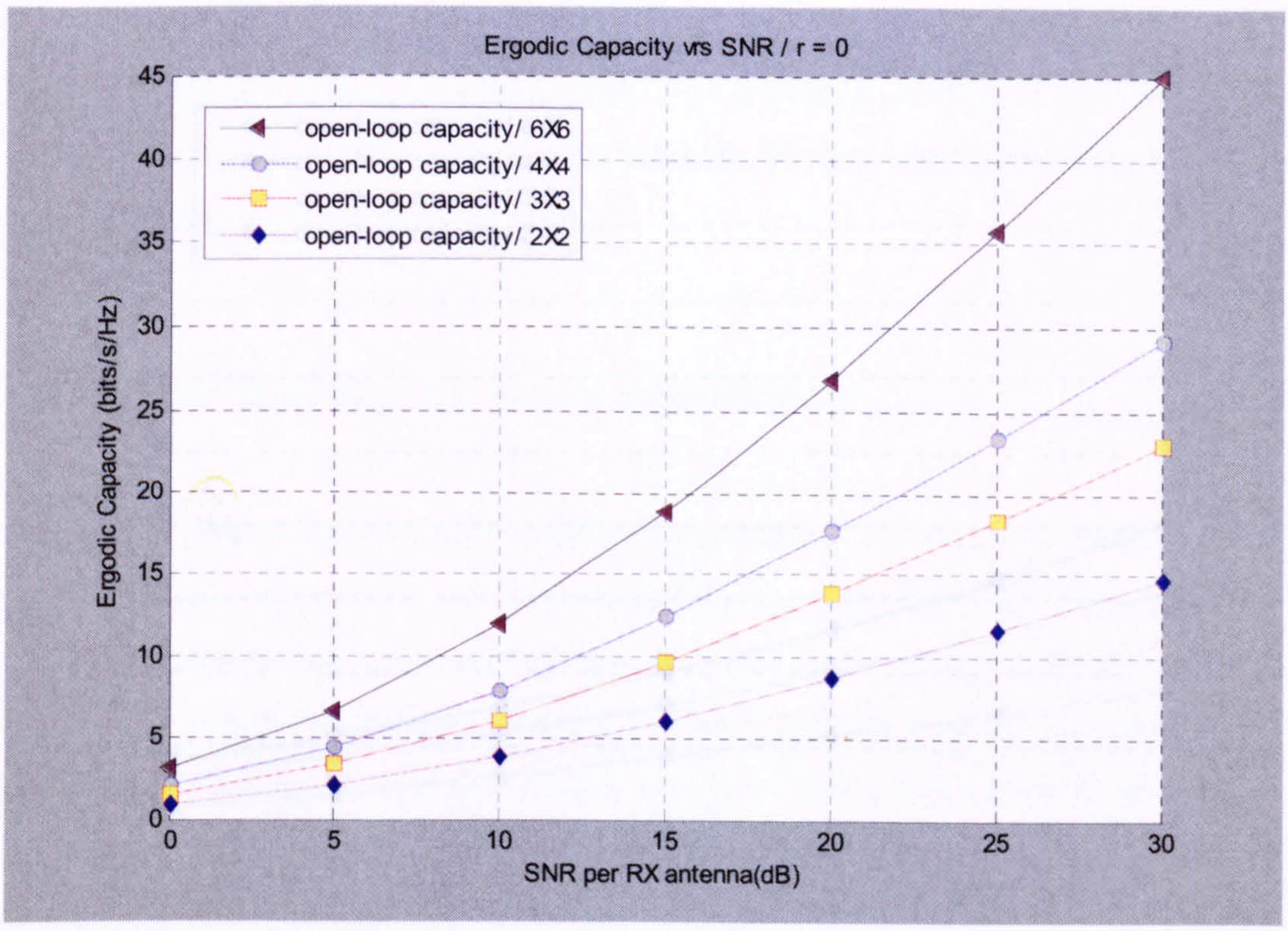


**Figure 3.2: Ergodic channel capacity for different MIMO configuration and a correlation coefficient equal to 0**

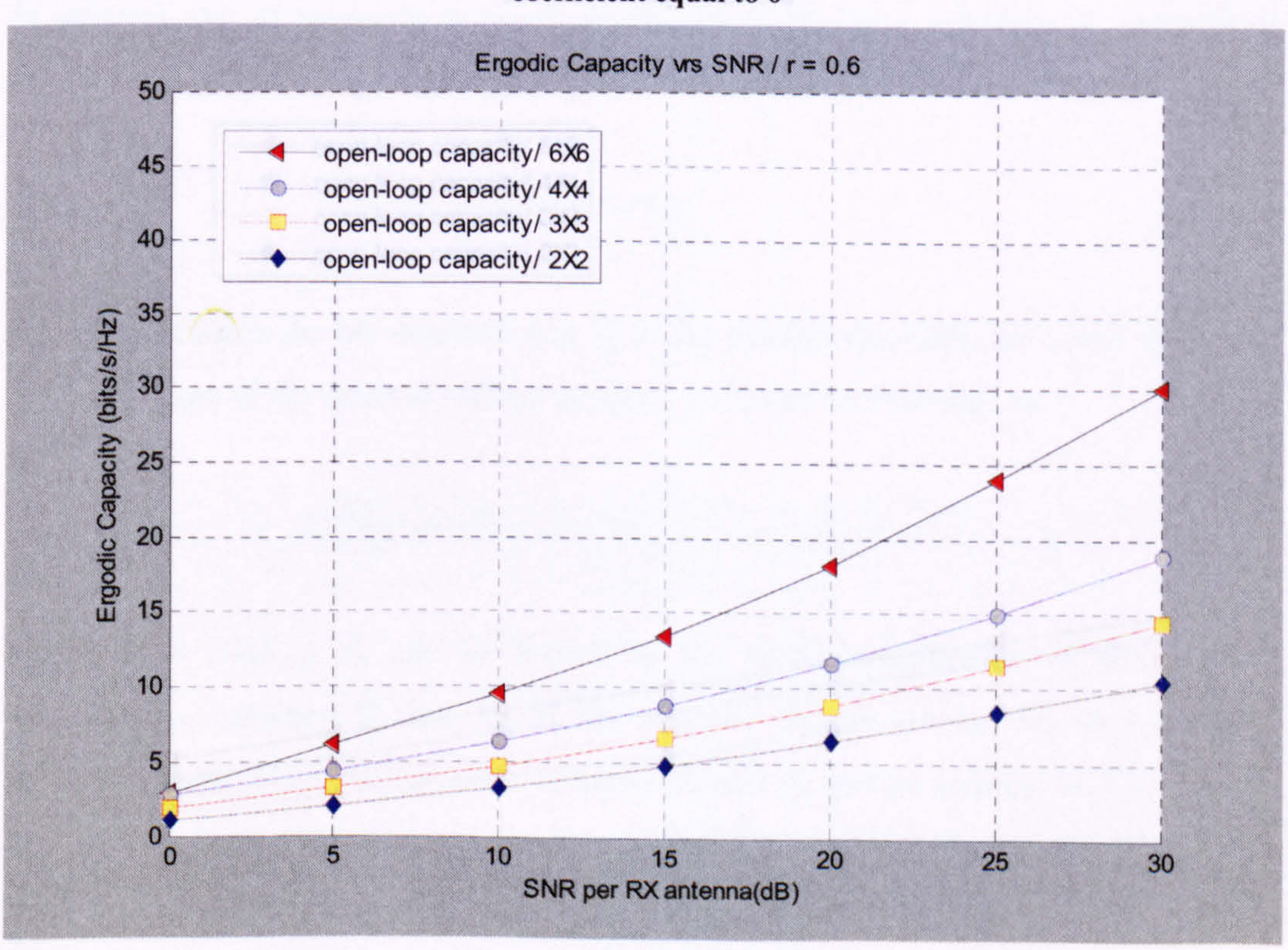


**Figure 3.3: Ergodic channel capacity for different MIMO configuration and a correlation coefficient equal to 0.6**

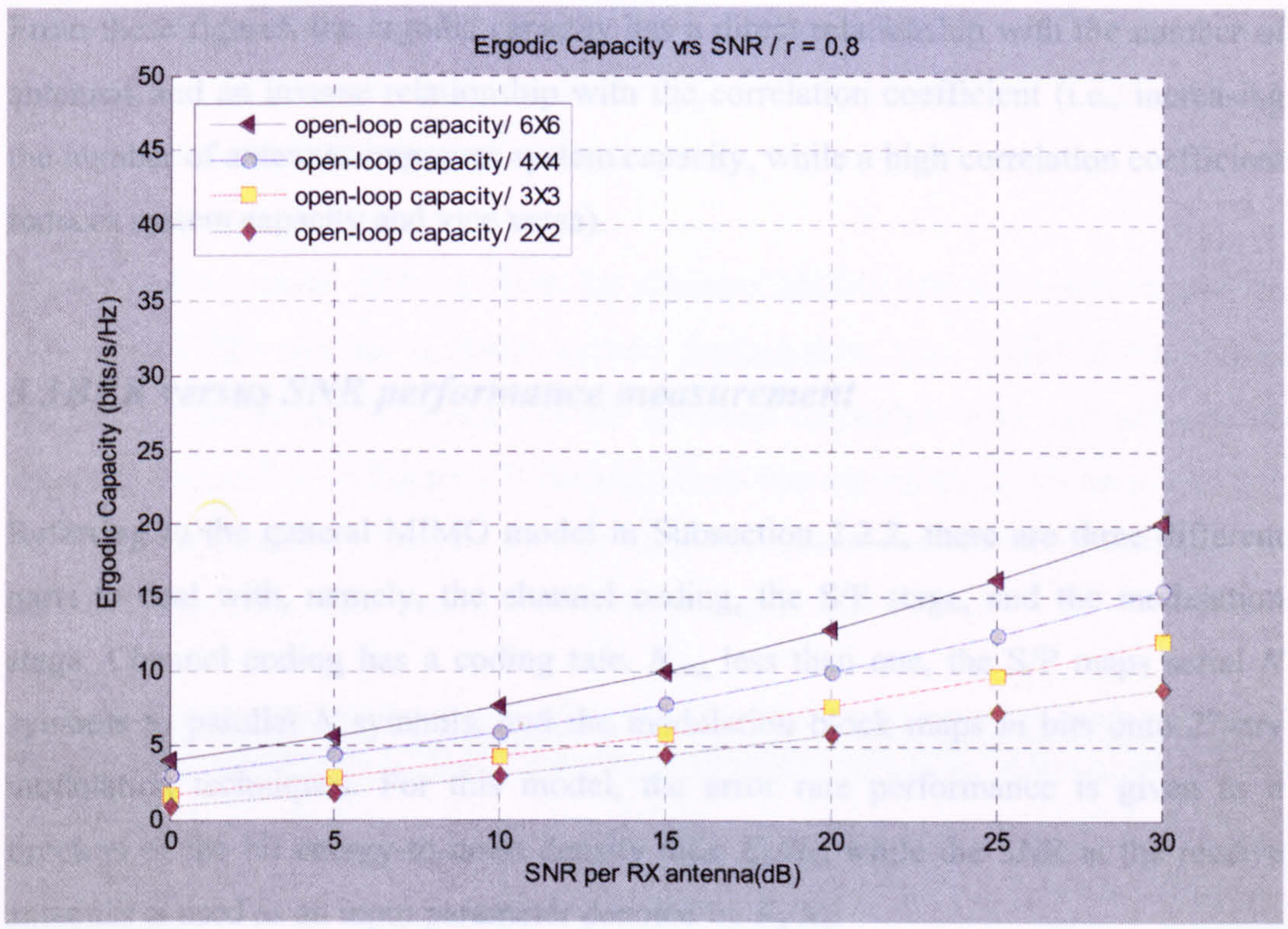


**Figure 3.4: Ergodic channel capacity for different MIMO configuration and a correlation coefficient equal to 0.8**

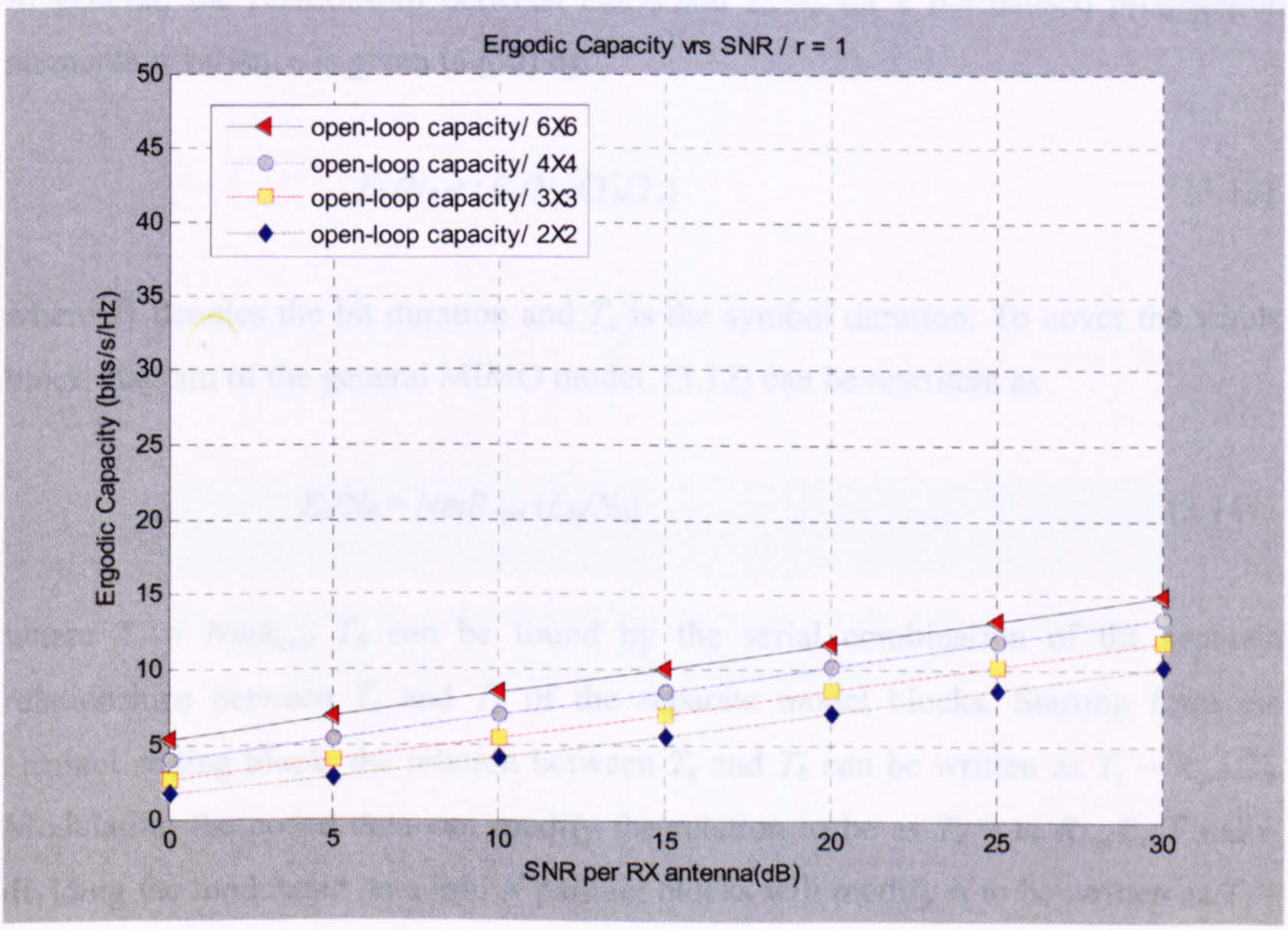


**Figure 3.5: Ergodic channel capacity for different MIMO configuration and a correlation coefficient equal to one**

From these figures, the ergodic capacity has a direct relationship with the number of antennas and an inverse relationship with the correlation coefficient (i.e., increasing the number of antennas improves system capacity, while a high correlation coefficient reduces system capacity and vice versa).

## *3.3BER versus SNR performance measurement*

Referring to the general MIMO model in Subsection 2.2.2, there are three different parts to deal with, namely, the channel coding, the S/P stage, and the modulation stage. Channel coding has a coding rate, $R_{cod,}$ less than one, the S/P maps serial $N$ symbols to parallel $N$ symbols, and the modulation block maps $m$ bits onto $2^m$-ary modulation techniques. For this model, the error rate performance is given as a function of the bit energy-to-noise density ratio $E_b/N_0$, while the SNR at the receive antennas is used as an input parameter denoted by $E_s/N_0$.

In general, the relationship between $E_b/N_0$ and $E_s/N_0$ for a normalised propagation attenuation variance is given in [30] by

$$E_b/N_0 = (E_s/N_0)(T_b/T_s) \tag{3.13}$$

where $T_b$ denotes the bit duration and $T_s$ is the symbol duration. To cover the whole block diagram of the general MIMO model, (3.13) can be rewritten as

$$E_s/N_0 = NmR_{cod}\,(E_b/N_0) \tag{3.14}$$

where $T_s = NmR_{cod}\ T_b$ can be found by the serial combination of the separate relationships between $T_s$ and $T_b$ of the separate model blocks. Starting form the channel coding block, the relation between $T_s$ and $T_b$ can be written as $T_s = R_{cod}\ T_b$. Modulating the coded data can modify the relation to be as $T_s = m\ R_{cod}T_b$. Finally, dividing the modulated data into $N$ parallel blocks will modify it to be written as $T_s = mN\ R_{cod}\ T_b$. From (3.14), the spectral efficiency, $\eta$, can be defined as $NmR_{cod}$.

Different MATLAB programs were generated to calculate the ZF and the MMSE and obtain their performance characteristics. The BER performance is obtained by averaging over 10,000 realisation of the channel.

Figures 3.6-3.9 show BER *vs*. SNR for different MIMO detection techniques (i.e., MMSE and ZF) and for different system configuration (i.e., different number of antennas). The results of using MMSE detection algorithm with 2x2 antennas is shown in Figure 3.6. In Figure 3.7, the same detection algorithm is still used with 3x3 antennas configuration. Figures 3.8 and Figure 3.9 show the results of changing the detection algorithm to ZF with 2x2 and 3x3 antennas, respectively.

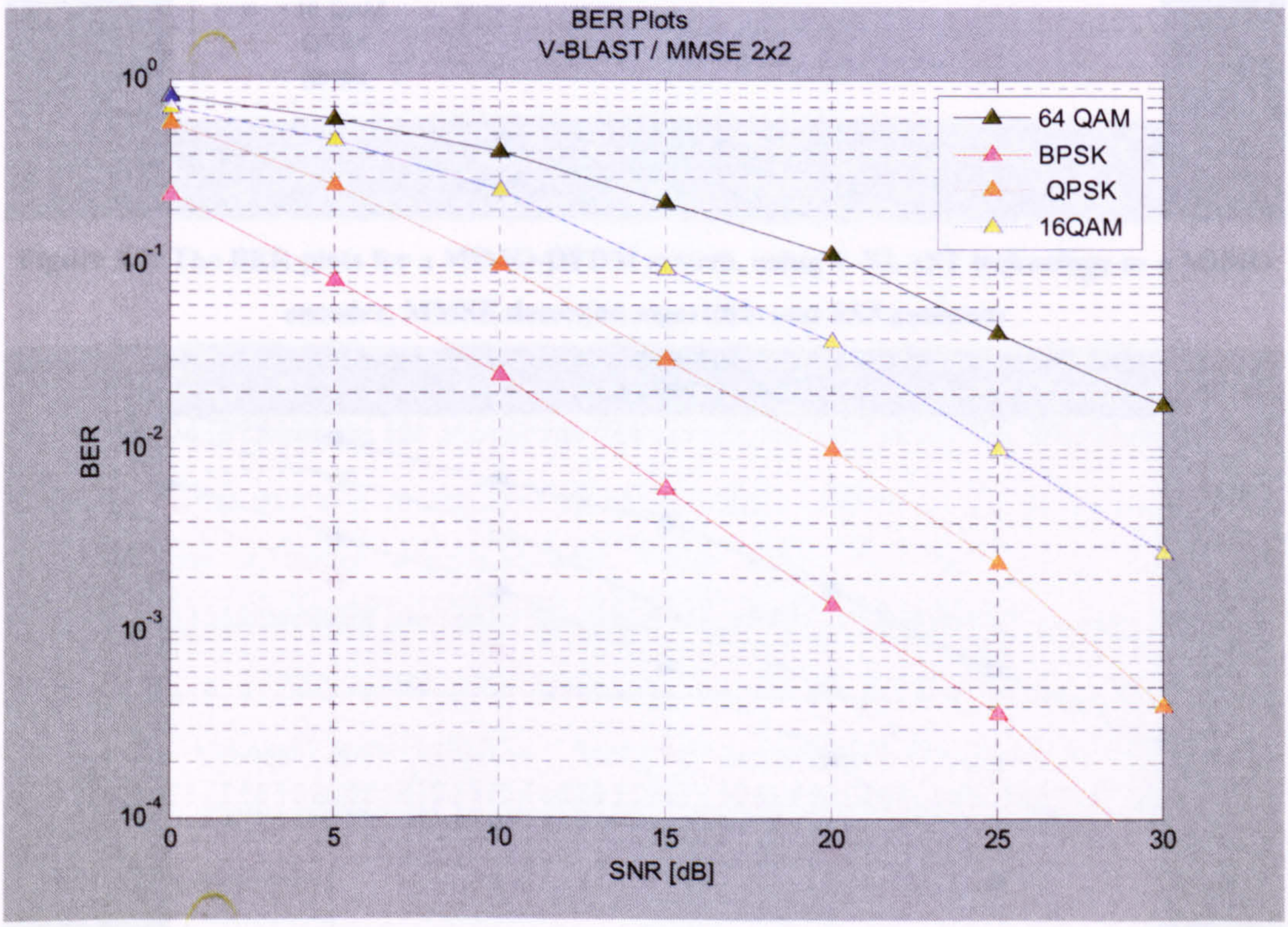


**Figure 3.6: The BER plots for a MIMO-OFDM system, using V-BLAST technology as a MIMO encoder, MMSE detection algorithm and 2X2 antennas**

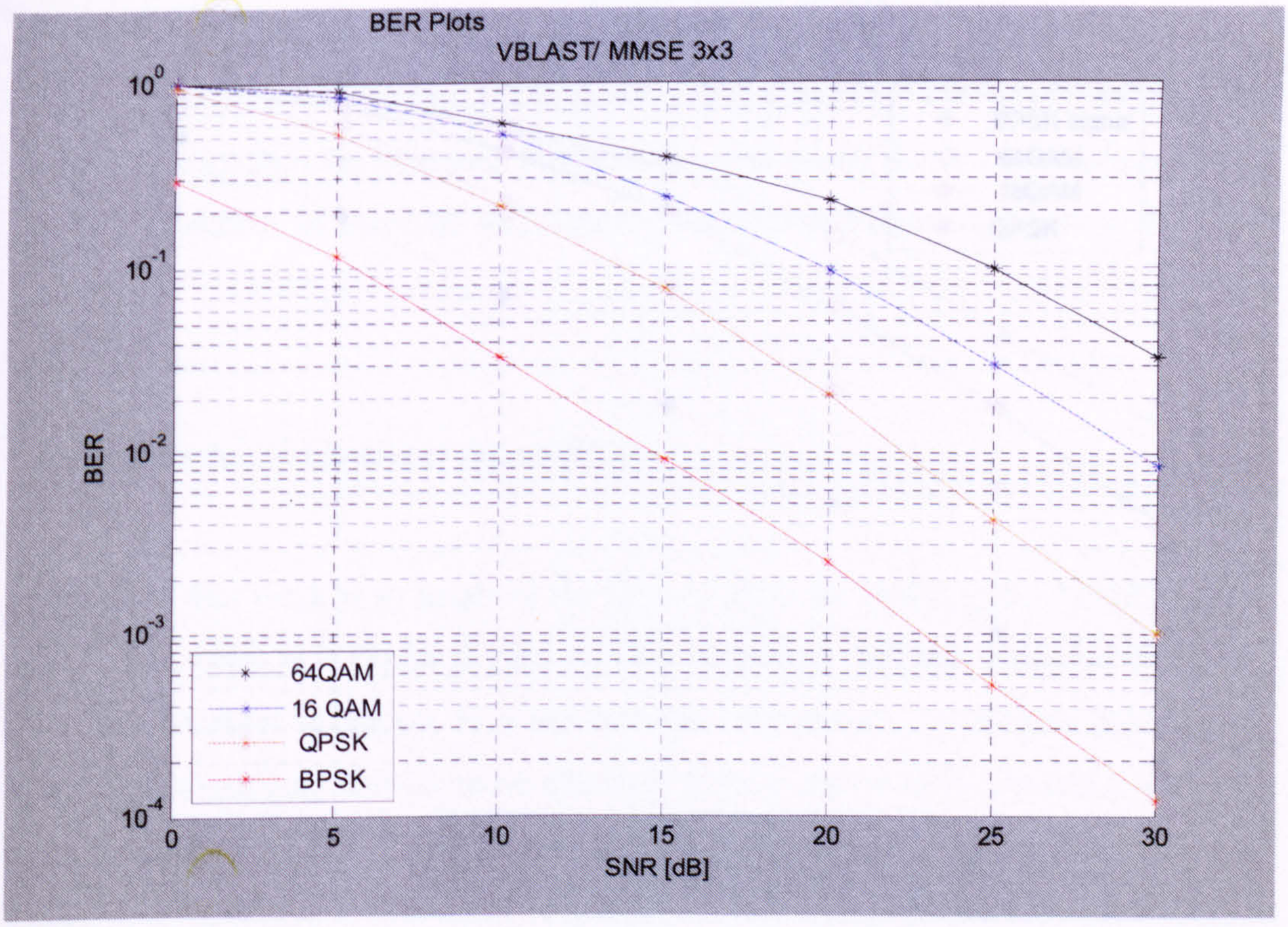


**Figure 3.7: The BER plots for a MIMO-OFDM system, using V-BLAST technology as a MIMO encoder, MMSE detection algorithm and 3X3 antennas**

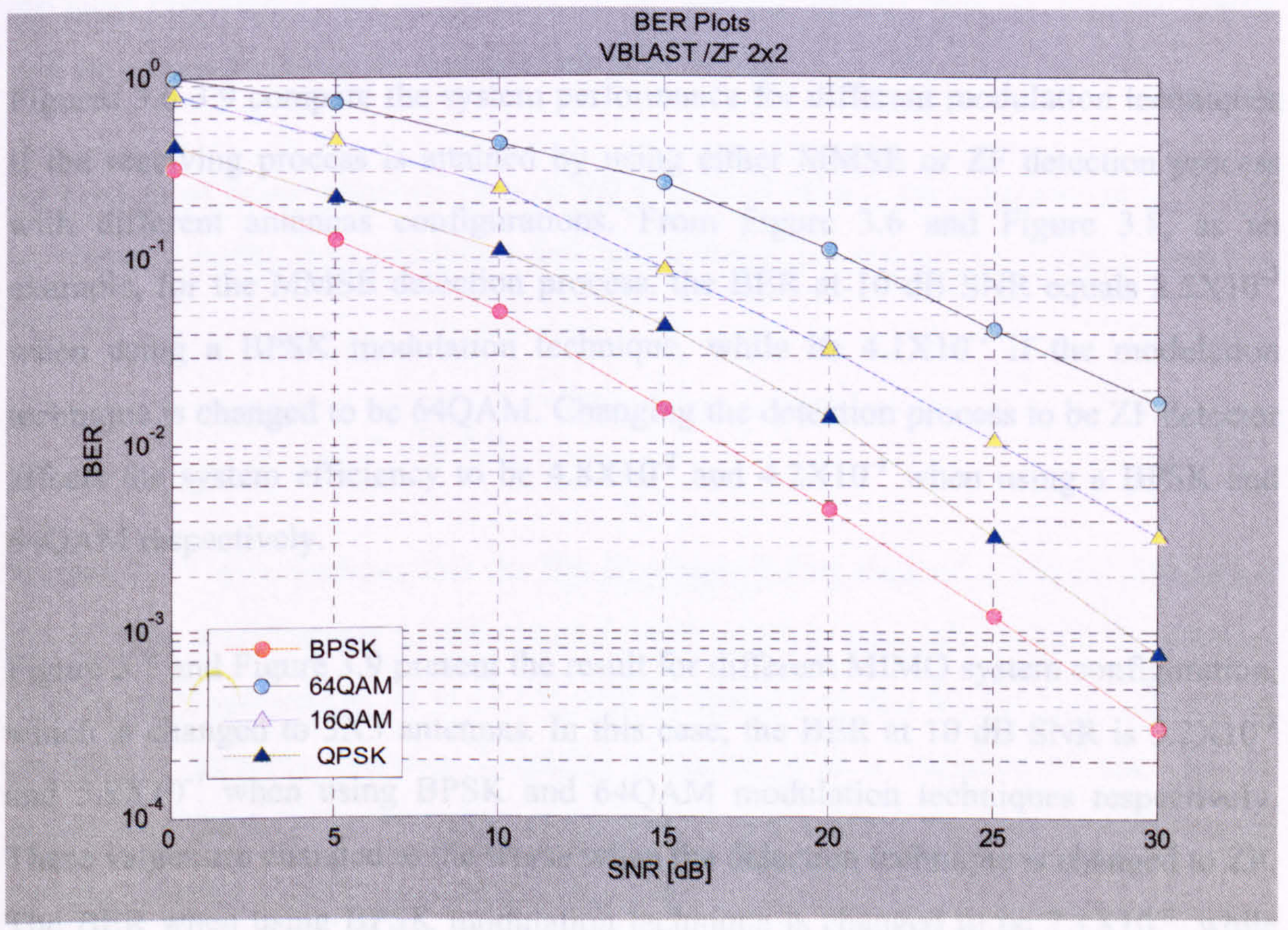


**Figure 3.8: The BER plots for a MIMO-OFDM system, using V-BLAST technology as a MIMO encoder, ZF detection algorithm and 2X2 antennas**

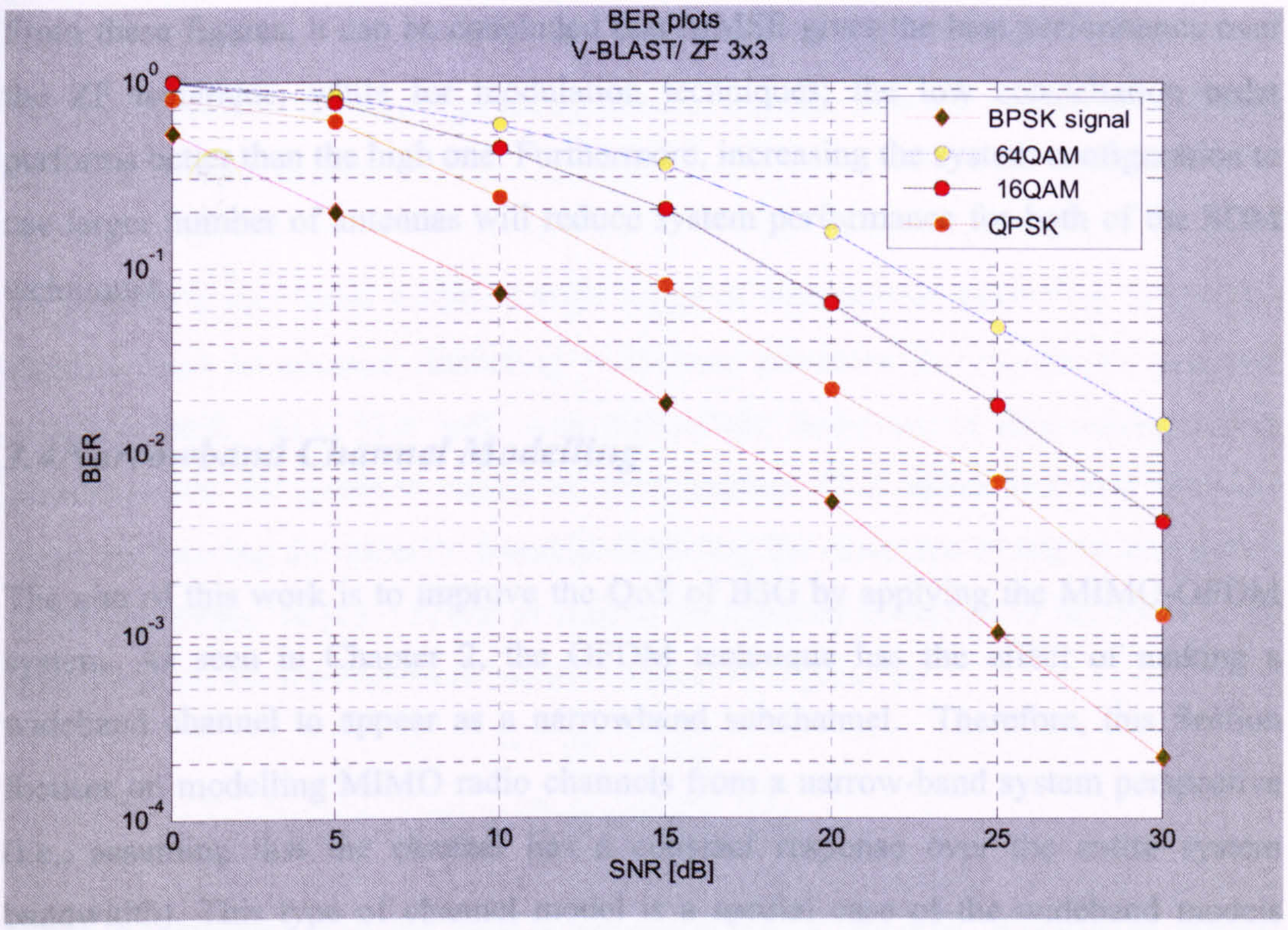


**Figure 3.9: The BER plots for a MIMO-OFDM system, using V-BLAST technology as a MIMO encoder, ZF detection algorithm and 3X3 antennas**

Figures 3.6-3.9 compare the system performance for different modulation techniques if the receiving process is attained by using either MMSE or ZF detection process with different antennas configurations. From Figure 3.6 and Figure 3.8, as an example, for the MMSE detection process, the BER at 10 dB SNR equals $2.5X10^{-2}$ when using a BPSK modulation technique, while its $4.1X10^{-1}$ if the modulation technique is changed to be 64QAM. Changing the detection process to be ZF detector affects the system efficiency to be $4.8X10^{-2}$ and $4.2X10^{-1}$ when using a BPSK and 64QAM respectively.

Figure 3.7 and Figure 3.9 present the result for different MIMO system configuration, which is changed to 3X3 antennas. In this case, the BER at 10 dB SNR is $3.2X10^{-2}$ and $5.9X10^{-1}$ when using BPSK and 64QAM modulation techniques respectively. These values are changed to the worse when the detection technique is changed to ZF. The BER when using BPSK modulation technique is changed to be $7.1X10^{-2}$, while changing the modulation technique to be 64QAM affects the result to equals $7.3X10^{-1}$.

From these figures, it can be concluded that MMSE gives the best performance over the ZF technique, while for modulation techniques; the low constellation order performs better than the high one. Furthermore, increasing the system configuration to use larger number of antennas will reduce system performance for both of the SDM techniques.

## *3.4Narrowband Channel Modelling*

The aim of this work is to improve the QoS of B3G by applying the MIMO-OFDM system. As seen in Chapter 2, the OFDM technique has the effect of making a wideband channel to appear as a narrowband subchannel. Therefore, this Section focuses on modelling MIMO radio channels from a narrow-band system perspective (i.e., assuming that the channel has a constant response over the entire system bandwidth). This type of channel model is a special case of the wideband models described in Section 2.2.1. This will give the first tap of the wideband channel model the most importance, due to the fact that the MIMO channel impulse response matrix will be reduced to have the first tap only (i.e., **G**(0)).

As a result of being a special case of the wideband model, the notations in (2.1) will be changed under the assumption that normalising the average path loss is equal to one, as

$$\mathbf{v} = \mathbf{Hs} + \mathbf{n} \tag{3.15}$$

Section 2.2.1 demonstrates that the flat Rayleigh fading channel could be obtained if the *TC* (the total number of the channel taps) is set to one, after which the channel impulse response matrix, **H** in (3.15), will be defined as $\mathbf{H}_{iid}$ for the i.i.d. zero-mean, circularly-symmetric complex Gaussian elements with a variance of one. At the presence of the LOS or specular component **H** will contain the part of the specular complex Gaussian distributed matrix $\mathbf{H}_{spec}$, as

$$\mathbf{H} = \beta_{K1}\ \mathbf{H}_{spec} + \ \beta_{K2}\ \mathbf{H}_{iid} \tag{3.16}$$

As in Section 2.2.1, $\beta_{K1}$ and $\beta_{K2}$ are components related to the Ricean factor and (3.16) will produce the Rayleigh fading channel impulse response matrix if the Ricean factor, $K$, is equal to zero.

To propose a very good model, a wide range of scenarios in modelling the MIMO channel must be covered (including worst-case scenarios for correlation matrices, capacity, BER, etc.). This will raise difficulties, however, in determining which parameter has the greatest impact on performance. This subsection will therefore focus on deriving the capacity formula, including the existence of spatial correlation as the worst case. In [13, 93] and as seen in the capacity definition in Section 3.2, the capacity of an *MxN* narrowband MIMO channel **H** is given by

$$C = \log_2 \det \left( \mathbf{I}_N + \frac{\rho}{N} \mathbf{H}\, \mathbf{H}^H \right) \text{ bits/s/Hz} \qquad (3.17)$$

where $\rho$ represents SNR per receive antenna and $\mathbf{I}_N$ is the *NxN* dimensional identity matrix. Furthermore, the channel matrix **H** is normalised, meaning that the elements of **H** have an average power of one.

The spatial correlation is a key factor in the performance calculations of MIMO systems and negatively influences the results. Thus, to keep the spatial correlation to a minimum, the antenna spacing must be chosen to be equal or greater than $\lambda/2$, while $\lambda$ is the carrier wave length [13]. However, if the space is limited, the spatial correlation must be taken into consideration. Starting from the definition of the MIMO channel spatial correlation matrix, as in [94, 95]

$$\mathbf{R}_H = E\left[\text{vec}(\mathbf{H})\, \text{vec}(\mathbf{H})^H\right] \qquad (3.18)$$

where **H** is the channel matrix with zero mean and unity variance elements, $(.)^H$ denotes the Hermitian transpose and vec(.) denotes the vec-operations of a matrix, defined as an *MNx*1 dimensional vector composed by stacking the column of **H**. Furthermore, based on the assumption that the correlation among receiver antennas is independent from the correlation between transmit antennas. The nonnegative definite correlation matrix can be defined as [96]

$$\mathbf{R}_H = \mathbf{R}_{Tx} \otimes \mathbf{R}_{Rx} \tag{3.19}$$

where $\otimes$ represents the Kronecker product, $\mathbf{R}_{Tx}$ is an $NxN$ dimensional nonnegative definite matrix denoting the transmitter side correlation matrix, and $\mathbf{R}_{Rx}$ is an $MxM$ dimensional nonnegative definite matrix denoting the receiver side correlation matrix. From (3.19), the correlation between different MIMO channel elements results from the Kronecker product, seen from the transmitter side, with that at the receiver side. After defining the correlation matrices, it is designed to generate the independent narrowband flat-fading MIMO channel with spatial correlation. The channel matrix, **H,** can be defined as in [97] by

$$\mathbf{H} = \text{unvec}\,(\mathbf{R}_H^{1/2}\ \mathbf{h}_{iid}) \tag{3.20}$$

The i.i.d. matrix contains i.i.d. zero-mean unit variance complex Gaussian elements, while **h** is an $NMx1$ stochastic vector, and the unvec (.) is the reverse of the vec-operation. The basic situation demonstrated by (3.20) is that the narrowband flat-fading MIMO channel matrix is based on the channel correlation matrix multiplied by i.i.d. elements with zero mean and unity variance. The channel correlation matrix can be resolved into its basic components (i.e., the eigenvalues and eigenvectors) as follows

$$\begin{aligned} \mathbf{R}_H &= \mathbf{U}\,\mathbf{\Lambda}_H\,\mathbf{U}^H \\ &= \mathbf{U}\,\mathbf{\Lambda}_H^{1/2}\mathbf{\Lambda}_H^{1/2}\,\mathbf{U}^H \\ &= \mathbf{U}\,\mathbf{\Lambda}_H^{1/2}(\mathbf{U}\,\mathbf{\Lambda}_H^{1/2})^H = \mathbf{R}_H^{1/2}(\mathbf{R}_H^{1/2})^H \end{aligned} \tag{3.21}$$

where $\mathbf{\Lambda}_H$ is a diagonal matrix with eigenvalues of $\mathbf{R}_H$ and **U** contains the $\mathbf{R}_H$ orthonormal eigenvectors in its columns. Similarly, in (3.21), $\mathbf{R}_{Tx}$ is reformulated to be equal to $\{\mathbf{R}_{Tx}^{1/2}(\mathbf{R}_{Tx}^{1/2})^H\}$ and $\mathbf{R}_{RX}$ equal to $\{\mathbf{R}_{Rx}^{1/2}(\mathbf{R}_{Rx}^{1/2})^H\}$. As a consequence, $\mathbf{R}_H^{1/2}$ can be defined, based on (3.19), as

$$\mathbf{R}_H^{1/2} = \mathbf{R}_{Tx}^{1/2} \otimes \mathbf{R}_{Rx}^{1/2} \tag{3.22}$$

By making use of the property for any matrices with proper dimensions, namely, **A**, **B**, and **C**, (see Appendix A) $\{\text{vec}(\mathbf{ABC}) = (\mathbf{C}^T \otimes \mathbf{A})\,\text{vec}(\mathbf{B})\}$ and (3.22), (3.20) will be reformulated as

$$\begin{aligned}\mathbf{H} &= \text{unvec}\,(\mathbf{R}_H^{1/2}\ \mathbf{h}_{\text{iid}}) \\ &= \text{unvec}\,((\mathbf{R}_{Tx}^{1/2} \otimes \mathbf{R}_{Rx}^{1/2})\,\mathbf{h}_{\text{iid}}) \\ &= \mathbf{R}_{Rx}^{1/2}\ \mathbf{H}_{\text{iid}}\,(\mathbf{R}_{Tx}^{1/2})^T\end{aligned} \tag{3.23}$$

Comparing with [96], the same result of the introduced spatial correlation model was obtained.

Substituting the result achieved from (3.23) to (3.17)

$$C = \log_2(\det(\mathbf{I}_N + \frac{\rho}{N}\mathbf{R}_{Rx}^{1/2}\,\mathbf{H}_{\text{iid}}(\mathbf{R}_{Tx}^{1/2})^T((\mathbf{R}_{Tx}^{1/2})^T)^H\,(\mathbf{H}_{\text{iid}})^H(\mathbf{R}_{Rx}^{1/2})^H)\ \text{bit/s/Hz} \tag{3.24}$$

Equation (3.24) can be reformatted under the assumption of high SNRs to achieve greater simplicity thus:

$$\begin{aligned}C &\approx \log_2 \det(\frac{\rho}{N}\ \mathbf{R}_{Rx}^{1/2}\ \mathbf{H}_{\text{iid}}\,(\mathbf{R}_{Tx}^{1/2})^T((\mathbf{R}_{Tx}^{1/2})^T)^H\,(\mathbf{H}_{\text{iid}})^H(\mathbf{R}_{Rx}^{1/2})^H) \\ &= \log_2(\det(\frac{\rho}{N}\mathbf{R}_{Rx}^{1/2})\det(\mathbf{H}_{\text{iid}})\det((\mathbf{R}_{Tx}^{1/2})^T)\det(((\mathbf{R}_{Tx}^{1/2})^T)^H)\det((\mathbf{H}_{\text{iid}})^H)\det((\mathbf{R}_{Rx}^{1/2})^H)) \\ &= \log_2(\det(\mathbf{H}_{\text{iid}})\det(((\mathbf{R}_{Tx}^{1/2})^T)^H)\det((\mathbf{R}_{Tx}^{1/2})^T)\det((\mathbf{H}_{\text{iid}})^H)\det(\frac{\rho}{N}\mathbf{R}_{Rx}^{1/2})\det((\mathbf{R}_{Rx}^{1/2})^H)) \\ &= \log_2(\det(\frac{\rho}{N}\mathbf{I}_M)\det(\mathbf{H}_{\text{iid}})\ \det((\mathbf{R}_{\text{Tx}})^T)\ \det((\mathbf{H}_{\text{iid}})^H)\ \det(\mathbf{R}_{\text{Rx}})) \\ &= \log_2(\det(\frac{\rho}{N}\mathbf{I}_M)) + \log_2(\det(\mathbf{H}_{\text{iid}})\ \det((\mathbf{R}_{\text{Tx}})^T)\ \det((\mathbf{H}_{\text{iid}})^H)\ \det(\mathbf{R}_{\text{Rx}}))\end{aligned} \tag{3.25}$$

The capacity achieved from (3.25) consists of, firstly, the capacity of each parallel independent subchannel, and secondly of the correlation between the subchannels. Thus, in a correlated channel, MIMO capacity can be achieved by evaluating the

determinant of the correlation matrices. From (3.19), $\mathbf{R}_{Tx}$ and $\mathbf{R}_{Rx}$ are as $\mathbf{R}_H$ defined as a nonnegative definite matrix; therefore from [98] the determinant of a squared nonnegative definite matrix is the product of its diagonal elements. As mentioned earlier, correlation matrices are nonnegative definite matrices. If a similar correlation matrices (*i.e.*, $\mathbf{R}_{Tx} = \mathbf{R}_{Rx}$) is assumed, thus, the determinant is lower bounded by zero. Furthermore, following from the assumption that $\mathbf{R}_{Tx} = \mathbf{R}_{Rx}$, the diagonal elements for the correlation matrices are ones. The conclusion must be that the determinant is bounded by one as a maximum and by zero as a minimum.

As mentioned earlier in this subsection, the correlation between two antennas will be neglected if the spacing is greater or equal to half the wavelength. In addition, the correlation will be taken into account due to the limited spacing. Then assuming that the maximum spacing between the first and the last antenna is equal to half the wavelength, the limits of the correlation between each two antennas will be as described in Figure 3.10. As an example, four antennas are used to describe this model, which may not be an accurate one for some real-world scenarios, but does helps in the study of the effect of correlation on MIMO capacity explicitly. Moreover, it is obviously quite a tenable model from the point of view of physical representation since the correlation will be decreased if the distance is increased.

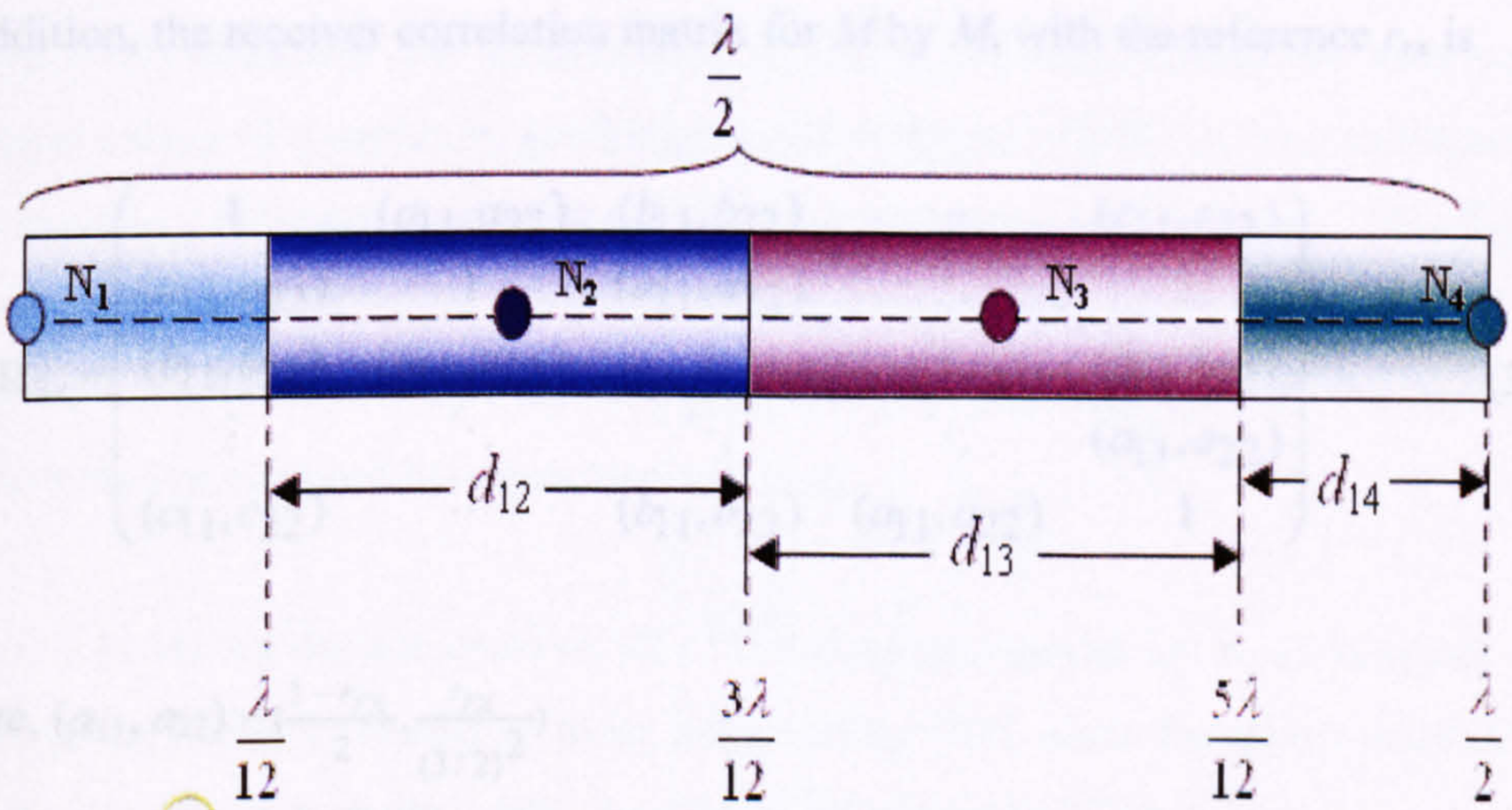


**Figure 3.10: The proposed model with four antennas**

Figure 3.10 shows that the Marwan-Omar Model (MOM), is distance-based. In addition, a reference correlation coefficient is assumed to be in the centre of $d_{12}$ and

equal to $r$. For example, $\mathbf{N_3}$ is placed in the distance-range $d_{13}$, $\lambda/4<d_{13}< 5\lambda/12$. Thus the correlation coefficient range is in between $\left(\left[\frac{r}{(\frac{(N-3)+(N-2)}{2})^2}\right],\left[\frac{r}{(\frac{(N-2)+(N-1)}{2})^2}\right]\right)$, where $r$ is the reference correlation coefficient. Moreover, when $\mathbf{N_2}$ is placed at the middle $d_{12}$ range, the correlation coefficient is equal to $r$, assuming that $r_{tx}$ is the reference correlation coefficient, the transmitter correlation matrix for $N$ by $N$ model is

$$\mathbf{R_{Tx}} = \begin{pmatrix} 1 & (a_1,a_2) & (b_1,b_2) & \cdots & (c_1,c_2) \\ (a_1,a_2) & 1 & (a_1,a_2) & \ddots & \vdots \\ (b_1,b_2) & (a_1,a_2) & 1 & \ddots & (b_1,b_2) \\ \vdots & \ddots & \ddots & \ddots & (a_1,a_2) \\ (c_1,c_2) & \cdots & (b_1,b_2) & (a_1,a_2) & 1 \end{pmatrix} \tag{3.26}$$

where, $(a_1, a_2) = (\frac{1-r_{tx}}{2}, \frac{r_{tx}}{(3/2)^2})$

$(b_1, b_2) = (\frac{r_{tx}}{(3/2)^2}, \frac{r_{tx}}{(5/2)^2})$

and $(c_1, c_2) = (\frac{r_{tx}}{(\frac{(N-2)+(N-1)}{2})^2}, \frac{r_{tx}}{(N-1)^2})$

In addition, the receiver correlation matrix for $M$ by $M$, with the reference $r_{rx}$ is

$$\mathbf{R_{Rx}} = \begin{pmatrix} 1 & (a_{11},a_{22}) & (b_{11},b_{22}) & \cdots & (c_{11},c_{22}) \\ (a_{11},a_{22}) & 1 & (a_{11},a_{22}) & \ddots & \vdots \\ (b_{11},b_{22}) & (a_{11},a_{22}) & 1 & \ddots & (b_{11},b_{22}) \\ \vdots & \ddots & \ddots & \ddots & (a_{11},a_{22}) \\ (c_{11},c_{22}) & \cdots & (b_{11},b_{22}) & (a_{11},a_{22}) & 1 \end{pmatrix} \tag{3.27}$$

where, $(a_{11}, a_{22}) = (\frac{1-r_{rx}}{2}, \frac{r_{rx}}{(3/2)^2})$

$(b_{11}, b_{22}) = (\frac{r_{rx}}{(3/2)^2}, \frac{r_{rx}}{(5/2)^2})$

and $(c_{11}, c_{22}) = (\frac{r_{rx}}{(\frac{(N-2)+(N-1)}{2})^2}, \frac{r_{rx}}{(N-1)^2})$

To simplify this model, it can be assumed that each antenna is placed at the middle of it is range area. Then $\mathbf{R}_{TX}$ and $\mathbf{R}_{RX}$ will be defined as

$$\mathbf{R}_{Tx} = \begin{pmatrix} 1 & r_{tx} & \frac{r_{tx}}{4} & \cdots & \frac{r_{tx}}{(N-1)^2} \\ r_{tx} & 1 & r_{tx} & \ddots & \vdots \\ \frac{r_{tx}}{4} & r_{tx} & 1 & \ddots & \frac{r_{tx}}{4} \\ \vdots & \ddots & \ddots & \ddots & r_{tx} \\ \frac{r_{tx}}{(N-1)^2} & \cdots & \frac{r_{tx}}{4} & r_{tx} & 1 \end{pmatrix} \tag{3.28}$$

$$\mathbf{R}_{Rx} = \begin{pmatrix} 1 & r_{rx} & \frac{r_{rx}}{4} & \cdots & \frac{r_{rx}}{(M-1)^2} \\ r_{rx} & 1 & r_{rx} & \ddots & \vdots \\ \frac{r_{rx}}{4} & r_{rx} & 1 & \ddots & \frac{r_{rx}}{4} \\ \vdots & \ddots & \ddots & \ddots & r_{rx} \\ \frac{r_{rx}}{(M-1)^2} & \cdots & \frac{r_{rx}}{4} & r_{rx} & 1 \end{pmatrix} \tag{3.29}$$

where, $r_{tx}$ and $r_{rx}$ are real-reference correlation coefficients for $\mathbf{R}_{Tx}$ and $\mathbf{R}_{Rx}$. $N$ and $M$ are the total number of antennas at the transmitter and receiver respectively. It is a powerful property of this model that the correlation is assigned starting from zero to one, *i.e.*, from fully uncorrelated to fully correlated.

Figure 3.11 describes the determinant changing of the correlation matrices for different values of correlation coefficients and different MIMO system configurations (i.e., choosing different number of transmitting and receiving antennas). This figure is limited to the use of equal numbers of transmitting and receiving antennas. The achieved determinant values are mapped between zero and one as the correlation coefficients are changed between zero and one.

Figure 3.11 shows the achieved result of the proposed model for $\mathbf{R}_{Tx}$ a function of $r_{tx}$, which gives a similar results to those achieved by [99], since the determinant for the modelled matrix is monotonically decreasing in the range of interest, *i.e.*, $0 \leq r_{tx} \leq 1$.

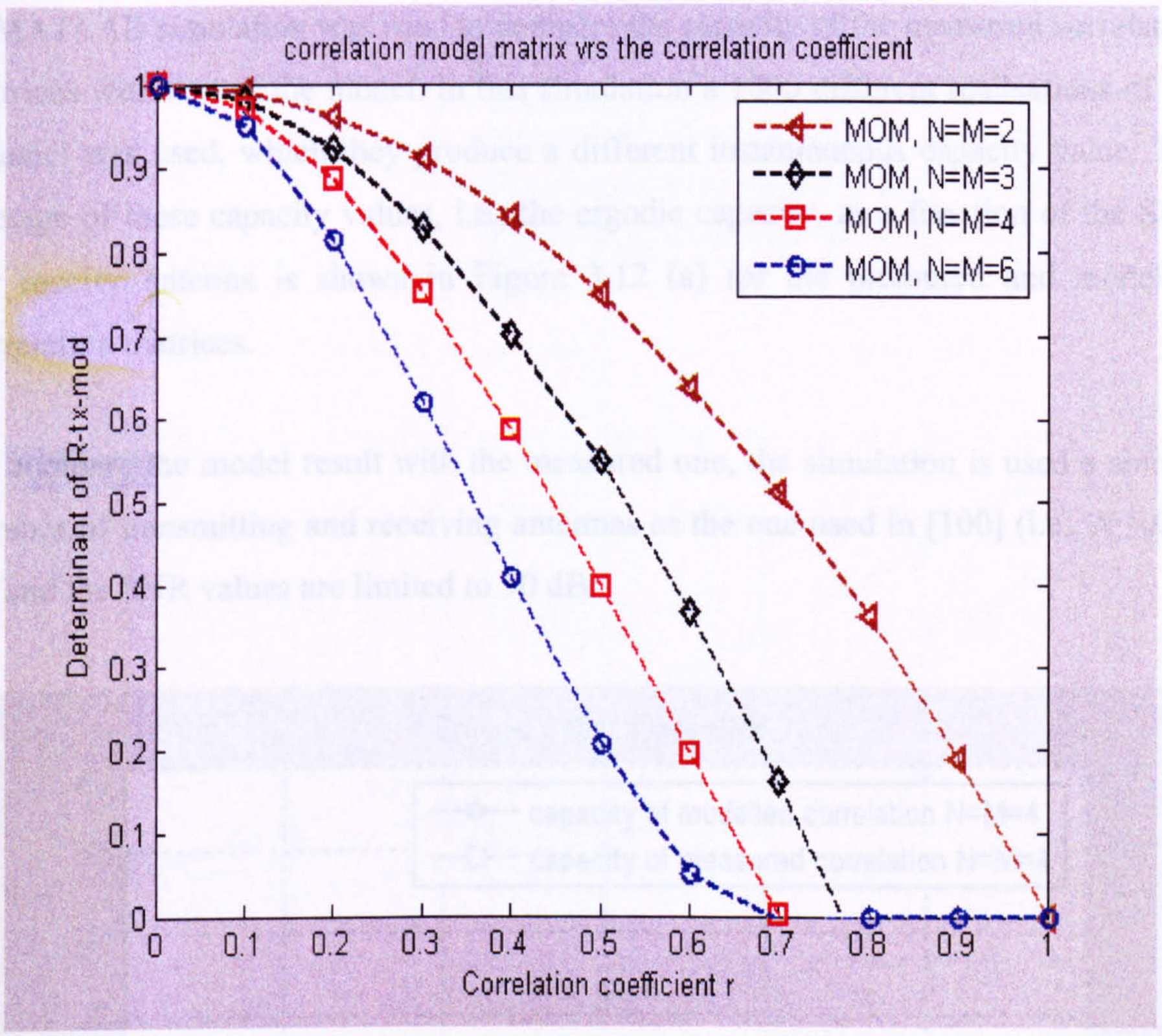


**Figure 3.11: The determinant of the correlation model matrix RTX, mod versus the correlation coefficient rtx for a various number of TX antennas**

To check the proposed model performance, a measured complex correlation matrices in a picocell environment is used to relate the capacity with the SNR. These matrices are found in [100] and given by

$$\mathbf{R}_{TX} = \begin{pmatrix} 1 & -0.61+0.77i & 0.14-0.94i & 0.24+0.89i \\ -0.61-0.77i & 1 & -0.85+0.5i & 0.57-0.78i \\ 0.14+0.94i & -0.85-0.5i & 1 & -0.91+0.4i \\ 0.24-0.89i & 0.57+0.78i & -0.91-0.4i & 1 \end{pmatrix} \tag{3.30}$$

$$\mathbf{R}_{RX} = \begin{pmatrix} 1 & -0.12-0.18i & 0.08+0.05i & -0.02-0.13i \\ -0.12+0.18i & 1 & -0.17-0.16i & 0.11+0.04i \\ 0.08-0.05i & -0.17+0.16i & 1 & -0.17-0.16i \\ -0.02+0.13i & 0.11-0.04i & -0.17+0.16i & 1 \end{pmatrix} \tag{3.31}$$

A MATLAB simulation was used to compare the capacity of the measured correlation matrices with that of the model. In this simulation a 1000 different realisations of the channel was used, which they produce a different instantaneous capacity value. The average of these capacity values, i.e., the ergodic capacity, as a function of the SNR per receive antenna is shown in Figure 3.12 (a) for the measured and modelled correlation matrices.

To compare the model result with the measured one, the simulation is used a similar number of transmitting and receiving antennas as the one used in [100] (i.e., $N = M = 4$), and the SNR values are limited to 30 dB.

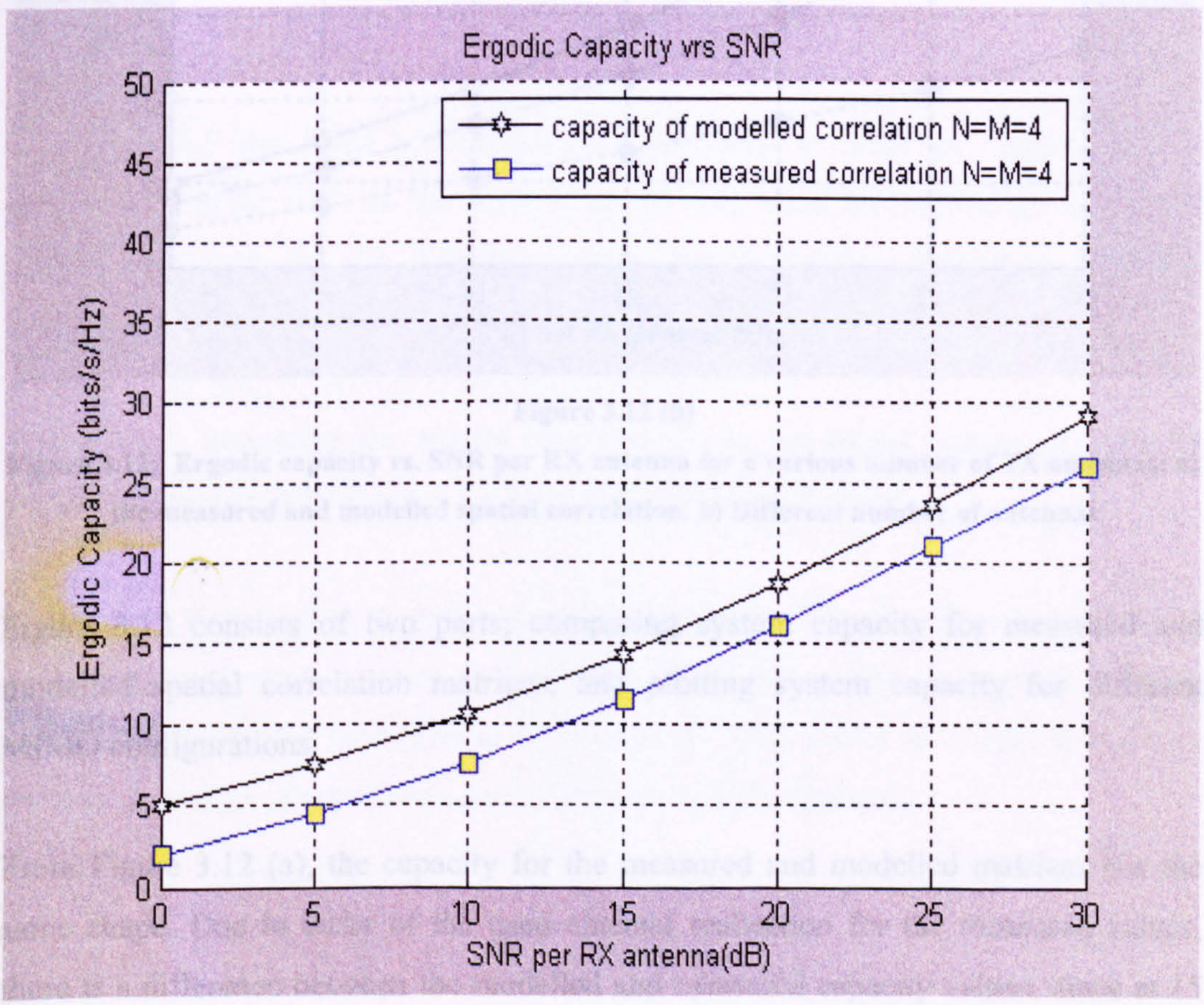


**Figure 3.12 (a)**

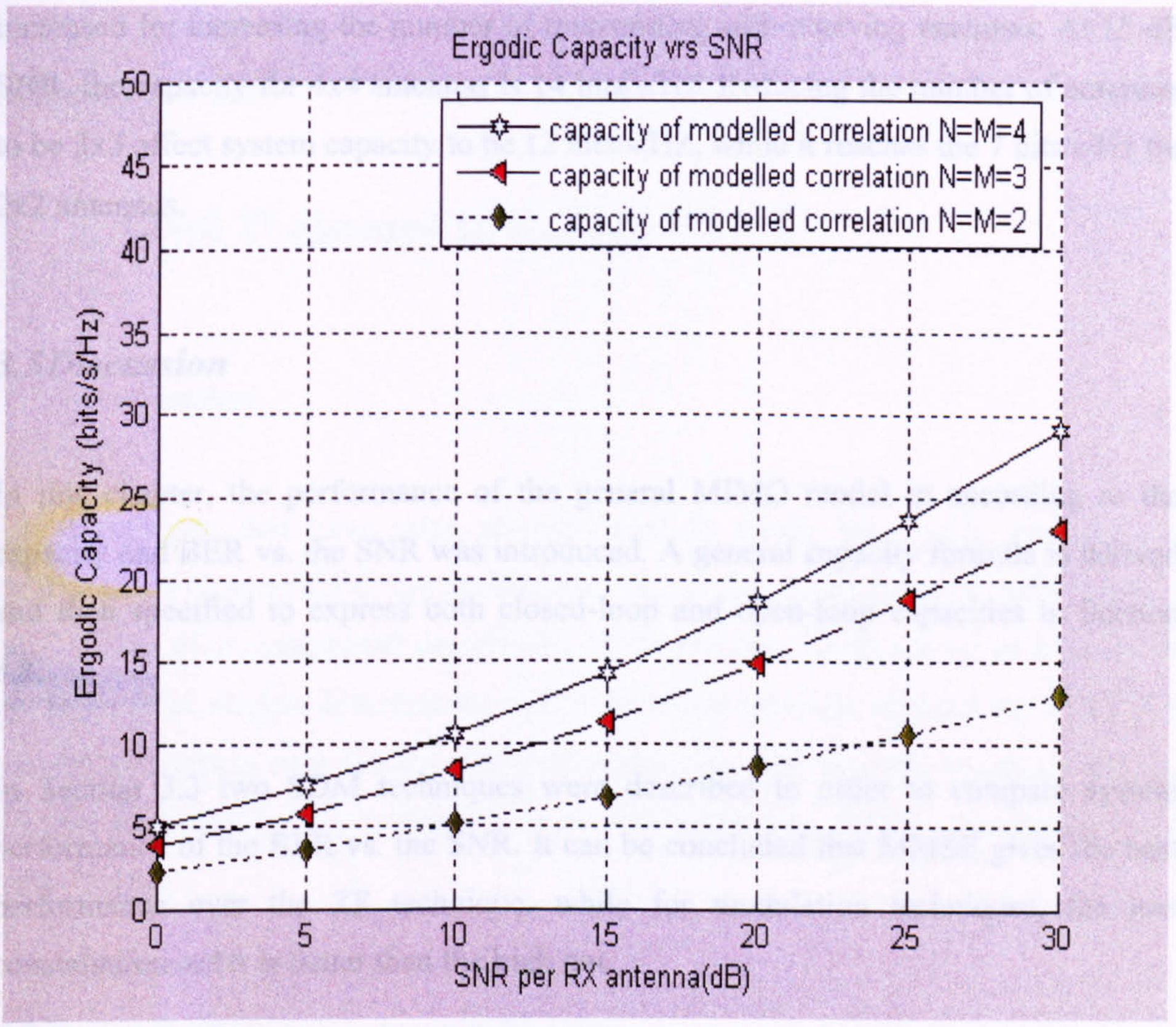


**Figure 3.12 (b)**

**Figure 3.12: Ergodic capacity vs. SNR per RX antenna for a various number of TX antennas: a) the measured and modelled spatial correlation. b) Different number of antennas**

Figure 3.12 consists of two parts; comparing system capacity for measured and modelled spatial correlation matrices; and plotting system capacity for different MIMO configurations.

From Figure 3.12 (a), the capacity for the measured and modelled matrices has the same shape. Due to lacks of the used channel realisation for the measured values, there is a difference between the modelled and measured capacity values, since at 15 dB SNR the capacity for the modelled matrices is 14 bits/s/Hz and equals 12 bits/s/Hz for the measured matrices.

Figure 3.12 (b) shows the relationship between the ergodic capacity and the SNR for different MIMO structures. Obviously from this figure, the achieved capacity is

increased for increasing the number of transmitting and receiving antennas. At 15 dB SNR, the capacity for 4x4 antennas is 14 bits/s/Hz. Reducing the number of antennas to be 3x3 affect system capacity to be 12 bits/s/HZ, while it reaches the 7 bits/s/Hz for 2x2 antennas.

## *3.5Discussion*

In this chapter, the performance of the general MIMO model in according to the capacity and BER vs. the SNR was introduced. A general capacity formula is derived and then specified to express both closed-loop and open-loop capacities in Section 3.2.

In Section 3.3 two SDM techniques were described in order to compare system performance of the BER vs. the SNR. It can be concluded that MMSE gives the best performance over the ZF technique, while for modulation techniques, the low constellation order is better than the high one.

Furthermore, increasing the system configuration to use larger number of antennas will reduce system performance for both of the SDM techniques.

In Section 3.4, according to spatial diversity, a model to examine the effect of spatial correlation on system capacity was introduced. In this section, a channel capacity model in a correlated environment is introduced. This model is simple and allows study of the effect of correlation on the MIMO capacity explicitly.

# Chapter Four

# 4. A Novel Technique to Reduce PAPR

## *4.1Introduction*

The techniques that have been already used to tackle the PAPR problem (as mentioned in Section 2.4.4) are divided into two groups. One of them suffers from a high degree of computational complexity, while the other suffers from an increase in the BER. This chapter describes the new proposition which is denoted by NTRPT. It has the advantages over the conventional techniques. For the sake of generalisation, the new technique is described based on two types of linear coding, convolutional and turbo coding.

## *4.2Novel PAPR Reduction Technique*

An OFDM symbol is produced when a number of signals, *F*, are added together in the IFFT stage. Occasionally, if the added signals are in phase with each other, IFFT will produce an OFDM symbol with high peak power. Comparing the high peak power of the OFDM symbol to its average power will define one of the main drawbacks of OFDM, namely, PAPR. The PAPR in dB can be written as

$$\text{PAPR}=10\log_{10}\left\{\frac{P_{peak}}{P_{avg}}\right\}\ \text{dB} \tag{4.1}$$

where $P_{\text{peak}}$ is the maximum power of an OFDM symbol, and $P_{\text{avg}}$ is the average power. Equation 4.1 can be written as

$$\text{PAPR}=10\log_{10}\left\{\frac{\max\limits_{0\le t\le FT}\left|x(t)\right|^2}{\frac{1}{FT}\int_0^{FT}\left|x(t)\right|^2 dt}\right\}\ \text{dB} \tag{4.2}$$

where, $T$ is the OFDM symbol period and $x(t)$ is the OFDM symbol which can be expressed as $x(t) = \frac{1}{\sqrt{F}} \sum_{n=0}^{F-1} X_n e^{j2\pi f_o nt}$ for $0 \le t \le F$T, where $X_n$ is the modulated data of the n-*th* subcarrier, $f_o$ is the subcarrier frequency, and j= $\sqrt{-1}$. From the definition of the OFDM symbol, the average power in (4.1) could be written as:

$$P_{avg} = E\{|x(t)|^2\} = \frac{1}{T}\int_0^T |x(t)|^2 dt$$

$$P_{avg} = \frac{1}{T}\int_0^T \left| \sum_{n=0}^{F-1} X_n e^{(j2\pi \frac{n}{FT} t_n)} \right|^2 dt$$

$$P_{avg} = \frac{1}{T}\int_0^T (\sum_{n=0}^{F-1} X_n \cos(2\pi \frac{n}{FT} t_n))^2 + (\sum_{n=0}^{F-1} X_n \sin(2\pi \frac{n}{FT} t_n))^2 dt$$

$$P_{avg} = \frac{1}{T}\int_0^T (\sum_{n=0}^{F-1} X_n^2) dt \qquad (4.3)$$

For simplicity, if a BPSK modulation scheme is used without any channel coding, the magnitude of $X_n$, $|x_n|$, will be equal to one, when t $\in$[0, $T$] (to be substituted in (4.3)). The result of this substitution leads to a direct relationship between average power and the total number of subcarriers (the number of the IFFT points), which can be taken directly from

$$P_{avg} = F \frac{1}{T}\int_0^T X_n^2 dt$$

$$= F \qquad (4.4)$$

From (4.4), it can be seen that average power is equal to the number of the BPSK-modulated orthogonal subcarriers. Then, from (4.1), the PAPR of uncoded BPSK will be equal to $10\log_{10}(F)$ dB.

This result will be the basis of the proposed technique, NTRPT. From the substitution result of (4.4) to (4.1), the PAPR ratio is equal to $10\log_{10}(P_{avg})$. Thus decreasing the average power of the OFDM symbol will decrease its PAPR.

After deriving the basis of NTRPT, Figure 4.1 will describe the NTRPT algorithm steps. This figure is divided into two main stages:

- Determination of the track of the OFDM symbol based on its PAPR value.
- Dealing with the processed OFDM symbol.

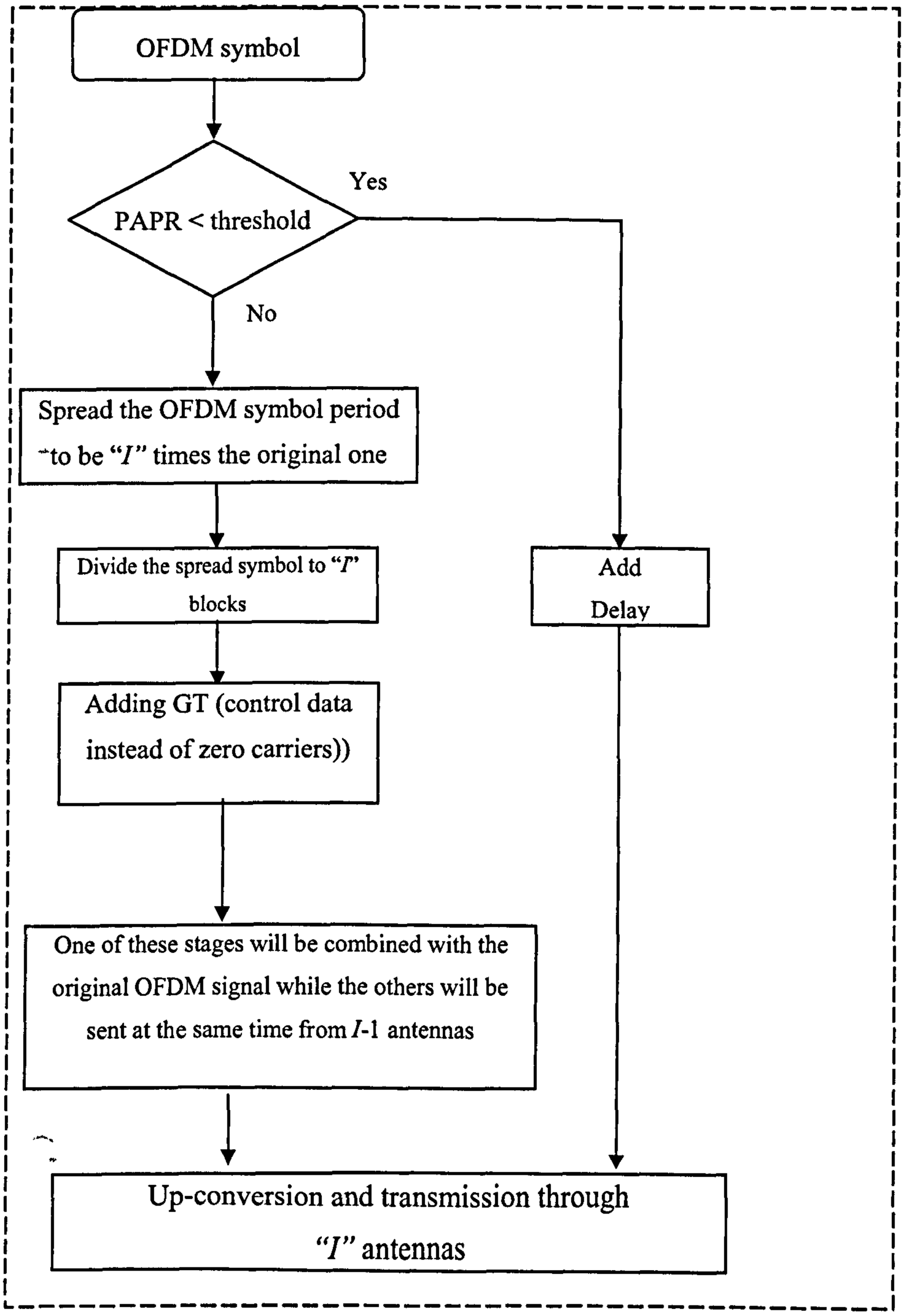


**Figure 4.1: The NTRPT flowchart**

In the first stage, the NTRPT begins by checking the OFDM symbol to determine if it suffers from high PAPR values. The obvious track for the symbol if it is not affected is that $I$ versions are transmitted through $I$ antennas. These versions are easily generated through a Space-Time encoder. On the other hand, if the symbol has high PAPR, it will pass through a time linear encoder after removing the guard interval. *The encoder will be used for spreading purposes*, since linear coding techniques increase the symbol period in the time domain. The period of the affected symbol will be spread according to the chosen spreading rate.

The second stage deals with the new symbol, and with choosing the data with the lowest PAPR value. The spread symbol will be mapped onto $I$ parallel blocks, each of which has the same duration as the conventional symbol duration with a PAPR value less than the PAPR of the conventional OFDM symbol. For more details, Figure 4.2 gives a brief description of the NTRPT block diagram according to the flowchart shown in Figure 4.1.

Unlike conventional techniques, most of which (as described in the previous section) suffer from a high degree of computational complexity, NTRPT reduces the computational complexity to the first order.

The added complexity is due to calculating the PAPR of each block and choosing are with the lowest value. The following formula shows the needed number of iterations

$$\text{Iterations} = [((I\text{-}1)\,F) + 1]$$

where $I$ is the spreading rate and $F$ is the number of the IFFT points.

For transmission purposes, the Zero Padded (ZP)-OFDM [101] is used to add a deterministic control sequence instead of the zero carriers. This control data is used to recover the affected OFDM symbol at the receiver. After that, these blocks will be transmitted through $I$ antennas.

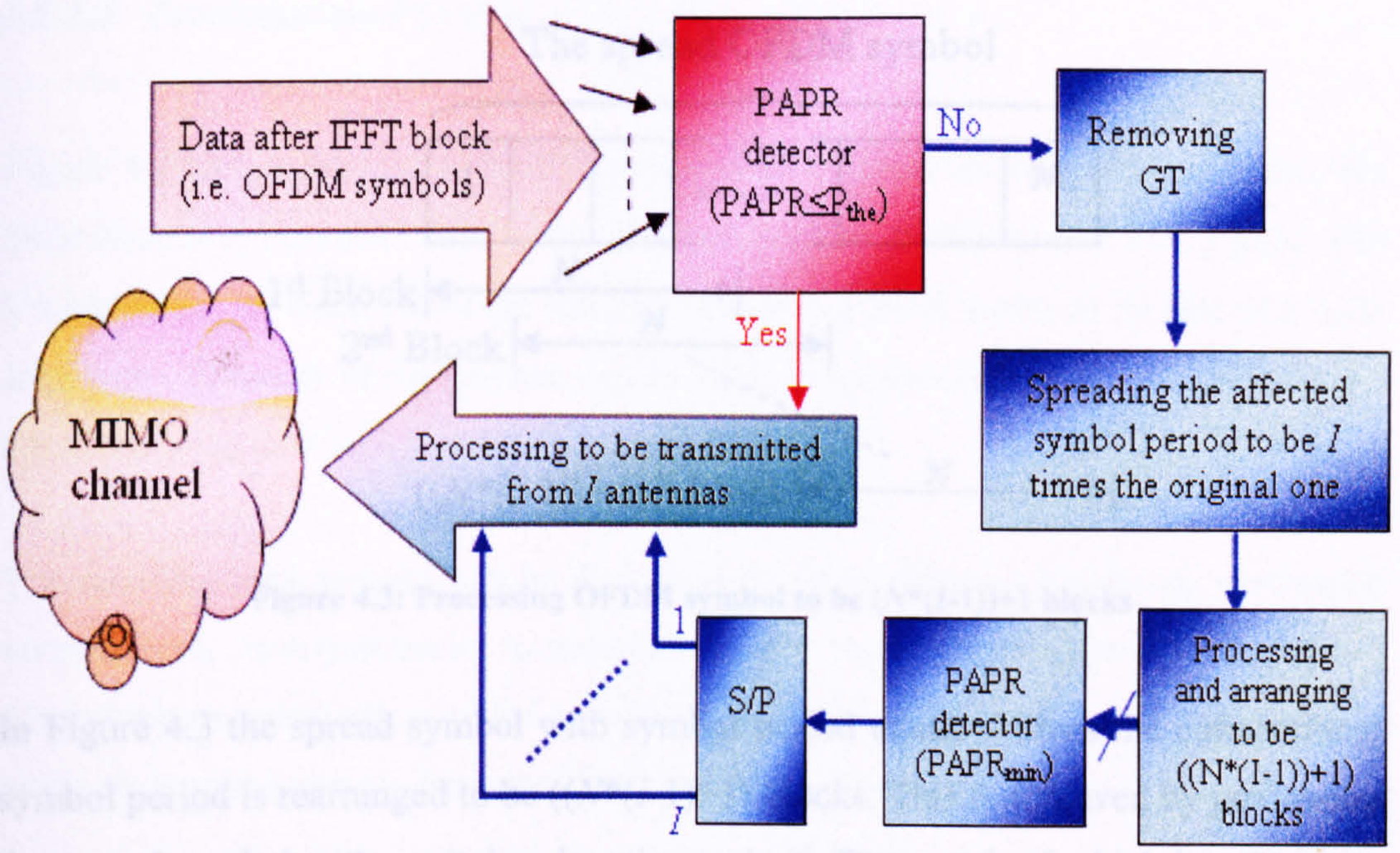


**Figure 4.2: The NTRPT block diagram**

Figure 4.2 describes NTRPT process to deal with both of the affected and unaffected OFDM symbols by a high PAPR. The OFDM symbol is produced after the IFFT stage, this symbol will be examined by a PAPR detector. If the symbol is unaffected by a high PAPR it will be processed to be in a suitable format to be sent through MIMO antennas. On the other hand, the guard interval will be removed and the conventional symbol will be sent to a spreading block. In this stage removing the guard interval is needed just to process the useful data without any redundant data. During the spreading block, the conventional symbol will be spread according to the spreading rate. The spread symbol will be processed and rearranged in blocks as described in Figure 4.3. Each of which has as the same symbol period as the conventional symbol before spreading. After that, these blocks are passed a PAPR detector, this detector will sort the blocks in ascending arrangement according their PAPR values. Then, the block which has the lowest PAPR will join the OFDM signal instead of the affected symbol, while the others will be processed to be transmitted through $I$-1 antennas. Figure 4.3 explains the processing that is held for the spread symbol before entering the PAPR detecting and S/P stages.

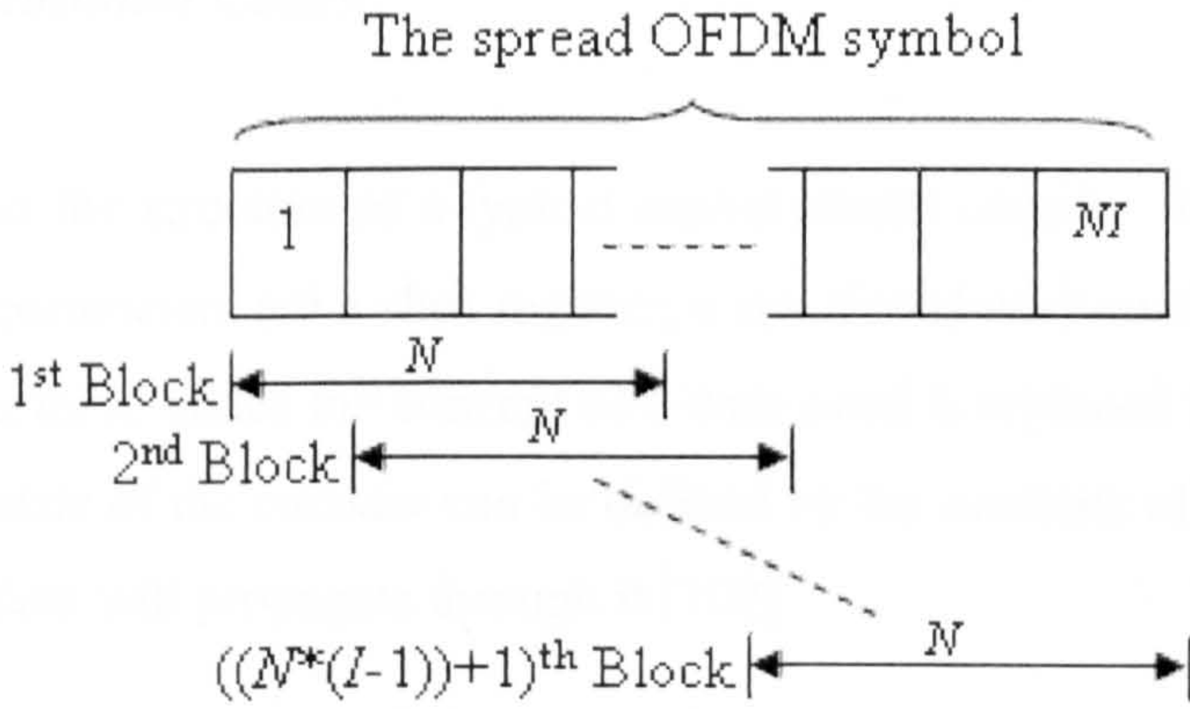


**Figure 4.3: Processing OFDM symbol to be (*N**(*I*-1))+1 blocks**

In Figure 4.3 the spread symbol with symbol period equals *I* times the conventional symbol period is rearranged to be ((*N**(*I*-1)+1) blocks. This is achieved by processing the spread symbol with a window length equals *N*. Thus, each of which has the same period as the original symbol. During this process, there will be ((*N**(*I*-1)+1) blocks to be processed by the second PAPR detector to choose the block with minimum PAPR in Figure 4.2.

These blocks are passed through a PAPR detector to choose the block with the lowest PAPR value to be sent instead of the conventional symbol. The rest of the spread data is sent through *I*-1 antennas after passing through an S/P block.

### 4.2.1 Linear Coding techniques

In this subsection, two types of linear coding techniques, convolutional codes and turbo codes, will be examined. Convolutional codes can be described in two ways: firstly in term of mechanisms for generating the coded data from the input data; and secondly in terms of trellis which describe constraint that will be satisfied by valid transmissions. Turbo codes are defined by a number of convolutional encoders and interleavers.

### *4.2.1.1 Convolutional Codes*

Figure 4.4 shows the structure of a typical convolutional encoder. In this figure, the main structural parameters are a shift register, a set of exclusive-OR (XOR) gates, and a multiplexer. In these codes the concept of a codeword is replaced by that of a code sequence. The state of the encoder can be defined by the contents of the shift register while the input data will propagate through it [102].

The convolutional encoder can be described by three different structures: systematic nonrecursive, nonsystematic nonrecursive, and systematic recursive structures. Systematic encoders are so called because the source bits are reproduced transparently in the transmitted stream. Nonrecursive encoders have no feedback.

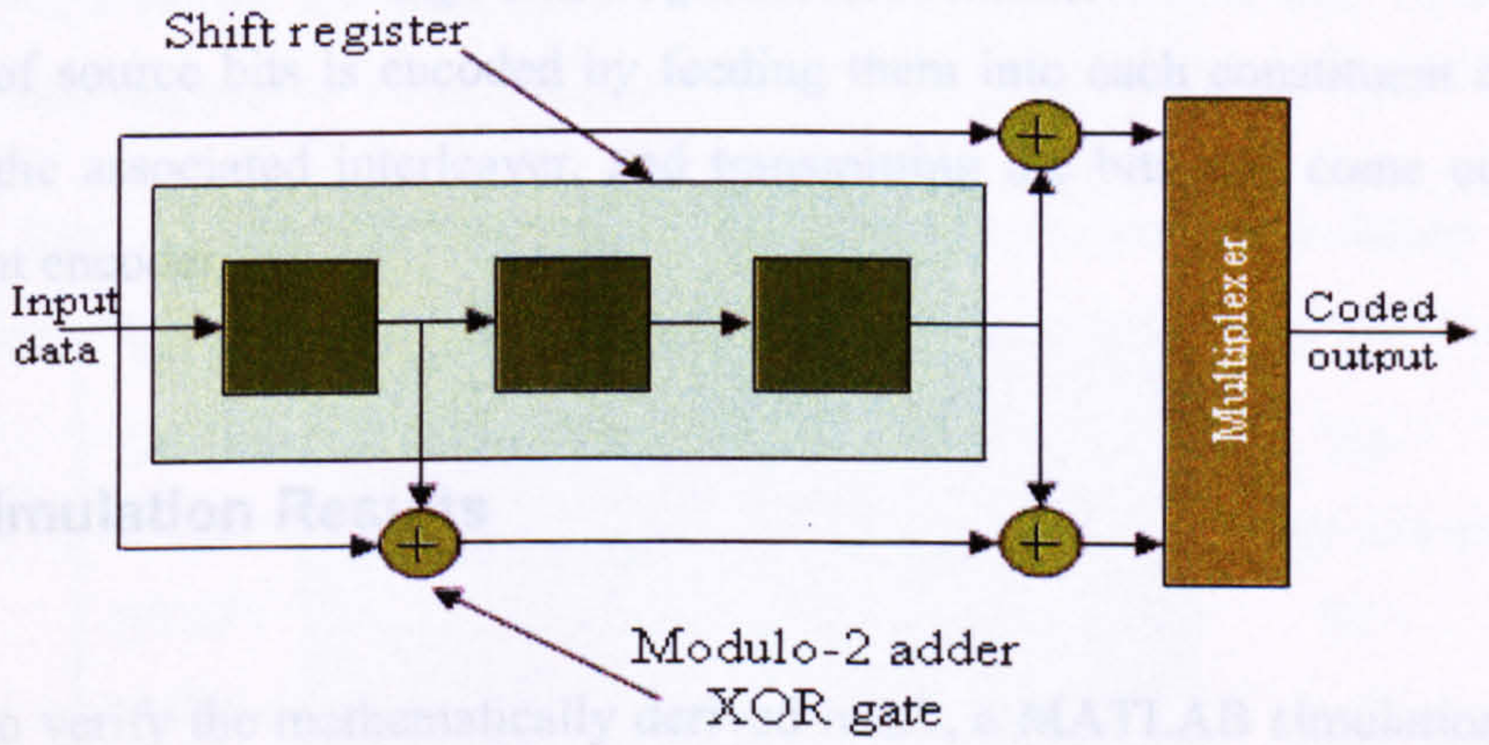


**Figure 4.4: Typical Convolutional Coder**

The present study concentrates on the nonsystematic nonrecursive encoders because; the nonsystematic codes have error-correcting abilities. The proposed technique aims to increase the length of the affected symbol and change the sample as much as possible.

### *4.2.1.2 Turbo Codes*

A turbo code is defined by a number of constituent convolutional encoders (the constituent encoders may be different, but in practice they are normally identical) and

an equal number of interleavers which are permutation matrices (i.e. they rearrange the order of the data bits in a prescribed, but irregular, manner). Without the interleaver, the two constituent encoders would receive the data in exactly same order and thus - assume identical constituent encoders - their outputs would be the same [103]. A generic structure for generating turbo codes is shown in Figure 4.5.

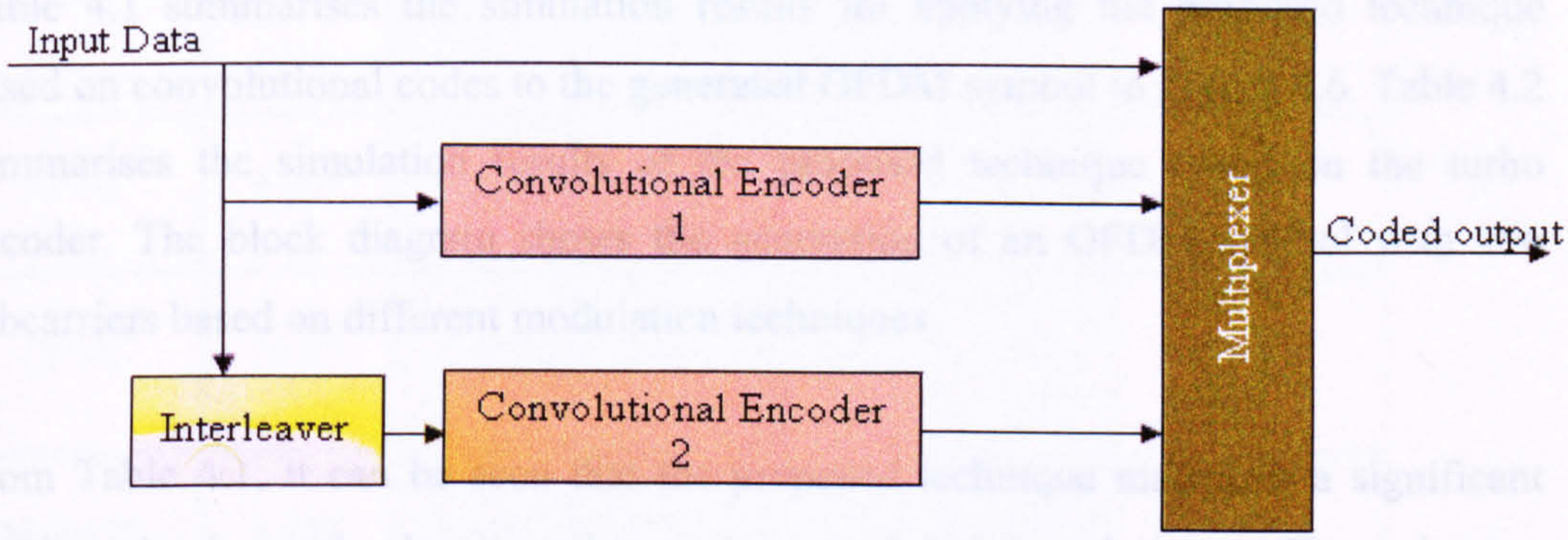


**Figure 4.5: A generic turbo encoder**

A string of source bits is encoded by feeding them into each constituent encoder in order of the associated interleaver, and transmitting the bits that come out of each constituent encoder.

### 4.2.2 Simulation Results

In order to verify the mathematically derived result, a MATLAB simulation program was developed for a basic OFDM symbol. Figure 4.6 shows the block diagram of generating a basic OFDM symbol.

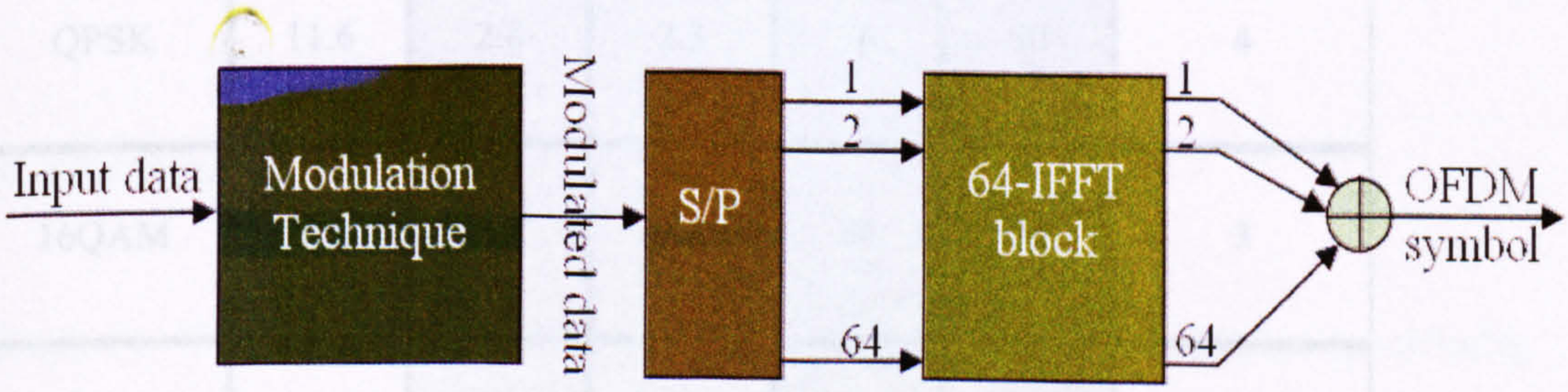


**Figure 4.6: Generating an OFDM symbol block diagram**

A uniformly distributed randomly generated data sequence is generated. The variable

system parameters were:

- different modulation techniques (BPSK, QPSK, 16QAM, and 64QAM)
- IFFT size of 256
- two different spreading rates: $i = 2$ and 3

Table 4.1 summarises the simulation results for applying the proposed technique based on convolutional codes to the generated OFDM symbol in Figure 4.6. Table 4.2 summarises the simulation results of the proposed technique based on the turbo encoder. The block diagram shows the generation of an OFDM symbol with 256 subcarriers based on different modulation techniques.

From Table 4.1, it can be seen that the proposed technique maintains a significant PAPR reduction ratio despite using various modulation techniques. The reduction ratio of PAPR for the block diagram in Figure 4.6 reaches 80% and 76% when the spreading rate is equal to 3 and 2 respectively.

**Table 4.1: The NTRPT simulation results based on convolutional encoder**

| Modulation tech. | PAPR before the NTRPT (dB) | PAPR after the NTRPT(dB) | | The reduction ratio (%) | | The improvement (%) |
|---|---|---|---|---|---|---|
| | | Spreading rate | | Spreading rate | | |
| | | 2 | 3 | 2 | 3 | |
| BPSK | 7.3 | 3.3 | 3.1 | 55 | 58 | 3 |
| QPSK | 11.6 | 2.8 | 2.3 | 76 | 80 | 4 |
| 16QAM | 12.4 | 3.2 | 2.8 | 74 | 77 | 3 |
| 64QAM | 10.7 | 3.6 | 3.1 | 66 | 71 | 5 |

**Table 4.2: The NTRPT simulation results based on turbo encoder**

| Modulation tech. | PAPR before the NTRPT (dB) | PAPR after the NTRPT(dB) | | The reduction ratio (%) | | The improvement (%) |
|---|---|---|---|---|---|---|
| | | Spreading rate | | Spreading rate | | |
| | | 2 | 3 | 2 | 3 | |
| BPSK | 4.054 | 1.133 | 1.01 | 72.1 | 75.1 | 3 |
| QPSK | 10.07 | 1.617 | 1.3445 | 83.8 | 83.9 | 0.1 |
| 16QAM | 9.418 | 1.579 | 1.056 | 83.2 | 88.7 | 5.5 |
| 64QAM | 8.189 | 2.059 | 1.706 | 74.9 | 79.1 | 4.2 |

From Table 4.2 it can be seen that the proposed technique maintains better results than those summarised in Table 4.1. The reduction ratios of the PAPR increase to 88.7% and 83.8% when the spreading rate is equal to 3 and 2 respectively.

Moreover, a slight improvement in PAPR reduction ratios is shown as a consequence of using different spreading rates. The improvement yielded by increasing the spreading rate to 3 is shown in the last column. This improvement varies depending on the modulation techniques themselves.

## *4.3Summary*

Due to the main disadvantages of the conventional techniques, specifically computational complexity and high data loss, a new technique based on the linear coding techniques such as the convolutional and the turbo encoders is proposed. Part of this work is already accepted for publication in [104, 105]. The work added a first order computational complexity instead of the high computational complexity in the

literature; it also guaranteed that there is no data loss incurred as a result of improving the PAPR process. The simulation results show a significant PAPR reduction with a simple computational complexity from the first order based on the number of subcarriers.

For convenience, applying this technique to a complete MIMO-OFDM system will be described in the next chapter.

# Chapter Five

## 5. The NTRPT-MIMO-OFDM System

### *5.1 Introduction*

In general, the MIMO and OFDM techniques described in Chapter 2 provide an interesting basis for the next generations of wireless communication systems, such as WLANs, and DVB-H. This leads to the promising combination of SDM's data rate enhancement with OFDM's relatively high spectral efficiency and the resistance to frequency selective fading and narrow band interferences of OFDM. Moreover, the combination between MIMO and OFDM techniques results in a number of issues, which need to be dealt with, including MIMO channel performance (i.e. a proper channel, the capacity and the BER) and the main problems of the OFDM techniques, must also be addressed such as those concerning nonlinearity, and synchronisation.

In chapter 3, a new MIMO channel model was proposed which would give in-depth understanding of the capacity of the MIMO channel and the effect of the correlation parameters on the channel performance [106]. In Chapter 4, a proposition of a novel technique was presented to combat one of the main problems of OFDM techniques, namely PAPR [105].

This chapter presents the application of the proposed technique in Chapter 4 to a MIMO-OFDM system. In Section 5.2, MIMO-OFDM system architecture will be described as will the MIMO-OFDM signal model will be described in Section 5.3. The simulation results will be given and discussed in Section 5.4, while a conclusion is drawn in Section 5.5.

## *5.2NTRPT-MIMO-OFDM system architecture*

In the MIMO-OFDM system, the NTRPT is placed after the IFFT stages in Figure 5.1. The NTRPT is based on linear coding techniques, which reduces the PAPR by adding redundant data to reduce the OFDM symbol average power. This redundant data is added based on the coding rate. As an example, if the coding rate is 1/2 then the resultant data rate will be twice the original rate. The best combination of the original data and the redundant data will then be chosen to give the lowest PAPR to be sent, whilst the rest of data will be sent to be used at the receiver to recover the original data (as presented in Chapter 4). The data will be transmitted through N stages, each of which has *I* antennas through a MIMO channel to be received by *M* antennas. Figure 5.1 depicts the baseband discrete-time block equivalent model of an N stage NTRPT-MIMO-OFDM transmission part with *F* subcarriers for each stage.

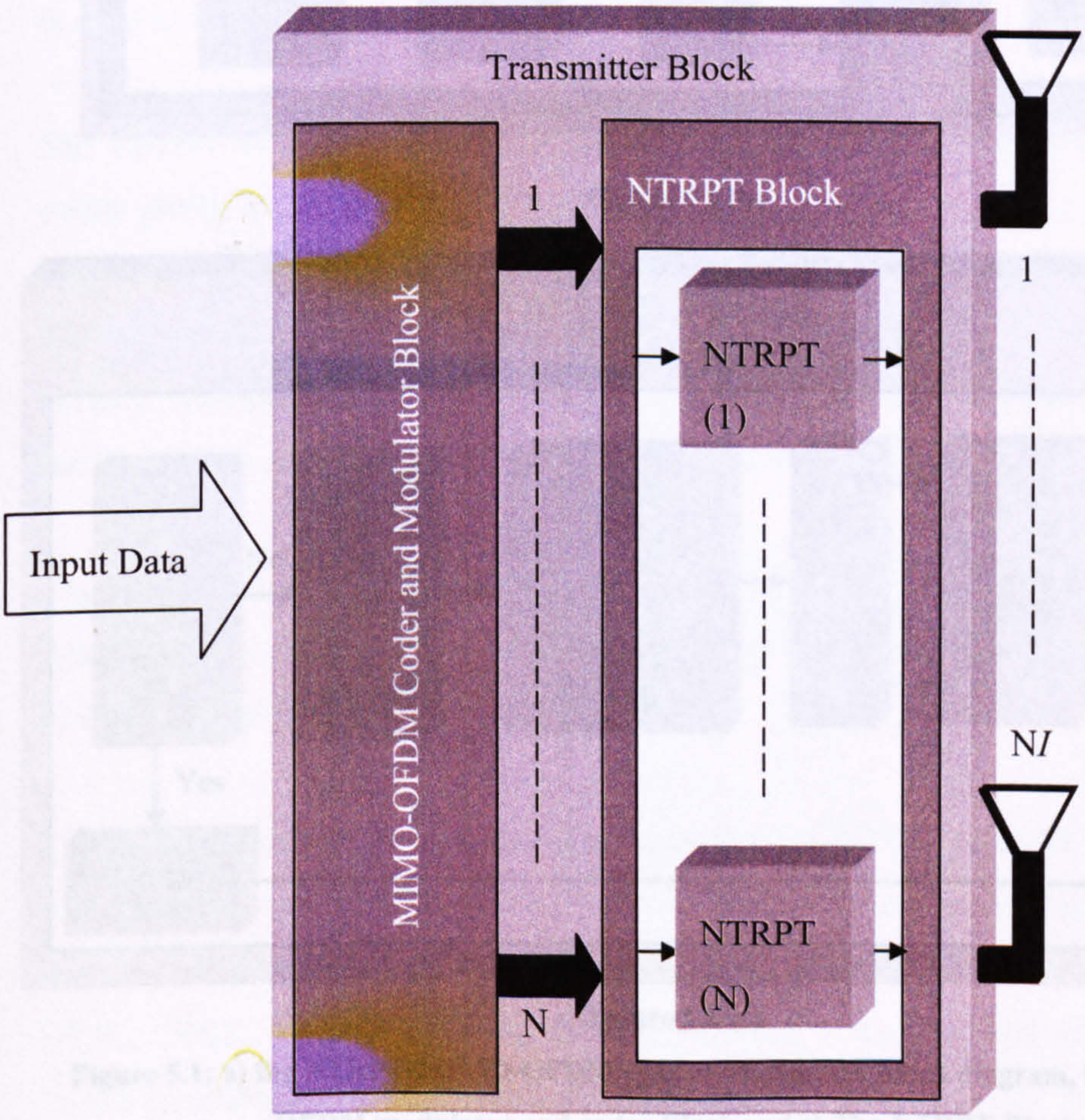


**Figure 5.1 (a)**

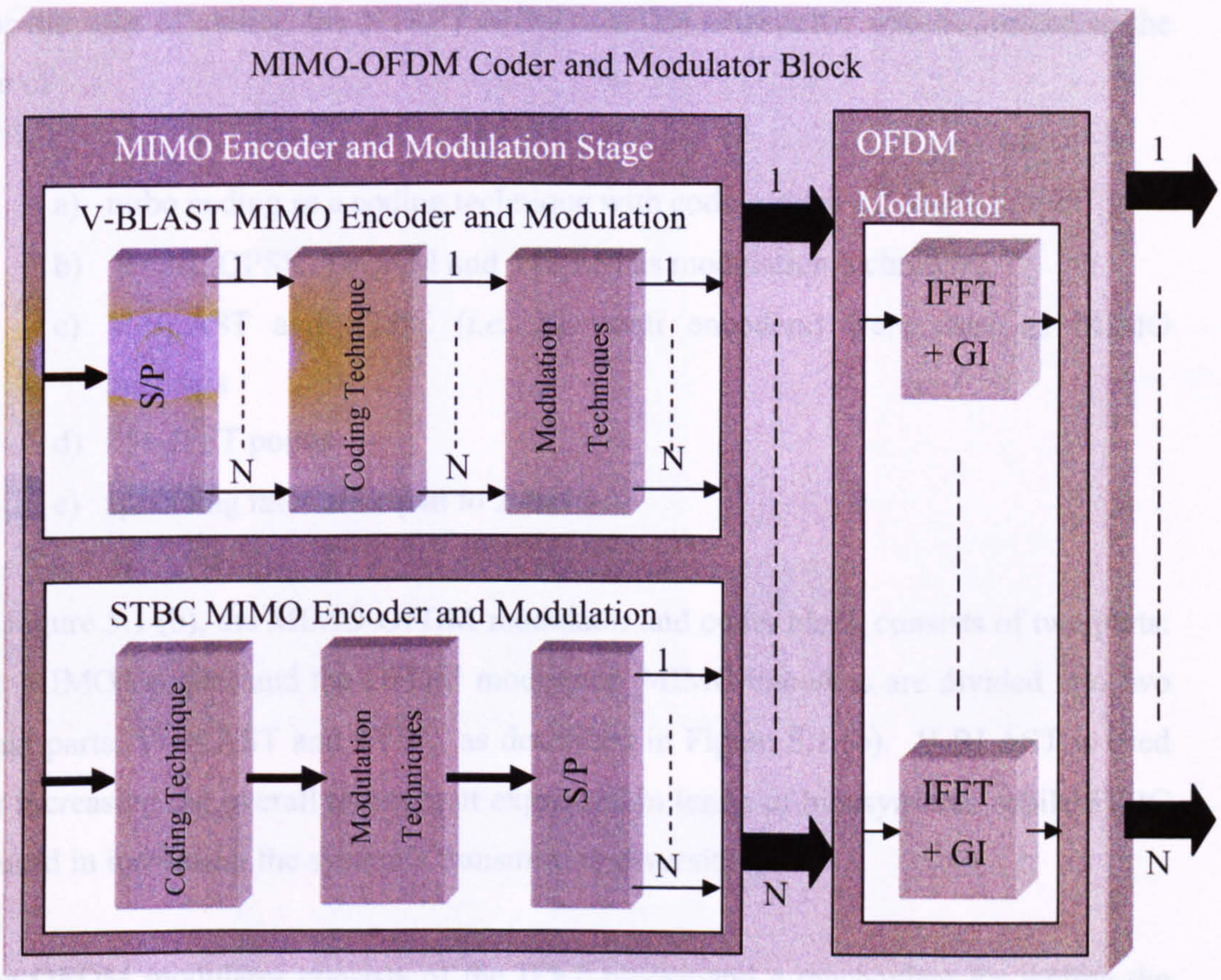


**Figure 5.1 (b)**

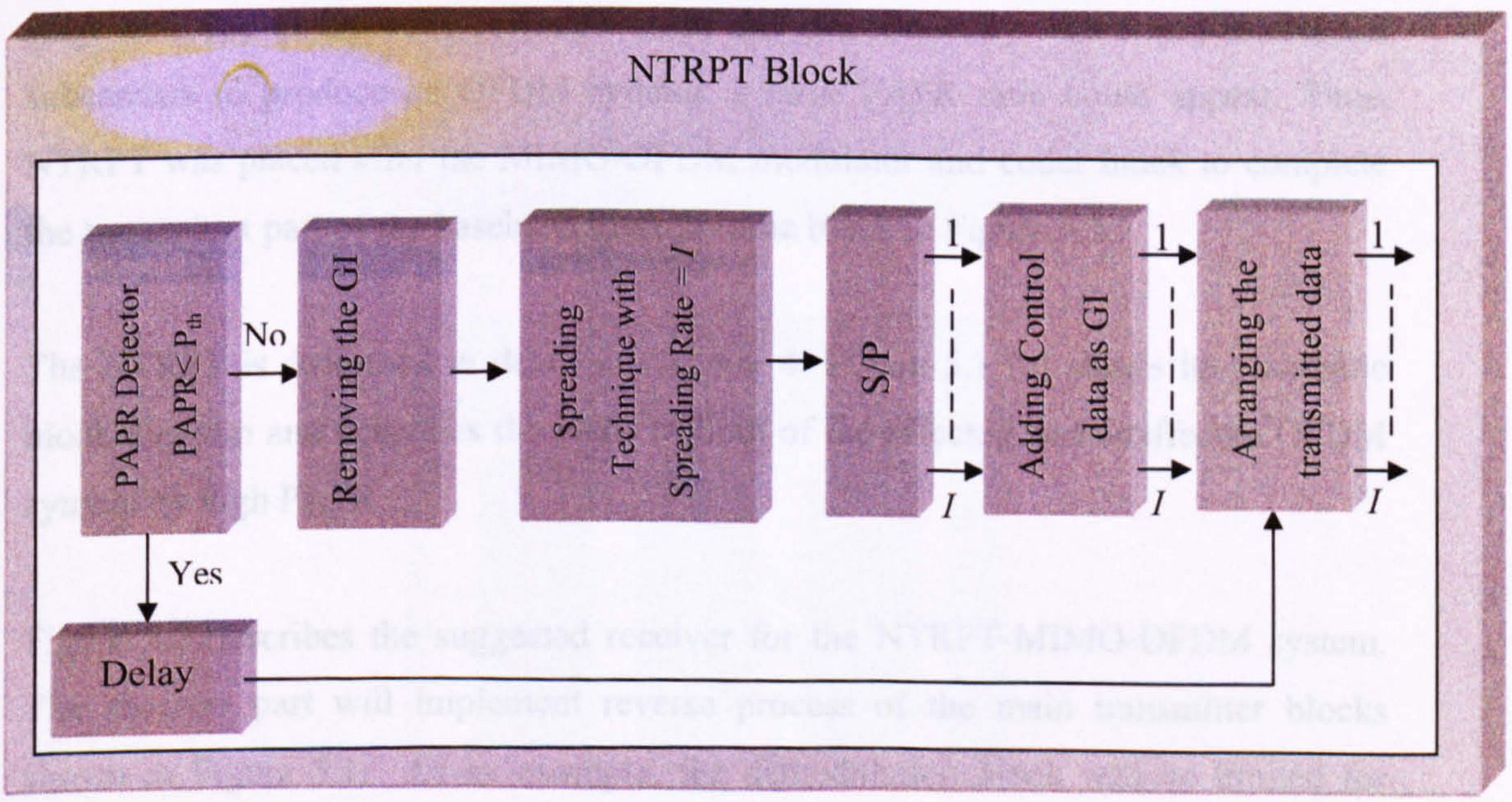


**Figure 5.1 (c)**

**Figure 5.1: a) the NTRPT-MIMO-OFDM system transmitter block diagram, b) The MIMO-OFDM modulator and coder Block and c) The NTRPT Block**

For the sake of clarity, the NTRPT-MIMO-OFDM transmitter will be limited to the use of

a) turbo coding as a coding technique with coding rates 1/2 and 1/3
b) BPSK, QPSK, 16QAM and 64QAM as modulation techniques
c) V-BLAST and STBC (*i.e.* Alamouti encoders) were used as MIMO encoders
d) 256-IFFT points
e) spreading rates are equal to 2 and 3

In Figure 5.1 (b), the MIMO-OFDM modulator and coder block consists of two parts: the MIMO encoder and the OFDM modulator. MIMO encoders are divided into two main parts, V-BLAST and STBC, as described in Figure 5.1 (b). V-BLAST is used for increasing the overall throughput expressed in terms of bits/symbols, while STBC is used in increasing the system's transmitting diversity gain.

The OFDM modulator consists of the IFFT blocks and a mechanism for adding the cyclic prefix in order to form the OFDM symbol with guard interval. After the IFFT stage and due to the coherent addition of the independently coded and modulated subcarriers to produce an OFDM symbol, a large PAPR ratio could appear. Thus, NTRPT was placed after the MIMO-OFDM modulator and coder block to complete the transmitter part of the baseband discrete-time block in Figure 5.1.

The NTRPT is described in detail in Chapter 4. Figure 5.1 (c) shows its schematic block diagram and describes the paths of both of the affected and unaffected OFDM symbol by high PAPR.

Figure 5.2 describes the suggested receiver for the NTRPT-MIMO-OFDM system. The receiver part will implement reverse process of the main transmitter blocks shown in Figure 5.1. As an example, the demodulation block will be limited for BPSK, QPSK, 16QAM and 64QAM demodulation techniques and the turbo decoder for the decoding block limited to a decoding rate of 1/2 and 1/3.

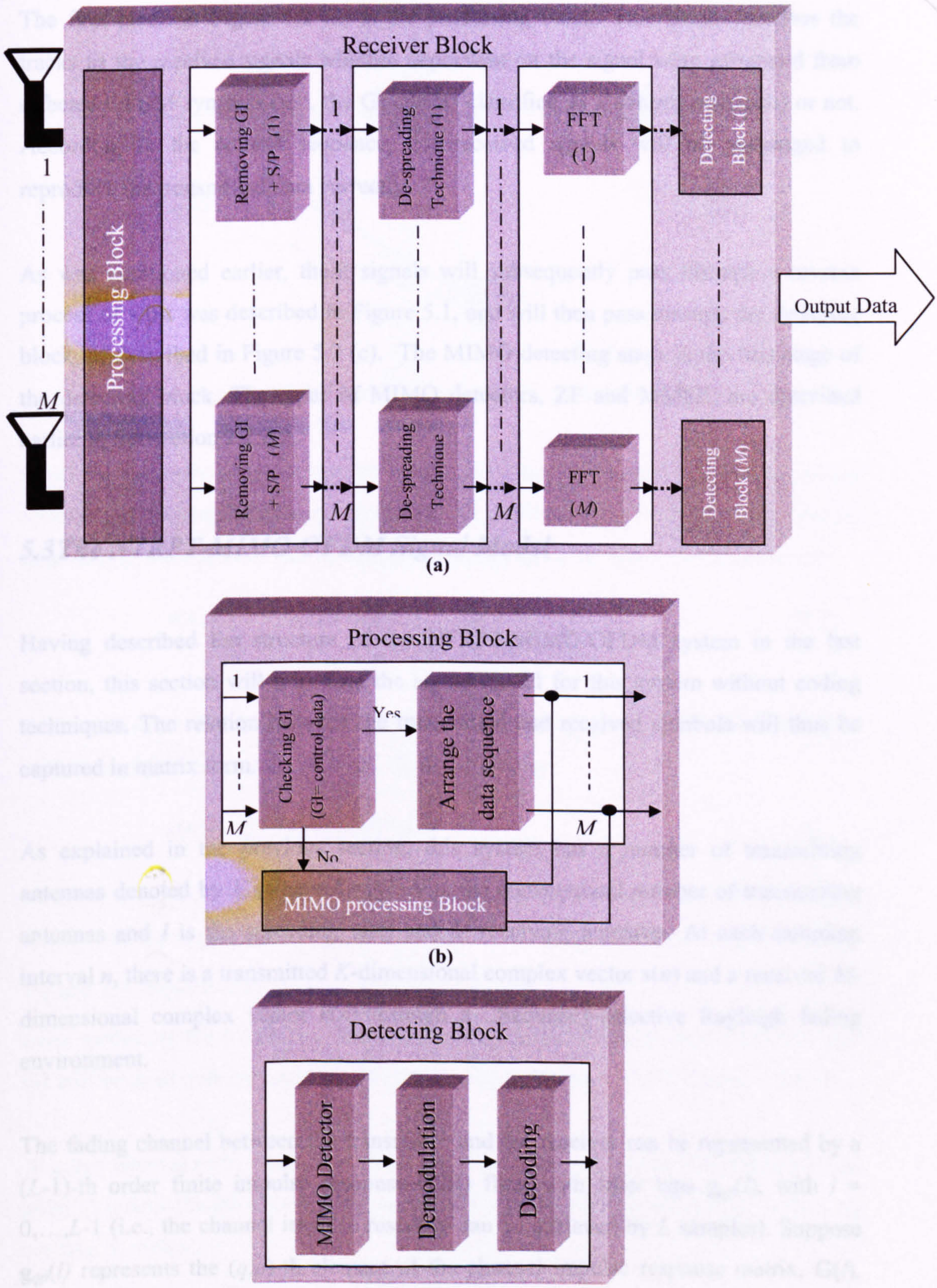


**Figure 5.2: a) the NTRPT-MIMO-OFDM system receiver block diagram, b) the processing Block and c) the detecting Block**

The first block in Figure 5.2 (a) is the processing block. This block describes the tracks of the received signals whether dependant on the signal were generated from affected OFDM symbols (i.e., the GI can be classified as a control sequence) or not. According to the control sequence, the received signals will be rearranged to reproduce the transmitted data correctly.

As was mentioned earlier, these signals will subsequently pass through a reverse process of what was described in Figure 5.1, and will then pass through the detecting block, as described in Figure 5.2 (c). The MIMO detecting stage is the first stage of the detecting block. The types of MIMO detectors, ZF and MMSE, are described earlier in Subsection 2.2.2.2.

## *5.3 The NTRPT-MIMO-OFDM Signal Model*

Having described the structure of the NTRPT-MIMO-OFDM system in the last section, this section will introduce the signal model for this system without coding techniques. The relation between the transmitted and received symbols will thus be captured in matrix form.

As explained in the previous section, this system has a number of transmitting antennas denoted by $K$ (where $K= NI$, $N$ is the conventional number of transmitting antennas and $I$ is the spreading rate) and $M$ receiving antennas. At each sampling interval $n$, there is a transmitted $K$-dimensional complex vector $\mathbf{s}(n)$ and a received $M$-dimensional complex vector $\mathbf{r}(n)$ through a frequency-selective Rayleigh fading environment.

The fading channel between the transmitter and the receiver can be represented by a ($L$-1)-th order finite impulse response (FIR) filter with filter taps $\mathbf{g}_{qp}(l)$, with $l$ = 0,…,$L$-1 (i.e., the channel impulse response can be achieved by $L$ samples). Suppose $\mathbf{g}_{qp}(l)$ represents the ($q$,$p$)-th element of the channel impulse response matrix, $\mathbf{G}(l)$, with $p$=1,..,$K$ and $q$=1,..,$M$. Figure 5.3 describes the transformation between $\mathbf{S}(n)$ and $\mathbf{r}(n)$ through a line tapped delay line.

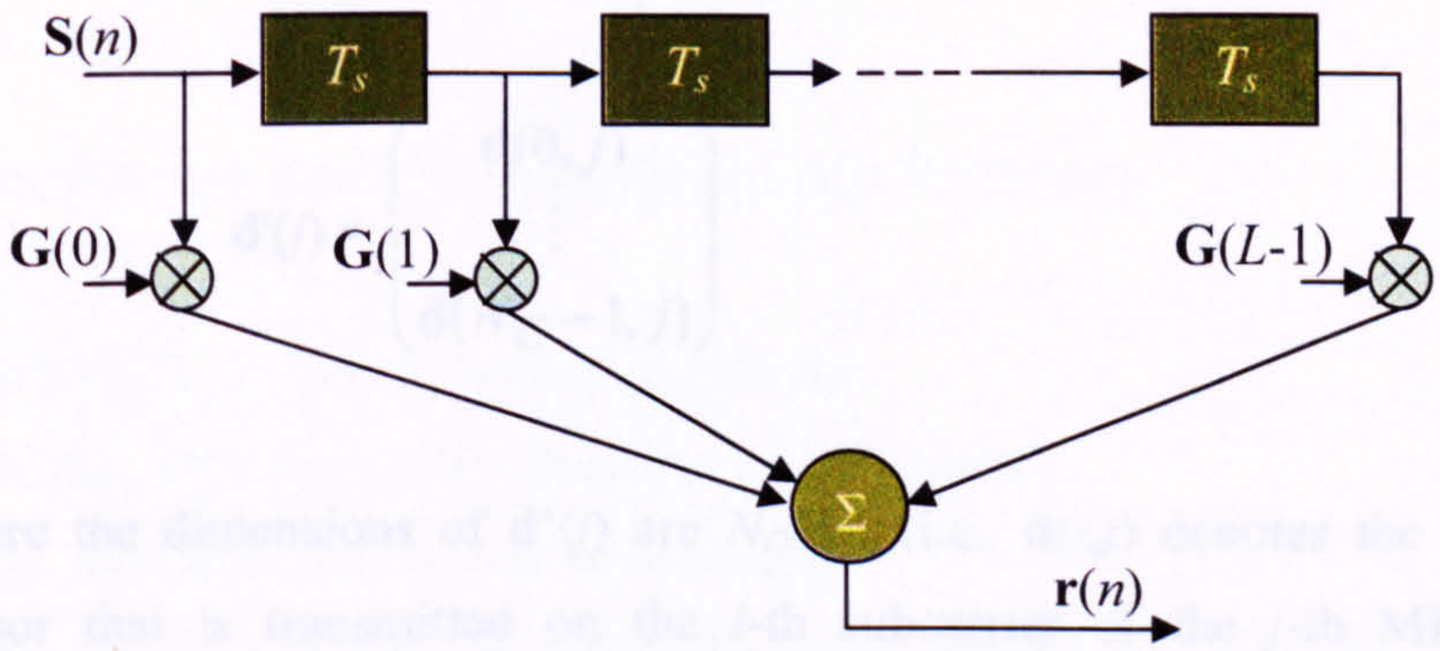


**Figure 5.3: MIMO signal representation by a tapped delay line**

From the assumption that movement of the user is negligible during transmission, the relationship between $\mathbf{S}(n)$ and $\mathbf{r}(n)$ can be defined by the quasi-static MIMO relationship. This relation can be described clearly from the figure shown above as

$$\mathbf{r}(n) = \sum_{l=0}^{L-1} \mathbf{G}(l)\, \mathbf{S}(n-l) \tag{5.1}$$

Furthermore, the thermal noise is usually added to the system as AWGN. Thus, (5.1) will be modified to accommodate the thermal noise as

$$\mathbf{r}(n) = \sum_{l=0}^{L-1} \mathbf{G}(l)\, \mathbf{S}(n-l)+\mathbf{n}(n) \tag{5.2}$$

where $\mathbf{n}(n)$ is the thermal noise added to the system at the $n$-th sample. The elements of $\mathbf{n}(n)$ and $\mathbf{S}(n)$, are assumed to be i.i.d zero mean complex elements with variance $\sigma_n^2$ and $\sigma_S^2$ respectively.

After modelling the MIMO by its signal representation, the frequency selectivity and ISI will be dealt with by applying OFDM, and by applying NTRPT to reduce PAPR.

A guard interval of $N_g$ samples must be added to an $N_C$ subcarriers-OFDM symbol in order to reduce the ISI effect. Thus, an OFDM symbol will consist of $N_{total} = N_C + N_g$ complex samples.

After defining the OFDM symbol structure, it will be introduced to (5.2) as follows:

1) The modulated symbols (as an example QAM symbols) to be sent on the $j$-th MIMO-OFDM symbol is defined by

$$\mathbf{d}'(j) = \begin{pmatrix} \mathbf{d}(0,j) \\ \vdots \\ \mathbf{d}(N_C - 1, j) \end{pmatrix} \tag{5.3}$$

where the dimensions of $\mathbf{d}'(j)$ are $N_C N x 1$ (i.e., $\mathbf{d}(i,j)$ denotes the $Nx1$ MIMO vector that is transmitted on the $i$-th subcarrier of the $j$-th MIMO-OFDM symbol).

2) The IFFT is applied at the transmitter to produce an OFDM symbol as shown in Figure 5.1(b). This process transforms the frequency domain into time the domain. Equation 2.20 will then represented as follows

$$\mathbf{S}(j) = \sqrt{N_c}\,(\mathbf{F}^{-1} \otimes \mathbf{I}_N)\,\mathbf{d}'(j) \tag{5.4}$$

where $\otimes$ represents the Kronecker product, $\mathbf{F}^{-1}$ equals the $N_C$ x$N_C$ IFFT matrix and $\mathbf{I}_N$ represents $NxN$ identity matrix.

$$\mathbf{F}^{-1} = \begin{pmatrix} 1 & 1 & 1 & \cdots & 1 \\ 1 & W^{-1} & W^{-2} & \cdots & W^{-(N_C-1)} \\ 1 & W^{-2} & W^{-4} & \cdots & W^{-2(N_C-1)} \\ \vdots & \vdots & \vdots & & \vdots \\ 1 & W^{-(N_C-1)} & W^{-2(N_C-1)} & \cdots & W^{-(N_C-1)^2} \end{pmatrix} \tag{5.5}$$

where $W = e^{(-j2\pi/Nc)}$.

3) The cyclic prefix can be stacked on top of the OFDM symbol in (5.4). This is done by taking the last $N_g N$ elements of $\mathbf{S}(j)$ and stacking them on its beginning to produce the vector $\mathbf{S}'(j)$. In matrix notation this can be written as

$$\mathbf{S'}(j) = \mathbf{A}_1\mathbf{S}(j) = \left(\begin{pmatrix} \mathbf{0} & \mathbf{I}_{N_g} \\ & \mathbf{I}_{N_C} \end{pmatrix} \otimes \mathbf{I}_N\right)\mathbf{S}(j) \tag{5.6}$$

where **0** is zero matrix with an $N_g$x ($N_C$-$N_g$) dimension.

4) The NTRPT process is defined as follows:

I) in case **S'**($j$) does suffer from the PAPR problem,

a) the cyclic prefix will be discarded.

b) **S**($j$) will go through a spreading technique to produce **Sc**($j$).

$$\mathbf{Sc}(j) = \begin{pmatrix} \mathbf{sc}(0, j) \\ \vdots \\ \mathbf{sc}(IN_C - 1, j) \end{pmatrix} \tag{5.7}$$

where **Sc**($j$) dimensions are $N_CK$x1 (i.e. **sc**($i$,$j$) denotes the $N$x1 MIMO vector that is transmitted on the $i$-th subcarrier of the $j$-th MIMO-OFDM symbol).

c) Equation (5.7) will be written to be $I$ blocks

$$\mathbf{Sc}(j) = \begin{pmatrix} \mathbf{sc_b}(0, j) \\ \vdots \\ \mathbf{sc_b}(I - 1, j) \end{pmatrix} \tag{5.8}$$

where $\mathbf{sc_b}(a,j)$ dimensions are $NN_C$x1 and $a$ denotes the block that is transmitted for the $j$-th MIMO-OFDM symbol

d) the control sequence data will be attached to (5.8) to complete the format of the MIMO-OFDM symbol

$$\mathbf{S'}\_new\,(j) = \begin{pmatrix} \mathbf{sc_b}'(0, j) \\ \vdots \\ \mathbf{sc_b}'(I - 1, j) \end{pmatrix} \tag{5.9}$$

where **scb'**($a$,$j$) dimensions are ($N_C$+$N_g$)$N$x1, and can be defined as

$$\mathbf{sc_b}'(a,j) = \begin{pmatrix} \mathbf{csd}(0) \\ \mathbf{sc_{b1}}(0,j) \\ \vdots \\ \mathbf{csd}(N-1) \\ \mathbf{sc_{b1}}(N-1,j) \end{pmatrix} \tag{5.10}$$

where **csd**($a$) is the control sequence data matrix with an $N_g$x1 dimension and and $\mathbf{sc_{b1}}$ is the OFDM symbol to be transmitted through the $a$-th antenna with $N_C$x1 dimension.

II) In case where **S'**($j$) does not suffer from the PAPR problem, (5.6) will be modified to

$$\mathbf{S'}\_new(j) = \begin{pmatrix} \mathbf{S'}(a) \\ \vdots \\ \mathbf{S'}(I-1) \end{pmatrix} \tag{5.11}$$

5) Finally, the signal is transmitted over the frequency-selective channel as in (5.2). In case ISI occurs, its assumed that the only significant interference comes from the preceding MIMO-OFDM symbol **S'**_*new*($j$-1). Under this assumption, the convolution in (5.2) can be represented as

$$\mathbf{r'}(j) = \mathbf{G'S'}\_new(j) + \mathbf{G_{ISI}S'}\_new(j-1) + \mathbf{n'}(j) \tag{5.12}$$

where the size of **G'** and $\mathbf{G_{ISI}}$ equals $M(N_c+N_g)$x$K(N_c+N_g)$, and **G'** is defined by

$$\mathbf{G'} = \begin{pmatrix} \mathbf{G}_0 & & & & \\ \vdots & \ddots & & & 0 \\ \mathbf{G}_{L-1} & \cdots & \mathbf{G}_0 & & \\ & \ddots & & \ddots & \\ 0 & \ddots & & & \ddots \\ & & \mathbf{G}_{L-1} & \cdots & \mathbf{G}_0 \end{pmatrix} \tag{5.13}$$

where **G'** represents $\mathbf{G}_l = \mathbf{G}(l)$. $\mathbf{G_{ISI}}$ is a matrix with all elements equal to zero, except for the $M(L-1)$x$K(L-1)$ elements of the upper-right corner, these are defined by the upper-triangular block matrix

$$\begin{pmatrix} \mathbf{G}(L-1) & \cdots & \mathbf{G}(L) \\ & \ddots & \vdots \\ 0 & & \mathbf{G}(L-1) \end{pmatrix} \tag{5.14}$$

Furthermore, $\mathbf{S'}\_new(j)$ and $\mathbf{n'}(j)$ are, respectively, defined by

$$\mathbf{S'}\_new(j) = \begin{pmatrix} \mathbf{S'}\_new(jT_{total}+0) \\ \vdots \\ \mathbf{S'}\_new(jT_{total}+T_{total}-1) \end{pmatrix}$$

and

$$\mathbf{n'}(k) = \begin{pmatrix} \mathbf{n}(jT_{total}+0) \\ \vdots \\ \mathbf{n}(jT_{total}+T_{total}-1) \end{pmatrix} \tag{5.15}$$

Note that when ISI from more than one MIMO-OFDM symbol has to be taken into account, matrix notation becomes impractical and one should use (5.2).

At the receiver, the received data can be transformed to a matrix representation as follows:

1) First the guard interval is checked.
   a) If it is a cyclic prefix, it will be discarded. This is done by discarding the first $N_gM$ samples of $\mathbf{r'}(j)$ as follows

$$\mathbf{r'}\_new(j) = \mathbf{A}_2\mathbf{r'}(j) \tag{5.16}$$

   where $\mathbf{A}_2$ can be defined as $((\mathbf{0}_{NcXNg} \quad \mathbf{I}_{Nc}) \otimes \mathbf{I}_M)$.

   b) If it is a control sequence data, then the received data will be rearranged to be in the correct sequence.

2) The FFT is then performed:

$$\mathbf{x'}(j) = \frac{1}{\sqrt{N_c}}(\mathbf{F} \otimes \mathbf{I}_M)\mathbf{r'}\_new(j) \tag{5.17}$$

where $\mathbf{F}$ denotes the $NcxNc$ Fourier matrix, and $\mathbf{x'}(j)$ is defined as

$$\mathbf{x}'(j) = \begin{pmatrix} \mathbf{x}(0, j) \\ \vdots \\ \mathbf{x}(Nc-1, j) \end{pmatrix} \tag{5.18}$$

where $\mathbf{x}(i,k)$ denotes the $Mx1$ received MIMO vector on the $i$-th subcarrier of the $j$-th MIMO-OFDM symbol.

## *5.4Simulation Results*

The NTRPT technique proposed in this chapter for a MIMO-OFDM system has been simulated in MATLAB in order to evaluate its performance. The main parameters that are used for the simulation are shown in Table 5.1.

**Table 5.1: The main paarmeters that are used in the simulation**

| | |
|---|---|
| Modulation techniques | BPSK, QPSK, 16-QAM and 64-QAM |
| Coding technique | Turbo encoder, Convolutional encoder |
| Coding rate | 1/2 and 1/3 |
| Number of subcarriers | 256 |
| MIMO encoders | V-BLAST and STBC |
| Spreading rate | 2 and 3 |
| Guard Interval | 0.25 |

In this simulation, a larger number of subcarriers were used, than WLAN IEEE 802.11, which uses 256 subcarriers. This is because of the aim, which is supporting the high quality multimedia applications by increasing the overall system data rate. Increasing the number of data subcarriers will increase the data accommodated in the OFDM symbols, but will also increase the PAPR as will. Moreover, this section a comparison will be draw between the results of the NTRPT in combating the PAPR with those of some conventional techniques, clipping and Partial Transmit Sequence

(PTS) techniques, and will compare the performance of NTRPT with different linear encoding techniques. The main parameters that are used for this simulation are shown in the following table.

## 5.4.1 NTRPT based on Turbo encoder Compared to the Conventional Techniques

Subsection 5.4.1.1 will concentrate on the results achieved from applying the NTRPT-based turbo coding to MIMO-OFDM systems. These results will be compared to those of the conventional clipping and PTS techniques as shown in Subsection 5.4.1.2 and Subsection 5.4.1.3 respectively.

### *5.4.1.1 NTRPT to reduce the PAPR problem*

The following tables and figures will give a sample from the achieved results to give a brief idea about the effectiveness of achieved improvement in reducing the PAPR. Table 5.2 shows the results achieved by using NTRPT-MIMO-OFDM based on a BPSK, QPSK, 16QAM and 64QAM modulation techniques.

From this table, the success of the proposed technique in combating PAPR is clearly noticeable, since a significant PAPR reduction ratio was achieved for different MIMO-OFDM configurations (i.e., different combinations of modulation techniques, MIMO encoders, coding rates and spreading rates). In case of using a BPSK modulation technique, PAPR reduction ratio reaches 88.4% and 86.7% when using a spreading rate of 3 and 2 respectively. These ratios remain approximately the same when the modulation technique is changed to 64QAM, which they reach the 89% for spreading rate equals 3 and 86.4% when the used spreading rate was 2.

Moreover, increasing the spreading rate will increase the achieved PAPR reduction for both situations; BPSK and 64QAM. The improvement in the reduction ratio when the spreading rate is changed from 2 to 3 equals 8.7% and 6.2% when using BPSK and 64QAM modulation techniques respectively.

**Table 5.2: Applying the NTRPT to a MIMO-OFDM system based on turbo encoder**

| Modulation tech. | Coding rate | MIMO encoding | PAPR before applying NTRPT (dB) | PAPR after applying NTRPT(dB) | | Reduction ratio (%) | | Improvement in reduction ratios according the spreading rates (%) |
|---|---|---|---|---|---|---|---|---|
| | | | | Spreading rate | | Spreading rate | | |
| | | | | 2 | 3 | 2 | 3 | |
| BPSK | 1/2 | STBC | 12.264 | 2.989 | 1.916 | 75.6 | 84.3 | 8.7 |
| | | V-BLAST | 12.851 | 2.77 | 1.832 | 78.5 | 85.7 | 7.2 |
| | 1/3 | STBC | 10.366 | 2.575 | 2.012 | 73.4 | 80.6 | 7.2 |
| | | V-BLAST | 13.994 | 1.855 | 1.625 | 86.7 | 88.4 | 1.7 |
| QPSK | 1/2 | STBC | 10.394 | 2.386 | 2.354 | 77.0 | 77.4 | 0.4 |
| | | V-BLAST | 14.397 | 2.977 | 2.706 | 79.3 | 81.2 | 1.9 |
| | 1/3 | STBC | 11.252 | 4.022 | 3.879 | 64.3 | 65.6 | 1.3 |
| | | V-BLAST | 12.824 | 1.956 | 1.329 | 84.7 | 89.6 | 4.9 |
| 16QAM | 1/2 | STBC | 8.307 | 1.187 | 1.058 | 85.7 | 87.3 | 1.6 |
| | | V-BLAST | 10.601 | 1.956 | 1.430 | 81.5 | 86.5 | 5 |
| | 1/3 | STBC | 11.610 | 1.851 | 1.576 | 84.0 | 86.4 | 2.4 |
| | | V-BLAST | 11.980 | 1.750 | 1.709 | 85.4 | 85.7 | 0.3 |
| 64QAM | 1/2 | STBC | 9.517 | 1.401 | 1.314 | 85.2 | 86.2 | 1 |
| | | V-BLAST | 11.728 | 1.590 | 1.517 | 86.4 | 87.1 | 0.7 |
| | 1/3 | STBC | 13.180 | 2.261 | 1.444 | 82.8 | 89.0 | 6.2 |
| | | V-BLAST | 13.013 | 2.133 | 2.011 | 83.6 | 85.0 | 1.4 |

For clarity, the CCDF plots for the achieved results in the previous tables are displayed. The CCDF is calculated to show the probability of the PAPR that will exceed some threshold. Figures 5.4-5.11 show the calculated CCDF for the achieved results of using NTRPT-MIMO-OFDM based on different modulation techniques, BPSK, QPSK, 16QAM and 64QAM.

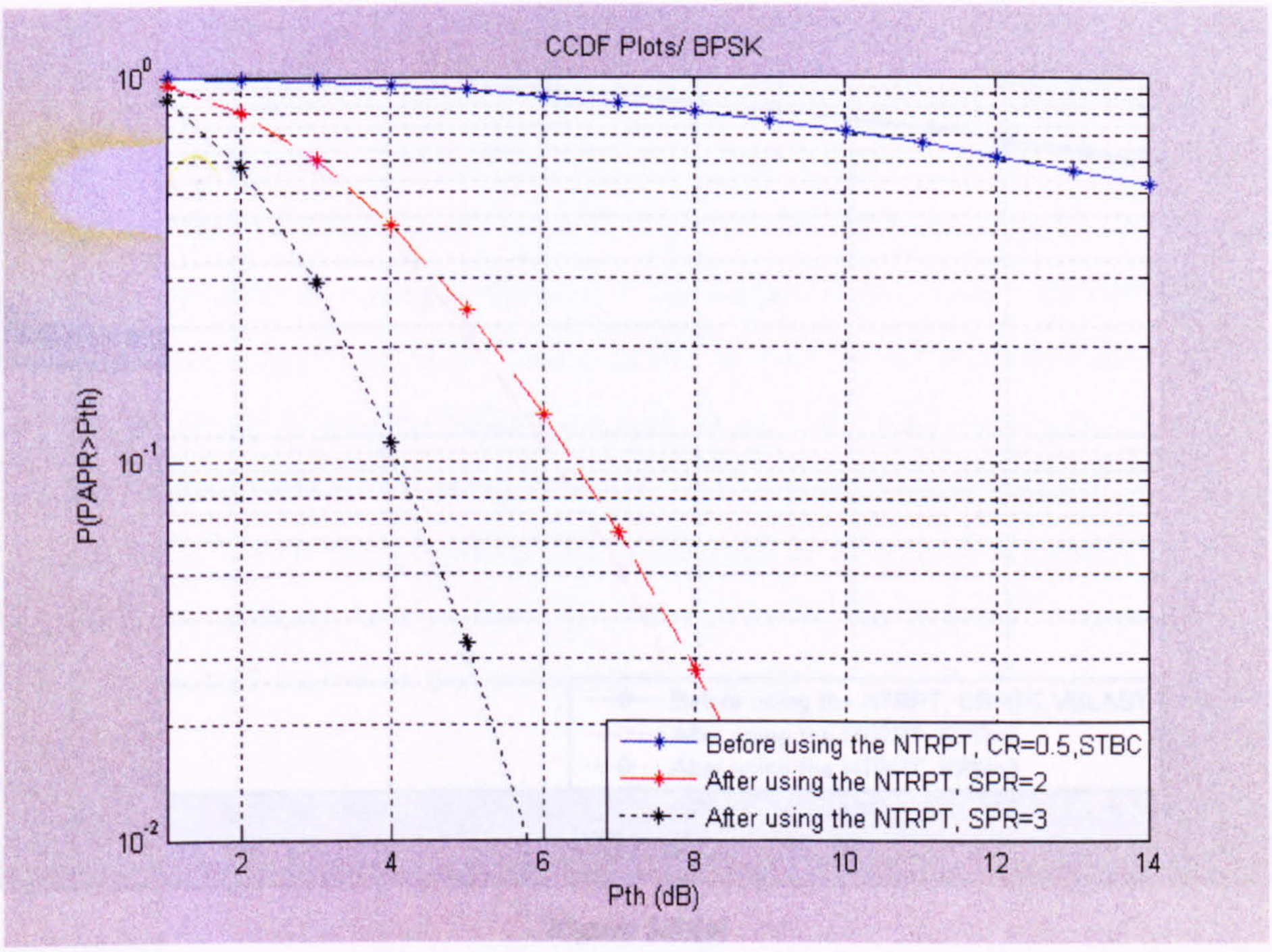


**Figure 5.4 (a)**

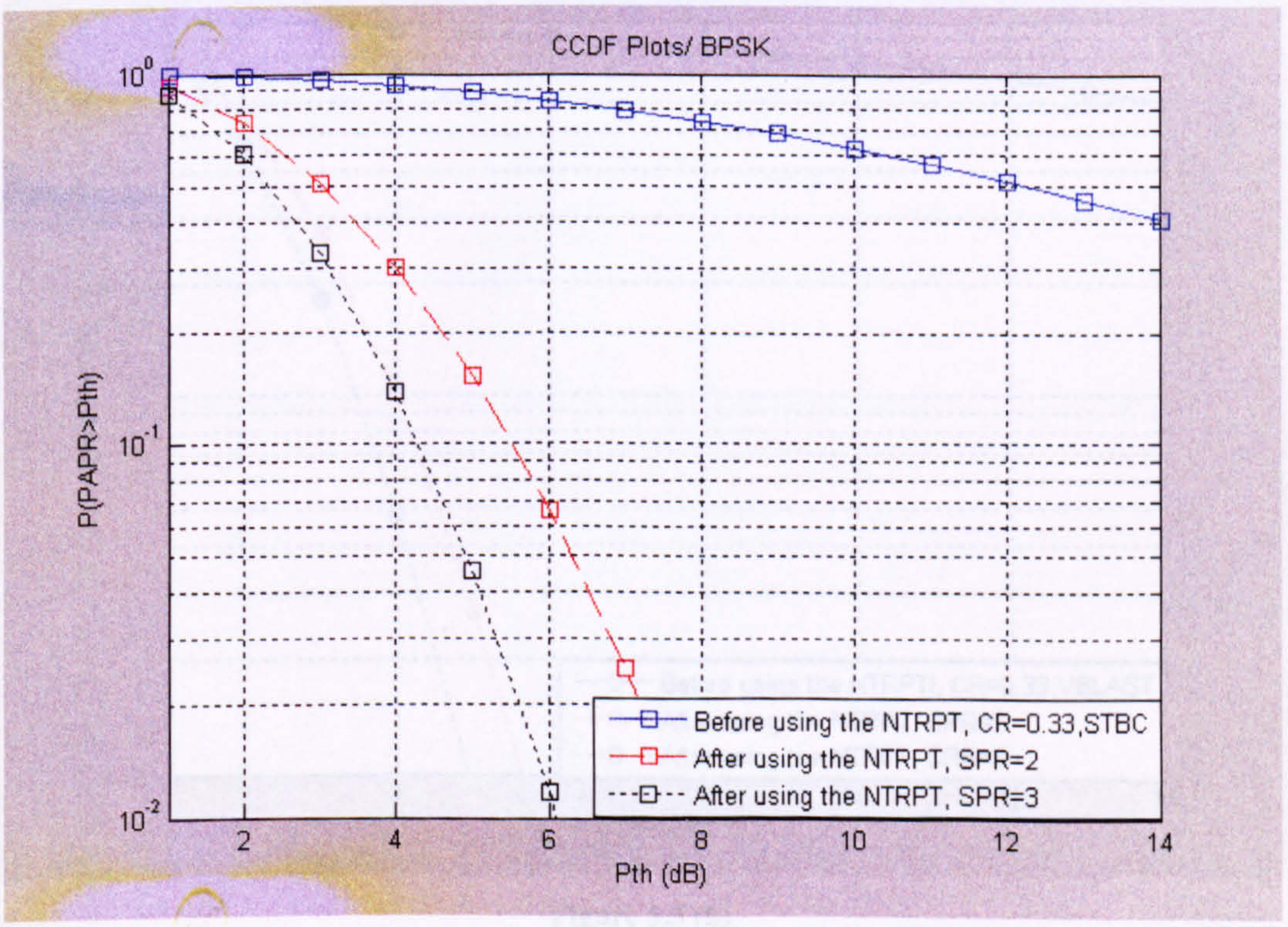


**Figure 5.4 (b)**

**Figure 5.4: The CCDF for the NTRPT-MIMO-OFDM system based on a BPSK modulation tehcnique. (a) STBC with coding rate 1/2, (b) STBC with coding rate 1/3.**

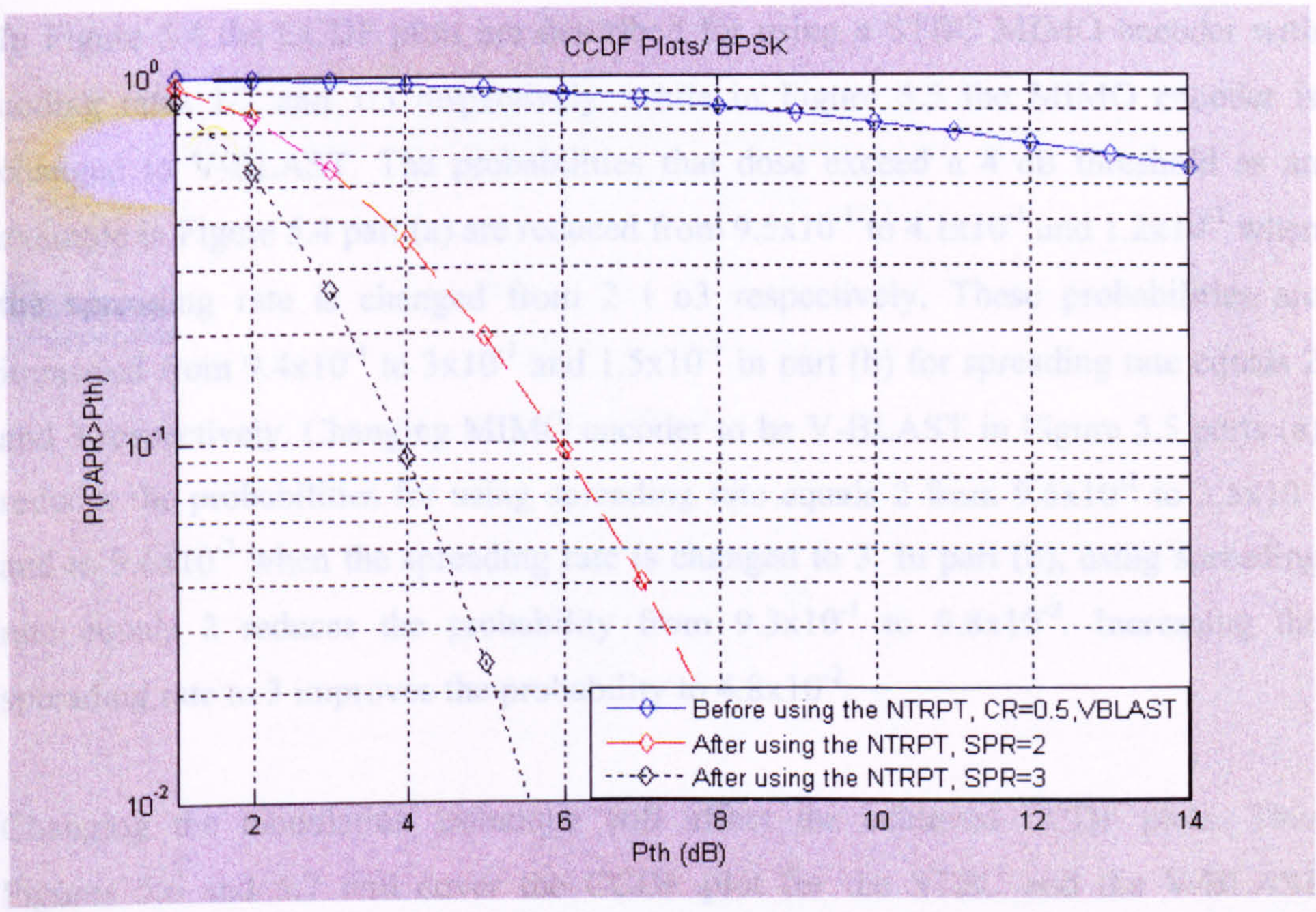


**Figure 5.5 (a)**

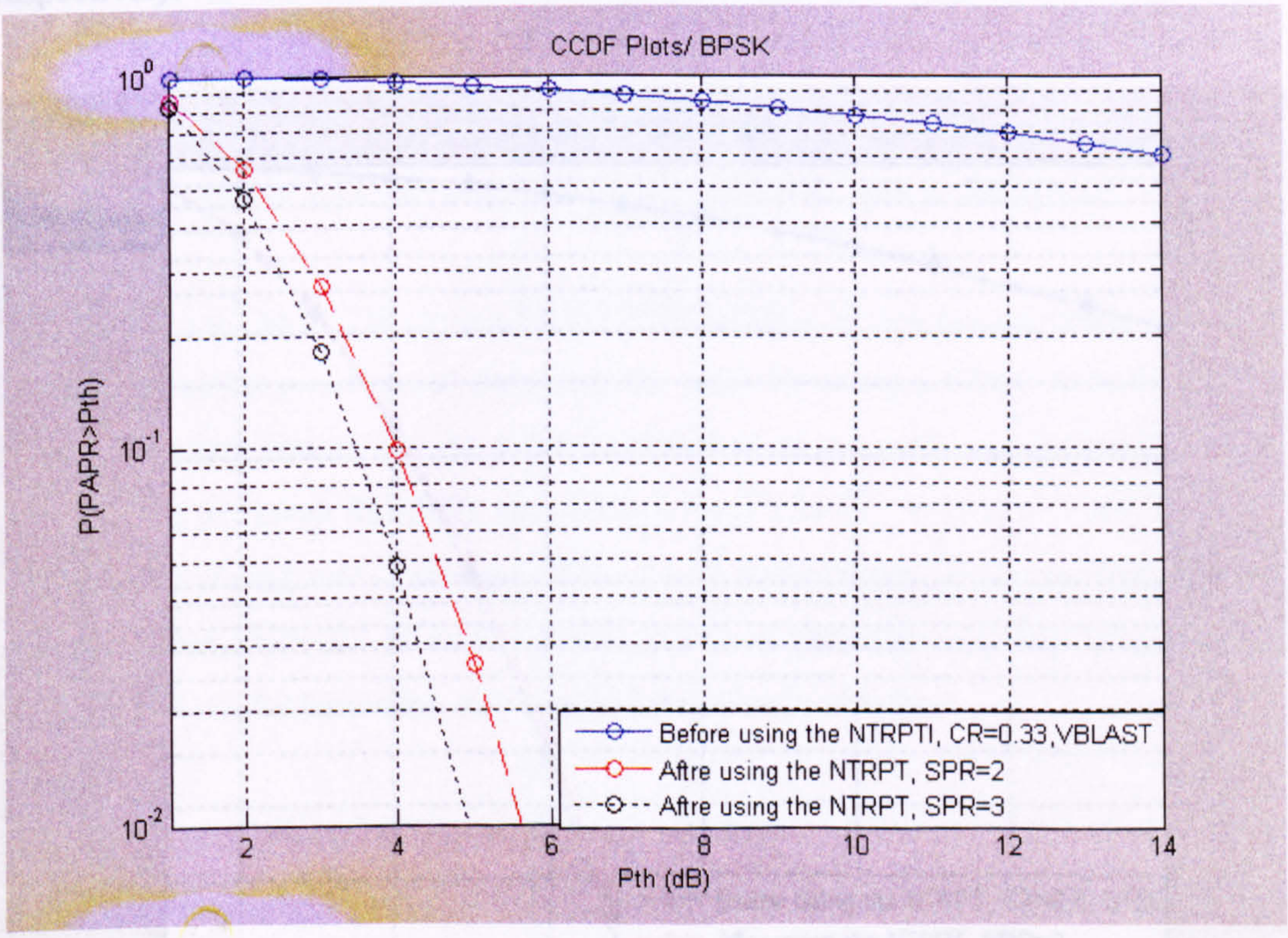


**Figure 5.5 (b)**

**Figure 5.5: The CCDF for the NTRPT-MIMO-OFDM system based on a BPSK modulation tehcnique. (a) V-BLAST with coding rate 1/2 ,and (b) V-BLAST with coding rate 1/3**

In Figure 5.4 the CCDF plots are described for using a STBC MIMO encoder with coding rates 1/2 and 1/3 respectively, while in Figure 5.5 the MIMO encoder is changed to V-BLAST. The probabilities that dose exceed a 4 dB threshold as an example in Figure 5.4 part (a) are reduced from $9.5x10^{-1}$ to $4.1x10^{-1}$ and $1.2x10^{-1}$ when the spreading rate is changed from 2 t o3 respectively. These probabilities are improved from $9.4x10^{-1}$ to $3x10^{-1}$ and $1.5x10^{-1}$ in part (b) for spreading rate equals 2 and 3 respectively. Changing MIMO encoder to be V-BLAST in Figure 5.5 parts (a) reduces the probabilities for using spreading rate equals 2 from $9.6x10^{-1}$ to $3.5x10^{-1}$ and to $9.6x10^{-2}$ when the spreading rate is changed to 3. In part (b), using spreading rate equals 2 reduces the probability from $9.3x10^{-1}$ to $9.8x10^{-2}$. Increasing the spreading rate to 3 improves the probability to $4.8x10^{-2}$.

Changing the modulation technique will affect the achieved CCDF plots. Thus Figures 5.6 and 5.7 will cover the CCDF plot for the STBC and the V-BLAST respectively.

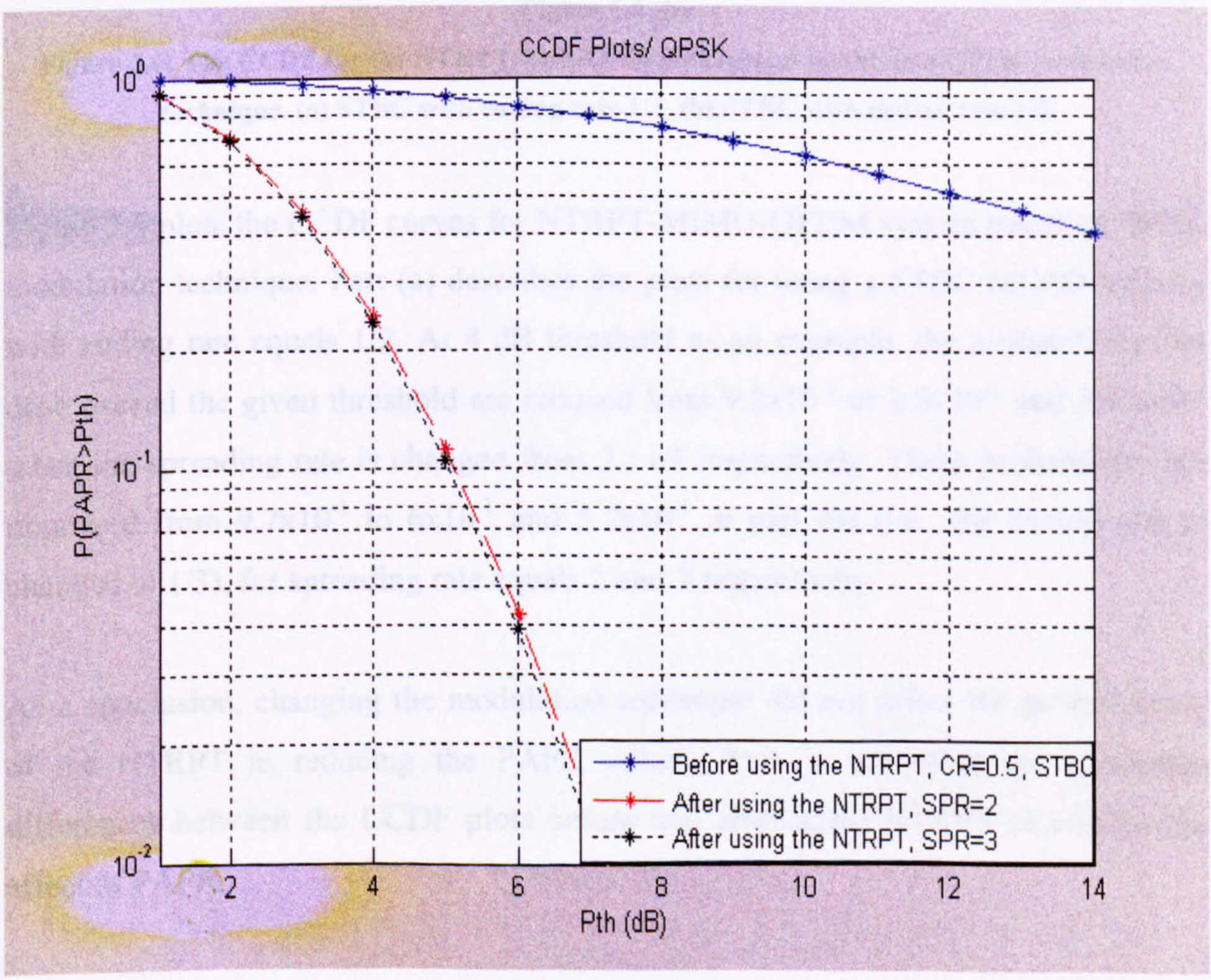


**Figure 5.6 (a)**

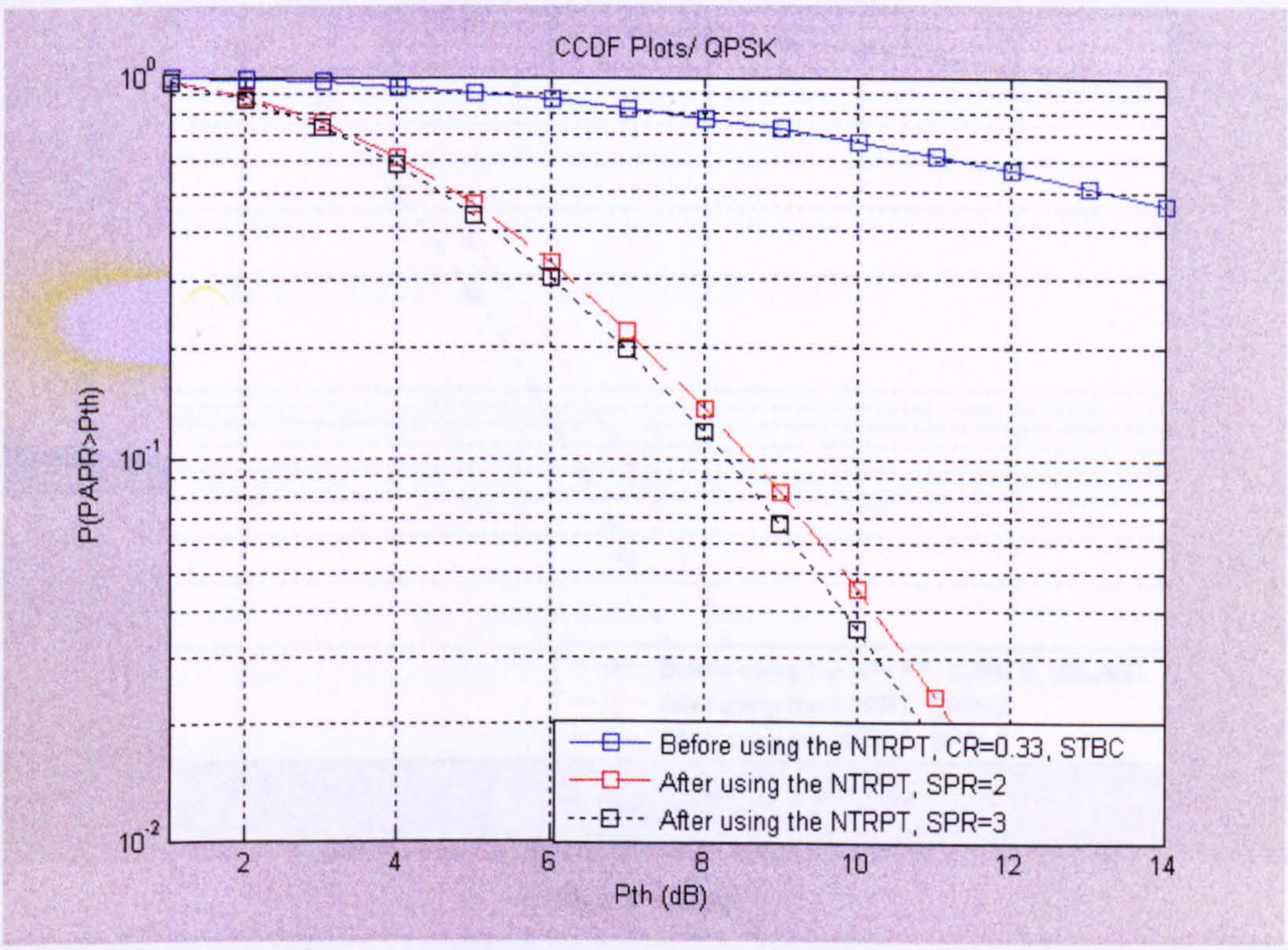


**Figure 5.6 (b)**

**Figure 5.6: The CCDF for the NTRPT-MIMO-OFDM system based on a QPSK modulation technique. (a) STBC with coding rate 1/2, (b) STBC with coding rate 1/3**

Figure 5.6 plots the CCDF curves for NTRPT-MIMO-OFDM system based on QPSK modulation technique. Part (a) describes the plots for using a STBC MIMO encoder with coding rate equals 1/2. At 4 dB threshold as an example, the probabilities that dose exceed the given threshold are reduced from $9.2x10^{-1}$ to $2.5x10^{-1}$ and $2.42x10^{-1}$ when the spreading rate is changed from 2 t o3 respectively. These probabilities are improved from $9.7x10^{-1}$ to $6x10^{-1}$ and $5.7x10^{-1}$ in part (b) (i.e., the coding rate is changed to 1/3), for spreading rate equals 2 and 3 respectively.

As a conclusion, changing the modulation technique did not affect the powerfulness of the NTRPT in reducing the PAPR values. This is according the noticeable differences between the CCDF plots before and after using NTRPT to combat the effect of PAPR.

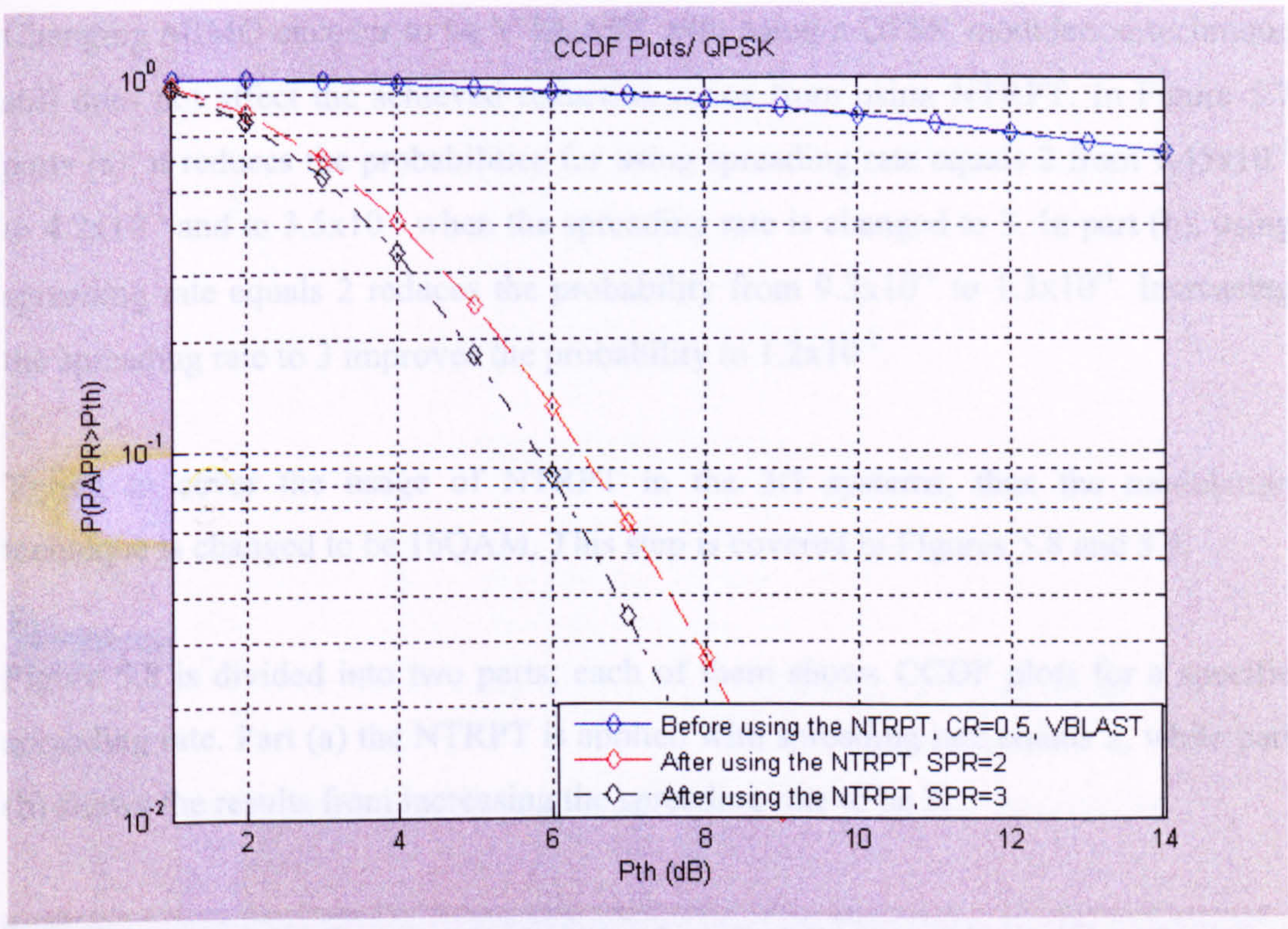


**Figure 5.7 (a)**

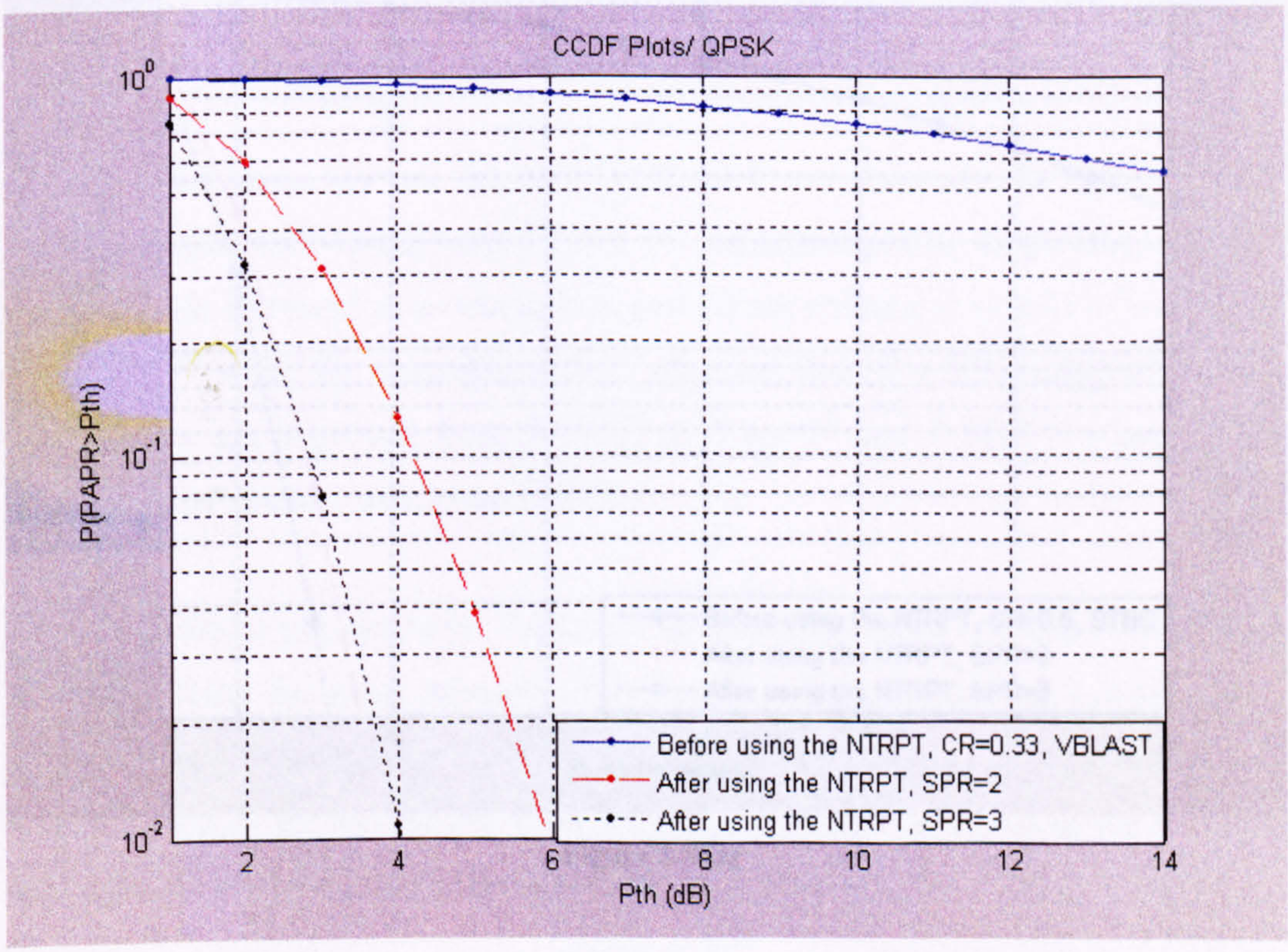


**Figure 5.7 (b)**

**Figure 5.7: The CCDF for the NTRPT-MIMO-OFDM system based on a QPSK modulation technique. (a) V-BLAST with coding rate 1/2 ,and (b) V-BLAST with coding rate 1/3**

Changing MIMO encoder to be V-BLAST with using a QPSK modulation technique still does not affect the achieved reduction ratios from using NTRPT. In Figure 5.7 parts (a), it reduces the probabilities for using spreading rate equals 2 from $9.45x10^{-1}$ to $4.2x10^{-1}$ and to $3.5x10^{-1}$ when the spreading rate is changed to 3. In part (b), using spreading rate equals 2 reduces the probability from $9.3x10^{-1}$ to $1.3x10^{-1}$. Increasing the spreading rate to 3 improves the probability to $1.2x10^{-2}$.

Trying to cover the usage of NTRPT in the 3G systems, thus the modulation technique is changed to be 16QAM. This step is covered in Figures 5.8 and 5.9.

Figure 5.8 is divided into two parts; each of them shows CCDF plots for a specific spreading rate. Part (a) the NTRPT is applied with spreading rate equals 2, while part (b) shows the results from increasing the spreading rate to be 3.

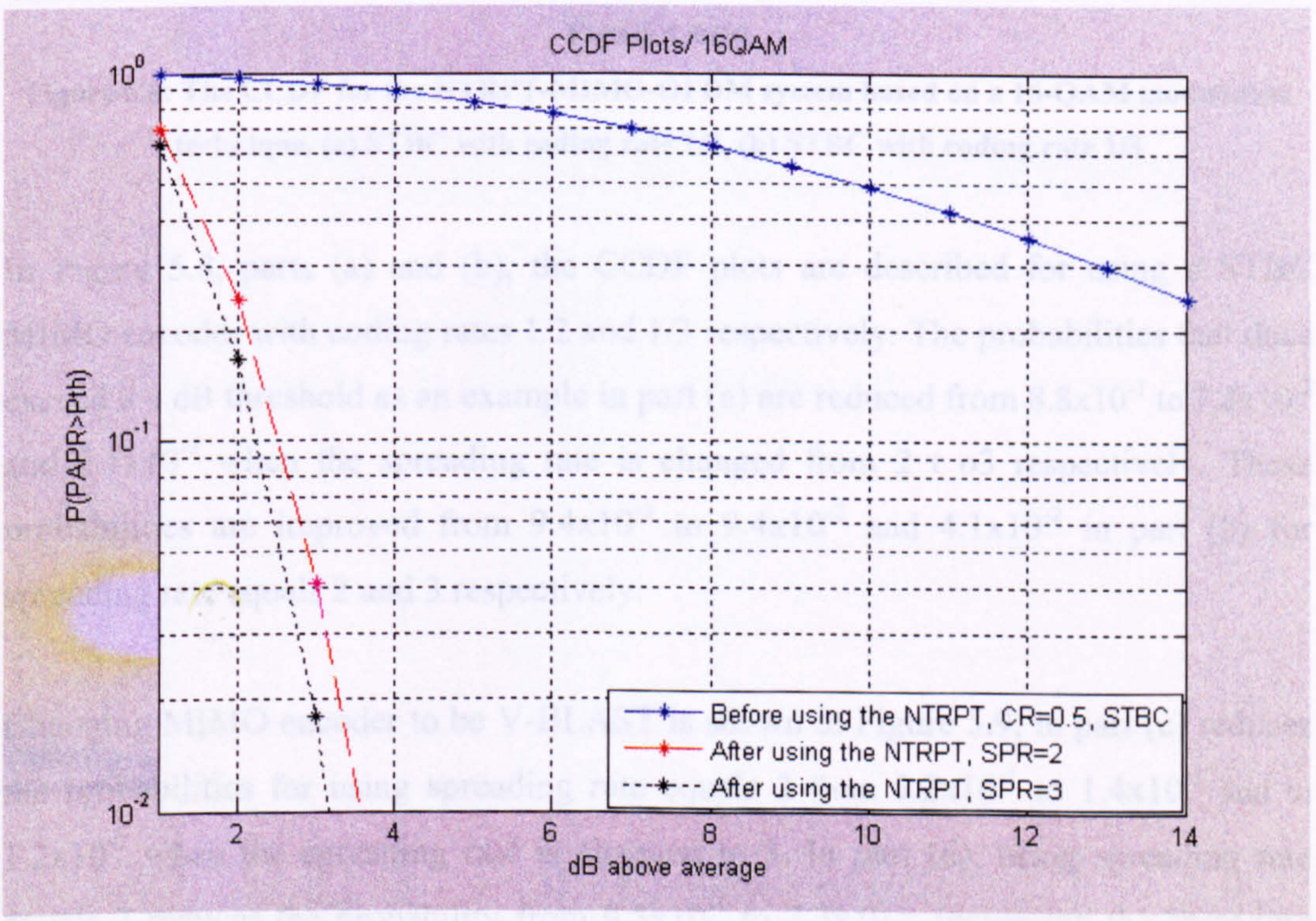


**Figure 5.8 (a)**

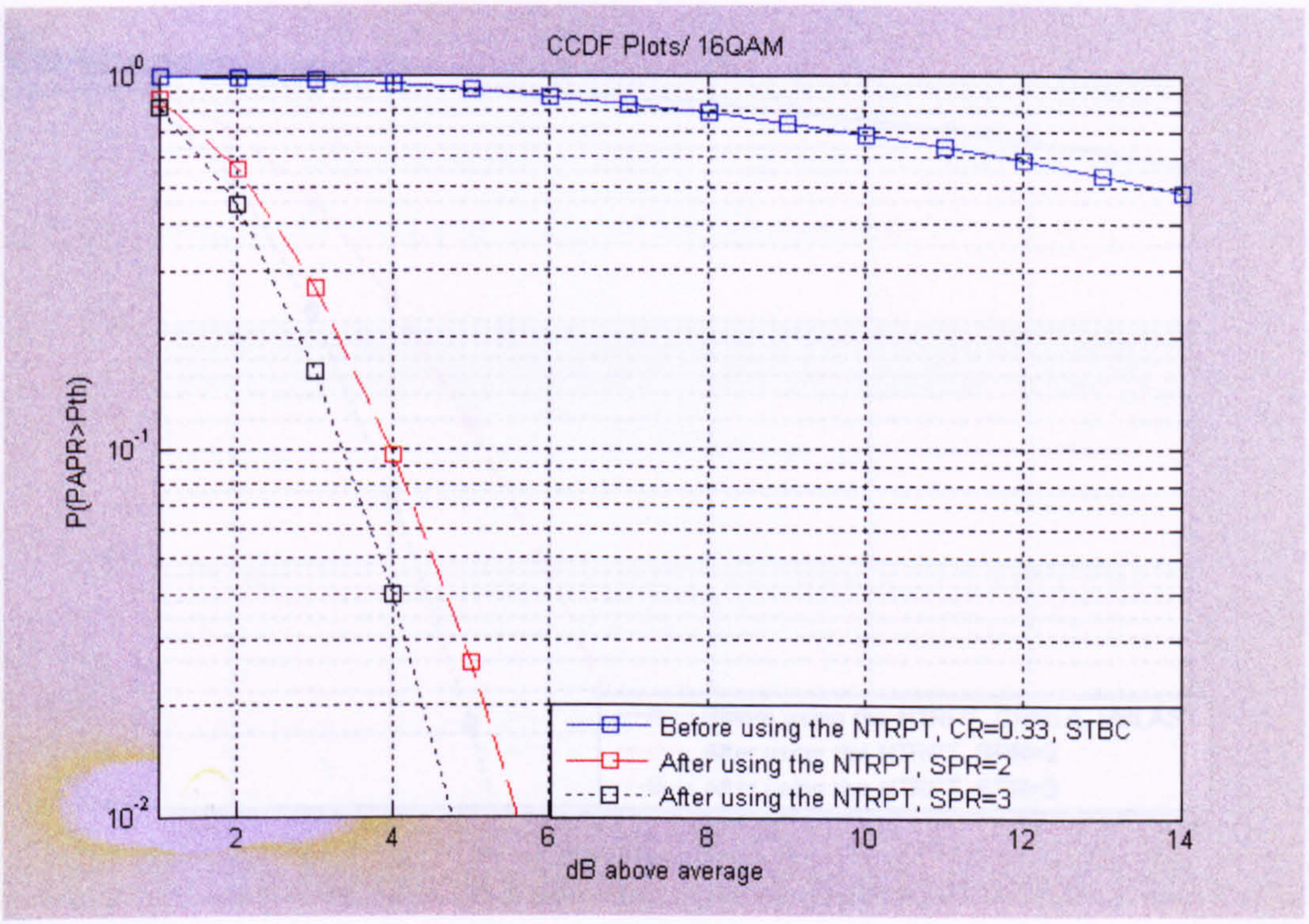


**Figure 5.8 (b)**

**Figure 5.8: The CCDF for the NTRPT-MIMO-OFDM system based on a 16-QAM modulation technique. (a) STBC with coding rate 1/2, (b) STBC with coding rate 1/3**

In Figure 5.8, parts (a) and (b), the CCDF plots are described for using a STBC MIMO encoder with coding rates 1/2 and 1/3 respectively. The probabilities that dose exceed a 4 dB threshold as an example in part (a) are reduced from $8.8x10^{-1}$ to $7.2x10^{-2}$ and $2.1x10^{-2}$ when the spreading rate is changed from 2 t o3 respectively. These probabilities are improved from $9.4x10^{-1}$ to $9.4x10^{-2}$ and $4.1x10^{-2}$ in part (b) for spreading rate equals 2 and 3 respectively.

Changing MIMO encoder to be V-BLAST is shown in Figure 5.9; in part (c) reduces the probabilities for using spreading rate equals 2 from $9.2x10^{-1}$ to $1.4x10^{-1}$ and to $1.2x10^{-2}$ when the spreading rate is changed to 3. In part (d), using spreading rate equals 2 reduces the probability from $9.5x10^{-1}$ to $7.3x10^{-2}$. Increasing the spreading rate to 3 improves the probability to $6.6x10^{-2}$.

Also from Figure 5.8 and 5.9, the reduction ratios are still high even the modulation technique is changed to 16QAM.

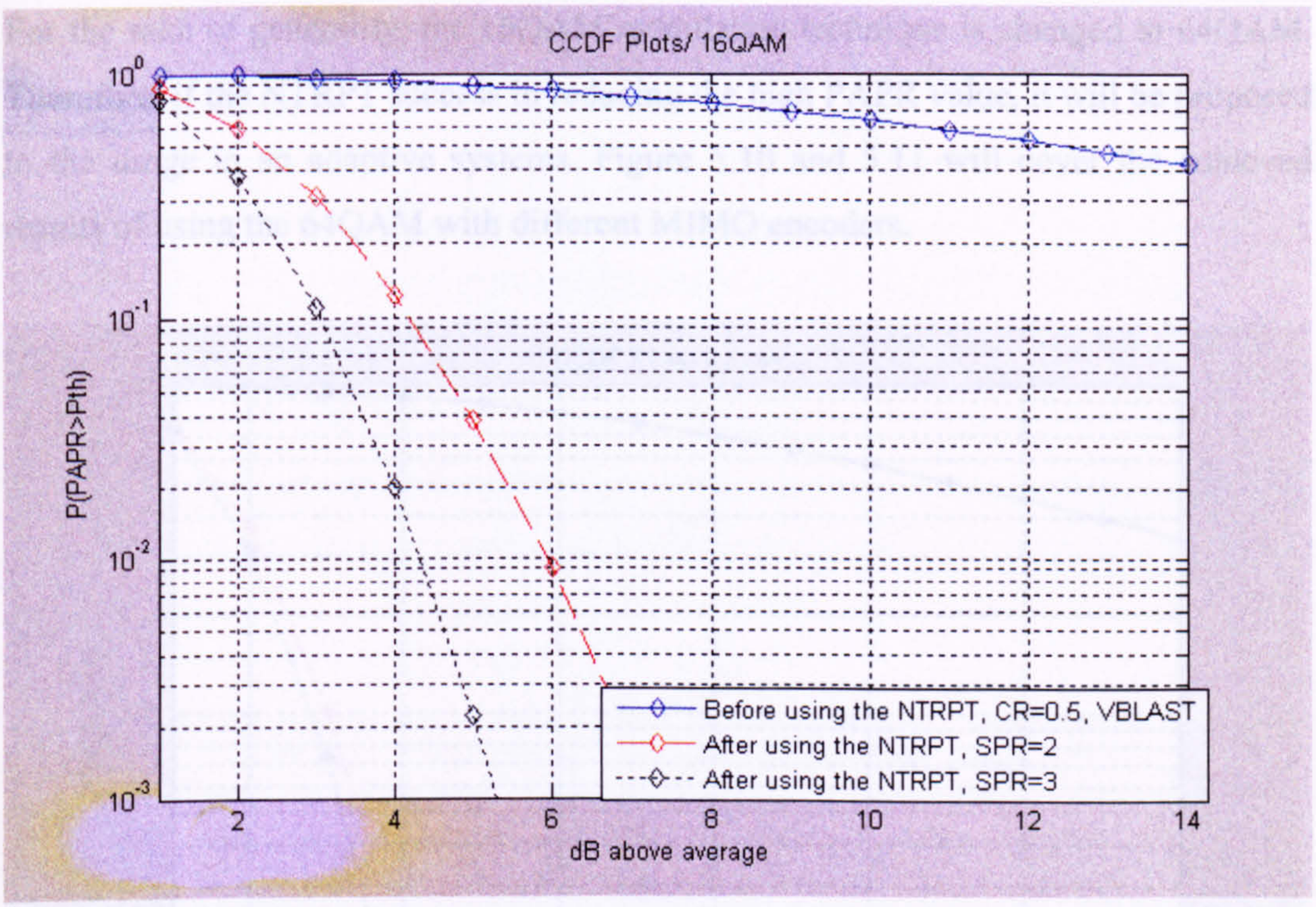


**Figure 5.9 (a)**

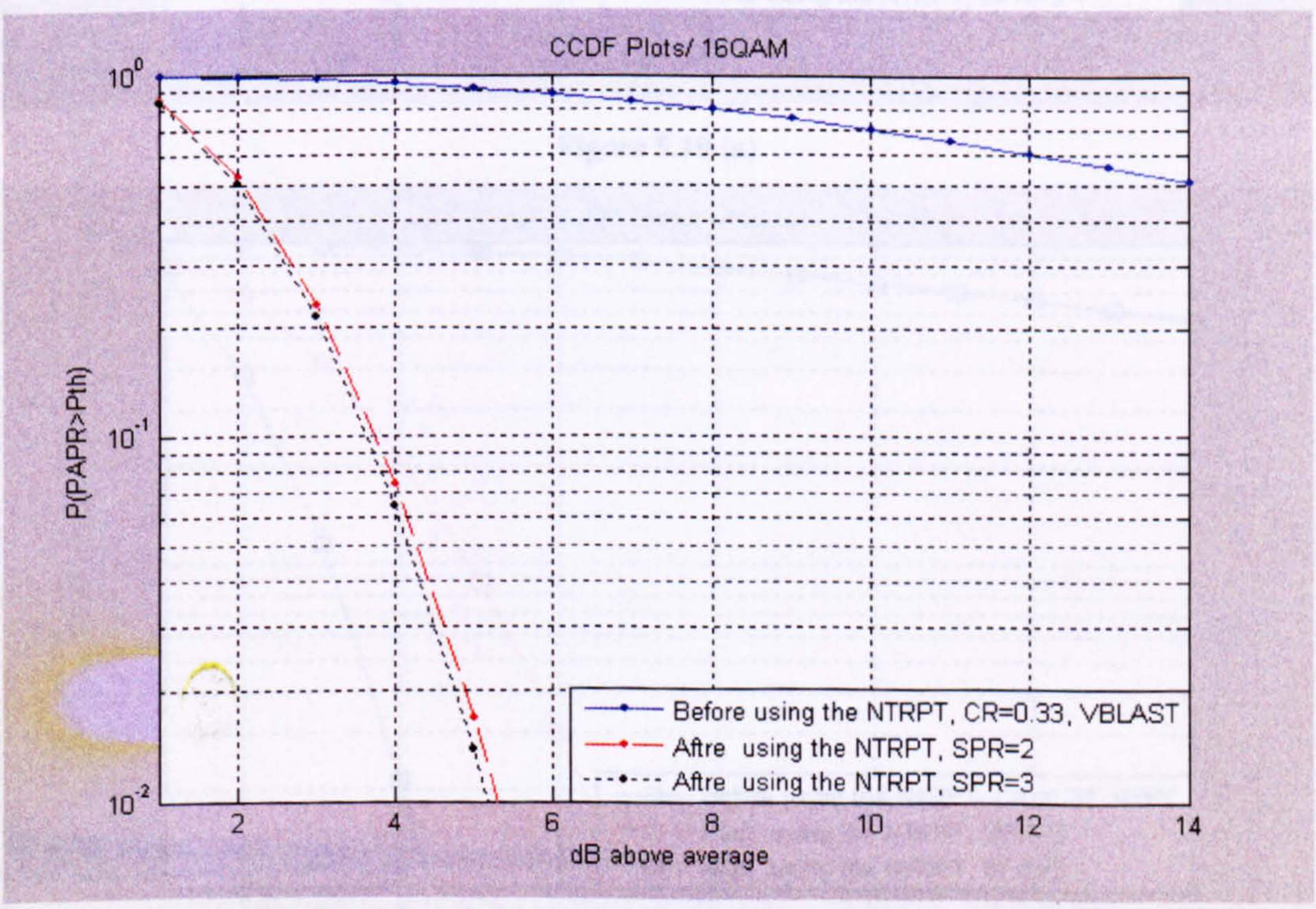


**Figure 5.9 (b)**

**Figure 5.9: The CCDF for the NTRPT-MIMO-OFDM system based on a 16-QAM modulation technique. (a) V-BLAST with coding rate 1/2 and (b) V-BLAST with coding rate 1/3**

For the sake of generality, the 16QAM modulation technique is changed to 64QAM. Therefore, if the NTRPT success in reducing the high PAPR value, it will be proposed to the usage in an adaptive systems. Figure 5.10 and 5.11 will cover the achieved results of using the 64QAM with different MIMO encoders.

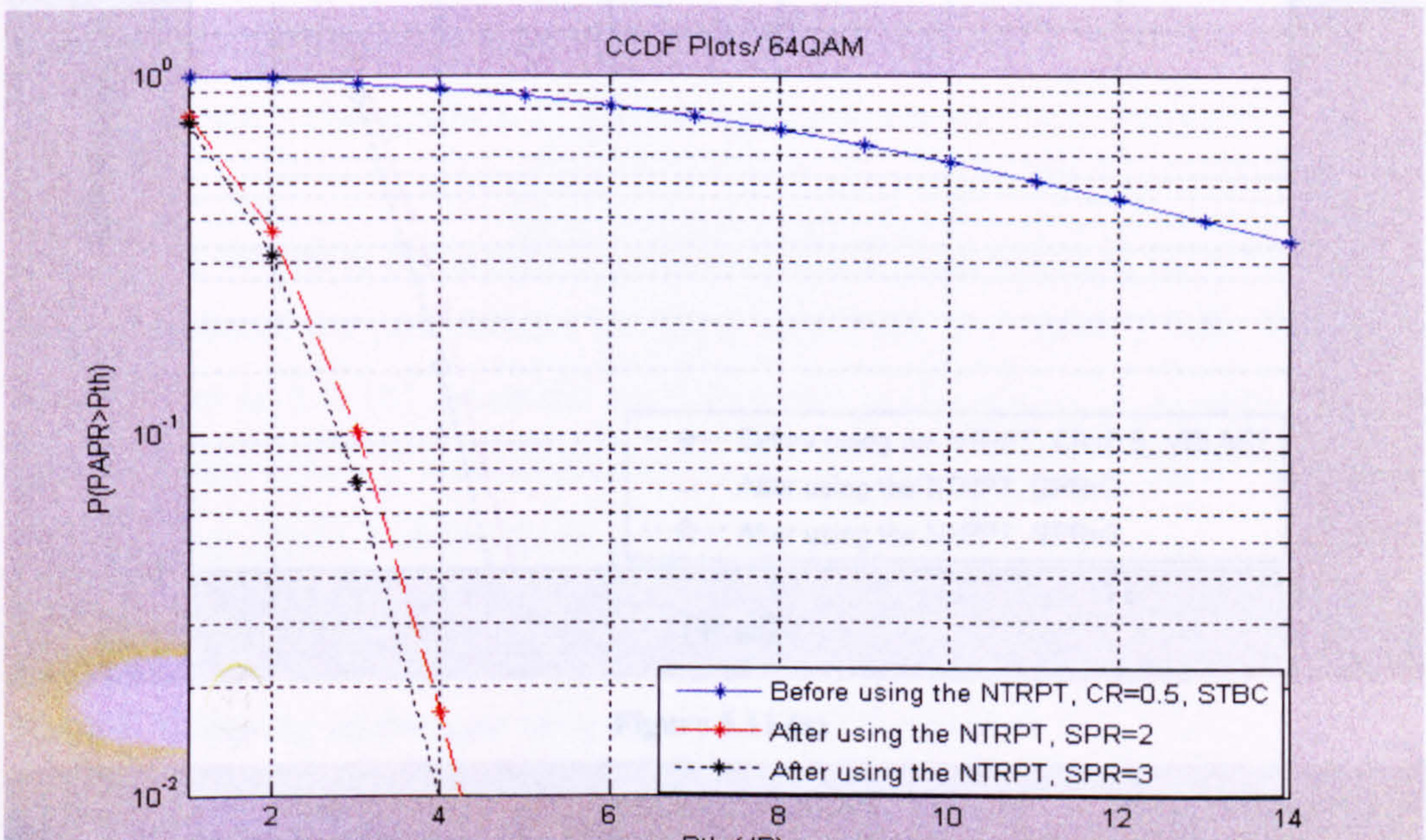


**Figure 5.10 (a)**

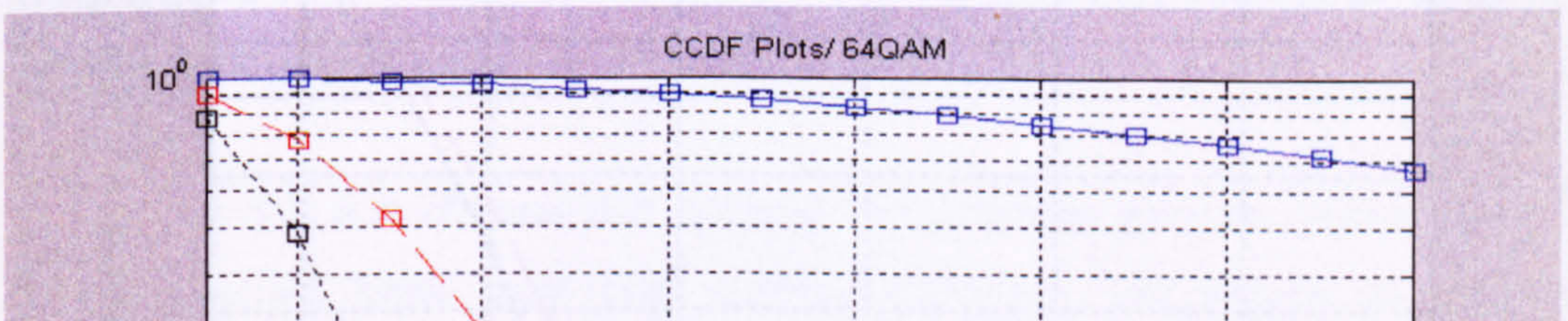


**Figure 5.10 (b)**

**Figure 5.10: The CCDF for the NTRPT-MIMO-OFDM system based on a 64-QAM modulation technique. (a) STBC with coding rate 1/2, (b) STBC with coding rate 1/3**

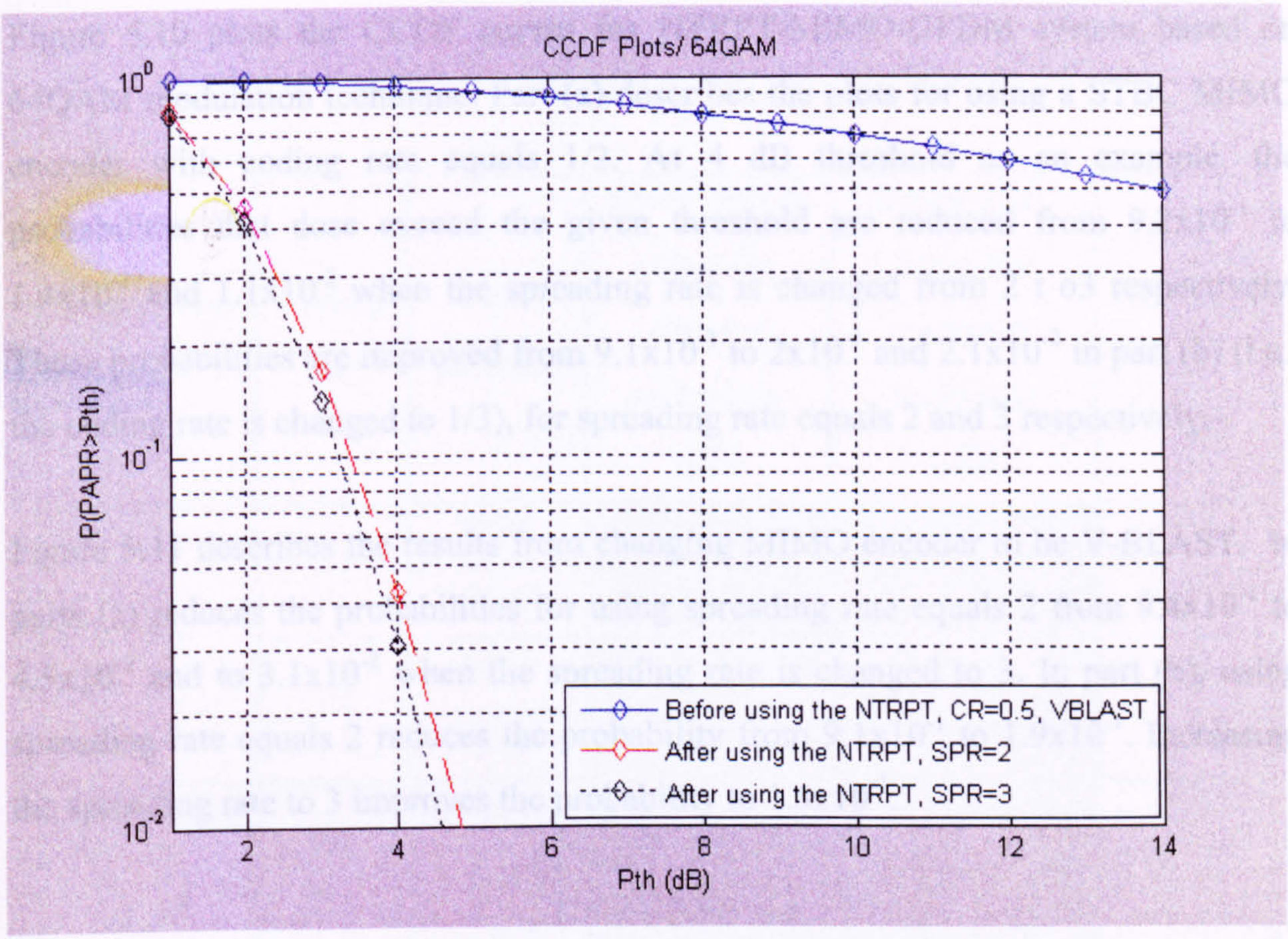


**Figure 5.11 (a)**

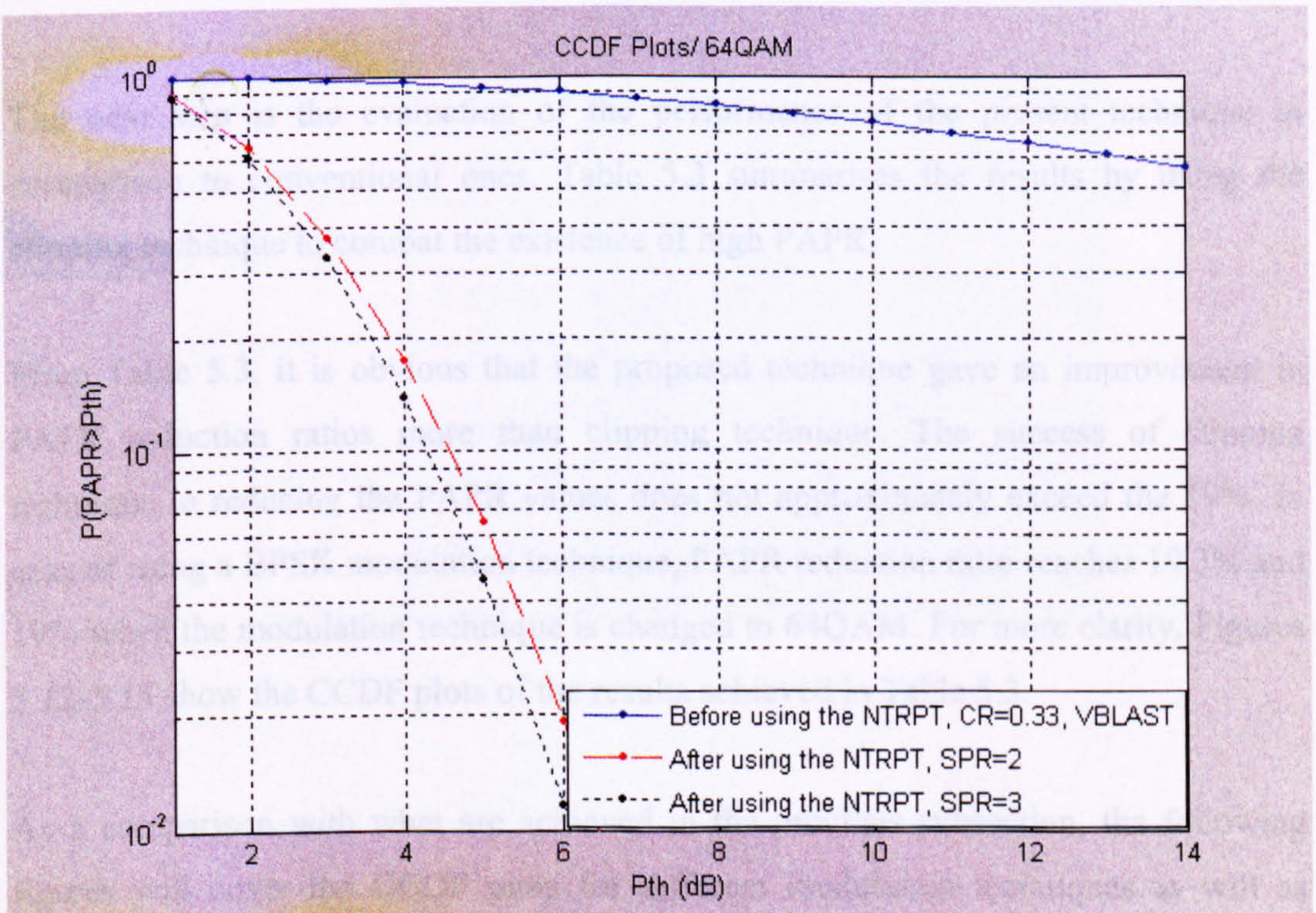


**Figure 5.11 (b)**

**Figure 5.11: The CCDF for the NTRPT-MIMO-OFDM system based on a 64-QAM modulation technique. (a) V-BLAST with coding rate ½ and (b) V-BLAST with coding rate 1/3**

Figure 5.10 plots the CCDF curves for NTRPT-MIMO-OFDM system based on 64QAM modulation technique. Part (a) describes the plots for using a STBC MIMO encoder with coding rate equals 1/2. At 4 dB threshold as an example, the probabilities that dose exceed the given threshold are reduced from $9.2x10^{-1}$ to $1.4x10^{-2}$ and $1.1x10^{-2}$ when the spreading rate is changed from 2 t o3 respectively. These probabilities are improved from $9.1x10^{-1}$ to $2x10^{-1}$ and $2.1x10^{-2}$ in part (b) (i.e., the coding rate is changed to 1/3), for spreading rate equals 2 and 3 respectively.

Figure 5.11 describes the results from changing MIMO encoder to be V-BLAST. In parts (a) reduces the probabilities for using spreading rate equals 2 from $9.4x10^{-1}$ to $4.5x10^{-2}$ and to $3.1x10^{-2}$ when the spreading rate is changed to 3. In part (b), using spreading rate equals 2 reduces the probability from $9.1x10^{-1}$ to $1.9x10^{-1}$. Increasing the spreading rate to 3 improves the probability to $1.5x10^{-1}$.

### *5.4.1.2 Clipping technique to reduce the PAPR problem*

The next step is the evaluation of the performance of the present technique in comparison to conventional ones. Table 5.3 summarises the results by using the clipping technique to combat the existence of high PAPR.

From Table 5.3, it is obvious that the proposed technique gave an improvement in PAPR reduction ratios more than clipping technique. The success of clipping technique in reducing the PAPR values does not approximately exceed the 19%. In case of using a BPSK modulation technique, PAPR reduction ratio reaches 19.3% and 19% when the modulation technique is changed to 64QAM. For more clarity, Figures 5.12-5.15 show the CCDF plots of the results achieved in Table 5.3.

As a comparison with what are achieved in the previous subsection, the following figures will cover the CCDF plots for different modulation techniques as will as different MIMO encoders.

**Table 5.3: Applying the clipping technique to a MIMO-OFDM system**

| Modulation tech. | Coding rate | MIMO encoding | PAPR before using the clipping technique (dB) | PAPR after using the clipping technique (dB) | The reduction ratio (%) |
|---|---|---|---|---|---|
| BPSK | 1/2 | STBC | 21.896 | 17.676 | 19.3 |
| | | V-BLAST | 21.250 | 19.363 | 8.8 |
| | 1/3 | STBC | 21.938 | 18.689 | 14.8 |
| | | V-BLAST | 23.938 | 22.163 | 7.4 |
| QPSK | 1/2 | STBC | 22.163 | 17.011 | 23.2 |
| | | V-BLAST | 22.126 | 20.2526 | 8.5 |
| | 1/3 | STBC | 22.995 | 17.848 | 22.4 |
| | | V-BLAST | 21.662 | 17.790 | 17.9 |
| 16QAM | 1/2 | STBC | 22.444 | 17.952 | 20.0 |
| | | V-BLAST | 23.810 | 19.163 | 19.5 |
| | 1/3 | STBC | 22.595 | 17.437 | 22.8 |
| | | V-BLAST | 20.498 | 17.214 | 16.0 |
| 64QAM | 1/2 | STBC | 19.901 | 16.928 | 14.9 |
| | | V-BLAST | 20.282 | 17.927 | 11.6 |
| | 1/3 | STBC | 23.876 | 18.780 | 21.3 |
| | | V-BLAST | 19.886 | 16.110 | 19.0 |

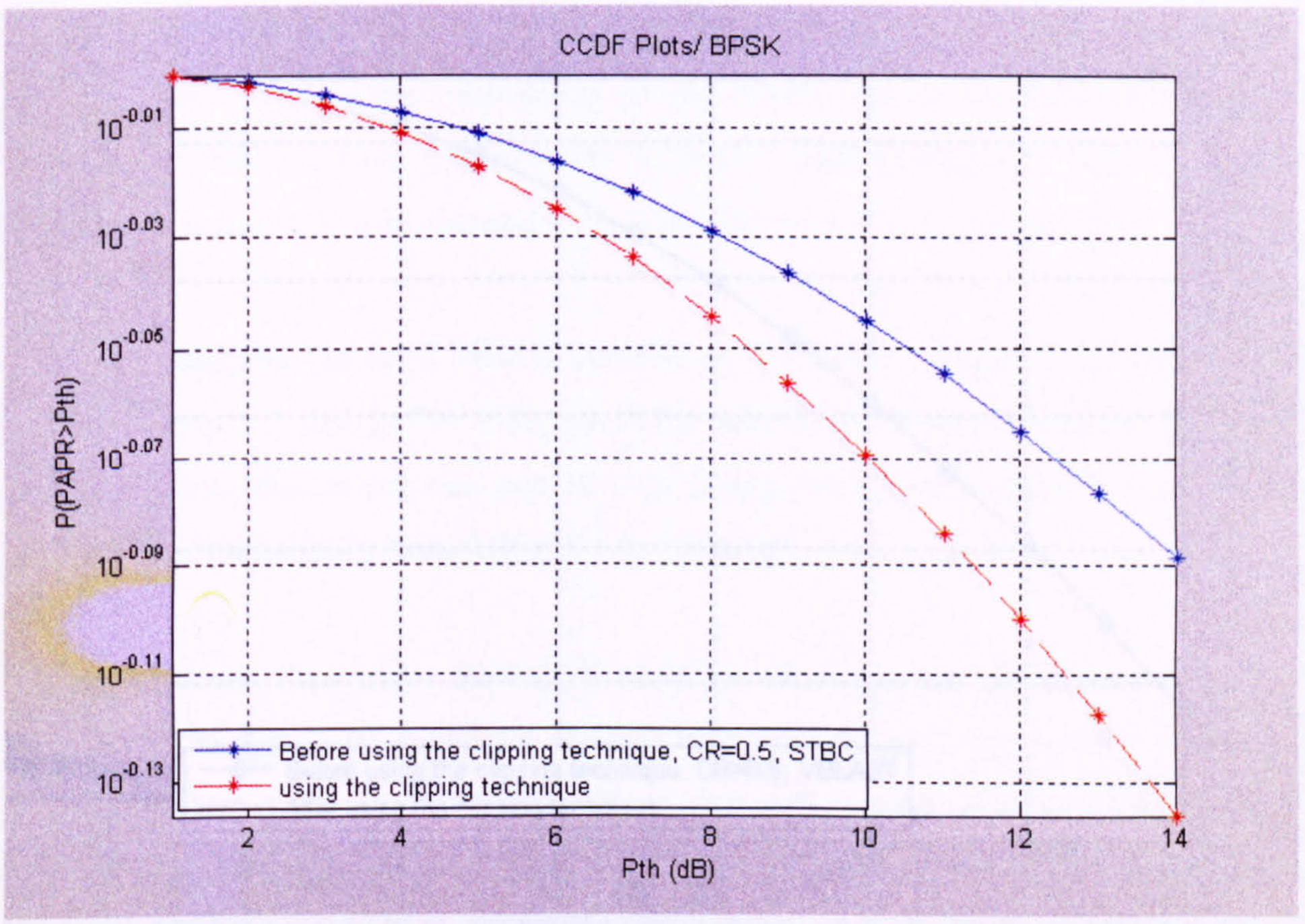


**Figure 5.12 (a)**

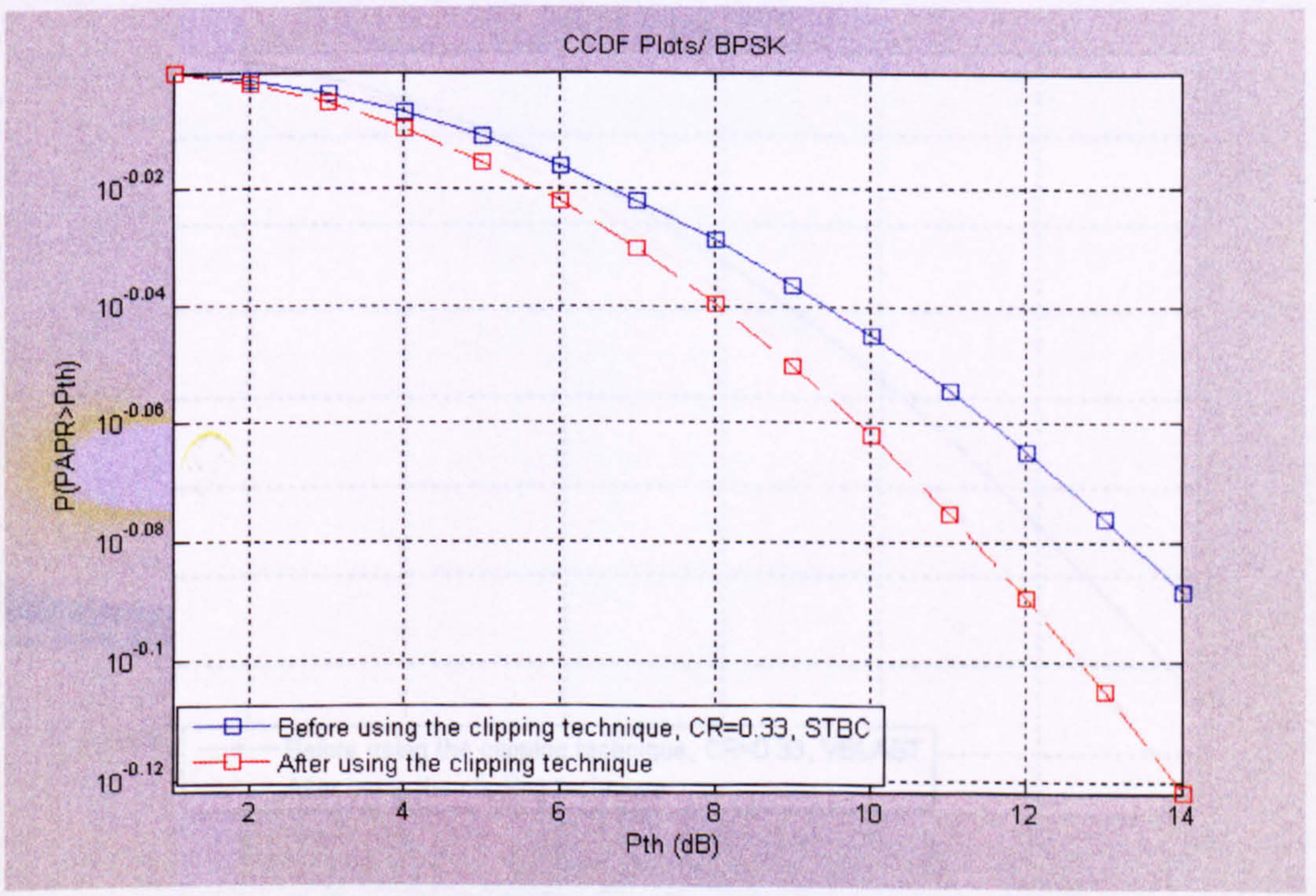


**Figure 5.12 (b)**

**Figure 5.12: The CCDF for using the clipping technique in a MIMO-OFDM system based on a BPSK modulation technique. (a) STBC with coding rate 1/2, (b) STBC with coding rate 1/3**

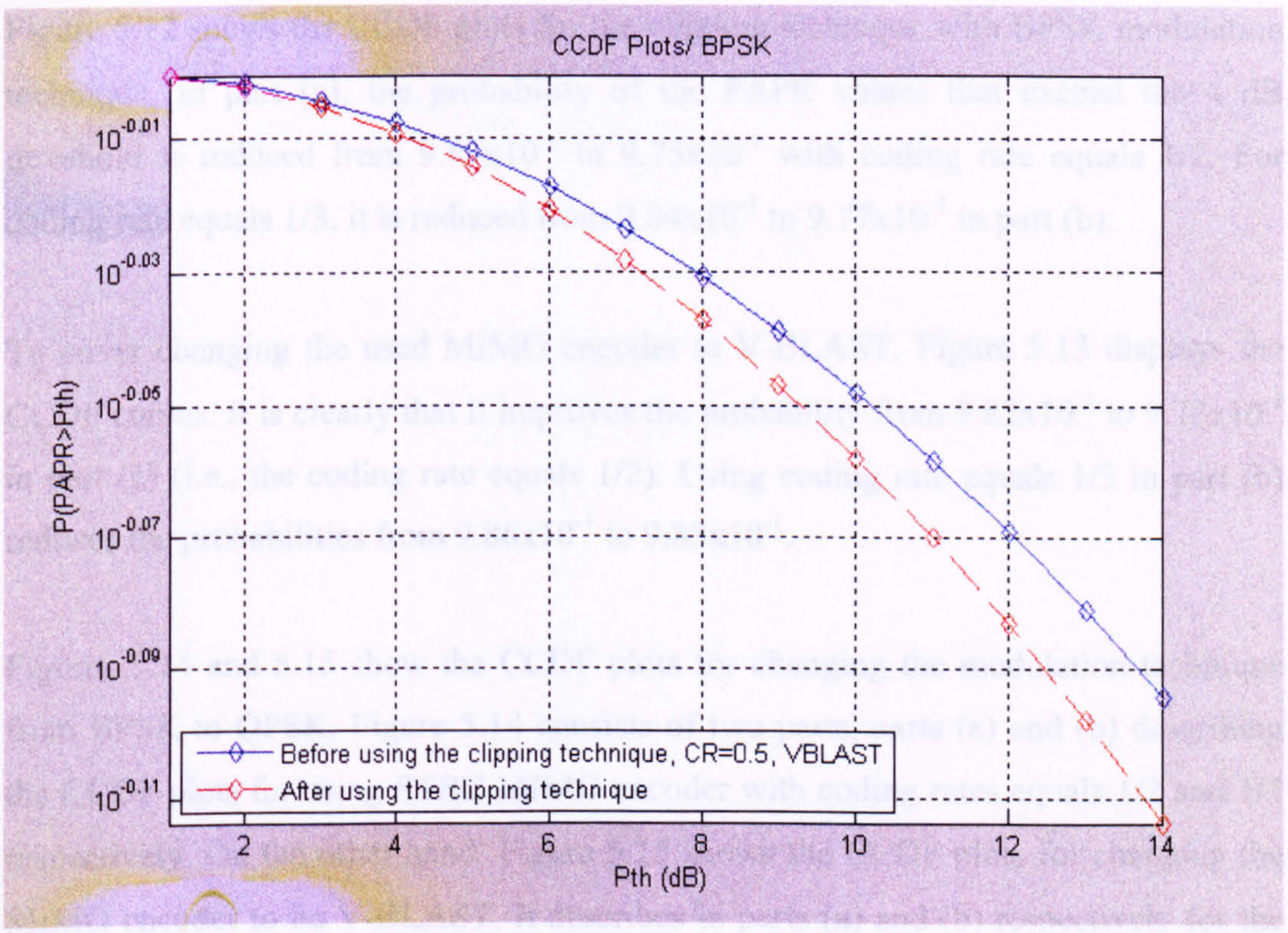


**Figure 5.13 (a)**

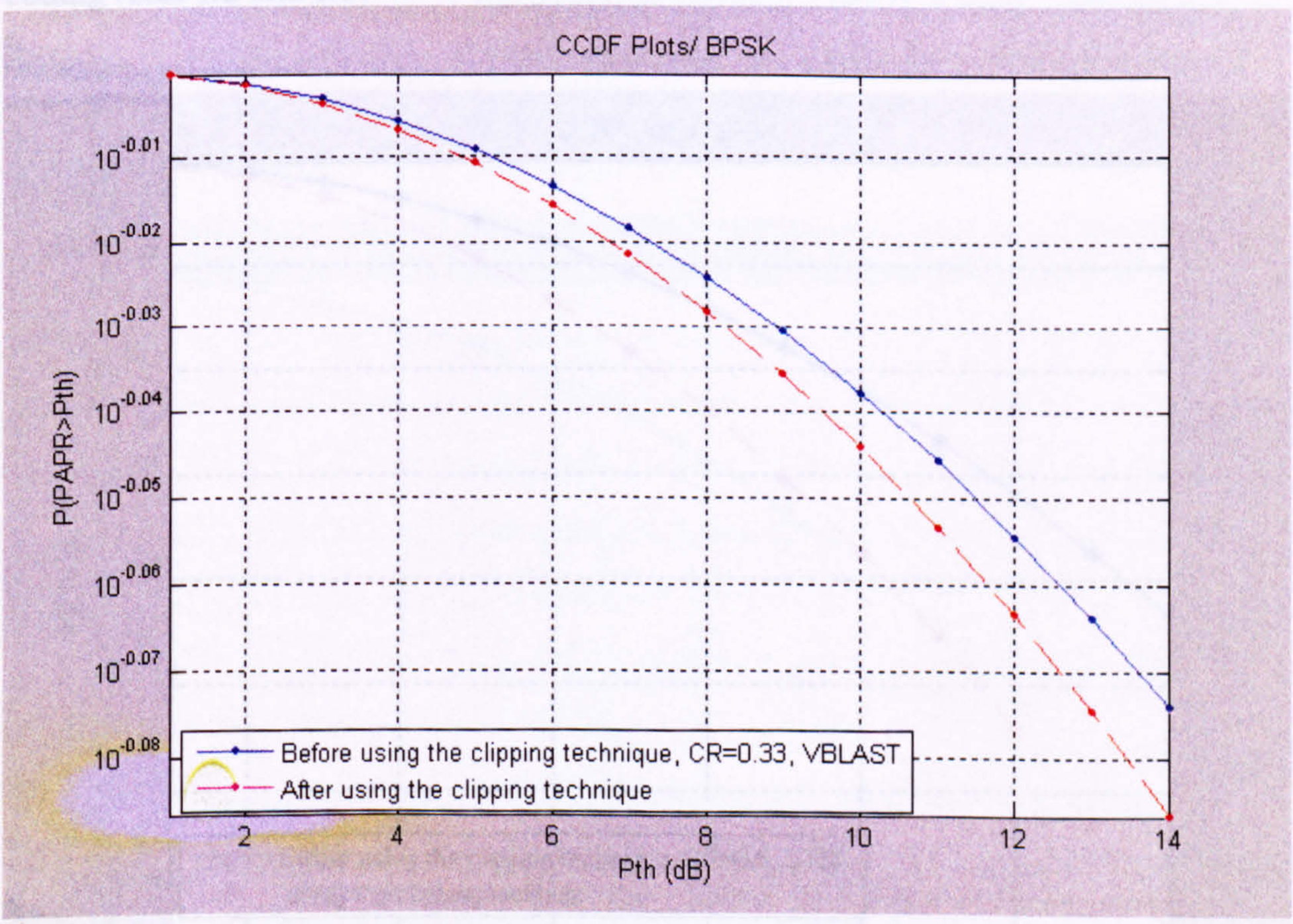


**Figure 5.13 (b)**

**Figure 5.13: The CCDF for using the clipping technique in a MIMO-OFDM system based on a BPSK modulation technique. (a) V-BLAST with coding rate 1/2 and (b) V-BLAST with coding rate 1/3.**

Figure 5.12 shows the CCDF plots for the clipping technique with BPSK modulation technique. In part (a), the probability of the PAPR values that exceed the 4 dB threshold is reduced from $9.83x10^{-1}$ to $9.75x10^{-1}$ with coding rate equals 1/2. For coding rate equals 1/3, it is reduced from $9.84x10^{-1}$ to $9.77x10^{-1}$ in part (b).

To cover changing the used MIMO encoder to V-BLAST, Figure 5.13 displays the CCDF curves. It is clearly that it improves the probability from $9.82x10^{-1}$ to $9.78x10^{-1}$ in part (c) (i.e., the coding rate equals 1/2). Using coding rate equals 1/3 in part (b) reduces the probabilities from $9.86x10^{-1}$ to $9.83x10^{-1}$.

Figures 5.14 and 5.15 show the CCDF plots for changing the modulation technique from BPSK to QPSK. Figure 5.14 consists of two parts, parts (a) and (b) describing the CCDF plots for using STBC MIMO encoder with coding rates equals 1/2 and 1/3 respectively. On the other hand, Figure 5.15 shows the CCDF plots for changing the MIMO encoder to be V-BLAST. It describes in parts (a) and (b) respectively for the coding rates 1/2 and 1/3.

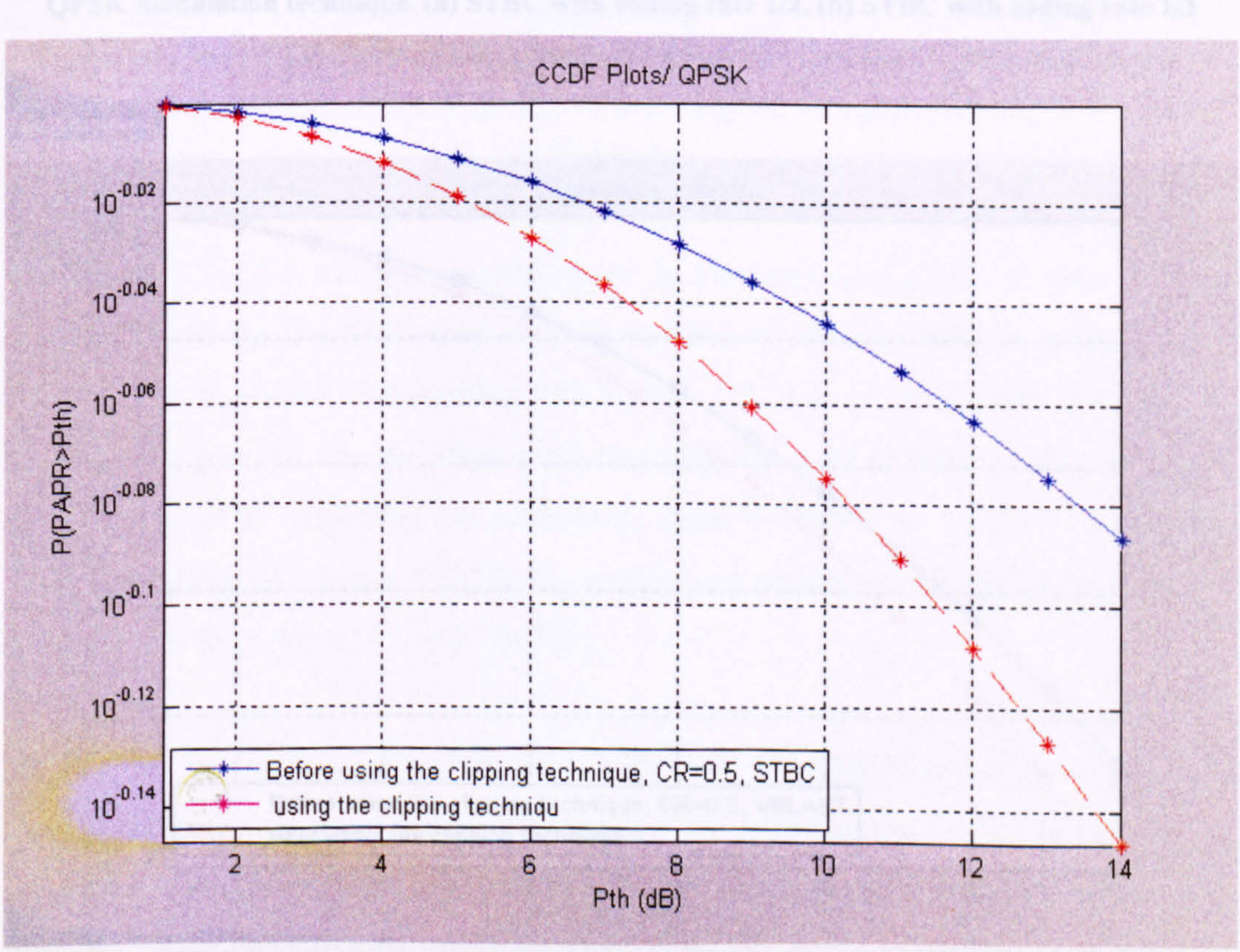


**Figure 5.14 (a)**

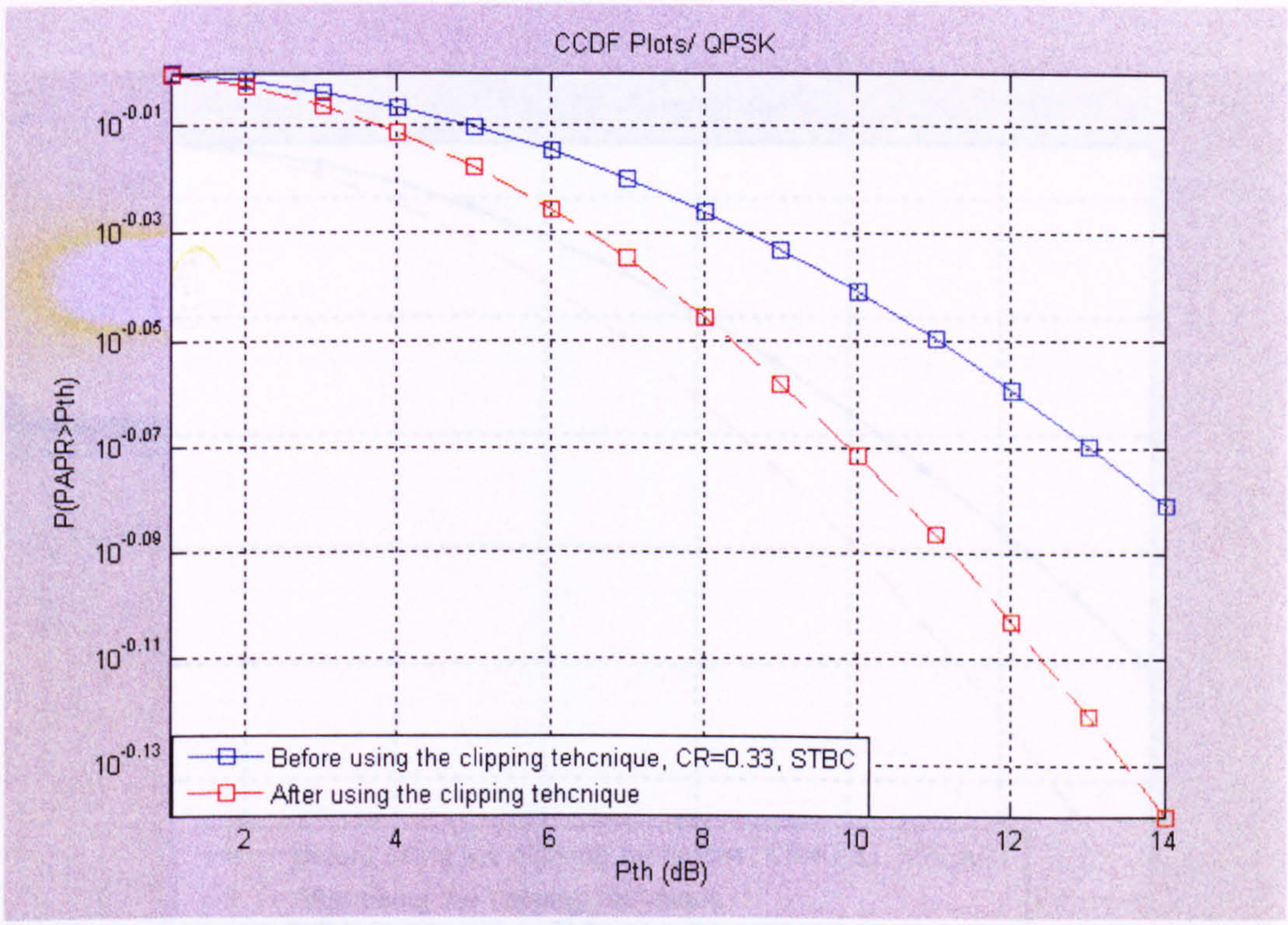


**Figure 5.14 (b)**

**Figure 5.14: The CCDF for using the clipping technique in a MIMO-OFDM system based on a QPSK modulation technique. (a) STBC with coding rate 1/2, (b) STBC with coding rate 1/3**

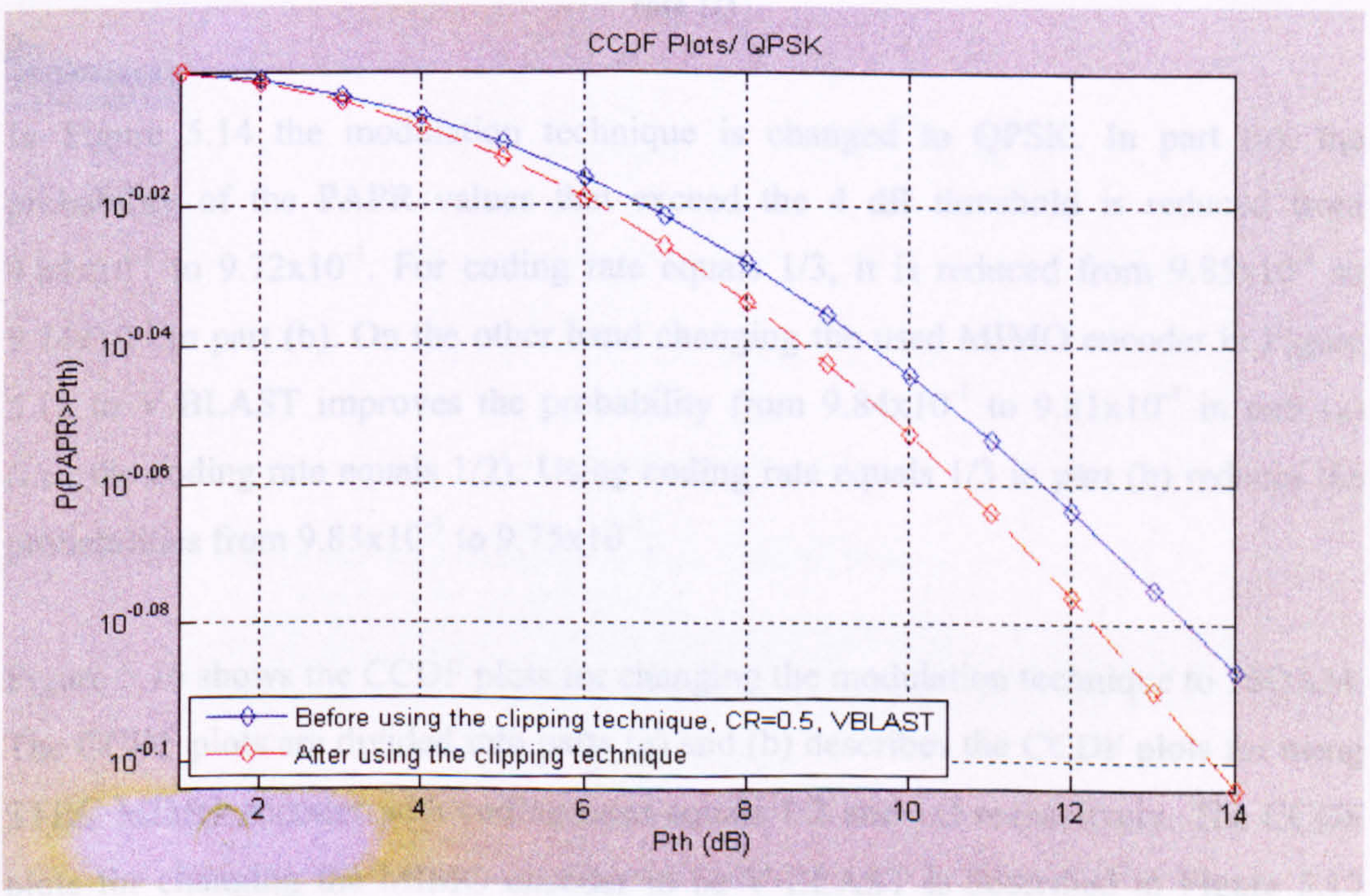


**Figure 5.15 (a)**

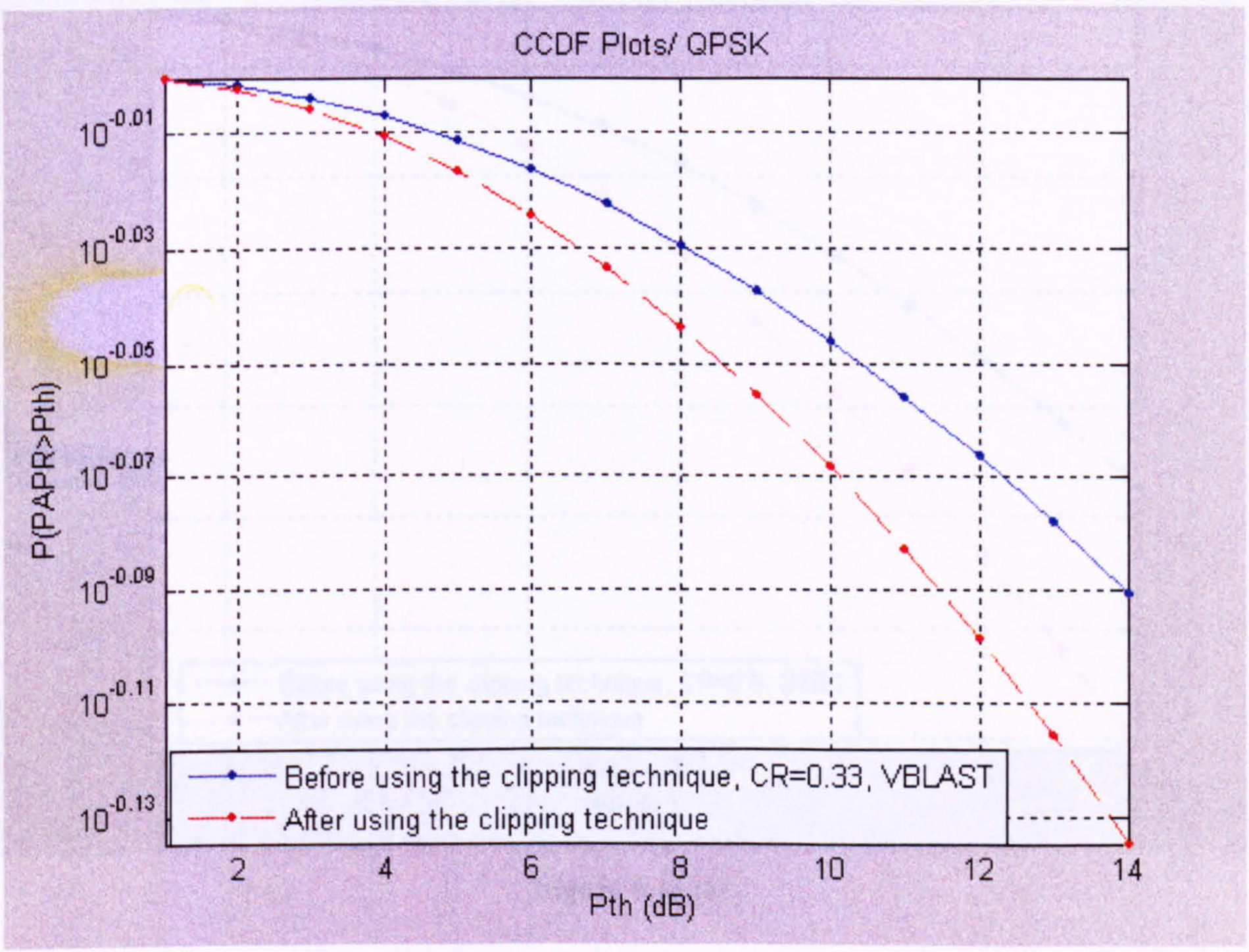


**Figure 5.15 (b)**

**Figure 5.15: The CCDF for using the clipping technique in a MIMO-OFDM system based on a QPSK modulation technique. (a) V-BLAST with coding rate 1/2 and (b) V-BLAST with coding rate 1/3**

In Figure 5.14 the modulation technique is changed to QPSK. In part (a), the probability of the PAPR values that exceed the 4 dB threshold is reduced from $9.84x10^{-1}$ to $9.72x10^{-1}$. For coding rate equals 1/3, it is reduced from $9.85x10^{-1}$ to $9.74x10^{-1}$ in part (b). On the other hand changing the used MIMO encoder in Figure 5.15 to V-BLAST improves the probability from $9.84x10^{-1}$ to $9.81x10^{-1}$ in part (a) (i.e., the coding rate equals 1/2). Using coding rate equals 1/3 in part (b) reduces the probabilities from $9.83x10^{-1}$ to $9.75x10^{-1}$.

Figure 5.16 shows the CCDF plots for changing the modulation technique to 16QAM. The CCDF plots are divided into parts (a) and (b) describes the CCDF plots for using STBC MIMO encoder with coding rates equals 1/2 and 1/3 respectively. The CCDF plots for changing the MIMO encoder to be V-BLAST is described in Figure 5.17 parts (a) and (b) respectively for the coding rates 1/2 and 1/3.

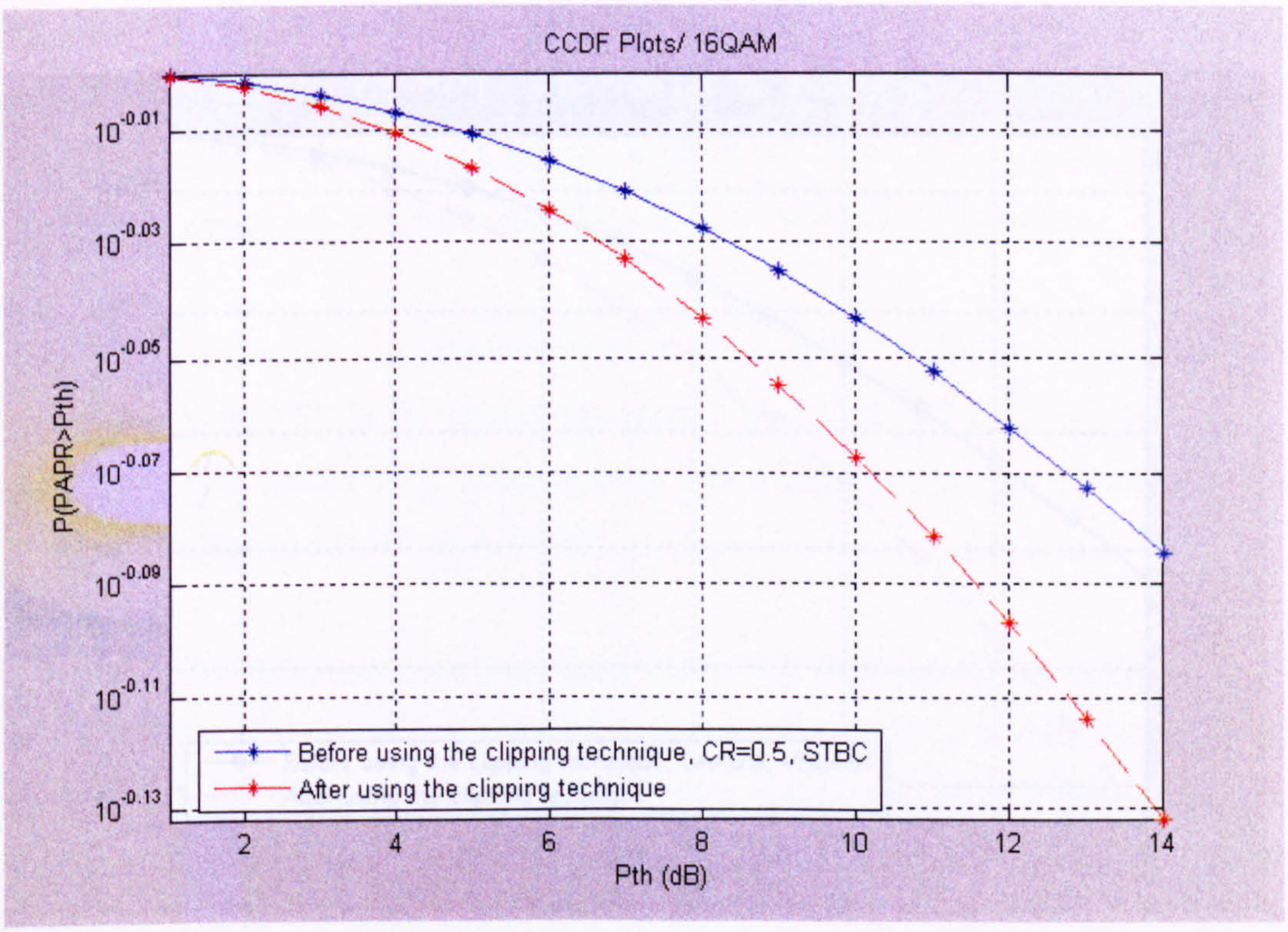


**Figure 5.16 (a)**

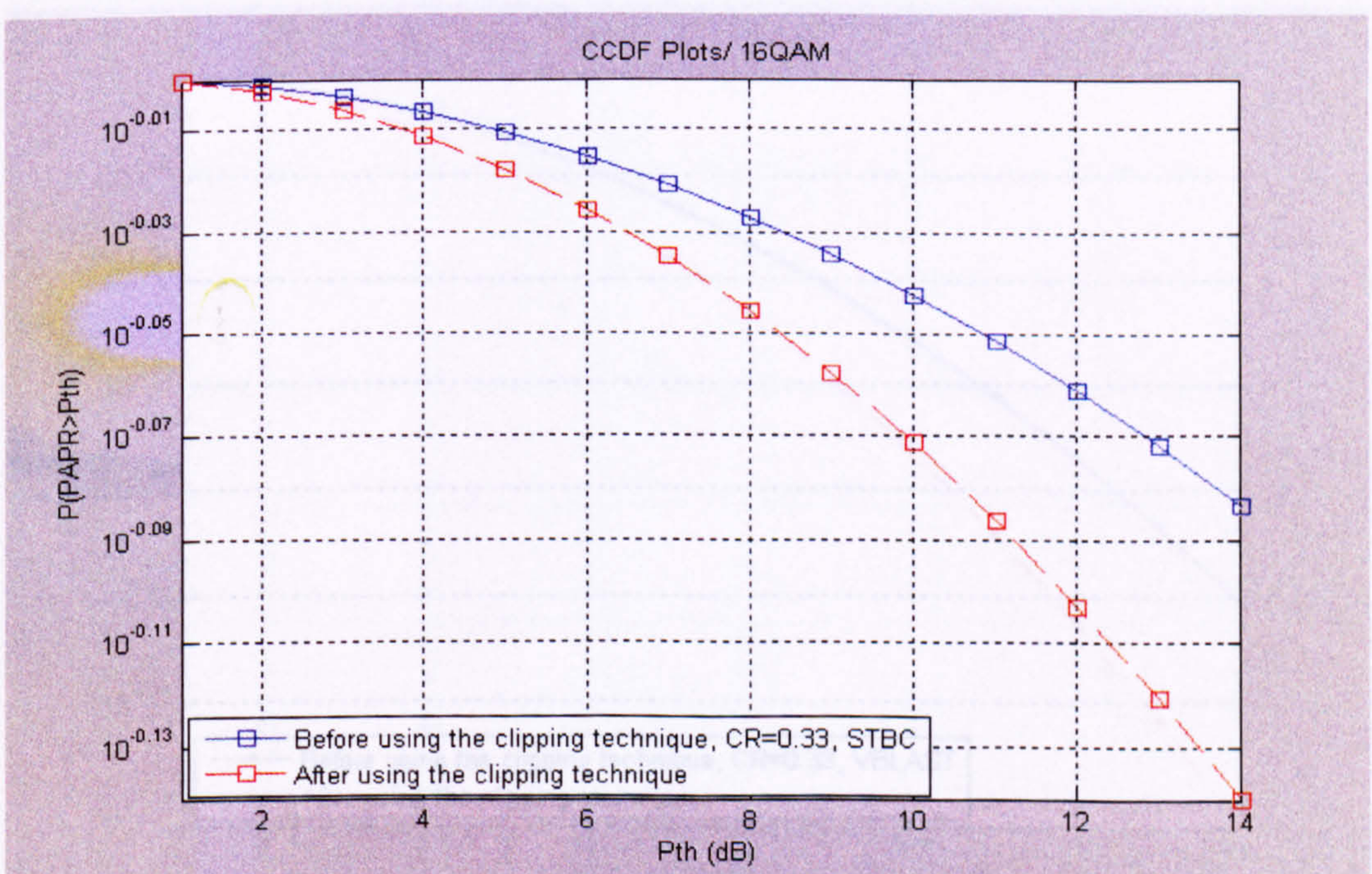


**Figure 5.16 (b)**

**Figure 5.16: The CCDF for using the clipping technique in a MIMO-OFDM system based on a 16-QAM modulation technique. (a) STBC with coding rate 1/2, (b) STBC with coding rate 1/3**

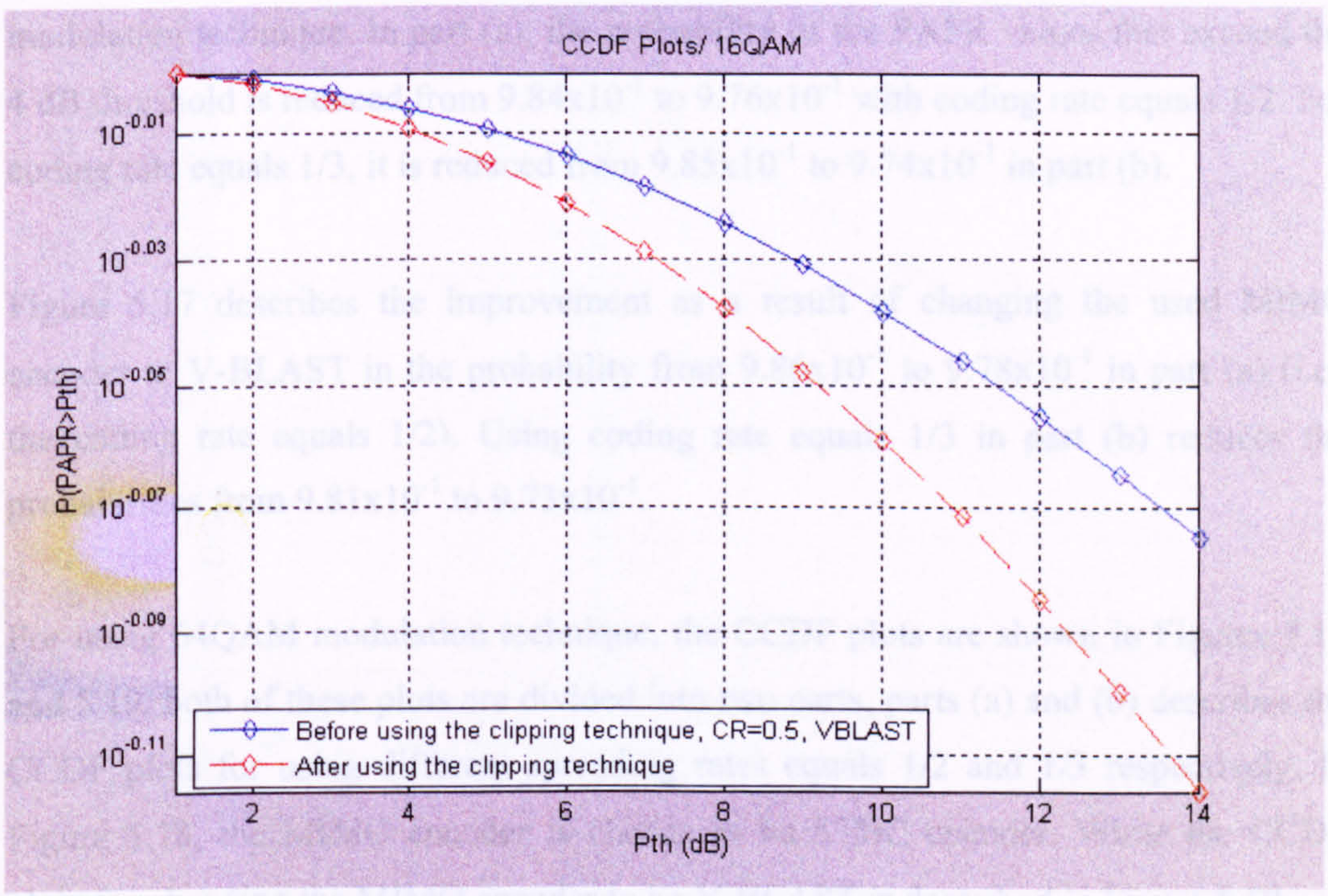


**Figure 5.17 (a)**

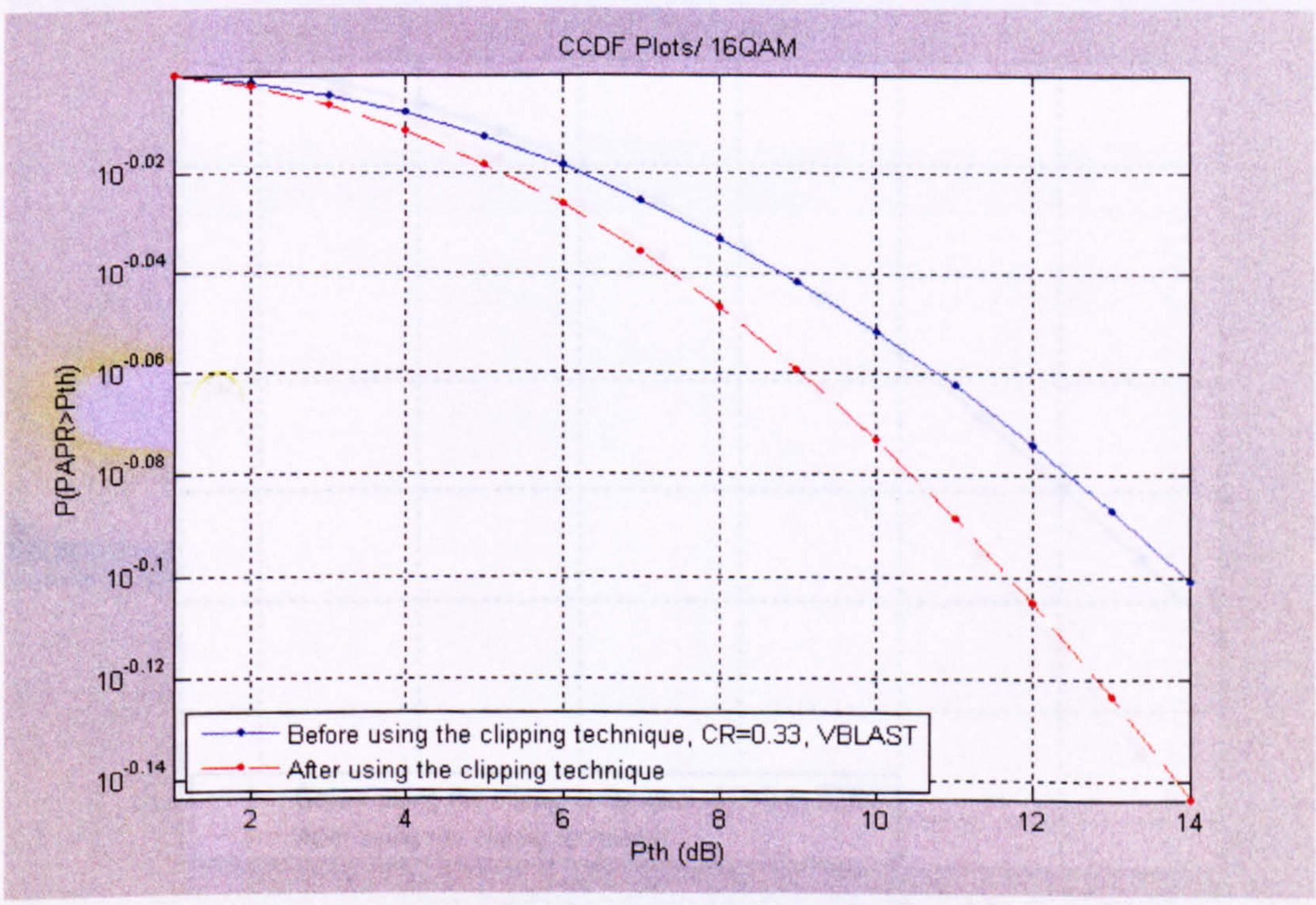


**Figure 5.17 (b)**

**Figure 5.17: The CCDF for using the clipping technique in a MIMO-OFDM system based on a 16-QAM modulation technique. (a) V-BLAST with coding rate 1/2 and (b) V-BLAST with coding rate 1/3**

Figure 5.16 shows the CCDF plots for the clipping technique with 16QAM modulation technique. In part (a), the probability of the PAPR values that exceed the 4 dB threshold is reduced from $9.84x10^{-1}$ to $9.76x10^{-1}$ with coding rate equals 1/2. For coding rate equals 1/3, it is reduced from $9.85x10^{-1}$ to $9.74x10^{-1}$ in part (b).

Figure 5.17 describes the improvement as a result of changing the used MIMO encoder to V-BLAST in the probability from $9.86x10^{-1}$ to $9.78x10^{-1}$ in part (a) (i.e., the coding rate equals 1/2). Using coding rate equals 1/3 in part (b) reduces the probabilities from $9.81x10^{-1}$ to $9.73x10^{-1}$.

For using 64QAM modulation technique, the CCDF plots are shown in Figures 5.18 and 5.19. both of these plots are divided into two parts, parts (a) and (b) describes the CCDF plots for using different spreading rates equals 1/2 and 1/3 respectively. In Figure 5.18, the MIMO encoder is chosen to be STBC encoder. While the CCDF plots for changing the MIMO encoder to be V-BLAST is described in Figure 5.19.

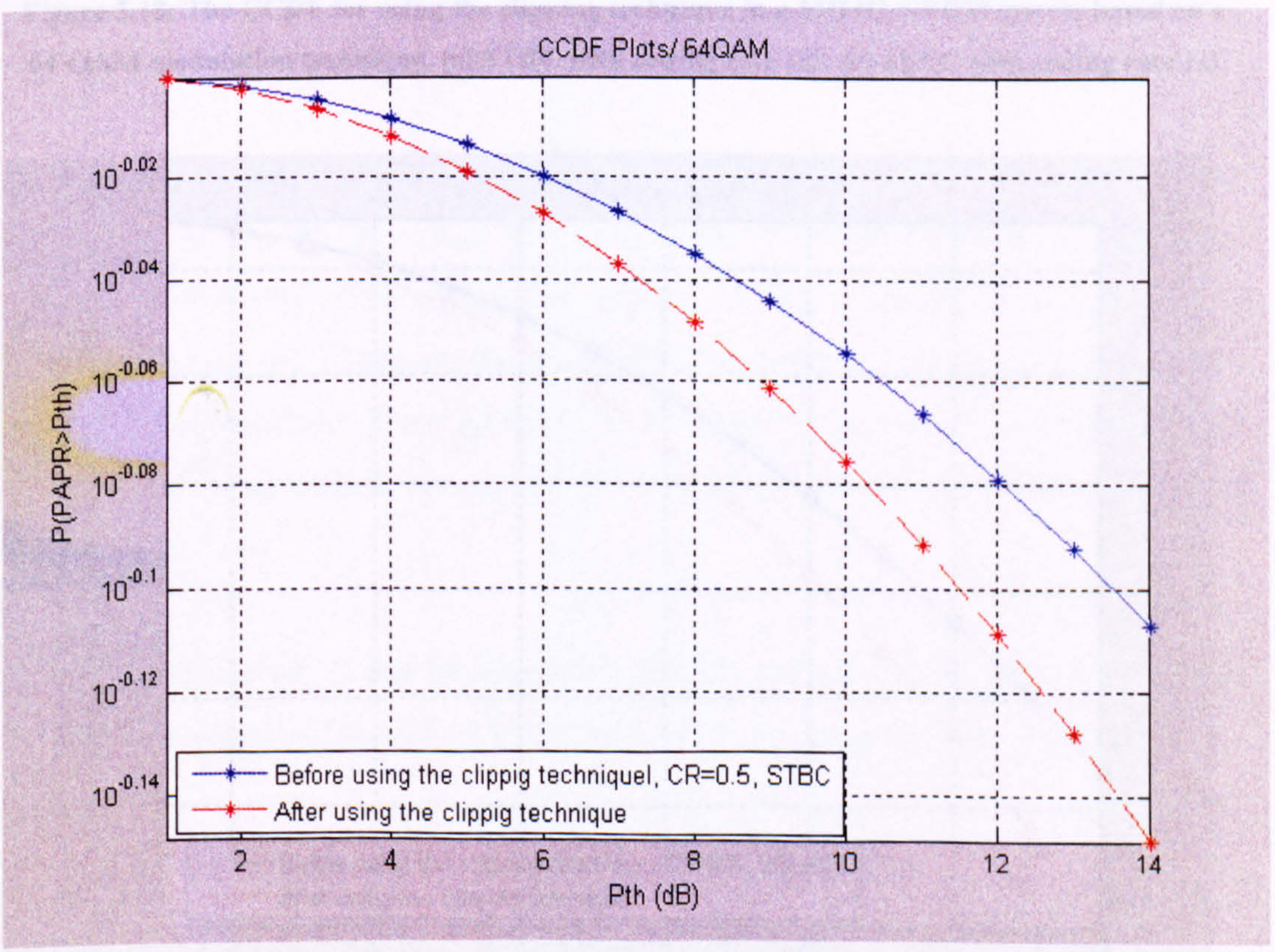


**Figure 5.18 (a)**

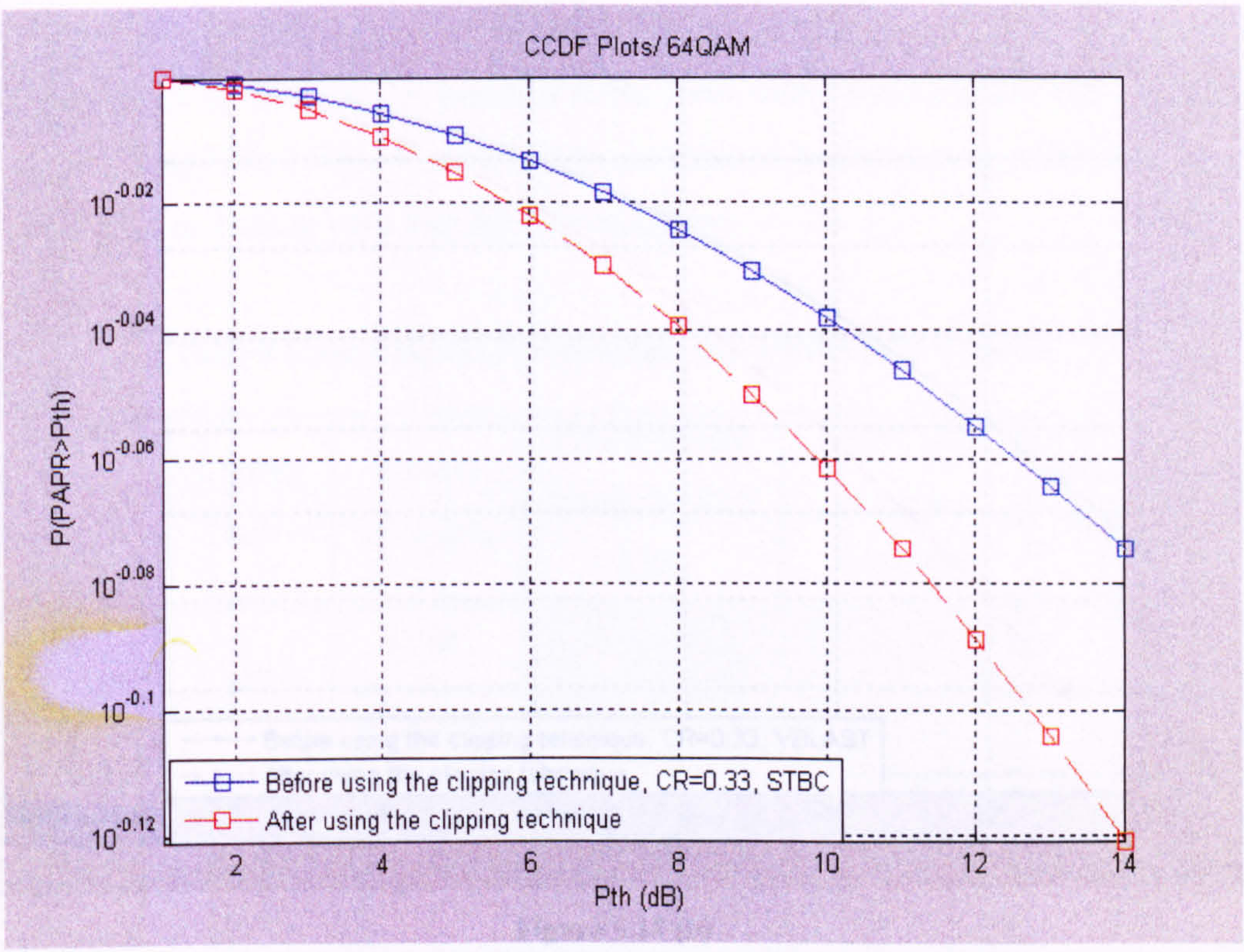


**Figure 5.18 (b)**

**Figure 5.18: The CCDF for using the clipping technique in a MIMO-OFDM system based on a 64-QAM modulation technique. (a) STBC with coding rate 1/2, (b) STBC with coding rate 1/3**

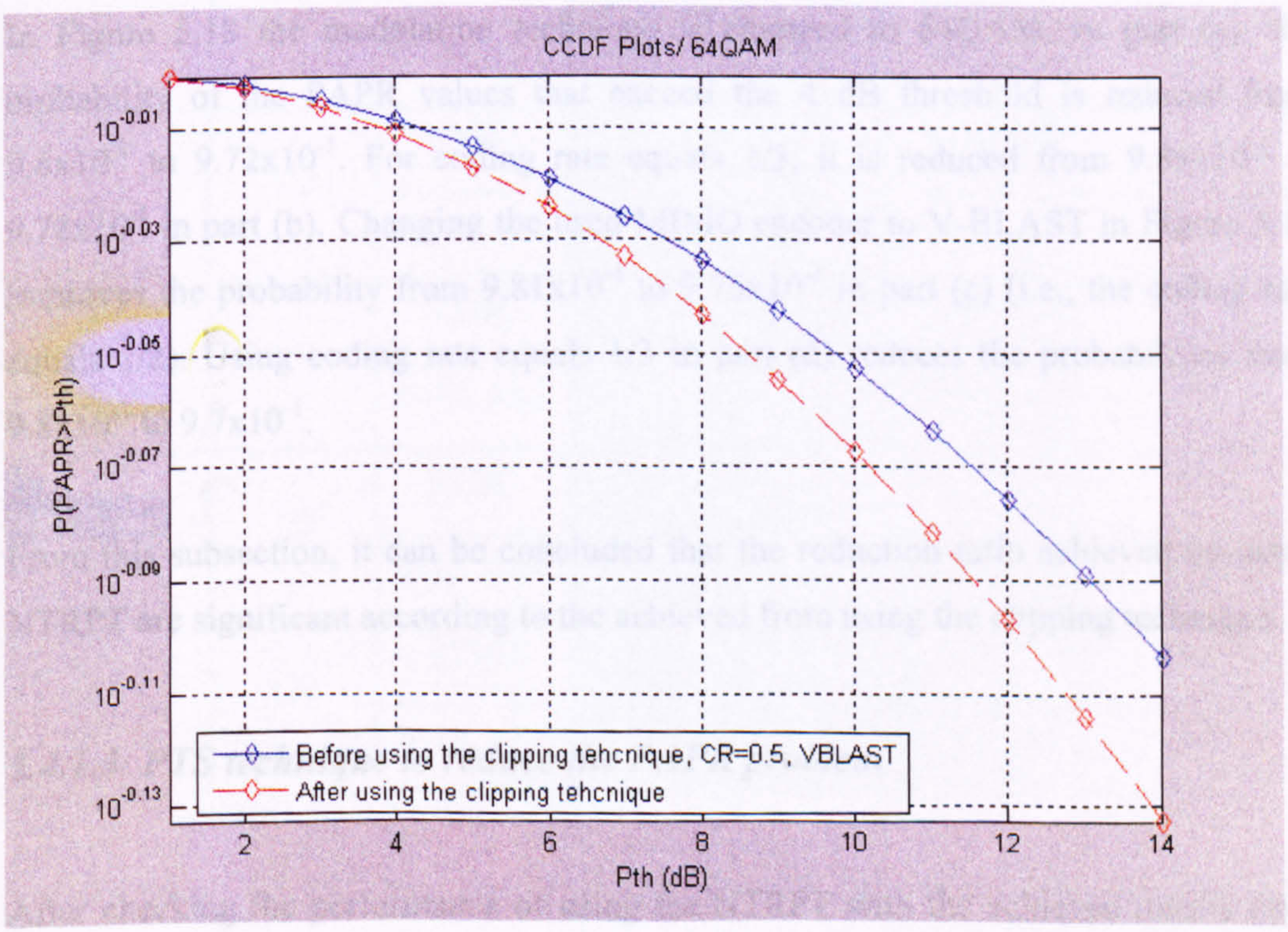


**Figure 5.19 (a)**

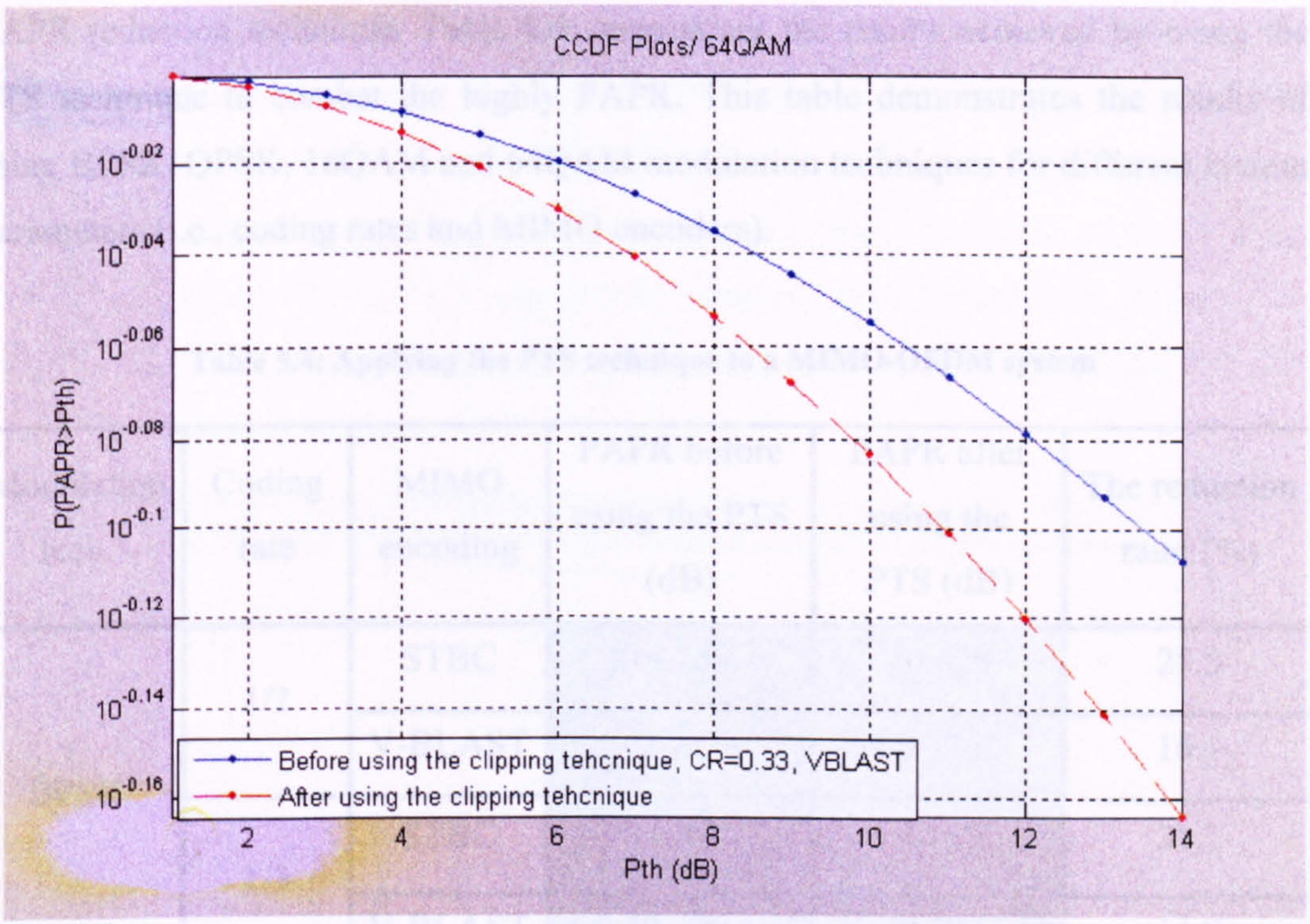


**Figure 5.19 (b)**

**Figure 5.19: The CCDF for using the clipping technique in a MIMO-OFDM system based on a 64-QAM modulation technique. (a) V-BLAST with coding rate 1/2 and (b) V-BLAST with coding rate 1/3**

In Figure 5.18 the modulation technique is changed to 64QAM. In part (a), the probability of the PAPR values that exceed the 4 dB threshold is reduced from $9.8x10^{-1}$ to $9.72x10^{-1}$. For coding rate equals 1/3, it is reduced from $9.86x10^{-1}$ to $9.78x10^{-1}$ in part (b). Changing the used MIMO encoder to V-BLAST in Figure 5.19 improves the probability from $9.81x10^{-1}$ to $9.75x10^{-1}$ in part (c) (i.e., the coding rate equals 1/2). Using coding rate equals 1/3 in part (d) reduces the probabilities from $9.8x10^{-1}$ to $9.7x10^{-1}$.

From this subsection, it can be concluded that the reduction ratio achieved by using NTRPT are significant according to the achieved from using the clipping technique.

### *5.4.1.3 PTS technique to reduce the PAPR problem*

After checking the performance of using the NTRPT with the achieved results from the clipping technique, this subsection shows the results of using another conventional

PAPR reduction technique. Table 5.4 summarises the results achieved by using the PTS technique to combat the highly PAPR. This table demonstrates the results of using BPSK, QPSK, 16QAM and 64QAM modulation techniques for different system parameters (i.e., coding rates and MIMO encoders).

**Table 5.4: Applying the PTS technique to a MIMO-OFDM system**

| Modulation tech. | Coding rate | MIMO encoding | PAPR before using the PTS (dB) | PAPR after using the PTS (dB) | The reduction ratio (%) |
|---|---|---|---|---|---|
| BPSK | 1/2 | STBC | 14.259 | 10.628 | 25.5 |
| | | V-BLAST | 9.987 | 8.376 | 16.1 |
| | 1/3 | STBC | 13.324 | 9.163 | 31.2 |
| | | V-BLAST | 13.571 | 11.965 | 11.8 |
| QPSK | 1/2 | STBC | 14.579 | 12.457 | 14.5 |
| | | V-BLAST | 13.214 | 11.001 | 16.7 |
| | 1/3 | STBC | 12.681 | 9.827 | 22.5 |
| | | V-BLAST | 15.189 | 13.635 | 10.2 |
| 16QAM | 1/2 | STBC | 13.240 | 12.884 | 2.7 |
| | | V-BLAST | 12.270 | 11.695 | 4.6 |
| | 1/3 | STBC | 11.152 | 9.354 | 16.1 |
| | | V-BLAST | 12.795 | 9.509 | 25.7 |
| 64QAM | 1/2 | STBC | 12.423 | 11.871 | 4.4 |
| | | V-BLAST | 11.687 | 10.013 | 14.3 |
| | 1/3 | STBC | 13.424 | 12.551 | 6.5 |
| | | V-BLAST | 12.252 | 11.125 | 9.2 |

Comparing to the achieved results in the previous two subsections, the reduction ratios according the PTS is not quite as high as the achieved from the clipping

technique. Furthermore, both of them did not reach the significant reduction ratios that are achieved by applying the NTRPT. The following figures present the CCDF plots of achieved results in Table 5.4 for different modulation technique, each of which is consists of two parts, parts (a) and (b) describes the CCDF plots for using coding rates equals 1/2 and 1/3 respectively. Starting from Figure 5.20, it shows the CCDF plots for a STBC MIMO encoder, while changing the MIMO encoder to be V-BLAST is described in Figure 5.21.

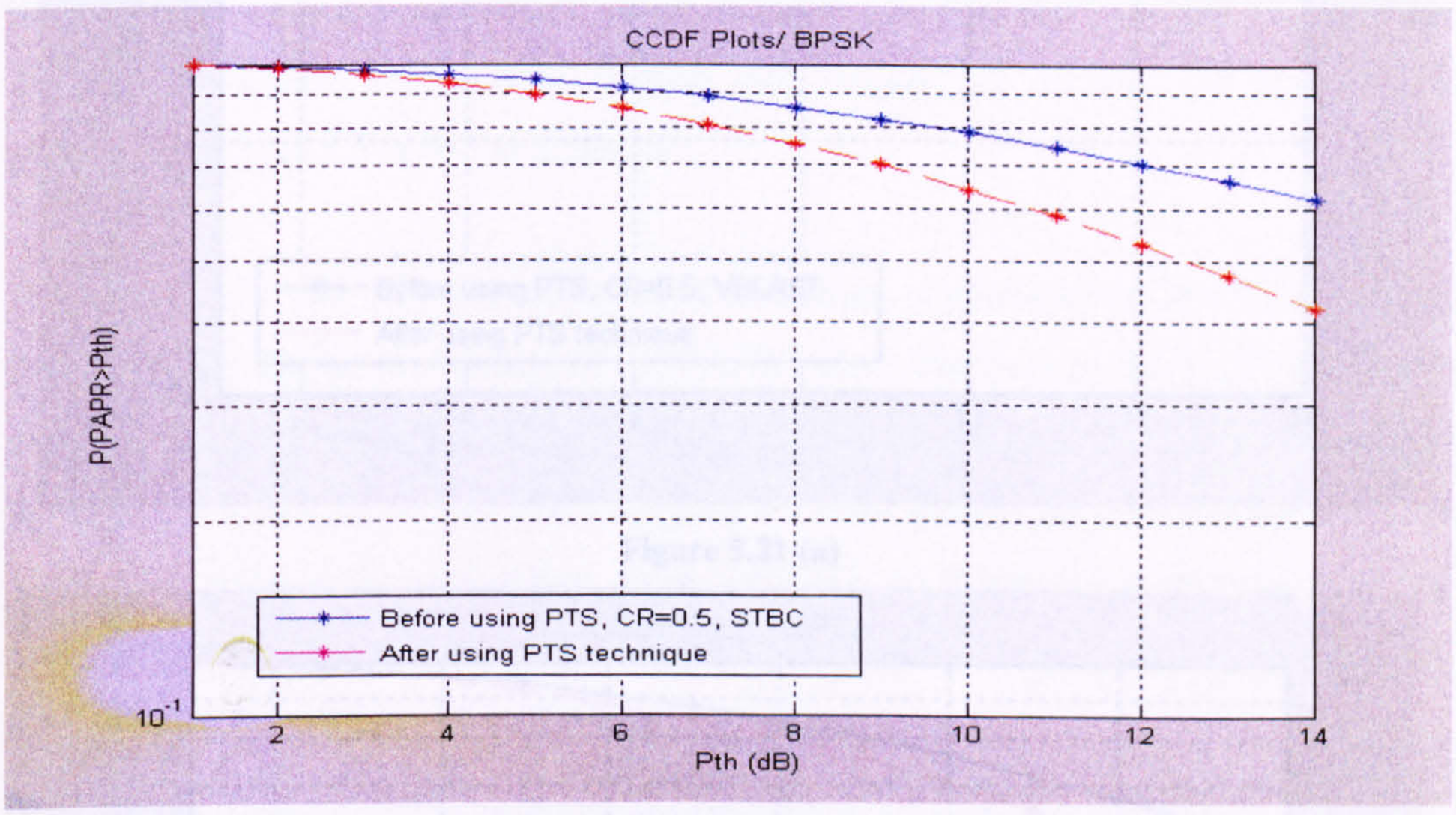


**Figure 5.20 (a)**

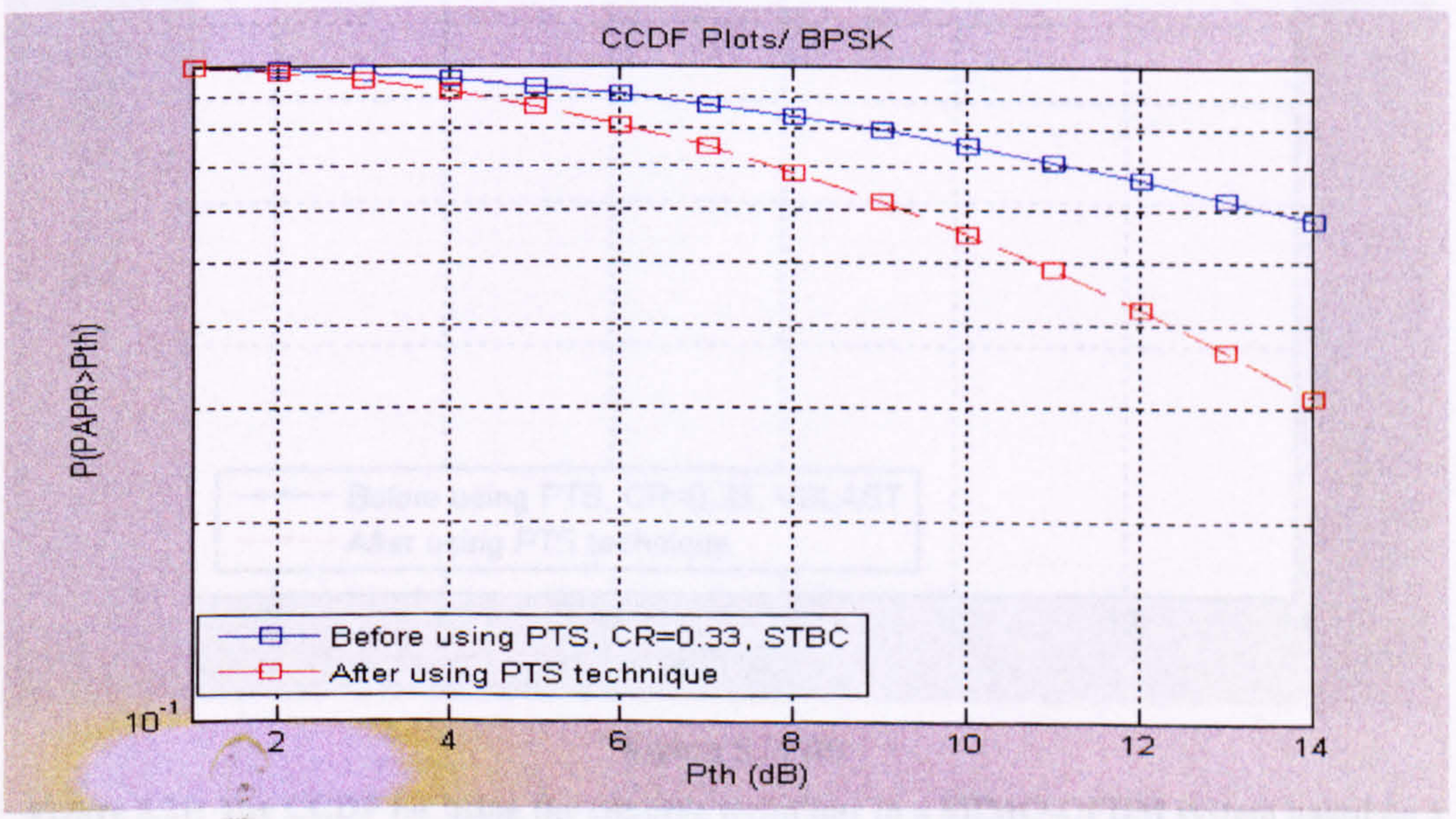


**Figure 5.20 (b)**

**Figure 5.20: The CCDF for using the PTS technique in a MIMO-OFDM system based on a BPSK modulation technique. (a) STBC with coding rate 1/2 (b) STBC with coding rate 1/3**

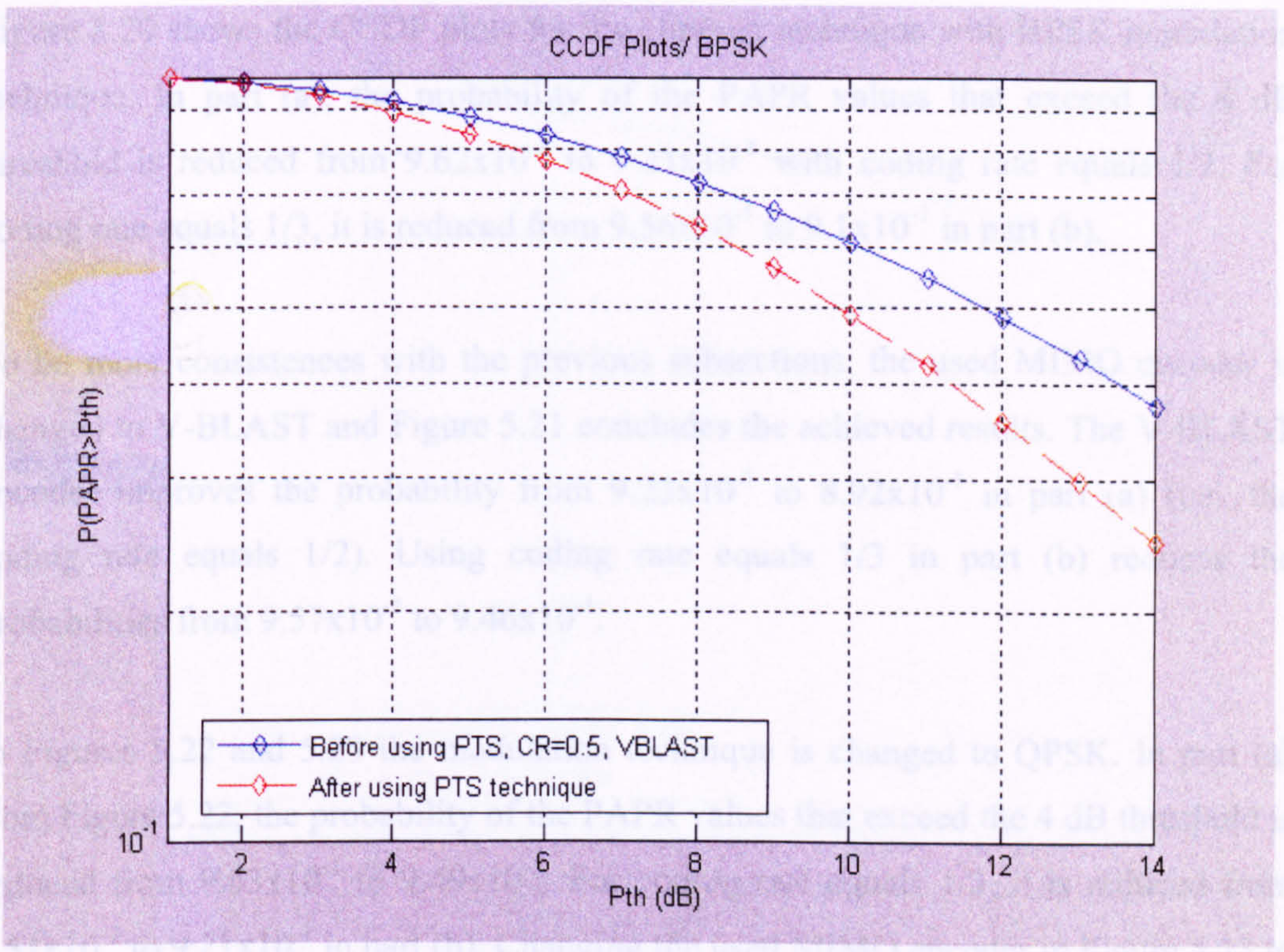


**Figure 5.21 (a)**

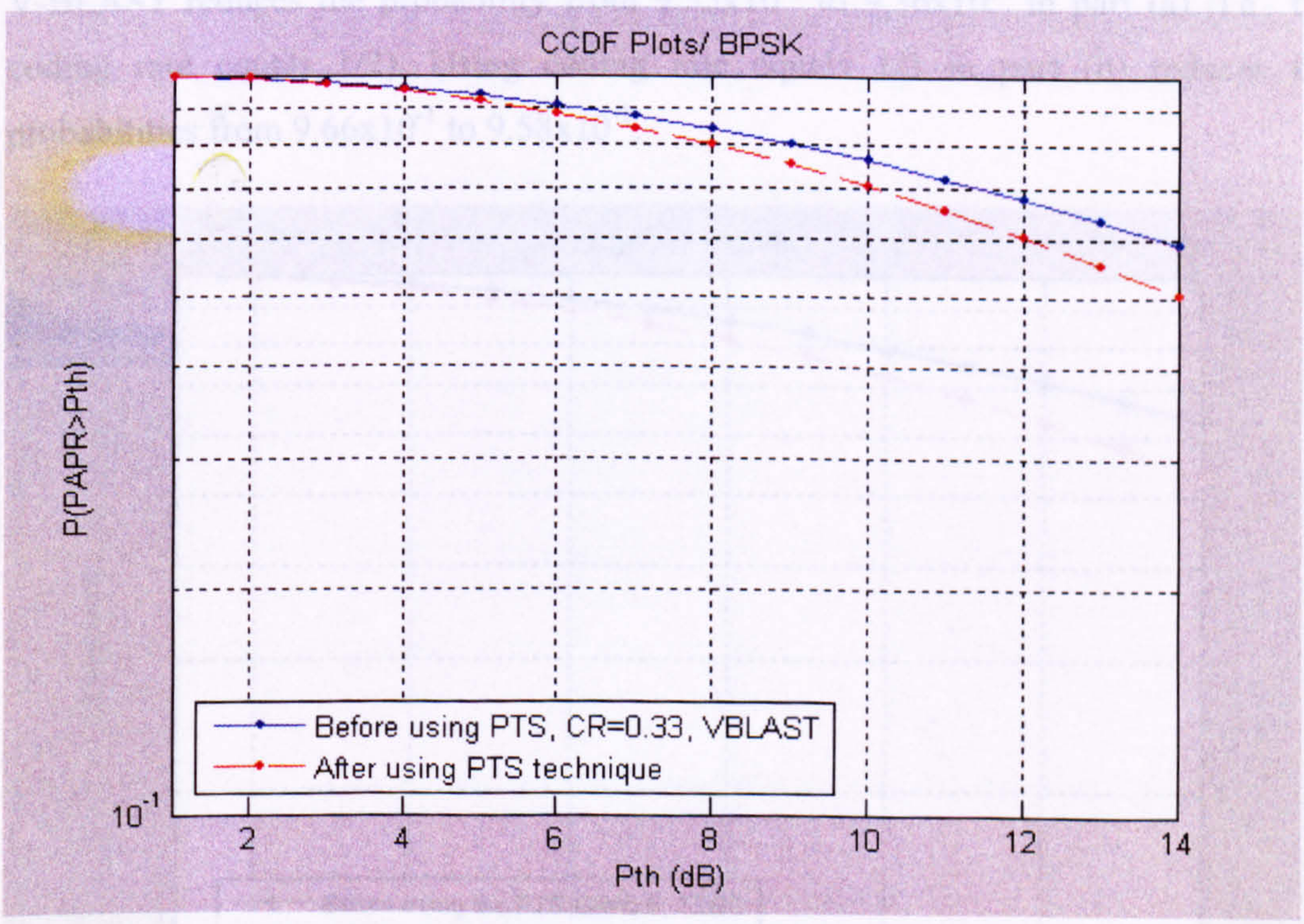


**Figure 5.21 (b)**

**Figure 5.21: The CCDF for using the clipping technique in a MIMO-OFDM system based on a BPSK modulation technique. (a) V-BLAST with coding rate 1/2 and (b) V-BLAST with coding rate 1/3**

Figure 5.20 shows the CCDF plots for the clipping technique with BPSK modulation technique. In part (a), the probability of the PAPR values that exceed the 4 dB threshold is reduced from $9.62x10^{-1}$ to $9.31x10^{-1}$ with coding rate equals 1/2. For coding rate equals 1/3, it is reduced from $9.56x10^{-1}$ to $9.1x10^{-1}$ in part (b).

To be more consistences with the previous subsections, the used MIMO encoder is changed to V-BLAST and Figure 5.21 concludes the achieved results. The V-BLAST encoder improves the probability from $9.23x10^{-1}$ to $8.92x10^{-1}$ in part (a) (i.e., the coding rate equals 1/2). Using coding rate equals 1/3 in part (b) reduces the probabilities from $9.57x10^{-1}$ to $9.46x10^{-1}$.

In Figures 5.22 and 5.23 the modulation technique is changed to QPSK. In part (a) from Figure 5.22, the probability of the PAPR values that exceed the 4 dB threshold is reduced from $9.63x10^{-1}$ to $9.49x10^{-1}$. For coding rate equals 1/3, it is reduced from $9.51x10^{-1}$ to $9.21x10^{-1}$ in part (b). Changing the used MIMO encoder in Figure 5.23 to V-BLAST reduces the probability from $9.55x10^{-1}$ to $9.36x10^{-1}$ in part (a) (i.e., the coding rate equals 1/2). Using coding rate equals 1/3 in part (b) reduces the probabilities from $9.66x10^{-1}$ to $9.58x10^{-1}$.

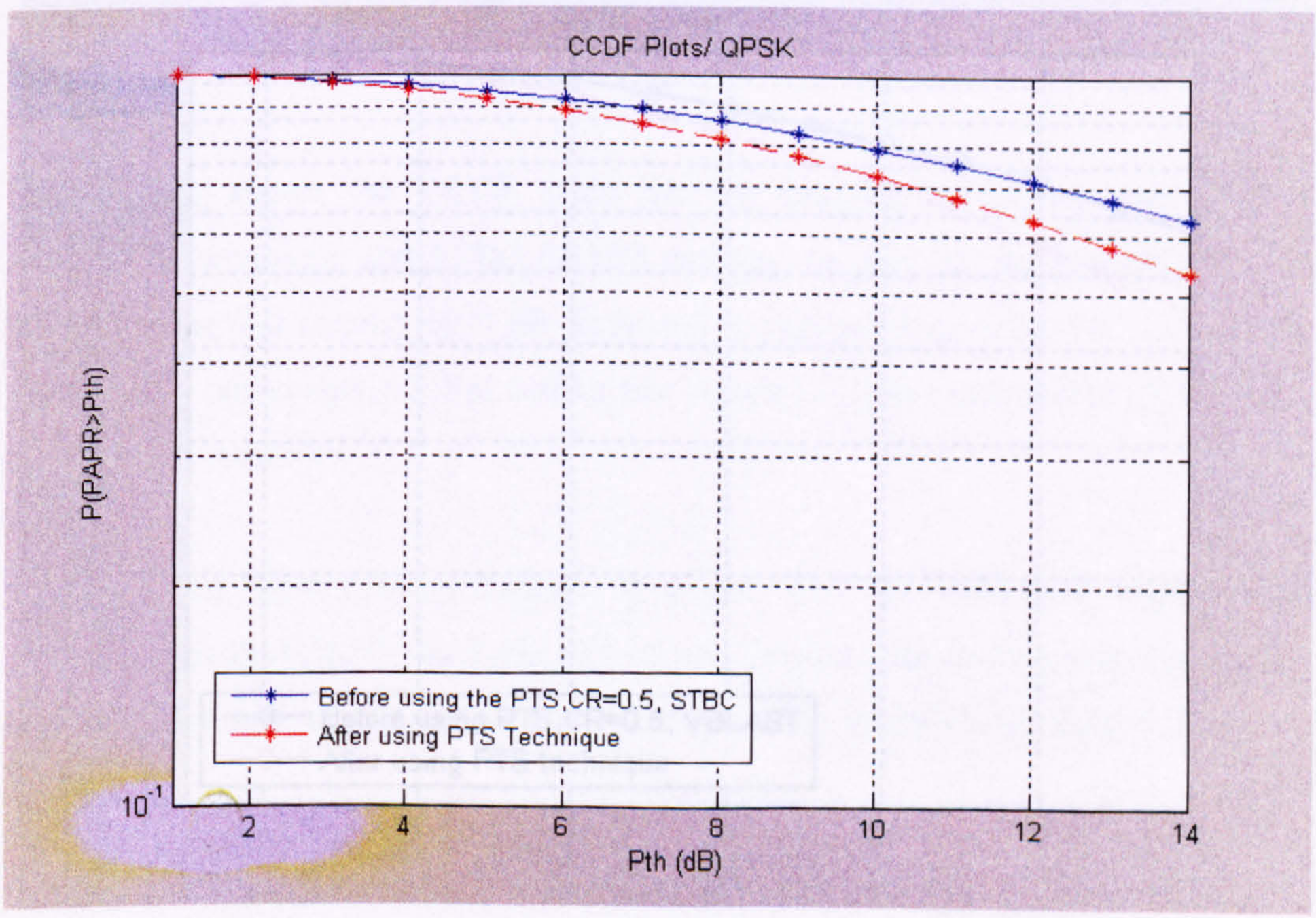


**Figure 5.22 (a)**

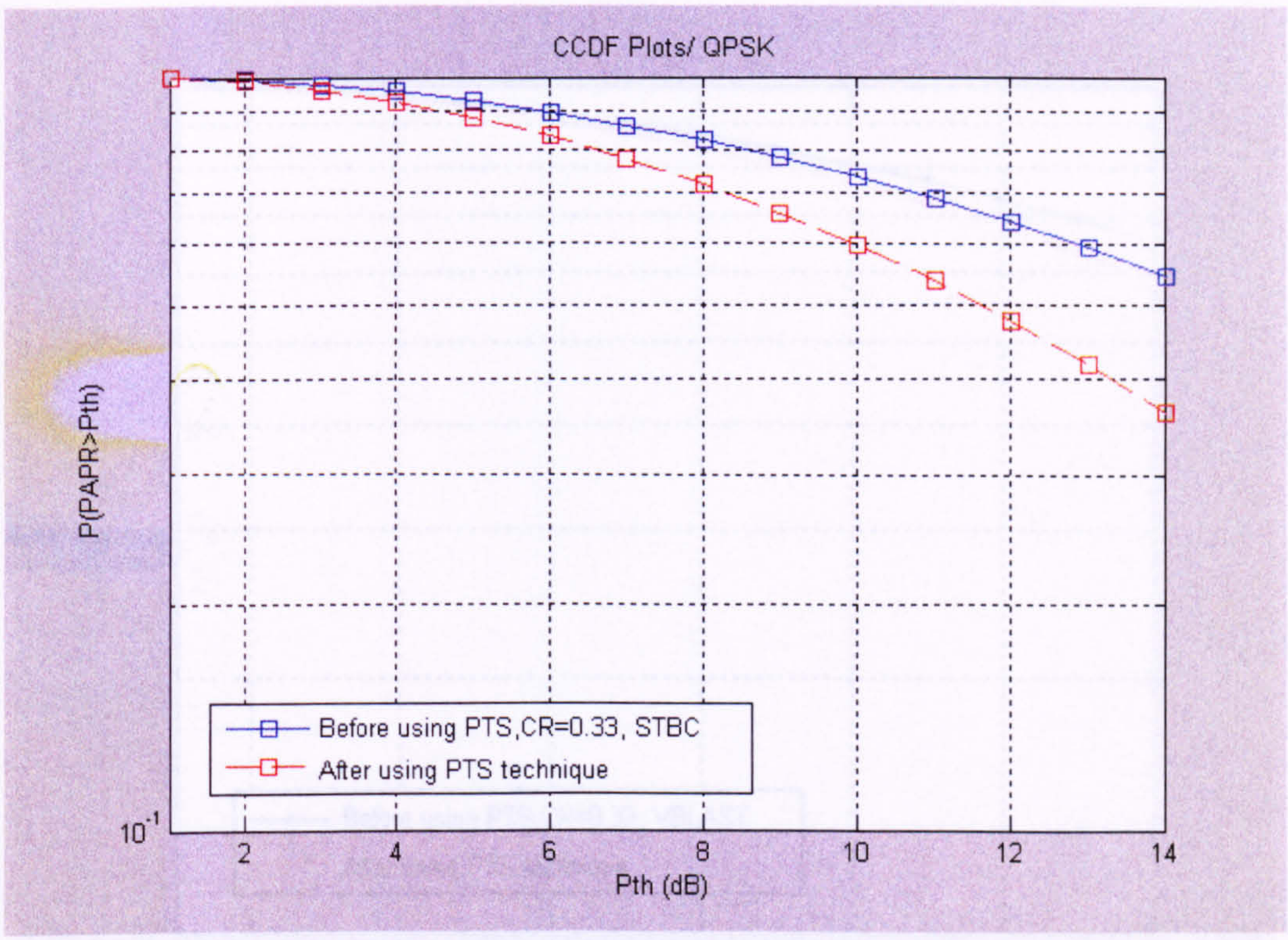


**Figure 5.22 (b)**

**Figure 5.22: The CCDF for using the PTS technique in a MIMO-OFDM system based on a QPSK modulation technique. (a) STBC with coding rate 1/2, (b) STBC with coding rate 1/3**

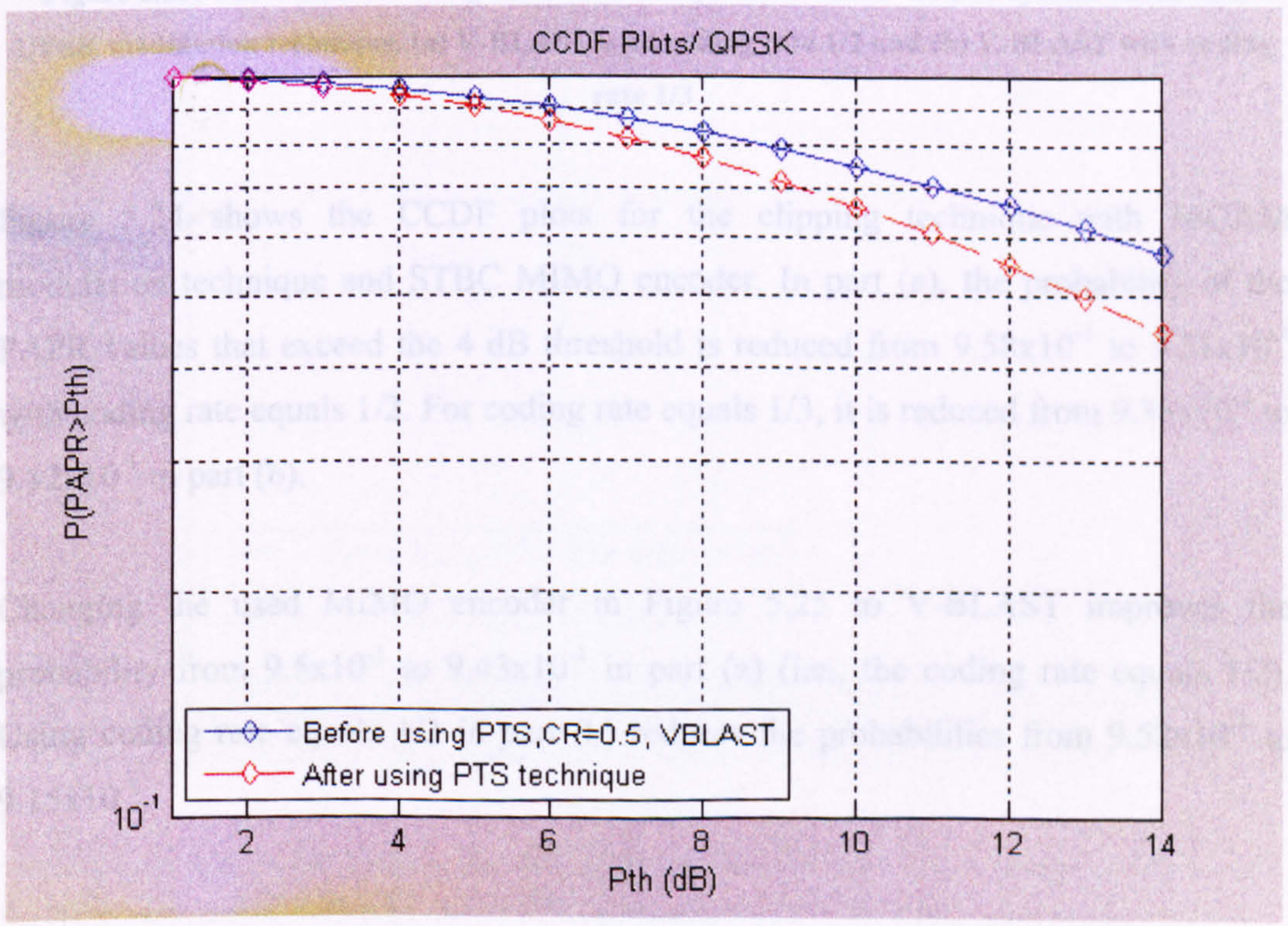


**Figure 5.23 (a)**

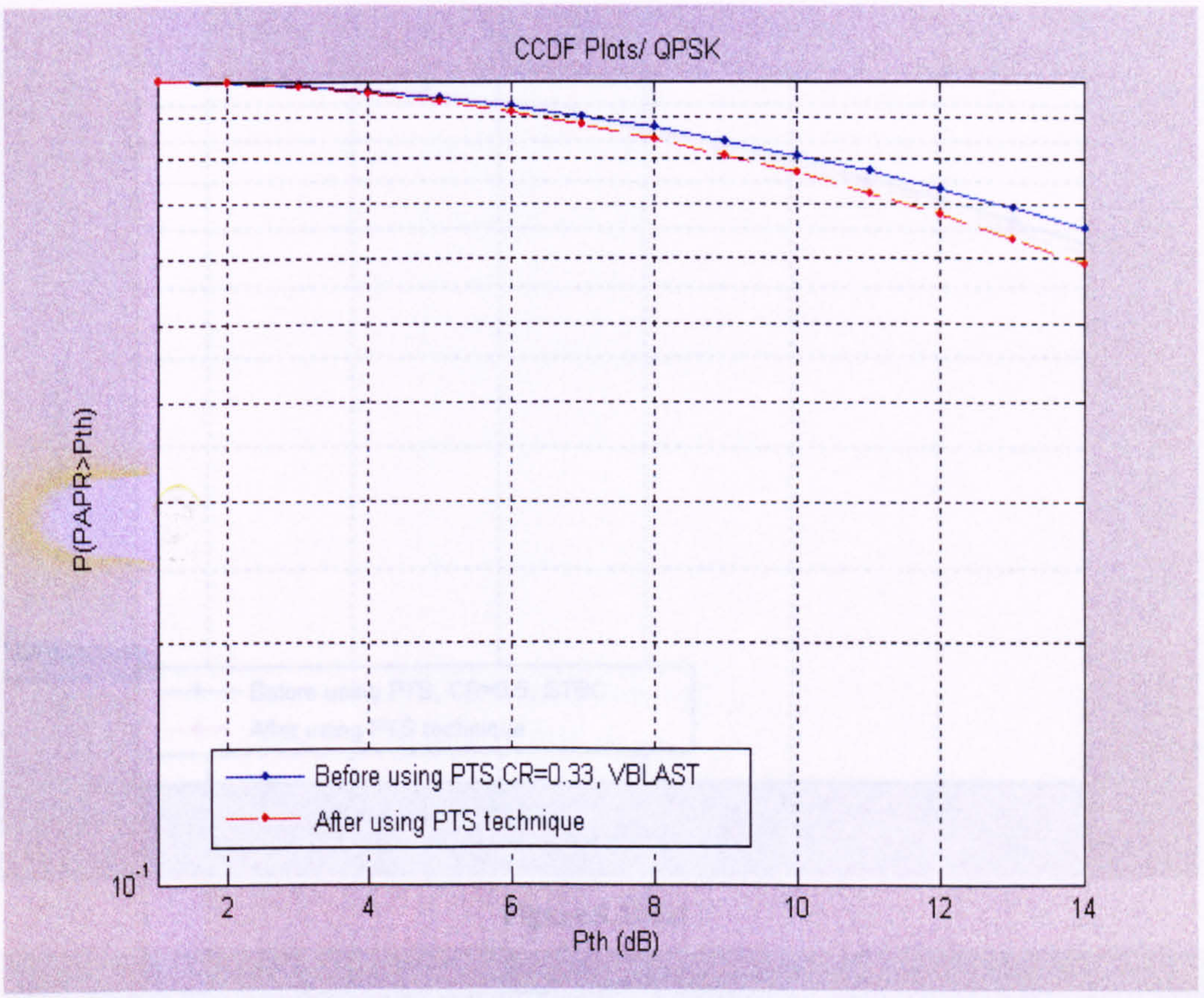


**Figure 5.23 (b)**

**Figure 5.23: The CCDF for using the PTS technique in a MIMO-OFDM system based on a QPSK modulation technique. (a) V-BLAST with coding rate 1/2 and (b) V-BLAST with coding rate 1/3**

Figure 5.24 shows the CCDF plots for the clipping technique with 16QAM modulation technique and STBC MIMO encoder. In part (a), the probability of the PAPR values that exceed the 4 dB threshold is reduced from $9.58x10^{-1}$ to $9.51x10^{-1}$ with coding rate equals 1/2. For coding rate equals 1/3, it is reduced from $9.38x10^{-1}$ to $9.12x10^{-1}$ in part (b).

Changing the used MIMO encoder in Figure 5.25 to V-BLAST improves the probability from $9.5x10^{-1}$ to $9.43x10^{-1}$ in part (a) (i.e., the coding rate equals 1/2). Using coding rate equals 1/3 in part (b) reduces the probabilities from $9.52x10^{-1}$ to $9.15x10^{-1}$.

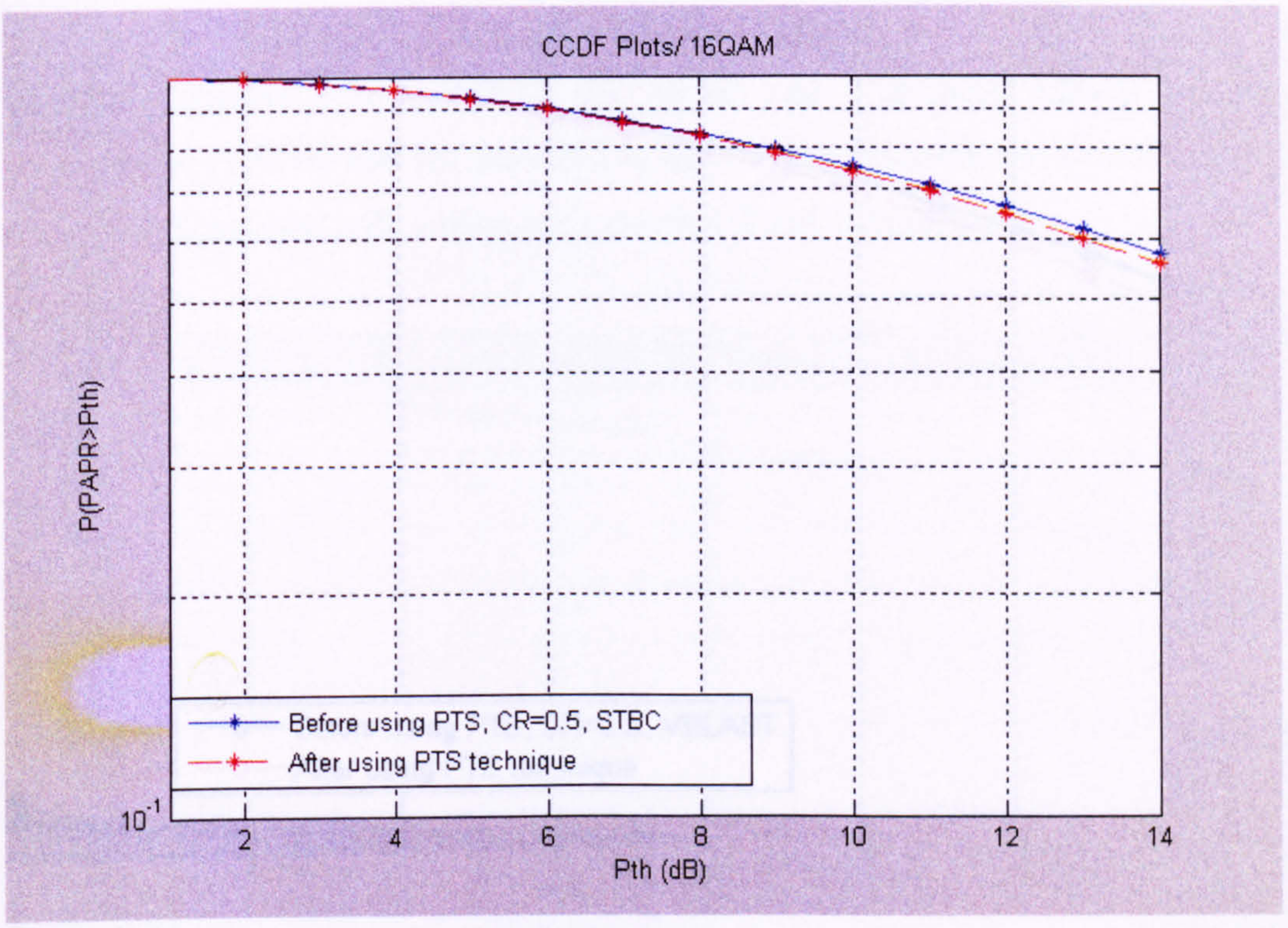


**Figure 5.24 (a)**

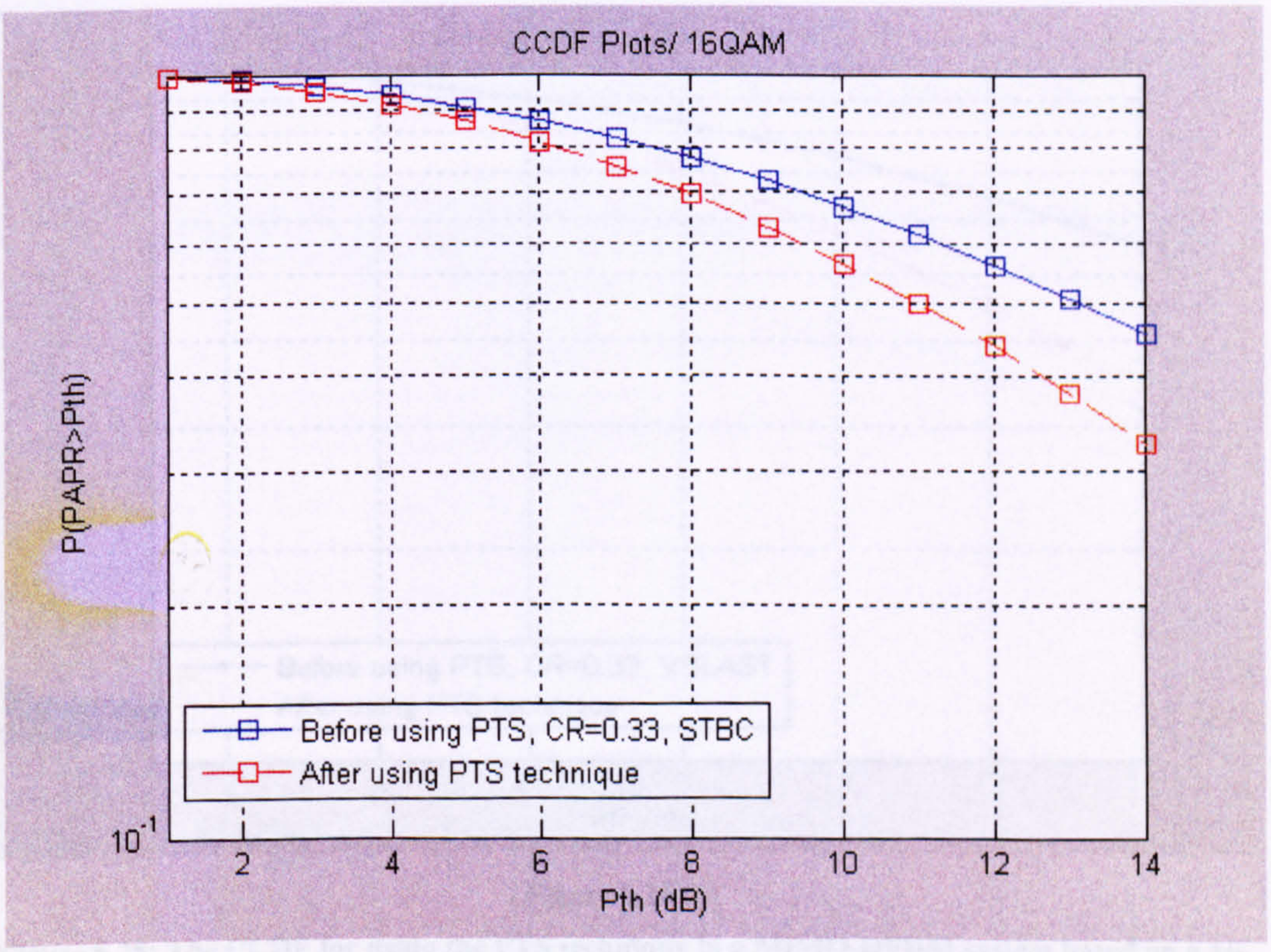


**Figure 5.24 (b)**

**Figure 5.24: The CCDF for using the PTS technique in a MIMO-OFDM system based on a 16-QAM modulation technique. (a) STBC with coding rate 1/2, (b) STBC with coding rate 1/3**

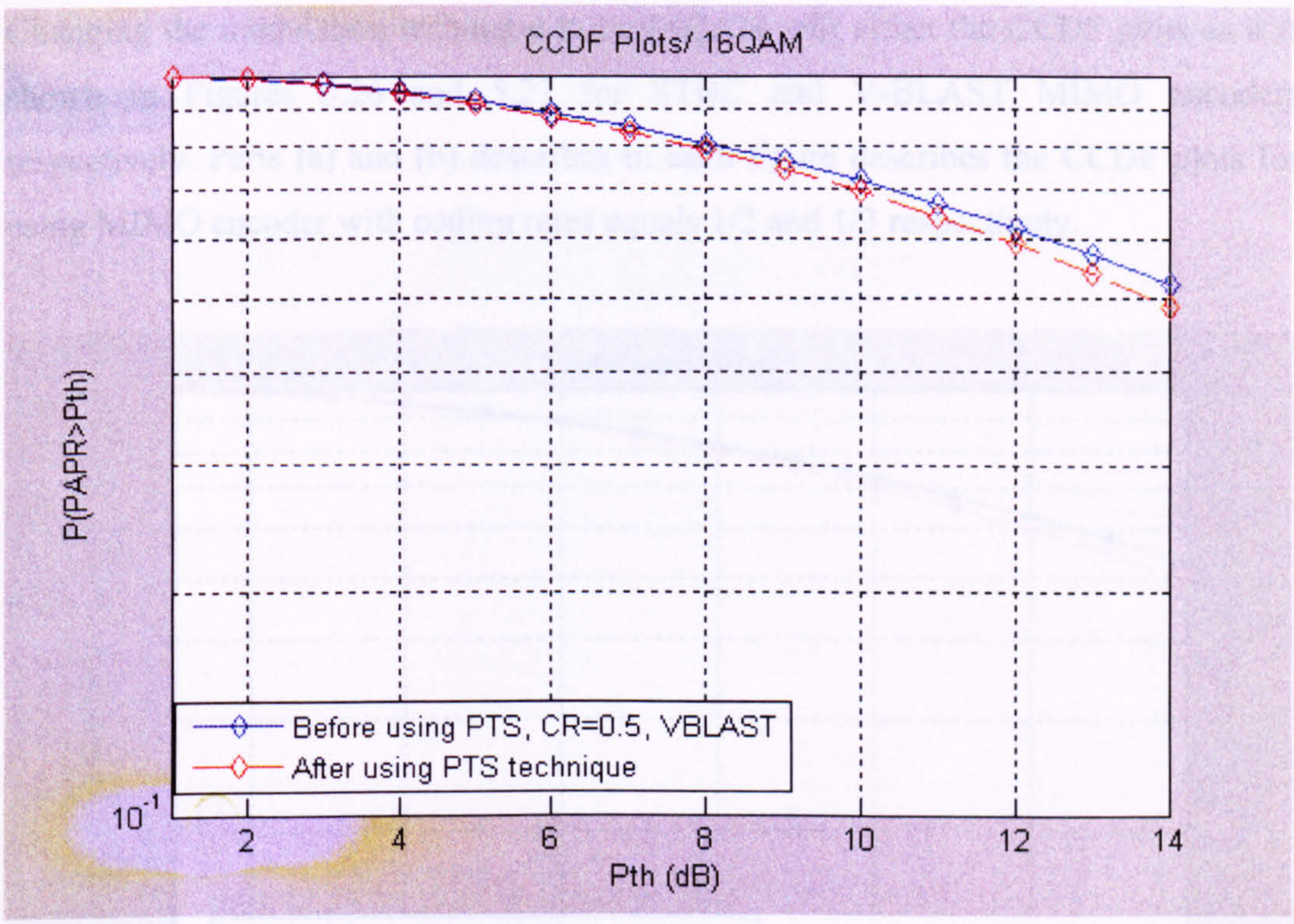


**Figure 5.25 (a)**

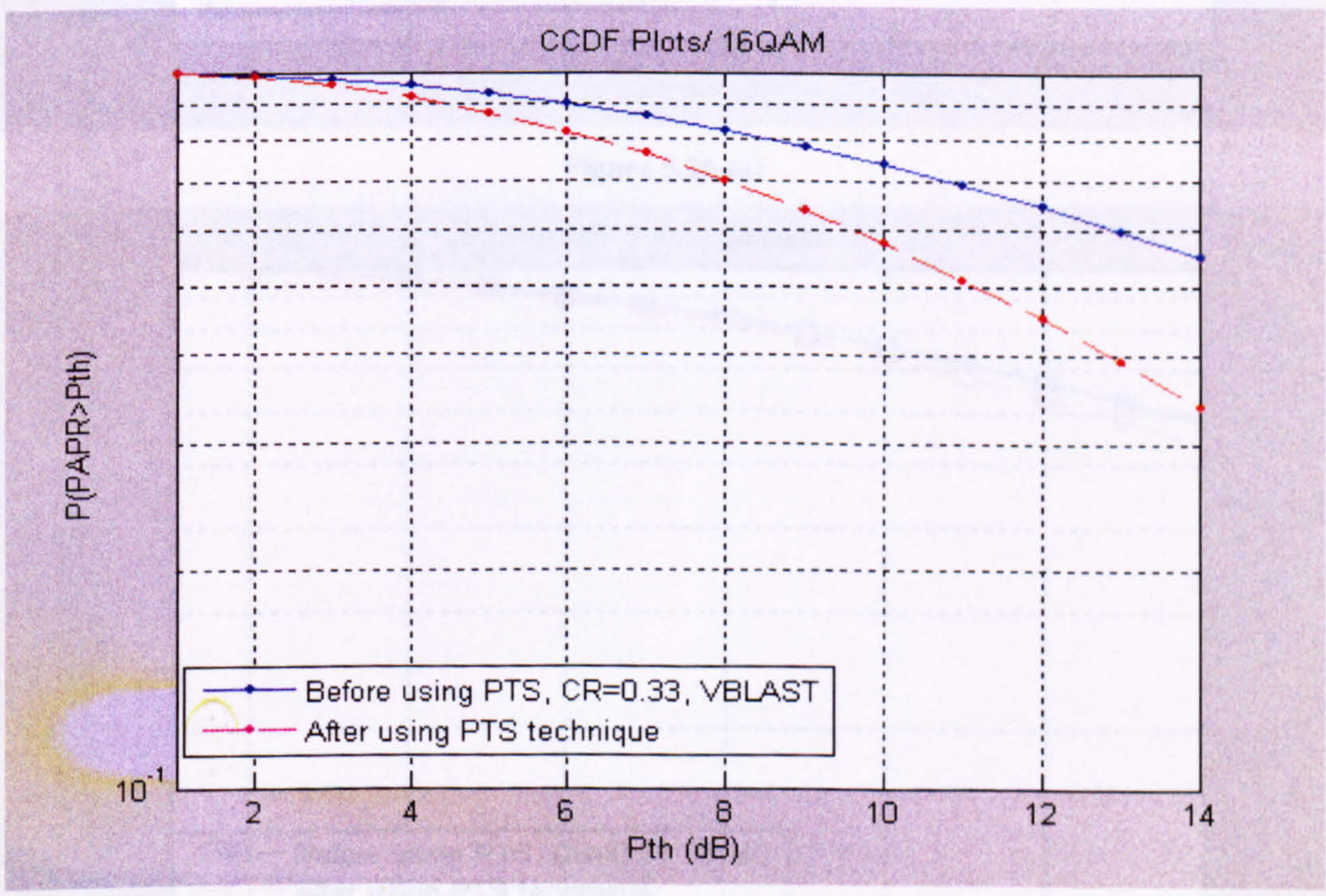


**Figure 5.25 (b)**

**Figure 5.25: The CCDF for using the PTS technique in a MIMO-OFDM system based on a 16-QAM modulation technique. (a) V-BLAST with coding rate 1/2 and (d) V-BLAST with coding rate 1/3**

Changing the modulation technique to be 64QAM will affect the CCDF plots as it is shown in Figures 5.26 and 5.27 for STBC and V-BLAST MIMO encoders respectively. Parts (a) and (b) describes in each figure describes the CCDF plots for using MIMO encoder with coding rates equals 1/2 and 1/3 respectively.

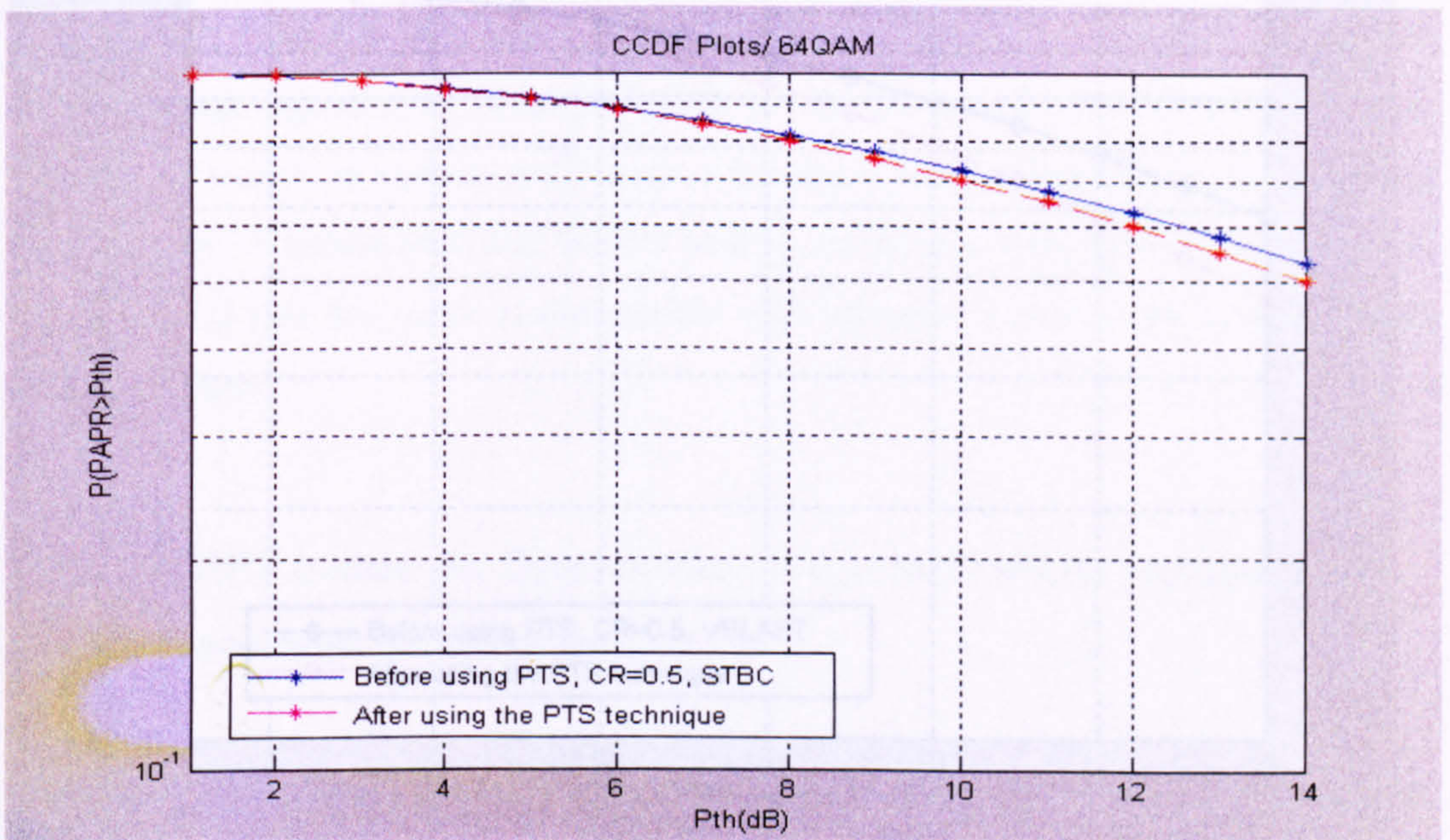


**Figure 5.26 (a)**

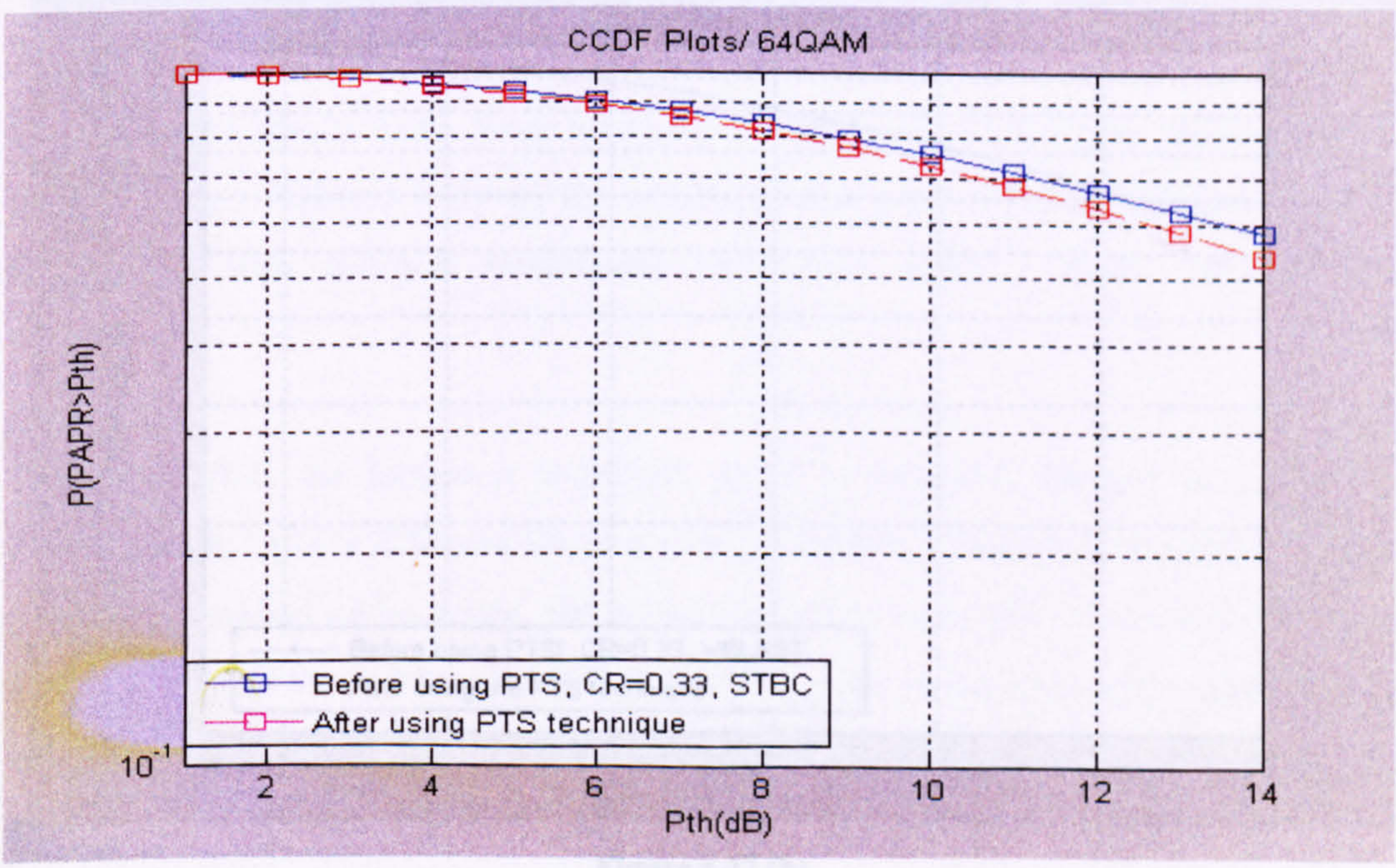


**Figure 5.26 (b)**

**Figure 5.26: The CCDF for using the PTS technique in a MIMO-OFDM system based on a 64-QAM modulation technique. (a) STBC with coding rate 1/2, (b) STBC with coding rate 1/3**

In Figure 5.26 part (a), the probability of the PAPR values that exceed the 4 dB threshold is reduced from $9.5x10^{-1}$ to $9.45x10^{-1}$. For coding rate equals 1/3, it is reduced from $9.57x10^{-1}$ to $9.5x10^{-1}$ in part (b).

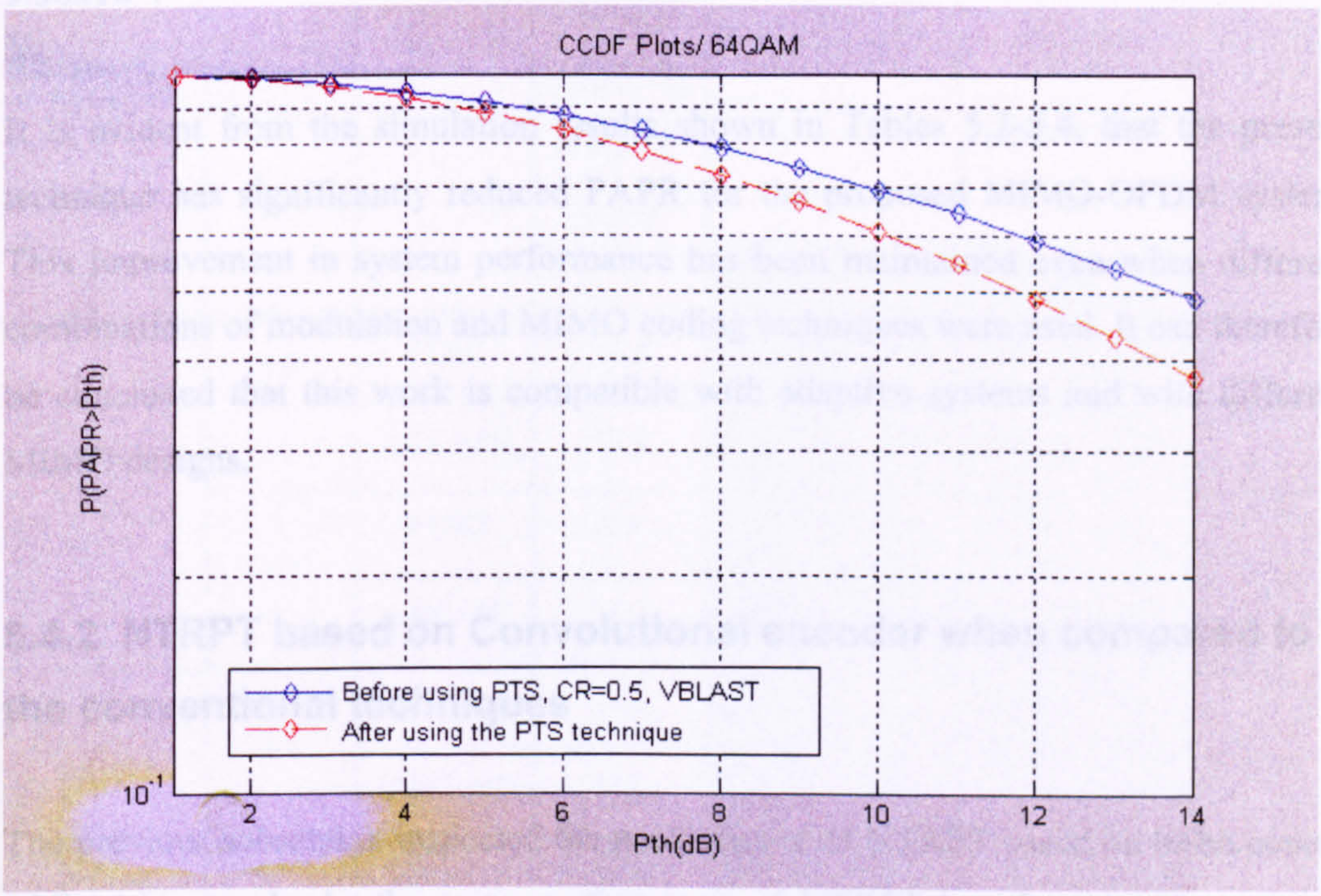


**Figure 5.27 (a)**

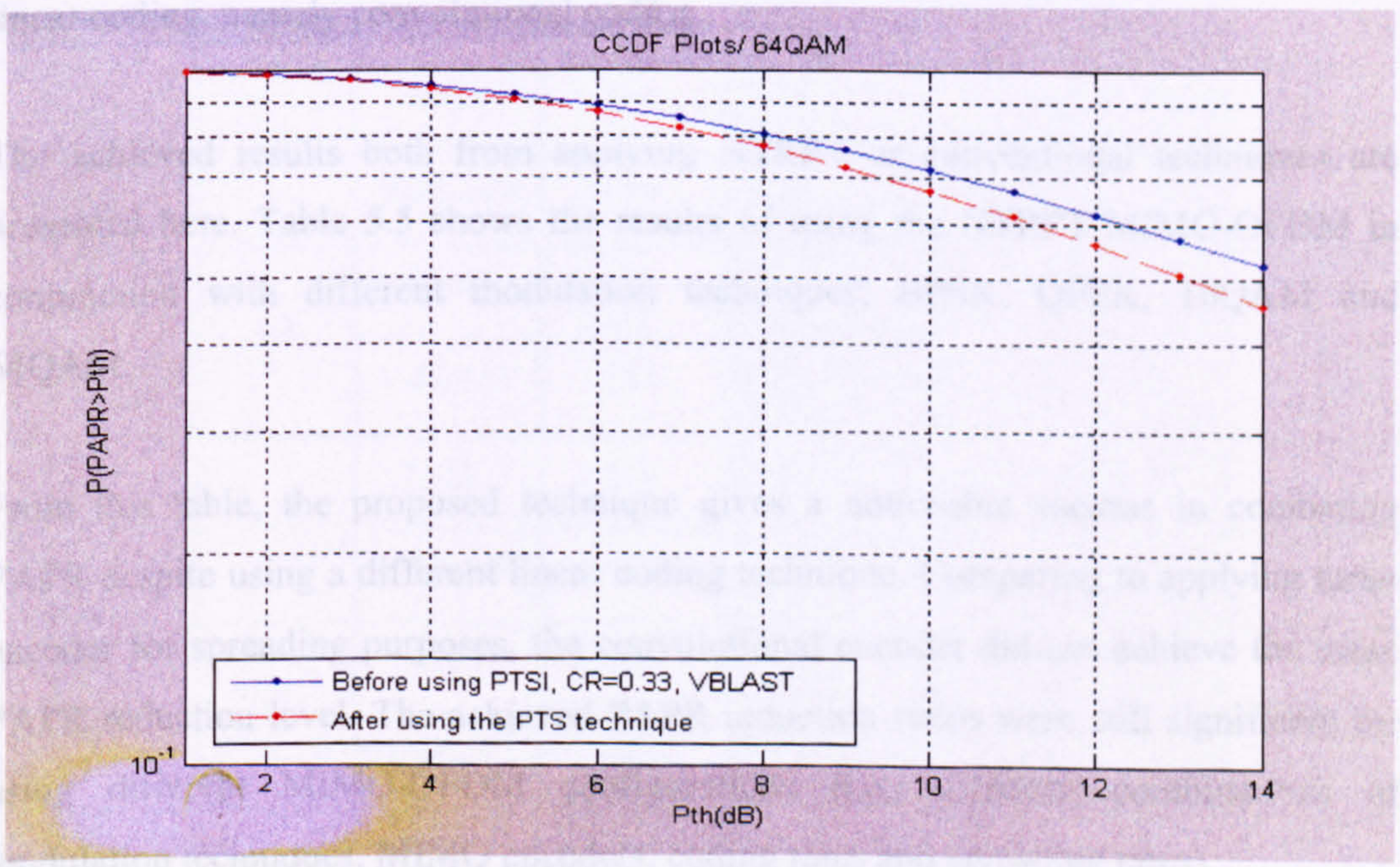


**Figure 5.27 (b)**

**Figure 5.27: The CCDF for using the PTS technique in a MIMO-OFDM system based on a 64-QAM modulation technique. (a) V-BLAST with coding rate 1/2 and (d) V-BLAST with coding rate 1/3**

In Figure 5.27 changing the used MIMO encoder to V-BLAST improves the probability from $9.43x10^{-1}$ to $9.23x10^{-1}$ in part (a) (i.e., the coding rate equals 1/2). Using coding rate equals 1/3 in part (b) reduces the probabilities from $9.48x10^{-1}$ to $9.38x10^{-1}$.

It is evident from the simulation results shown in Tables 5.2-5.4, that the present technique has significantly reduced PAPR for the proposed MIMO-OFDM system. This improvement in system performance has been maintained even when different combinations of modulation and MIMO coding techniques were used. It can therefore be concluded that this work is compatible with adaptive systems and with different MIMO designs.

### 5.4.2 NTRPT based on Convolutional encoder when compared to the conventional techniques

The previous subsection inspected the performance of NTRPT based on turbo coding while this one checks the same performance of NTRPT based on another type of linear coding, namely convolutional coding.

The achieved results both from applying NTRPT or conventional techniques are presented here. Table 5.5 shows the results of using the NTRPT-MIMO-OFDM in conjunction with different modulation techniques, BPSK, QPSK, 16QAM and 64QAM.

From this table, the proposed technique gives a noticeable success in combating PAPR despite using a different linear coding technique. Comparing to applying turbo encoder for spreading purposes, the convolutional encoder did not achieve the same PAPR reduction level. The achieved PAPR reduction ratios were still significant for using different MIMO-OFDM configurations (i.e., different combinations of modulation techniques, MIMO encoders, coding rates and spreading rates).

**Table 5.5: Applying the NTRPT to a MIMO-OFDM system based on convolutional encoder**

| Modulation tech. | Coding rate | MIMO encoding | PAPR before applying NTRPT (dB) | PAPR after applying NTRPT(dB) | | The reduction ratio (%) | | The improvement (%) |
|---|---|---|---|---|---|---|---|---|
| | | | | Spreading rate | | Spreading rate | | |
| | | | | 2 | 3 | 2 | 3 | |
| BPSK | 1/2 | STBC | 14.4 | 4.7 | 3.9 | 6.7 | 73 | 6 |
| | | V-BLAST | 10.9 | 3.4 | 2.9 | 69 | 72 | 3 |
| | 1/3 | STBC | 9.3 | 2.9 | 2.2 | 68 | 76 | 8 |
| | | V-BLAST | 13.1 | 3.7 | 2.4 | 72 | 82 | 10 |
| QPSK | 1/2 | STBC | 11.4 | 4.3 | 3.3 | 62 | 71 | 9 |
| | | V-BLAST | 12.6 | 2.9 | 2.5 | 77 | 80 | 3 |
| | 1/3 | STBC | 10.2 | 4.4 | 3.9 | 57 | 62 | 5 |
| | | V-BLAST | 11.8 | 2.6 | 1.8 | 78 | 85 | 7 |
| 16QAM | 1/2 | STBC | 9.3 | 1.9 | 1.4 | 80 | 85 | 5 |
| | | V-BLAST | 12.6 | 2.7 | 2.4 | 79 | 81 | 2 |
| | 1/3 | STBC | 9.6 | 1.8 | 1.5 | 81 | 84 | 3 |
| | | V-BLAST | 12.9 | 3.5 | 2.7 | 72 | 80 | 8 |
| 64QAM | 1/2 | STBC | 9.5 | 1.9 | 1.4 | 80 | 85 | 5 |
| | | V-BLAST | 13.7 | 4.1 | 3.8 | 70 | 72 | 2 |
| | 1/3 | STBC | 12.1 | 2.6 | 1.9 | 79 | 84 | 5 |
| | | V-BLAST | 11.2 | 2.1 | 1.8 | 81 | 84 | 3 |

In case of using a BPSK modulation technique, PAPR reduction ratio reaches 82% and 72% when using a spreading rate of 3 and 2 respectively. These ratios have a little

improvement when the modulation technique is changed to 64QAM, which they reach the 85% for spreading rate equals 3 and 81% when the used spreading rate was 2.

Moreover, increasing the spreading rate has the same effect in increasing the achieved PAPR reduction as the same as for using turbo encoder. This is true for both situations; BPSK and 64QAM. The improvement in the reduction ratio when the spreading rate is changed from 2 to 3 equals 10% and 5% when using BPSK and 64QAM modulation techniques respectively.

For clarity, the CCDF plots for the achieved results in the previous table are displayed. Figures 5.28-5.35 show the calculated CCDF for the achieved results of using NTRPT-MIMO-OFDM based on BPSK, QPSK, 16QAM and 64QAM respectively.

These Figures are divided into two parts each of which compares the CCDF plots for different system parameters. Parts (a) and (b), the CCDF plots are described for using different coding rates equals 1/2 and 1/3 respectively.

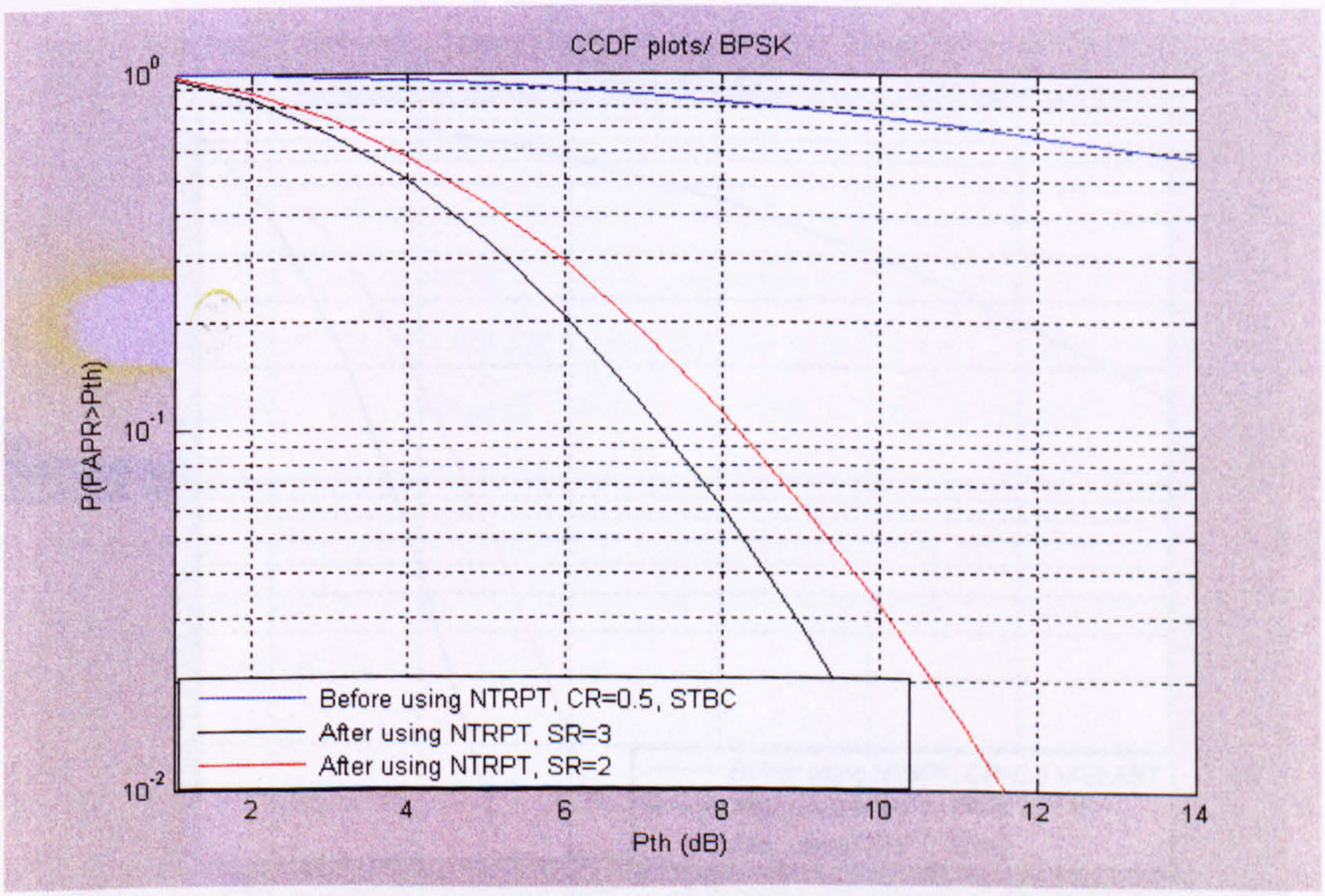


**Figure 5.28 (a)**

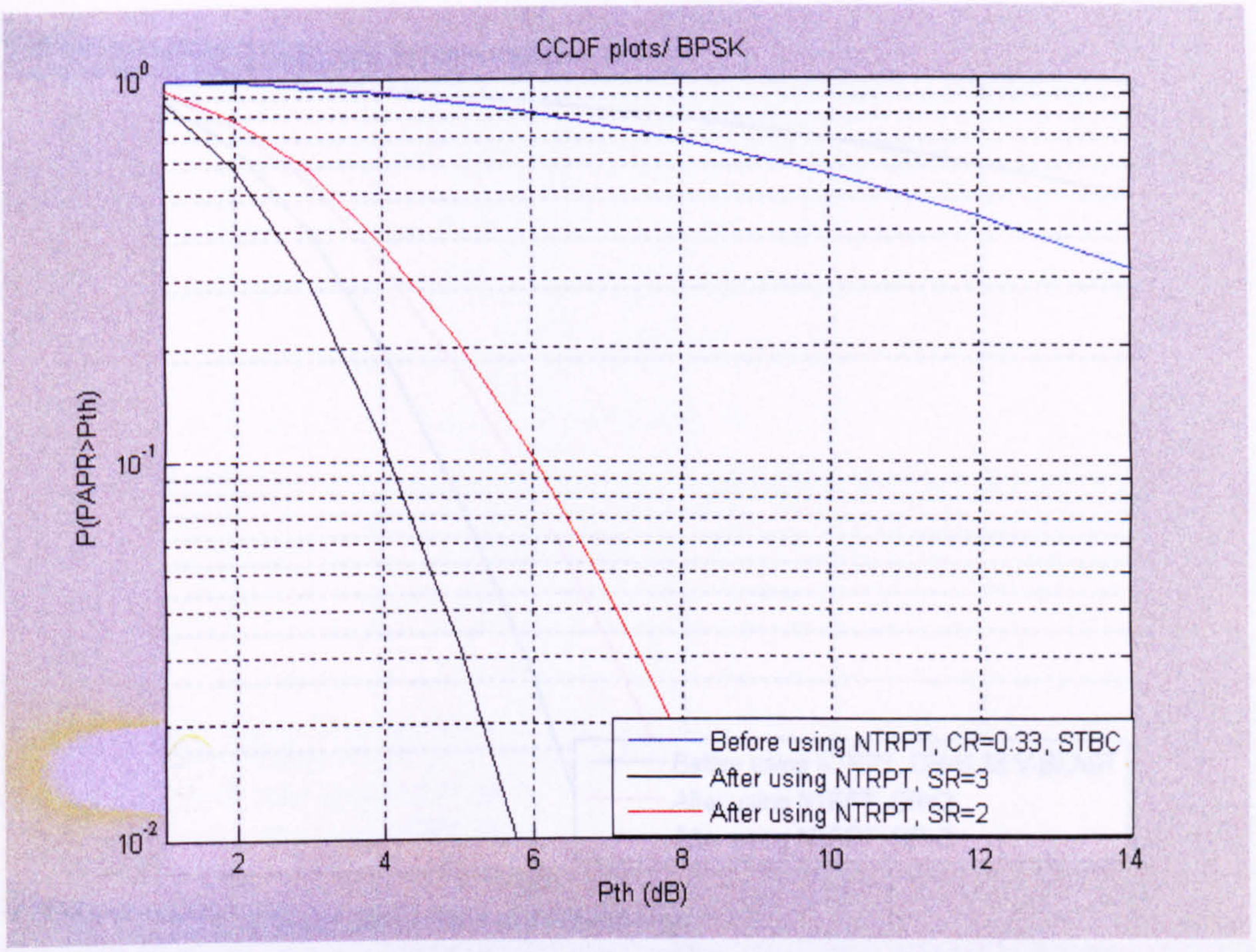


**Figure 5.28 (b)**

**Figure 5.28: The CCDF for the NTRPT-MIMO-OFDM system based on a BPSK modulation technique. (a) STBC with coding rate 1/2, (b) STBC with coding rate 1/3**

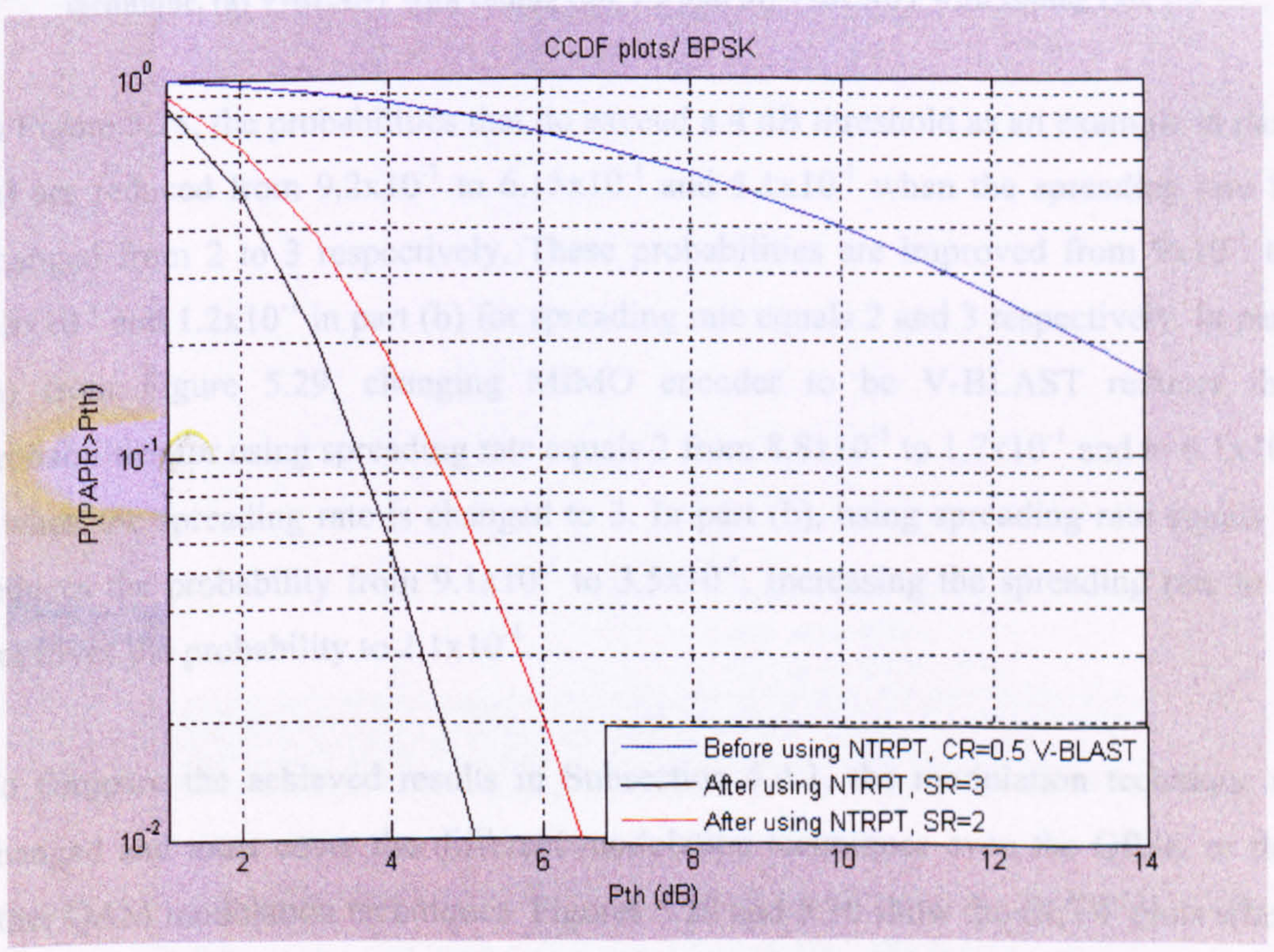


**Figure 5.29 (a)**

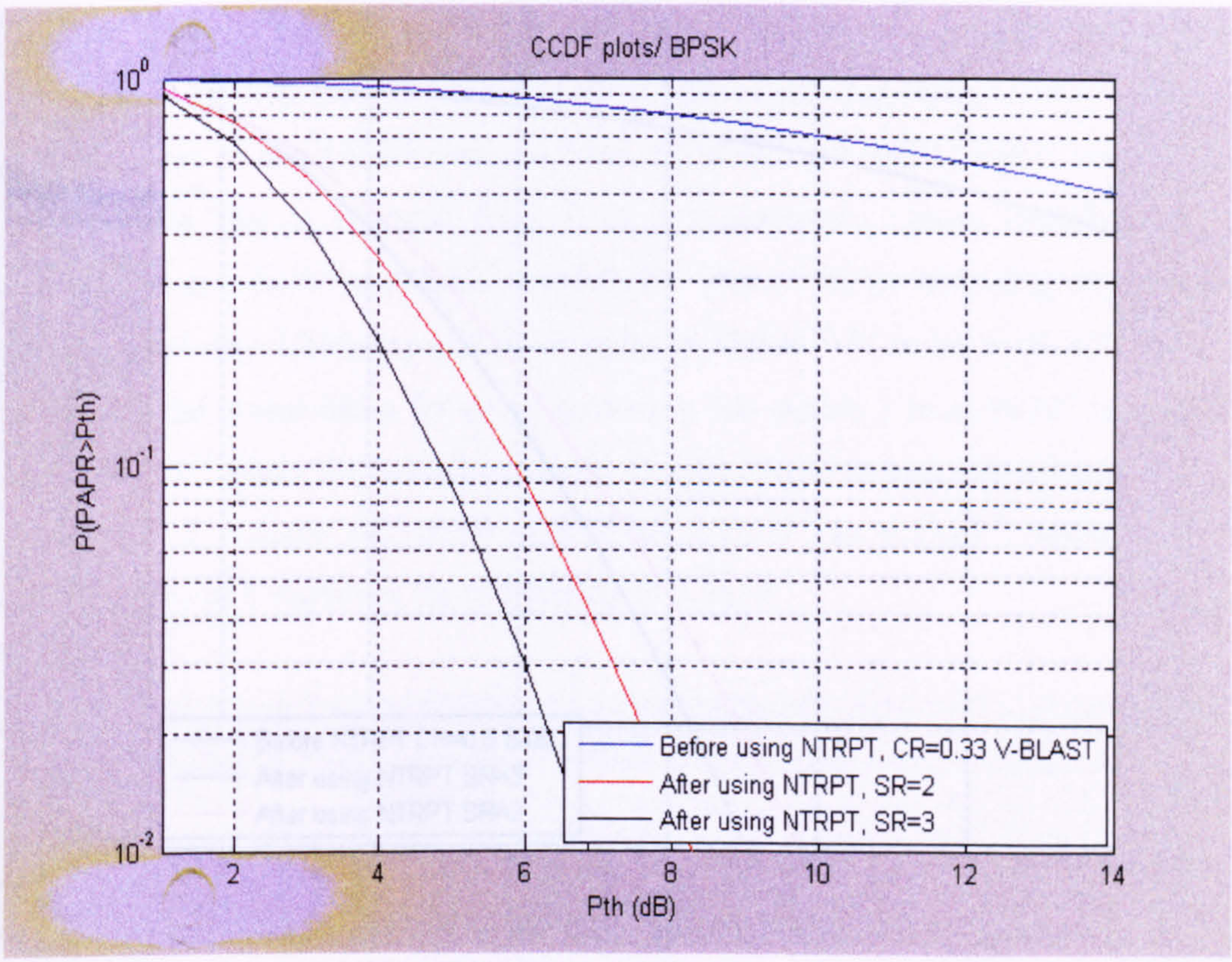


**Figure 5.29 (b)**

**Figure 5.29: The CCDF for the NTRPT-MIMO-OFDM system based on a BPSK modulation technique. (a) V-BLAST with coding rate 1/2 and (b) V-BLAST with coding rate 1/3**

In Figure 5.28, the probabilities that do exceed a 4 dB threshold as an example in part (a) are reduced from $9.2x10^{-1}$ to $6.15x10^{-1}$ and $5.1x10^{-1}$ when the spreading rate is changed from 2 to 3 respectively. These probabilities are improved from $9x10^{-1}$ to $3.8x10^{-1}$ and $1.2x10^{-1}$ in part (b) for spreading rate equals 2 and 3 respectively. In part (a) from Figure 5.29, changing MIMO encoder to be V-BLAST reduces the probabilities for using spreading rate equals 2 from $8.8x10^{-1}$ to $1.7x10^{-1}$ and to $6.1x10^{-2}$ when the spreading rate is changed to 3. In part (b), using spreading rate equals 2 reduces the probability from $9.1x10^{-1}$ to $3.5x10^{-1}$. Increasing the spreading rate to 3 improves the probability to $2.1x10^{-1}$.

To compare the achieved results in Subsection 5.4.1, the modulation technique is changed and must cover the different modulation techniques even the QPSK or the other QAM modulation techniques. Figures 5.29 and 5.30 show the CCDF plots when the modulation technique is changed from BPSK to QPSK.

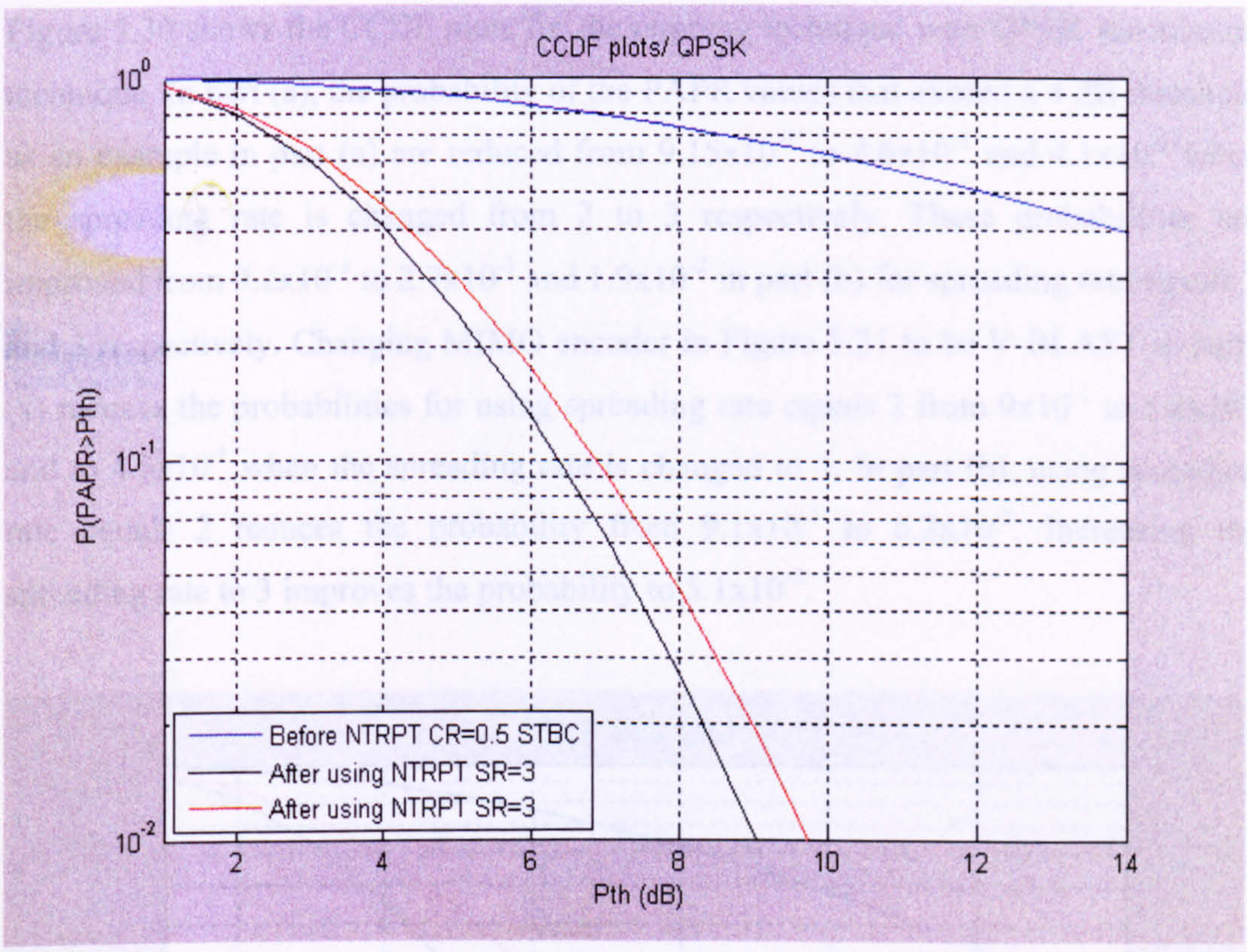


**Figure 5.30 (a)**

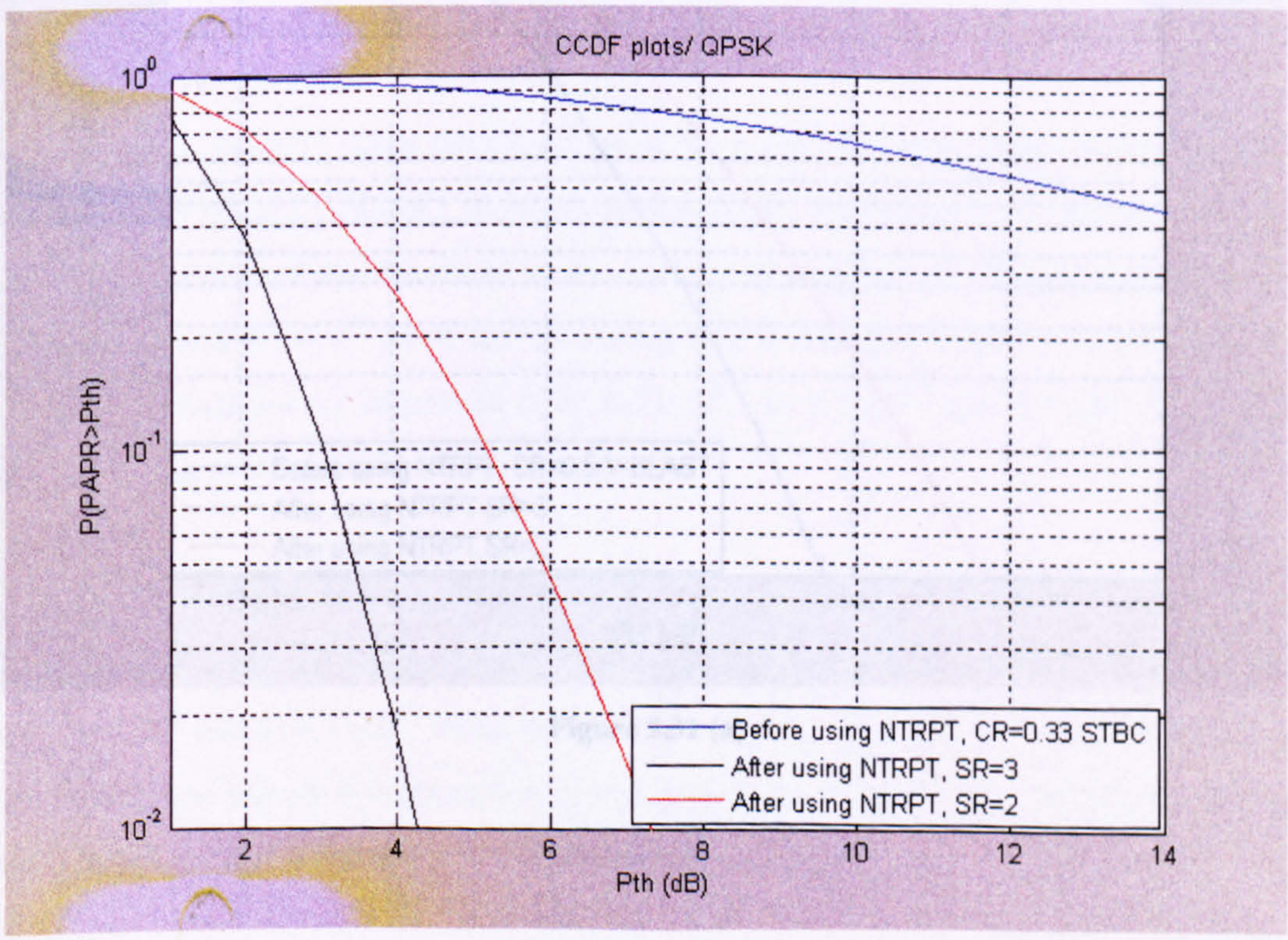


**Figure 5.30 (b)**

**Figure 5.30: The CCDF for the NTRPT-MIMO-OFDM system based on a QPSK modulation technique. (a) STBC with coding rate 1/2, (b) STBC with coding rate 1/3**

Figure 5.30 shows the CCDF plots for the clipping technique with QPSK modulation technique. In part (a), the probability of the PAPR values that exceed a 4 dB threshold as an example in part (a) are reduced from $9.15x10^{-1}$ to $4.6x10^{-1}$ and $4.1x10^{-1}$ when the spreading rate is changed from 2 to 3 respectively. These probabilities are improved from $9.2x10^{-1}$ to $2.7x10^{-1}$ and $1.9x10^{-2}$ in part (b) for spreading rate equals 2 and 3 respectively. Changing MIMO encoder in Figure 5.31 to be V-BLAST in parts (a) reduces the probabilities for using spreading rate equals 2 from $9x10^{-1}$ to $5.8x10^{-1}$ and to $4.5x10^{-1}$ when the spreading rate is changed to 3. In part (b), using spreading rate equals 2 reduces the probability from $9.1x10^{-1}$ to $6.2x10^{-2}$. Increasing the spreading rate to 3 improves the probability to $5.1x10^{-2}$.

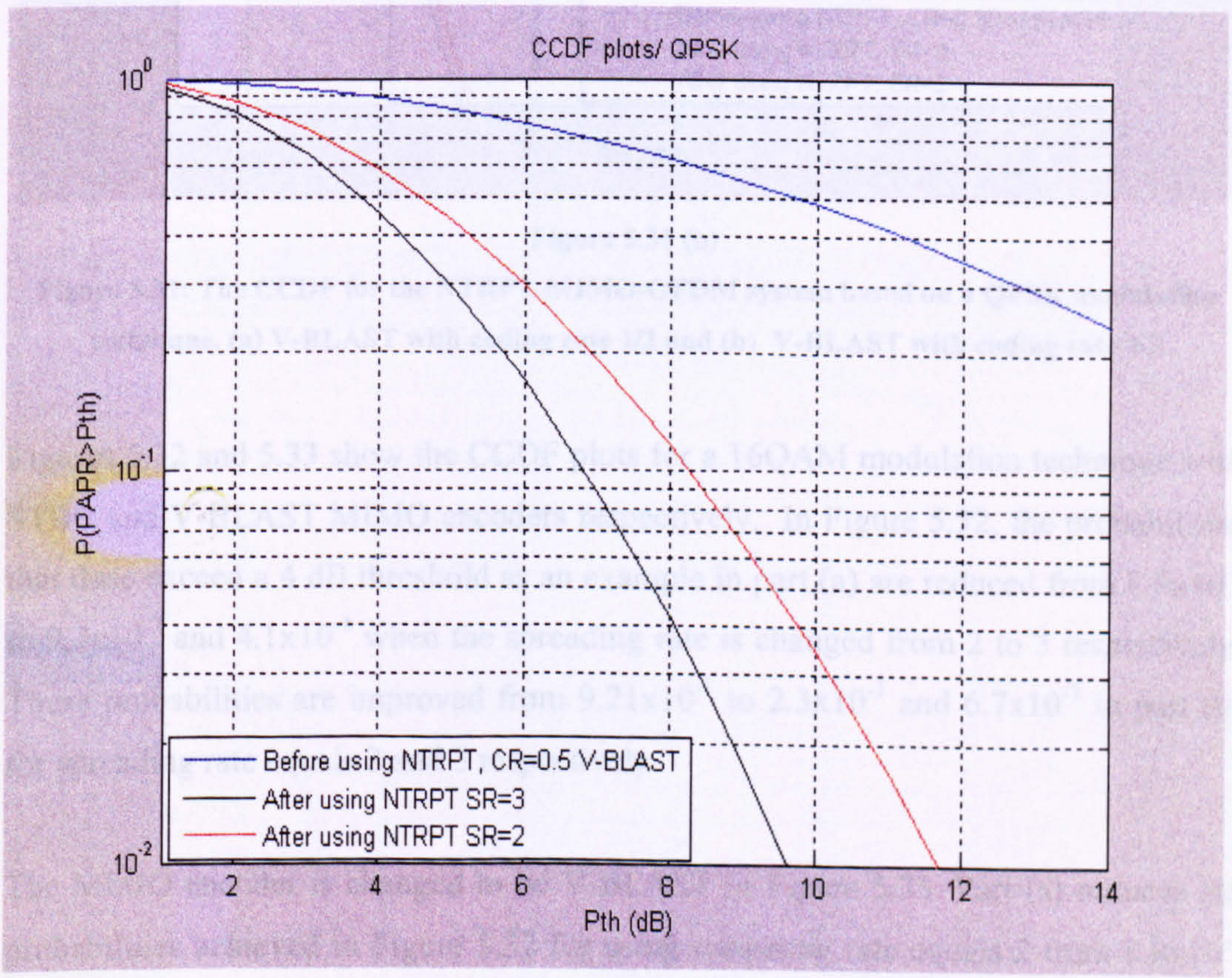


**Figure 5.31 (a)**

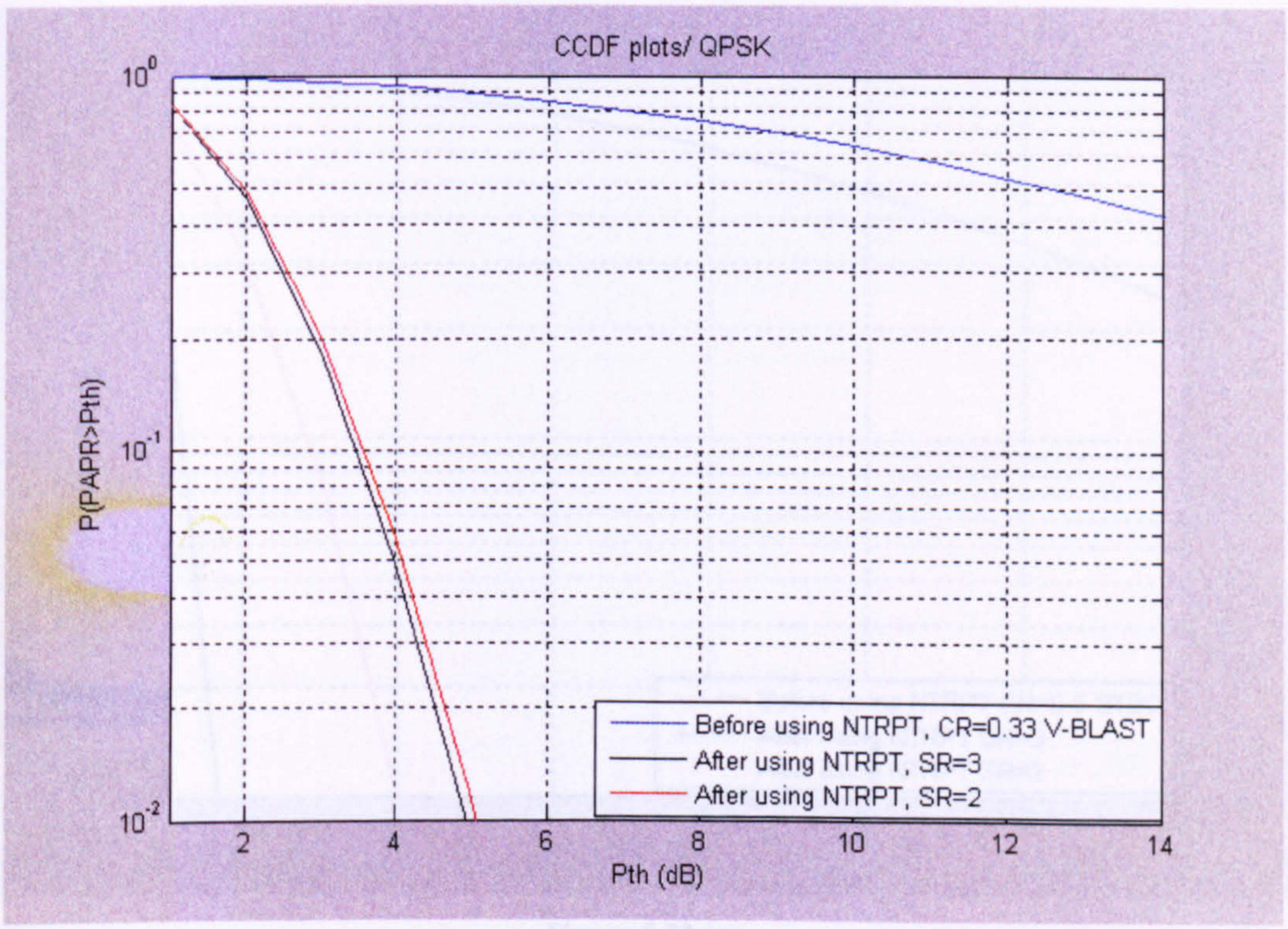


**Figure 5.31 (b)**

**Figure 5.31: The CCDF for the NTRPT-MIMO-OFDM system based on a QPSK modulation technique. (a) V-BLAST with coding rate 1/2 and (b) V-BLAST with coding rate 1/3**

Figures 5.32 and 5.33 show the CCDF plots for a 16QAM modulation technique with STBC and V-BLAST MIMO encoders respectively. In Figure 5.32, the probabilities that dose exceed a 4 dB threshold as an example in part (a) are reduced from $8.9x10^{-1}$ to $9.7x10^{-2}$ and $4.1x10^{-4}$ when the spreading rate is changed from 2 to 3 respectively. These probabilities are improved from $9.21x10^{-1}$ to $2.3x10^{-1}$ and $6.7x10^{-2}$ in part (b) for spreading rate equals 2 and 3 respectively.

The MIMO encoder is changed to be V-BLAST in Figure 5.33. Part (a) reduces the probabilities achieved in Figure 5.32 for using spreading rate equals 2 from $8.8x10^{-1}$ to $2.25x10^{-2}$ and to $4.3x10^{-5}$ when the spreading rate is changed to 3. In part (b), using spreading rate equals 2 reduces the probability from $9.1x10^{-1}$ to $3.1x10^{-1}$. Increasing the spreading rate to 3 improves the probability to $2.8x10^{-1}$.

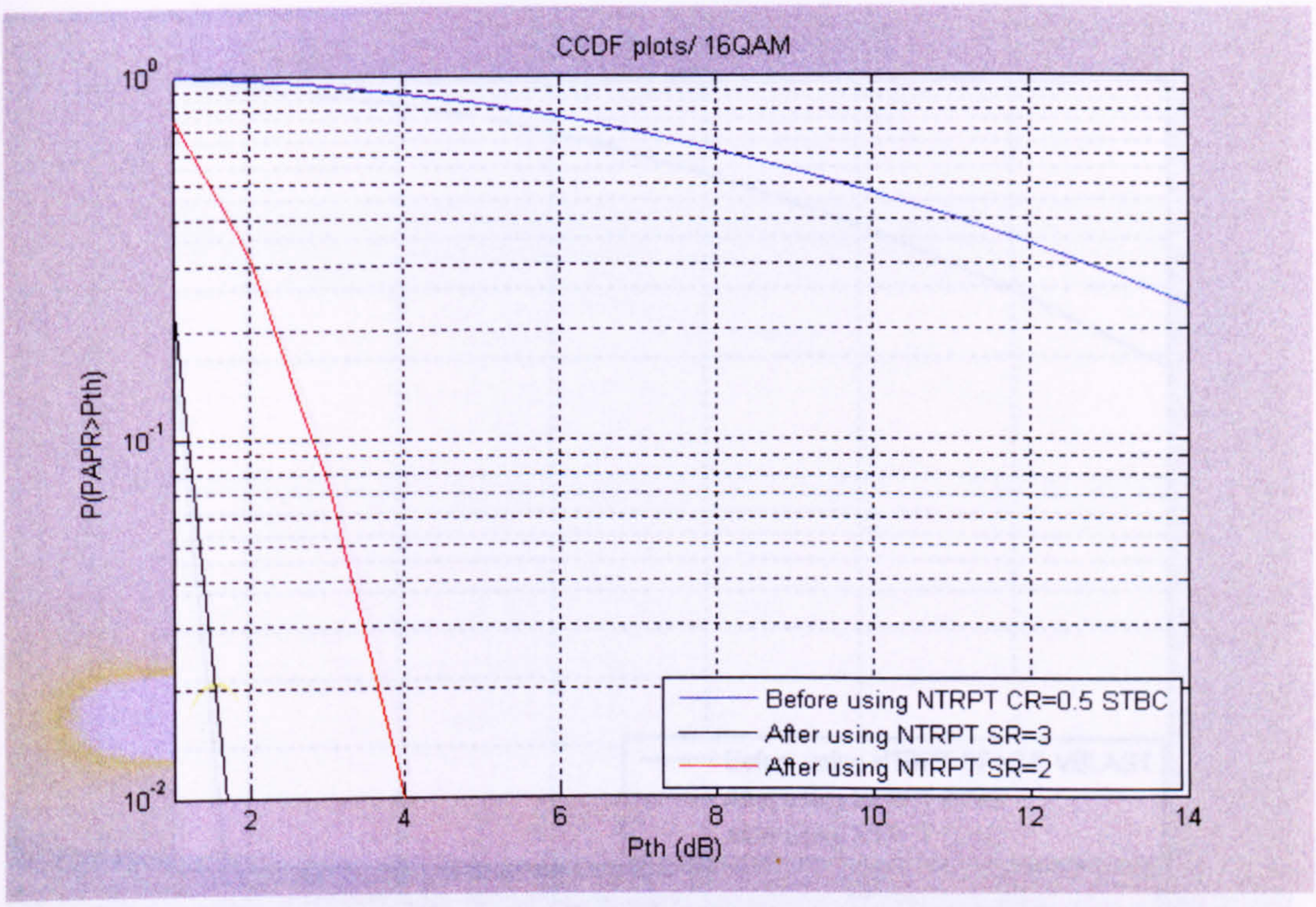


**Figure 5.32 (a)**

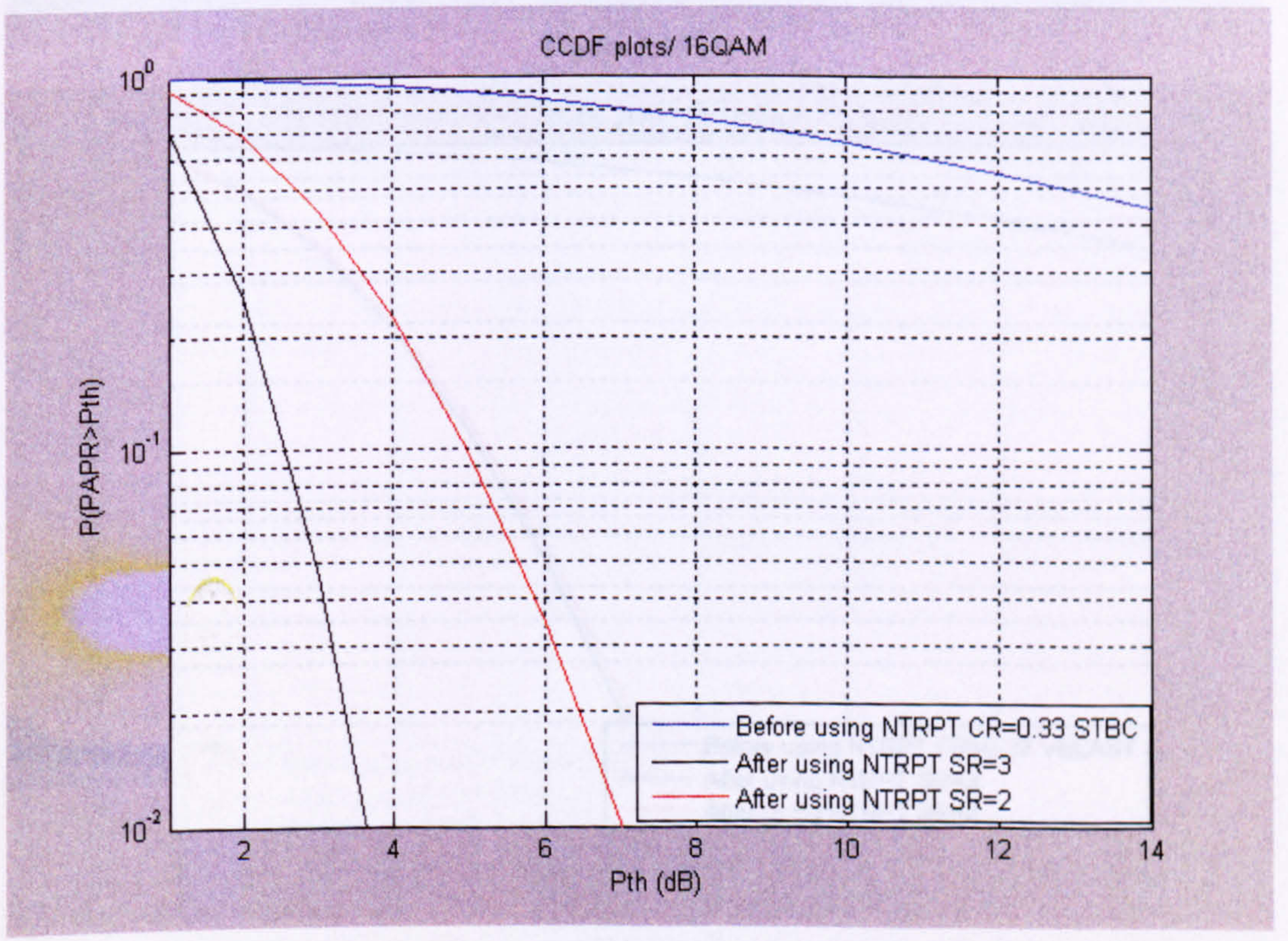


**Figure 5.32 (b)**

**Figure 5.32: The CCDF for the NTRPT-MIMO-OFDM system based on a 16QAM modulation technique. (a) STBC with coding rate 1/2, (b) STBC with coding rate 1/3**

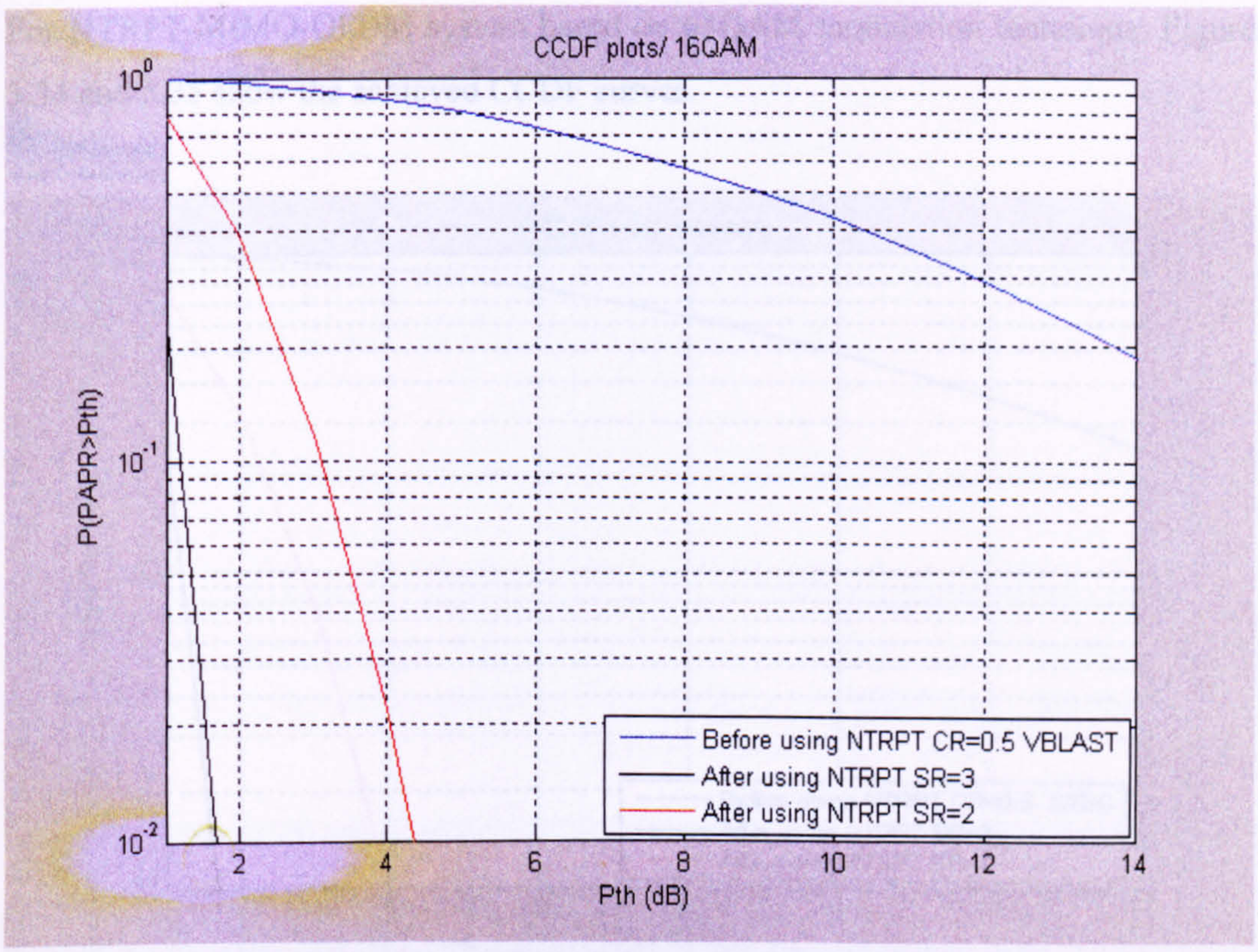


**Figure 5.33 (a)**




**Figure 5.33 (b)**

**Figure 5.33: The CCDF for the NTRPT-MIMO-OFDM system based on a 16QAM modulation technique. (a) V-BLAST with coding rate 1/2 and (d) V-BLAST with coding rate 1/3**

For NTRPT-MIMO-OFDM system based on 64QAM modulation technique, Figures 5.34 and 5.35 show the achieved CCDF curves.

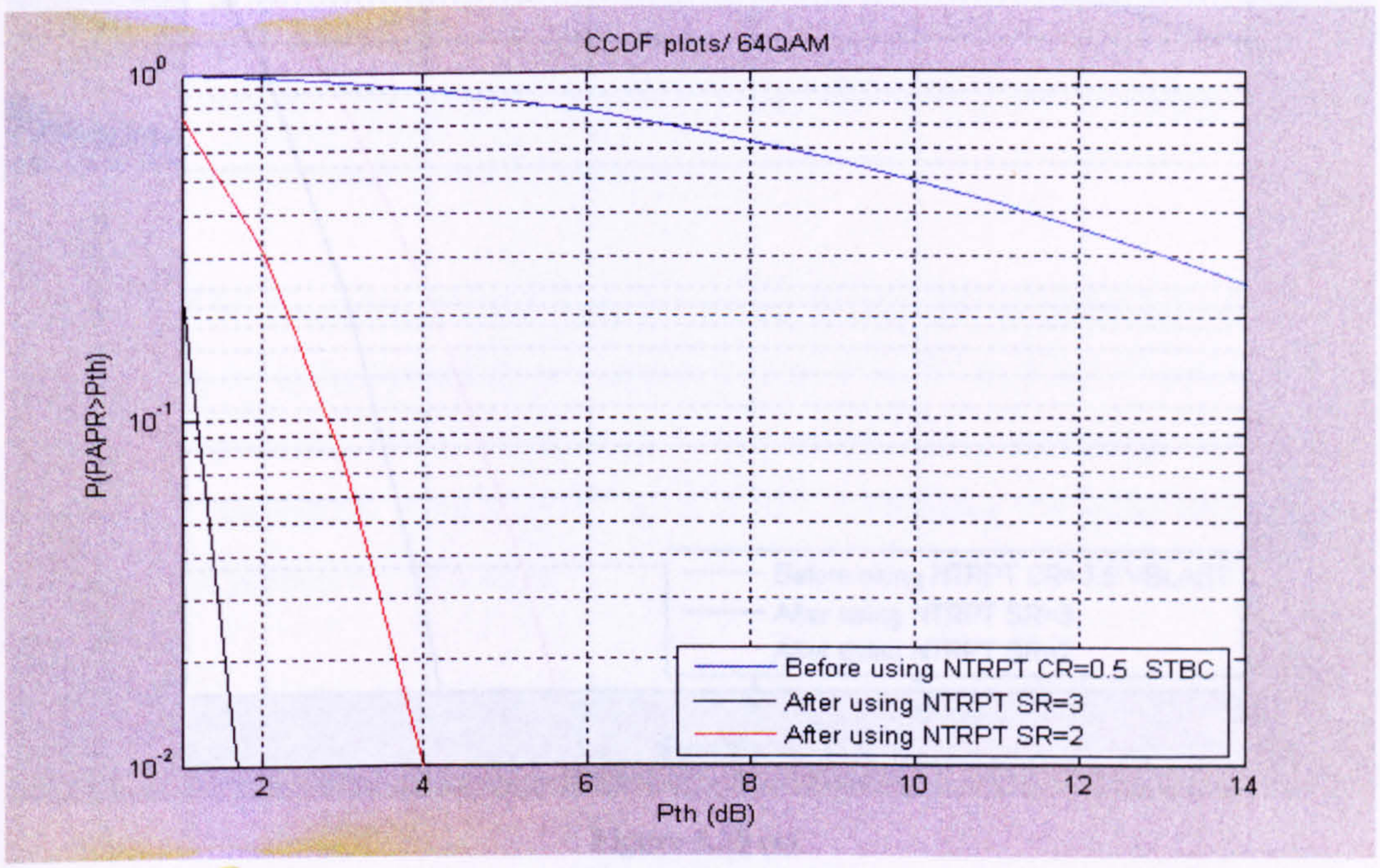


**Figure 5.34 (a)**

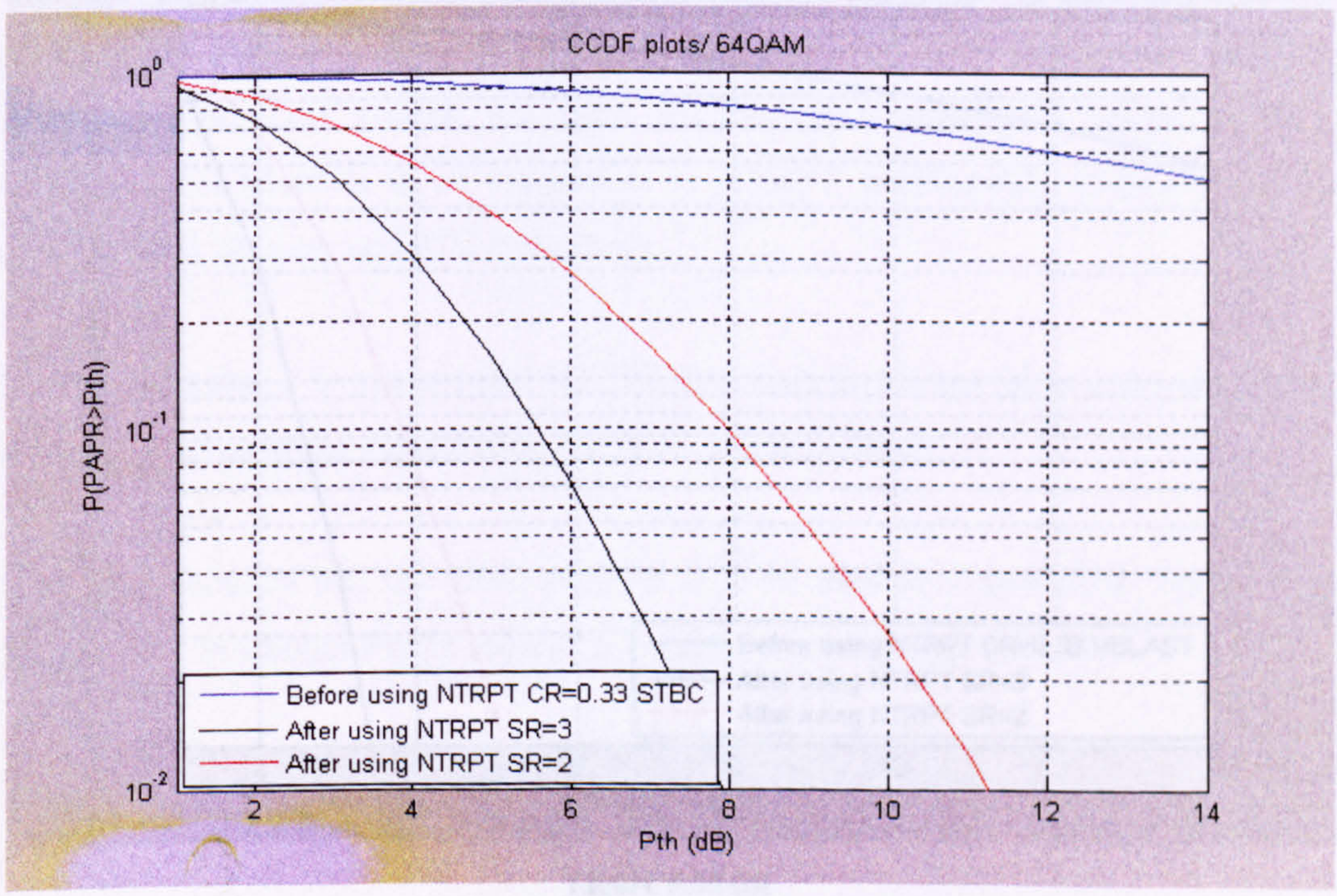


**Figure 5.34 (b)**

**Figure 5.34: The CCDF for the NTRPT-MIMO-OFDM system based on a 64QAM modulation technique. (a) STBC with coding rate 1/2, (b) STBC with coding rate 1/3**

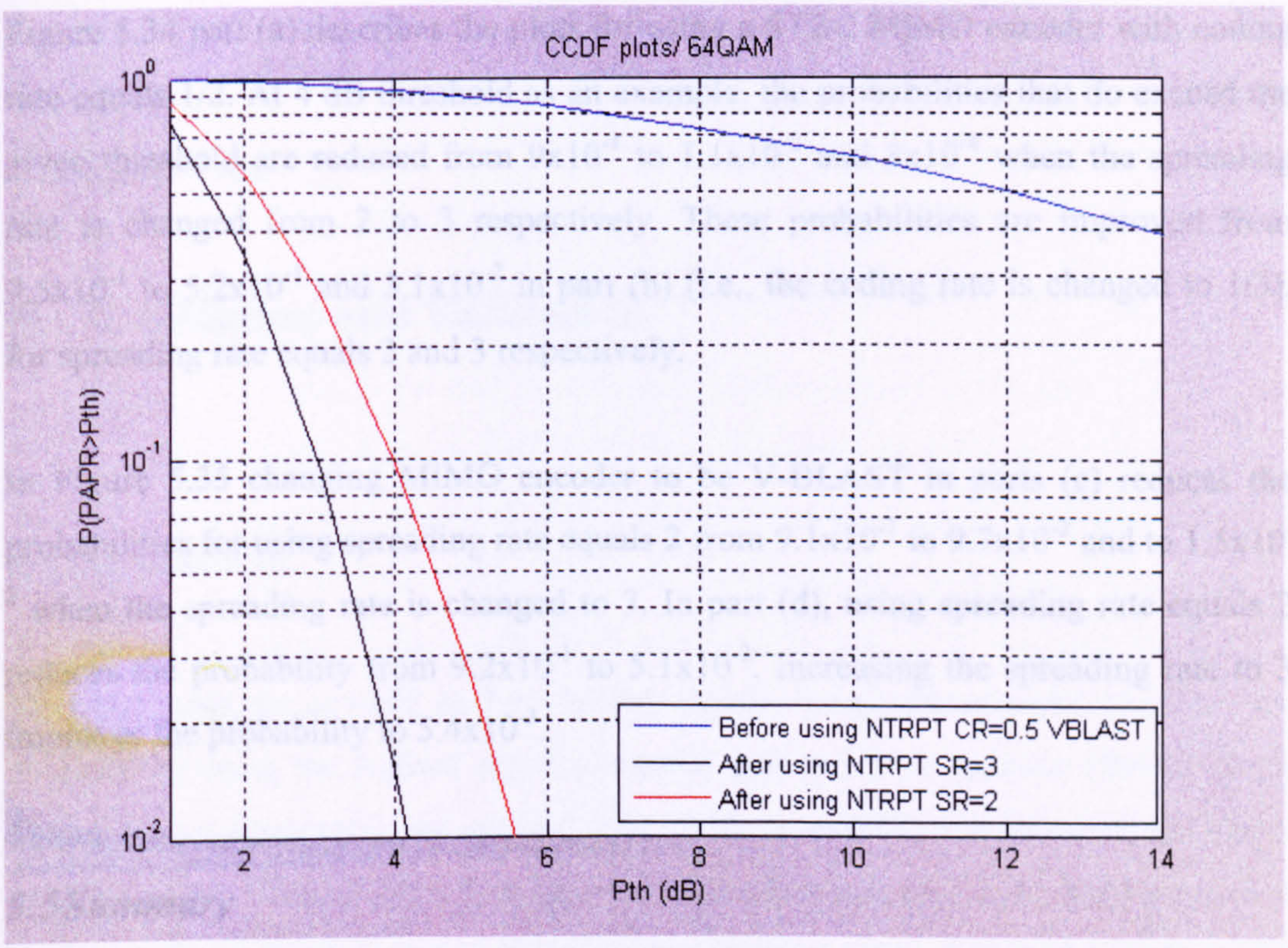


**Figure 5.35 (a)**

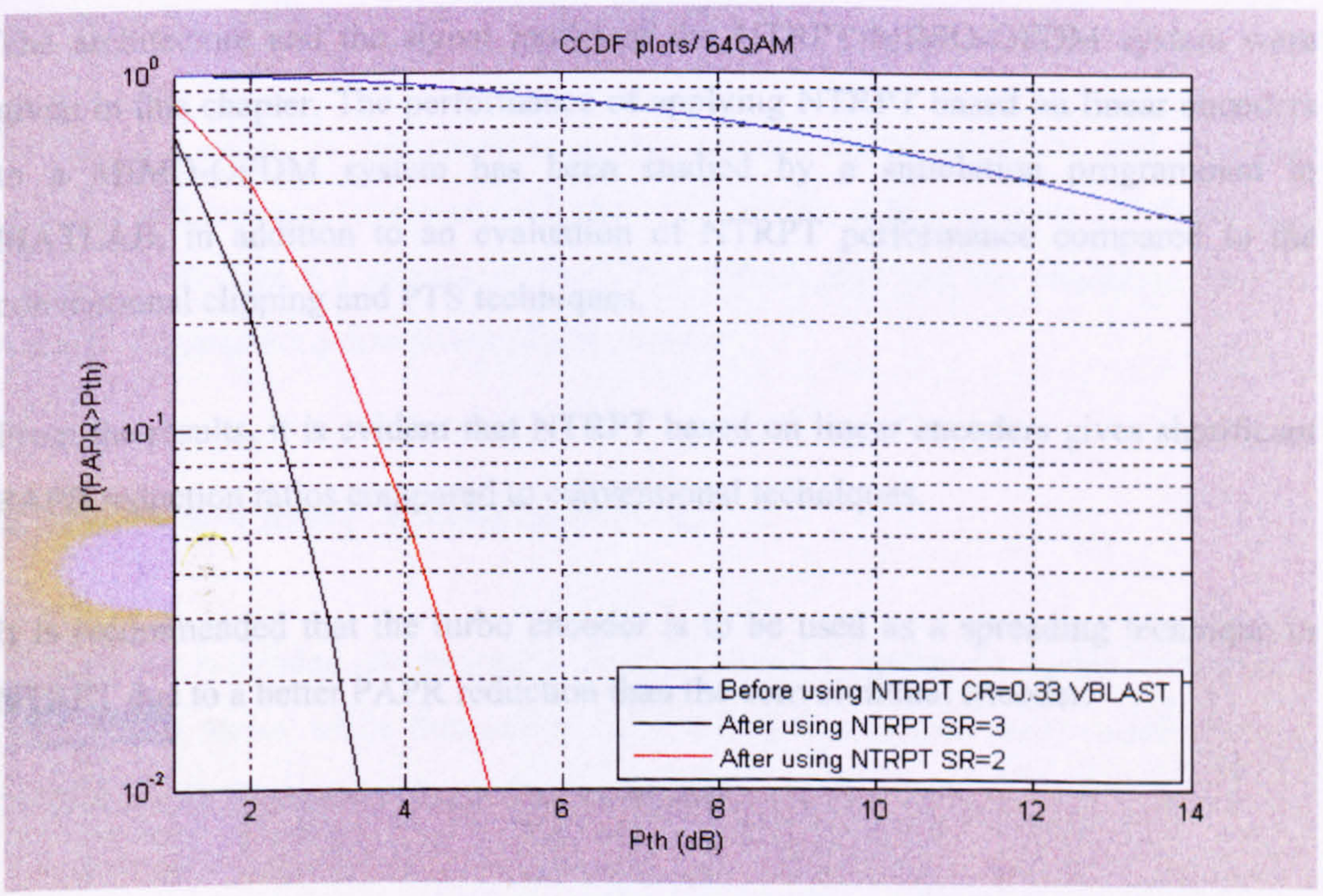


**Figure 5.35 (b)**

**Figure 5.35: The CCDF for the NTRPT-MIMO-OFDM system based on a 64QAM modulation technique. (a) V-BLAST with coding rate 1/2 and (d) V-BLAST with coding rate 1/3**

Figure 5.34 part (a) describes the plots for using a STBC MIMO encoder with coding rate equals 1/2. At 4 dB threshold as an example, the probabilities that do exceed the given threshold are reduced from $9x10^{-1}$ to $1.1x10^{-2}$ and $3x10^{-4}$ when the spreading rate is changed from 2 to 3 respectively. These probabilities are improved from $9.5x10^{-1}$ to $5.2x10^{-1}$ and $3.1x10^{-2}$ in part (b) (i.e., the coding rate is changed to 1/3), for spreading rate equals 2 and 3 respectively.

In Figure 5.35 changing MIMO encoder to be V-BLAST in parts (c) reduces the probabilities for using spreading rate equals 2 from $9.1x10^{-1}$ to $9.7x10^{-2}$ and to $1.5x10^{-2}$ when the spreading rate is changed to 3. In part (d), using spreading rate equals 2 reduces the probability from $9.2x10^{-1}$ to $5.1x10^{-2}$. Increasing the spreading rate to 3 improves the probability to $5.4x10^{-3}$.

## *5.5Summary*

The architecture and the signal model of the NTRPT-MIMO-OFDM system were given in this chapter. The performance of applying NTRPT based on linear encoders to a MIMO-OFDM system has been studied by a simulation programmed in MATLAB, in addition to an evaluation of NTRPT performance compared to the conventional clipping and PTS techniques.

From the results, it is evident that NTRPT based on linear encoders gives significant PAPR reduction ratios compared to conventional techniques.

It is recommended that the turbo encoder is to be used as a spreading technique in NTRPT due to a better PAPR reduction than the convolutional encoder.

# Chapter Six

# 6. Evaluation and Validation

## *6.1Introduction*

Two test cases are covered in this chapter. Firstly, the proposed technique's results, obtained by using the Agilent signal generator and spectrum analyser (89600 Series Vector Signal Analysers), are verified. The verification process is based on the Signal Studio Toolkit. Secondly, the proposed technique was designed to be implemented to a Xilinx Field Programmable Gate Array (FPGA) card for demonstrating and validating the results achieved from the simulation.

Section 6.2 gives an introduction to the Agilent signal generator and spectrum analyser and presents comparisons between the results achieved there and those from Chapter 4. Section 6.3 introduces the Xilinx FPGA card and the validation process. Section 6.4 presents a discussion of this chapter.

## *6.2Validation using Agilent technology*

This section is divided into two parts. Subsection 6.2.1 introduces Agilent technology; VSA 89600 series, while Subsection 6.2.2 shows simulation results based on those achieved with the Agilent Signal Studio Toolkit.

### 6.2.1 Introduction

The Agilent Technologies 89600 Series Vector Signal Analysers (VSAs) are tools for research, product development, manufacturing and field-testing. They can analyse a

wide variety of standard and non-standard signal formats. Twenty-three standard-signal presets cover the Global System for Mobile Communications (GSM), Enhanced Data GSM Environment (EDGE), WCDMA, 802.11a, 802.11b and others. Also, the analysis is supported through the use of statistical tools likes the CCDF and the pdf to characterise the noise-like behaviour of communications signals.

The signal studio toolkit for 802.11 WLAN provides a powerful signal creation tool for testing 802.11a/b/g transceivers. WLAN waveforms can easily be created on your PC with a graphical user interface. The generated WLAN signals can be downloaded to be analysed by the VSA signal analyser. Moreover, any MATLAB signal can be downloaded by using the Signal Studio Toolkit application. For more information, the reader can refer to the Agilent company website at www.Agilent.com.

### 6.2.2 Simulation Results and discussion

By making use of the signal studio toolkit application, the modulated signal generated using MATLAB was loaded to be analysed by the VSA and the compared to the signals generated using the toolkit for 802.11 WLAN.

The following figures show the CCDF plots for a MIMO-OFDM system based on reference signals, which is analysed by the VSA. These figures show the result of using a BPSK, QPSK, 16QAM and 64QAM modulation technique; STBC and V-BLAST MIMO encoders; two different spreading rates, 2 and 3; and a coding rate equal to ½.

Figures 6.1-6.4 is divided into two parts, the result of the CCDF plots of the MIMO-OFDM signals with V-BLAST encoder and CCDF plots of changing the MIMO encoder to be STBC.

These two figures show that the validation of the simulation is achieved, since the simulated and analysed signals were found in the same regions. This is achieved from

the calculation the standard deviation between these plots. The standard deviation results can be shown in Table 6.1.

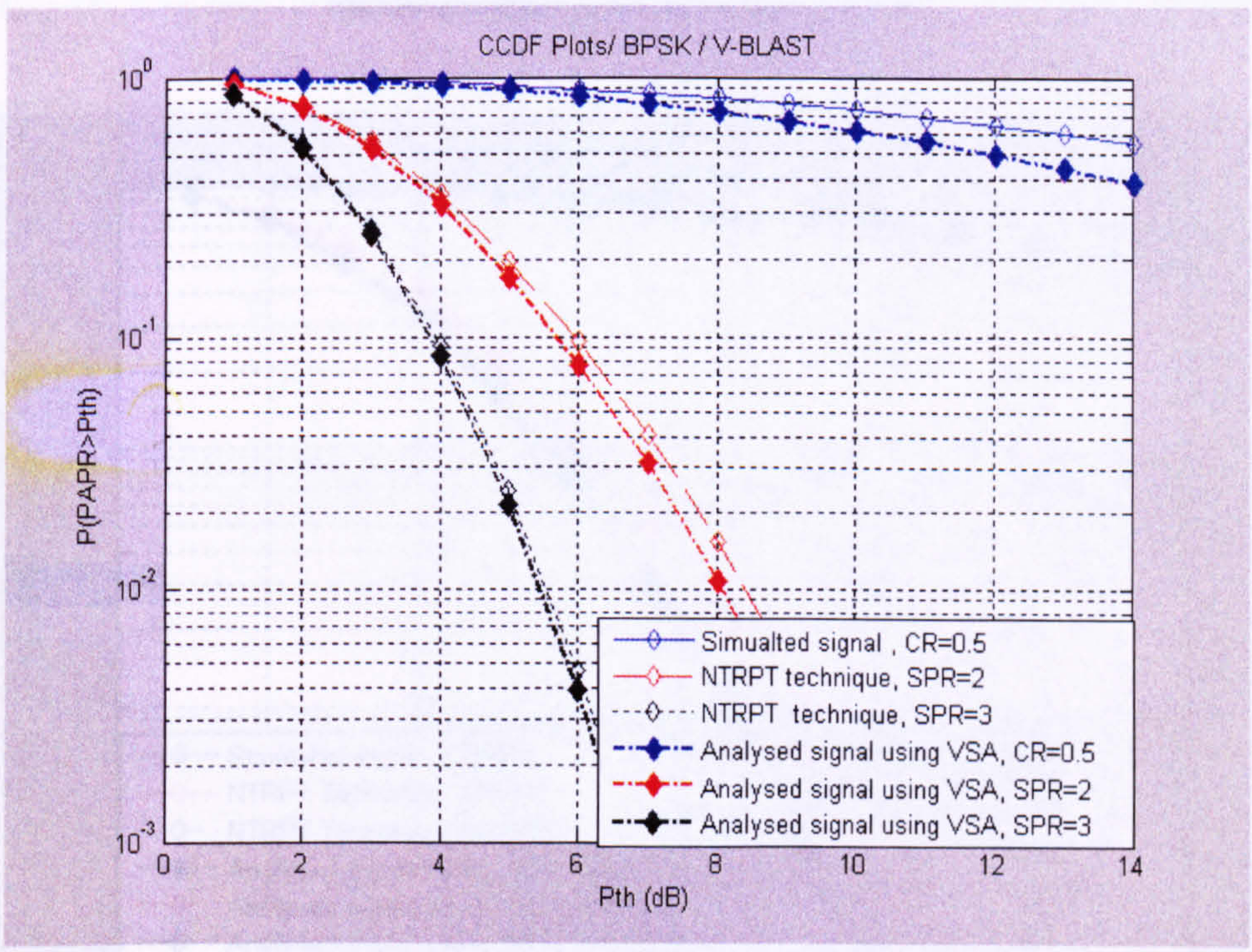


**Figure 6.1 (a)**

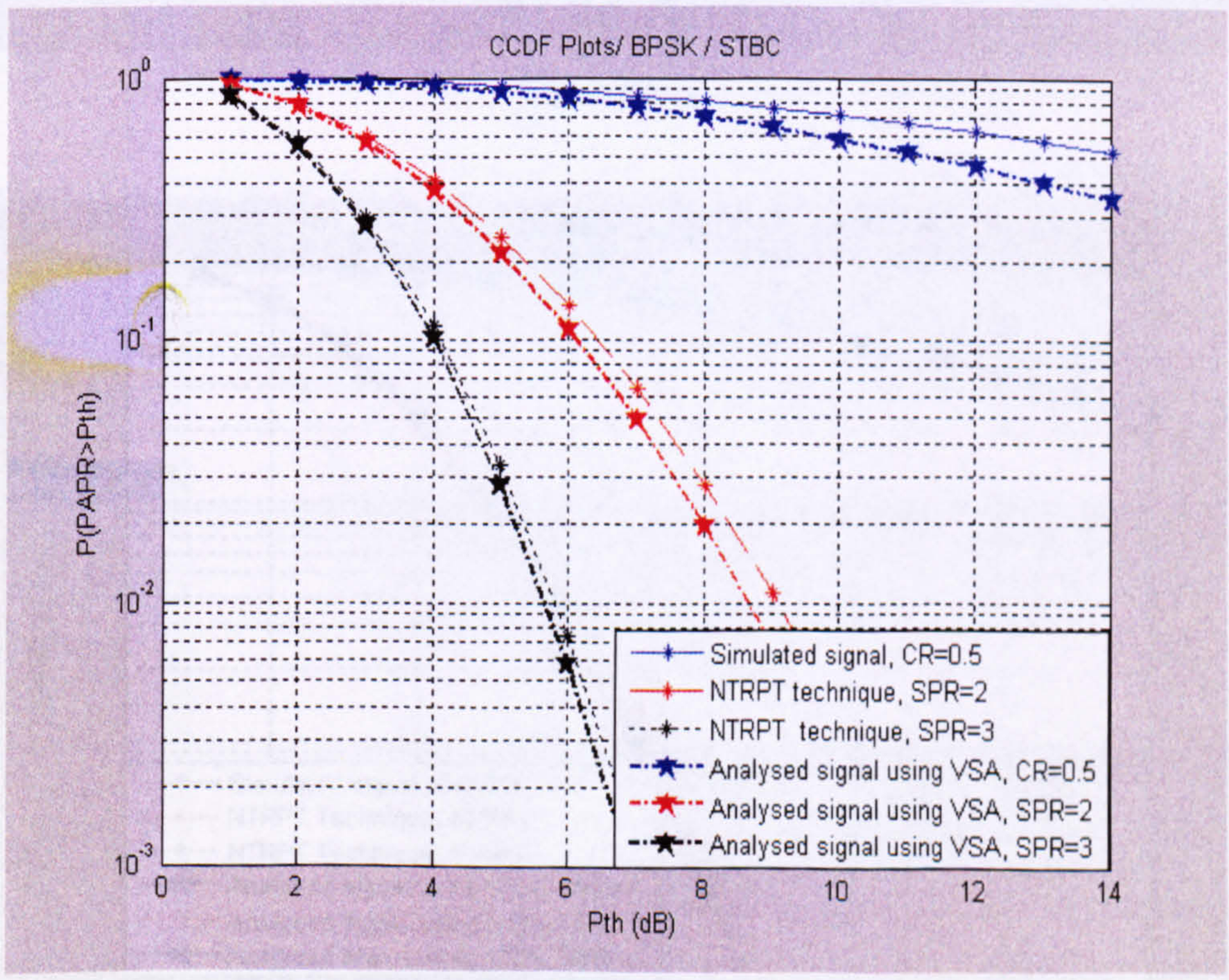


**Figure 6.1 (b)**

**Figure 6.1: Comparing the CCDF plots for simulated MIMO-OFDM signals with the analysed signals using VSA based on BPSK modulation technique and coding rate equal 1/2 (a) V-BLAST MIMO encoder (b) STBC MIMO encoder**

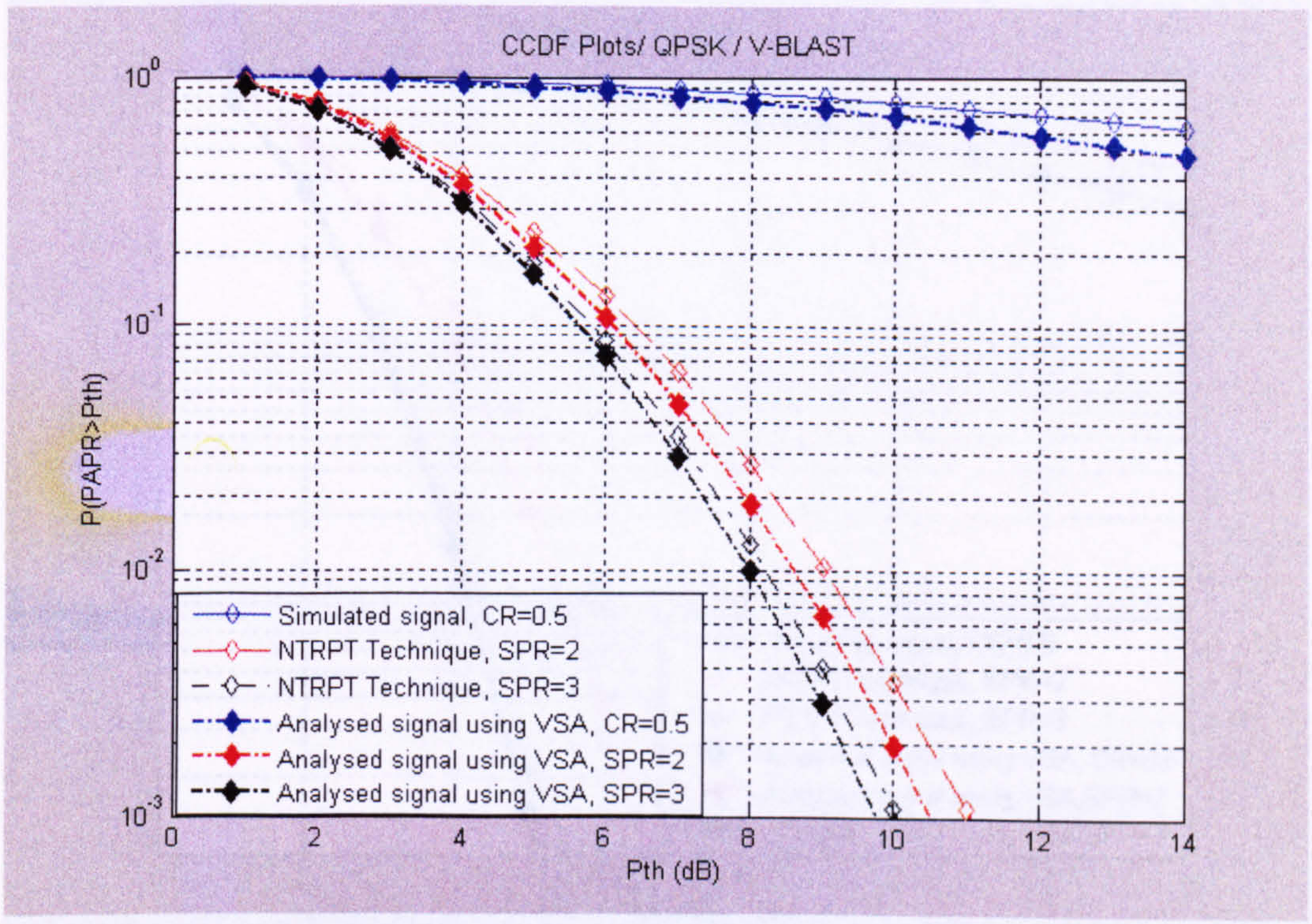


**Figure 6.2 (a)**

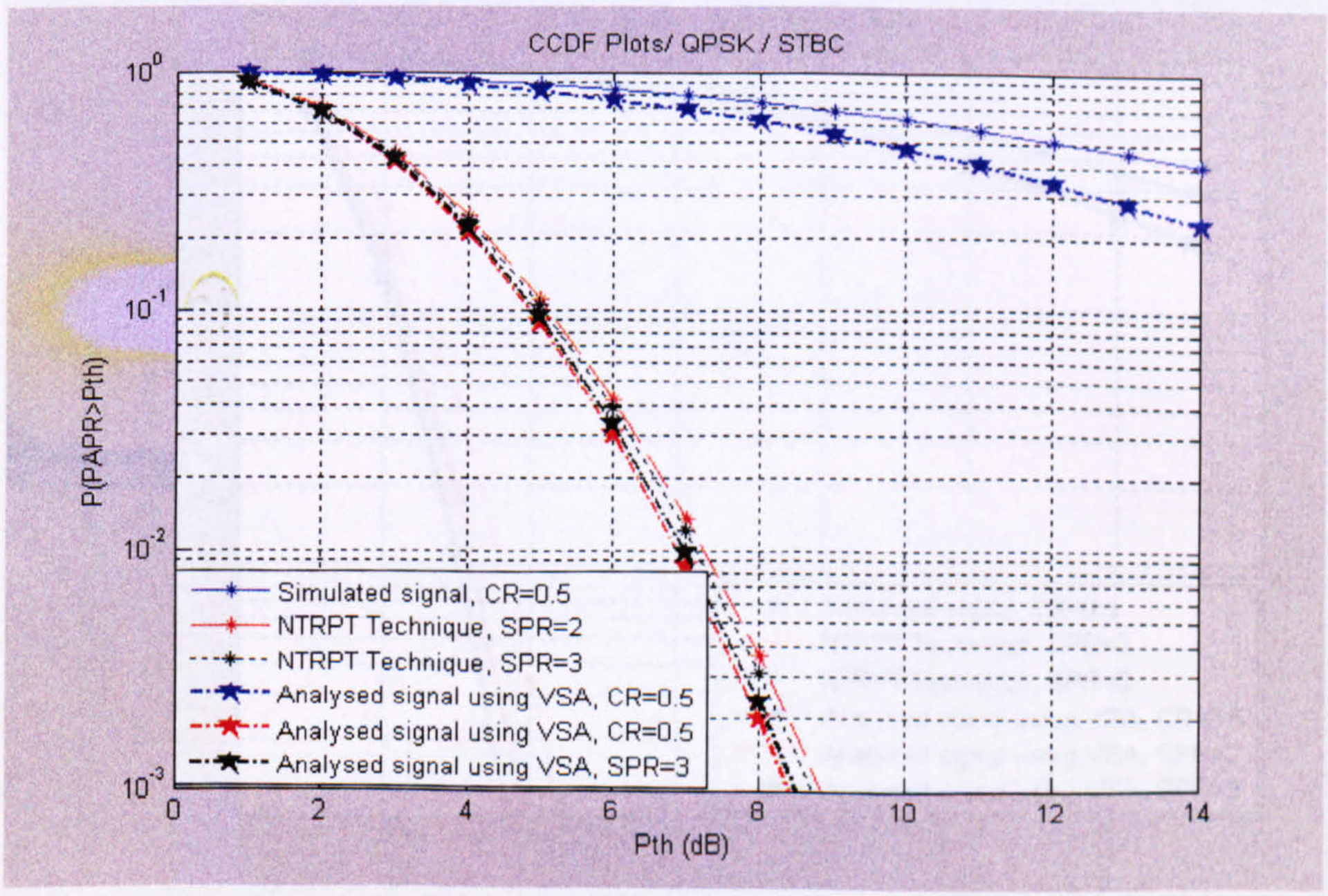

**Figure 6.2 (b)**

**Figure 6.2: Comparing the CCDF plots for simulated MIMO-OFDM signals with the analysed signals using VSA based on QPSK modulation technique and coding rate equal 1/2 (a) V-BLAST MIMO encoder (b) STBC MIMO encoder**

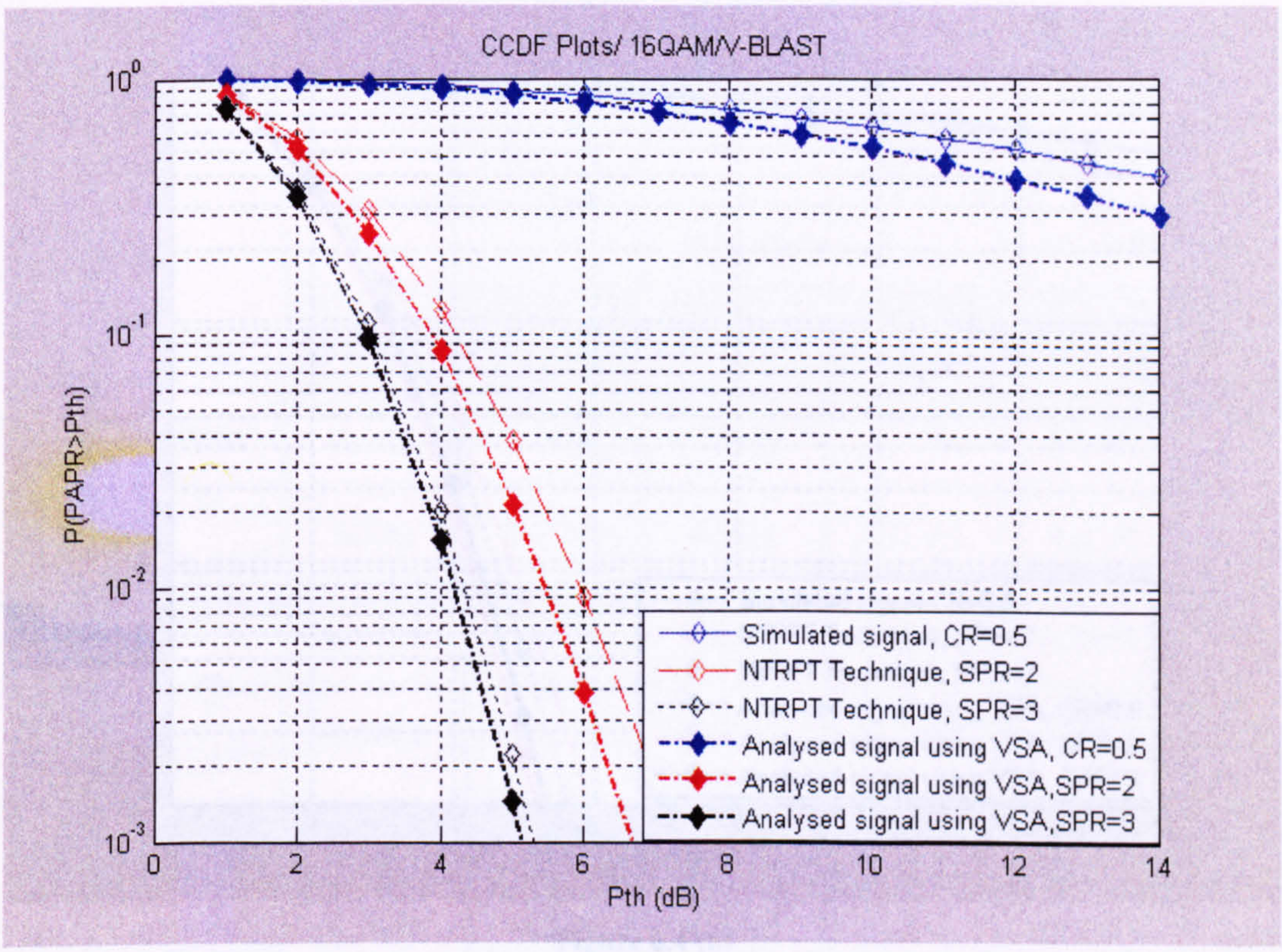


**Figure 6.3 (a)**

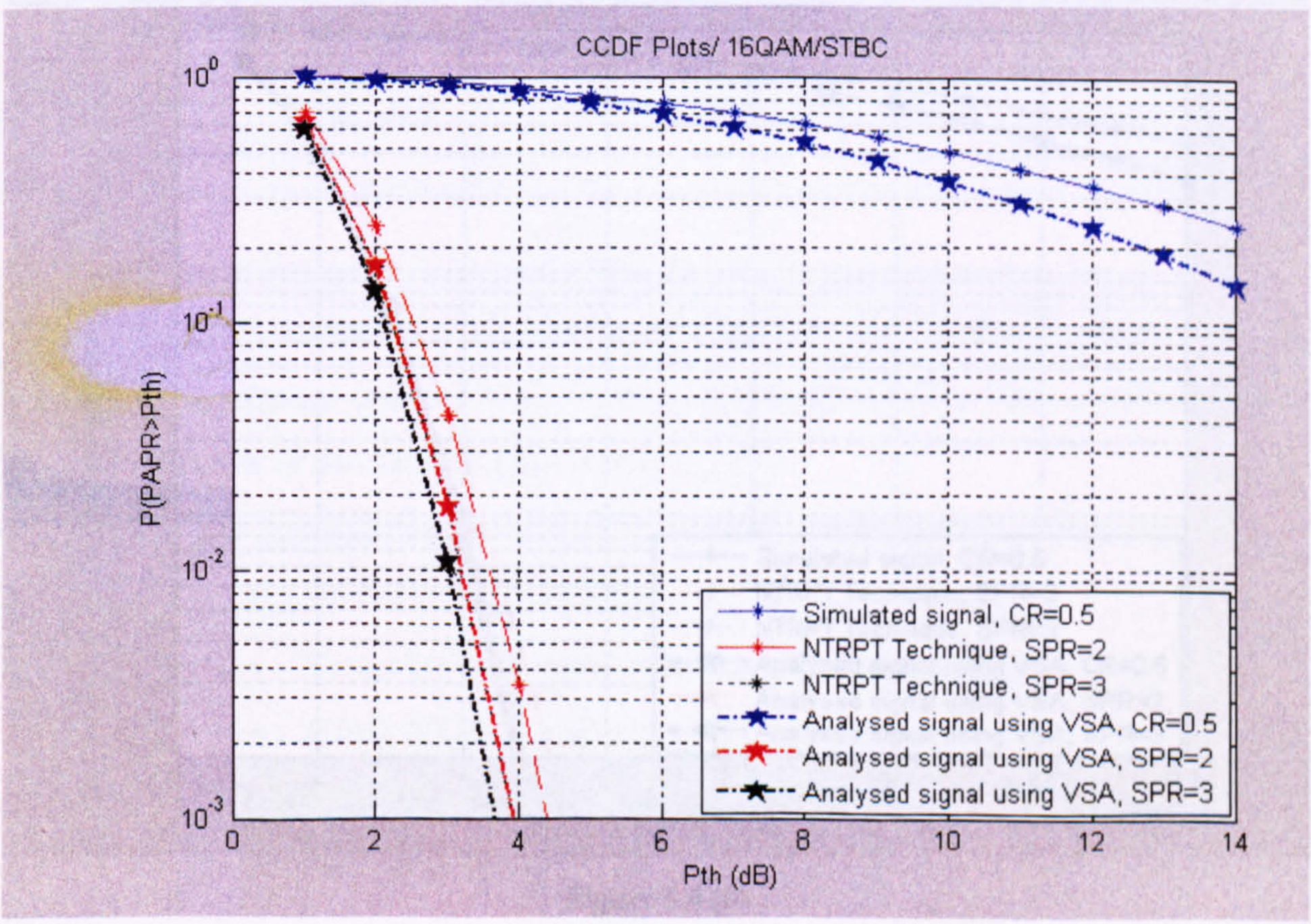

**Figure 6.3 (b)**

**Figure 6.3: Comparing the CCDF plots for simulated MIMO-OFDM signals with the analysed signals using VSA based on 16QAM modulation technique and coding rate equal 1/2 (a) V-BLAST MIMO encoder (b) STBC MIMO encoder**

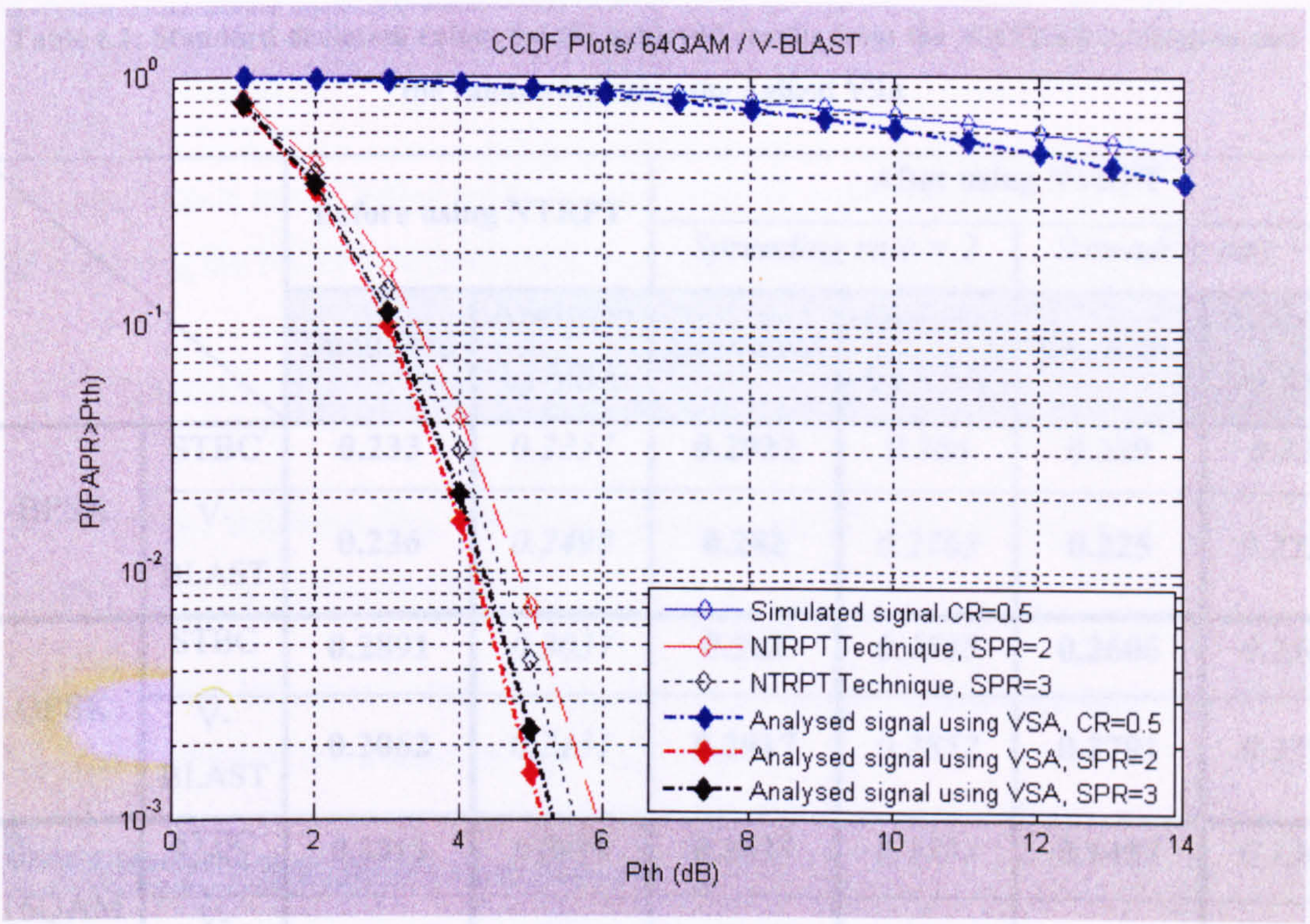


**Figure 6.4 (a)**

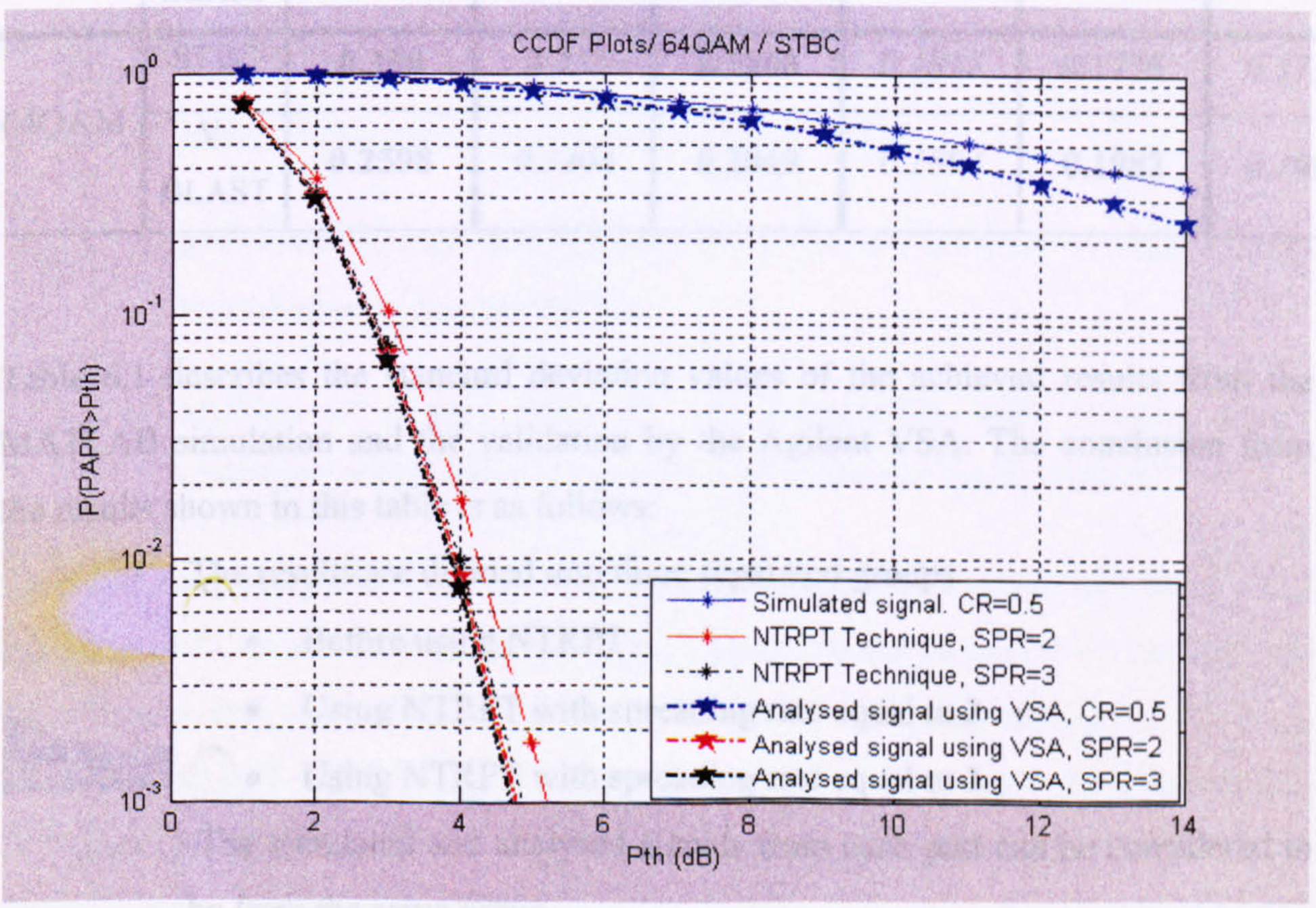


**Figure 6.4 (b)**

**Figure 6.4: Comparing the CCDF plots for simulated MIMO-OFDM signals with the analysed signals using VSA based on 64QAM modulation technique and coding rate equal 1/2 (a) V-BLAST MIMO encoder (b) STBC MIMO encoder**

**Table 6.1: Standard deviation values for the achieved results from the MATLAB simulation and the validatrion using the Agilent VSA**

| | | **Before using NTRPT** | | **After using NTRPT** | | | |
|---|---|---|---|---|---|---|---|
| | | | | *Spreading rate = 2* | | *Spreading rate = 3* | |
| | | Simulated | Analysed by VSA | Simulated | Analysed by VSA | Simulated | Analysed by VSA |
| BPSK | STBC | **0.233** | *0.2357* | **0.2922** | *0.286* | **0.229** | *0.228* |
| | V-BLAST | **0.236** | *0.2498* | **0.282** | *0.2765* | **0.225** | *0.2226* |
| QPSK | STBC | **0.2891** | *0.3037* | **0.262** | *0.2548* | **0.2606** | *0.2568* |
| | V-BLAST | **0.2062** | *0.2131* | **0.2917** | *0.2852* | **0.2791** | *0.2754* |
| 16QAM | STBC | **0.3313** | *0.3478* | **0.1627** | *0.1555* | **0.1457** | *0.1365* |
| | V-BLAST | **0.2846** | *0.319* | **0.2343** | *0.223* | **0.1897** | *0.1848* |
| 64QAM | STBC | **0.308** | *0.332* | **0.1868** | *0.1817* | **0.1775** | *0.1735* |
| | V-BLAST | **0.2598** | *0.2464* | **0.2049** | *0.1894* | **0.1982** | *0.1902* |

Table 6.1 describes the standard deviation values of the achieved results from the MATLAB simulation and the validation by the Agilent VSA. The conclusion from the results shown in this table is as follows:

- The results are divided into three separated groups
  - Before using NTRPT
  - Using NTRPT with spreading rate equal to 2
  - Using NTRPT with spreading rate equal to 3
- The simulated and analysed signals from each part can be considered to be from the same group.

## *6.3 Validation using Xilinx technology*

An introduction to the Xilinx technology is given in Subsection 6.3.1, and the process of validating the NTRPT-MIMO-OFDM systems is given in Subsection 6.3.2.

### 6.3.1 Introduction

Traditionally, implementing DSP algorithms is maintained by two main methods depending on the application speed:

(a) For low-speed applications, it is implemented using programmable DSP chips or fixed function DSP chip-sets

(b) For higher speeds Application-Specific Integrated Circuits (ASICs) is used

Advances in Field Programmable Gate Arrays (FPGAs) provide new options for DSP design. This is due to the following advantages:

(a) maintain the advantages of custom functionality

(b) avoidance of high development costs and the inability to make design modifications after production

(c) addition of design flexibility and adaptability with optimal device utilisation while conserving both board space and system power

The Field Programmable Gate Arrays (FPGA) device contains many logic blocks that can be used to realise different kinds of functions. The interconnections between the logic blocks and the realisation of the functionality are programmed by the user. Therefore, NTRPT-MIMO-OFDM is designed to be implemented to the Digilent D2-FT system board (for more information see Appendix B), which contains an FPGA device hence, simulation results can be validated. To help in programming the

Digilent D2-FT system board use was made of the Integrated Software Environment (ISE) and the verilog Hardware Description Language (HDL). The Digilent board employs an FPGA from Xilinx is from the Spartan-II family. The Spartan 2E series is a mature, readily available low cost family, showing clearly that the technique can be implemented using low-cost hardware. For more information, the reader can refer to www.xilinx.com.

### 6.3.2 The validation process

For the sake of simplicity in programming the NTRPT-MIMO-OFDM transmitter diagram shown in Figure 5.1 (a), the transmitter diagram was split into subblocks, beginning from generation of the input data block and ending with that of the NTRPT block.

Figure 6.5 shows the split blocks in sequential order according to their places in the transmitter diagram.

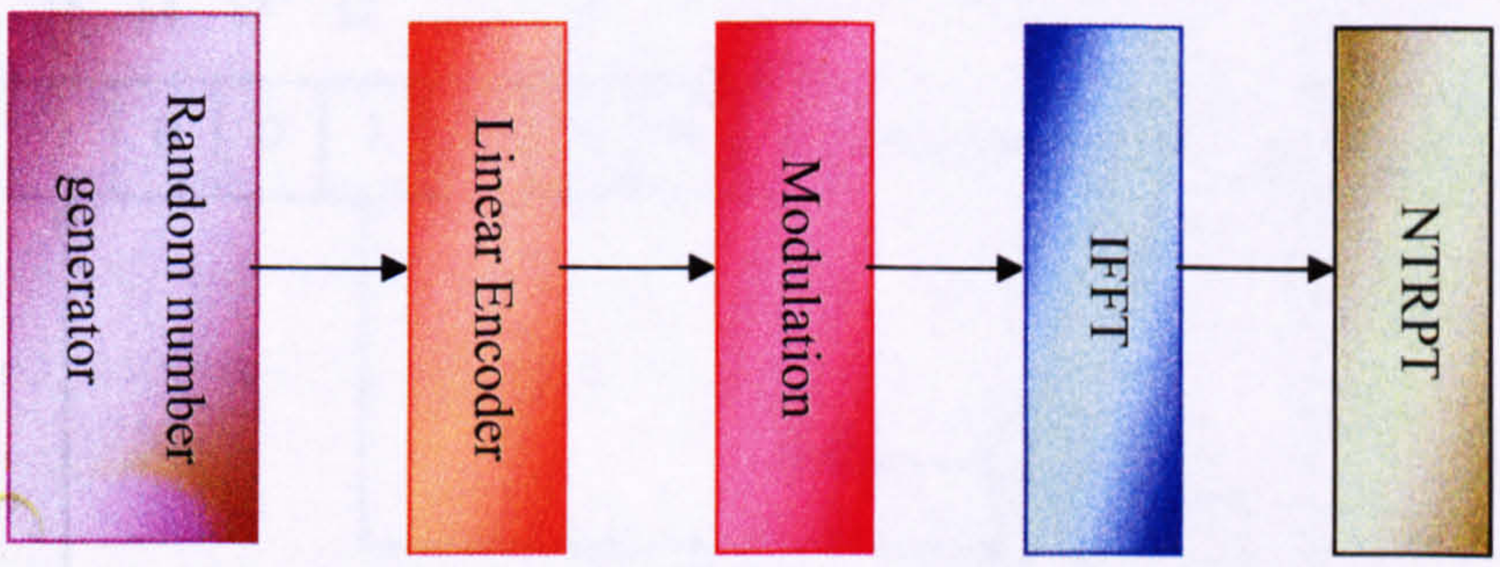


**Figure 6.5: The main subblocks in the transmitter diagram**

In Figure 6.5, for clarity, the model will be limited to the use of turbo coding with coding rate equal ½ as a linear encoder, 16QAM as a modulation technique, and spreading rate equals 2. The second step is to define the functionality of these subblocks, have therefore been built from their basic blocks.

After simulating the blocks that are shown in Figure 6.5 using the HDL language and ISE software, the simulated code can be downloaded to the Digilent D2-FT system

board, after which the outputs can be analysed and compared with the results from the simulated system using MATLAB.

The ISE facilitates checking the codes written by using the behavioural test. The checking process includes the feasibility of implementing the code into the system board as well as detecting the design errors. Unfortunately, after checking the codes, it appeared that the design needs a bigger FPGA device than the one in the Digilent D2-FT system board. Due to the time limitation the results achieved from the behavioural test have been used to validate the simulation results of the proposed technique.

The difference between the behavioural test and the real hardware design is that former excludes the effect of parameters such as processing time delay.

The random number generator can be easily built from a feed back shift register, which can be described in Figure 6.6.

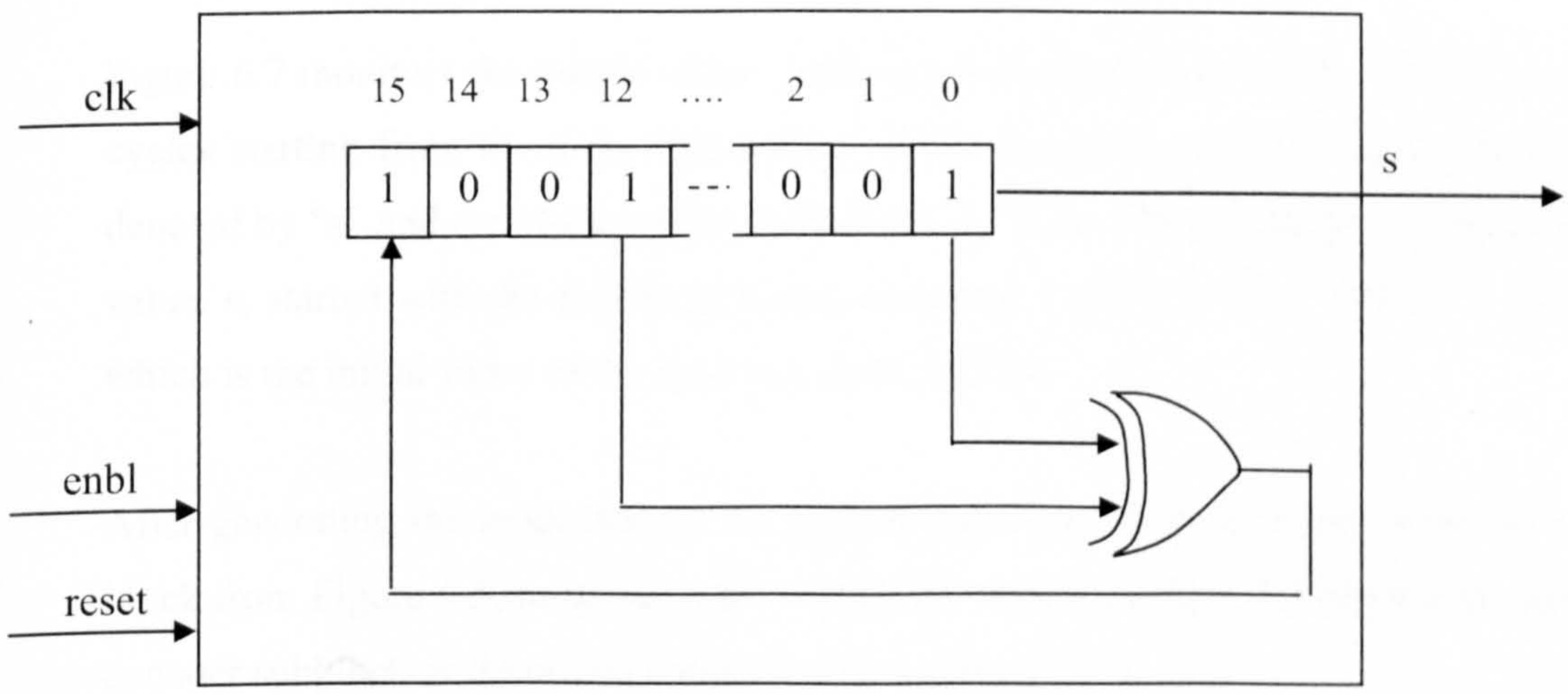


**Figure 6.6: Building a random number generator**

In Figure 6.6, the block consists of a 16 bit-shift register. An X-OR process for the bits number 12 and 0 is held to produce the value of bit number 16 by a feedback process.

The shift register initialised by specific values to ease the checking process of the designed block shown in Figure 6.6, which will be the firstly generated data as shown in Figure 6.7.

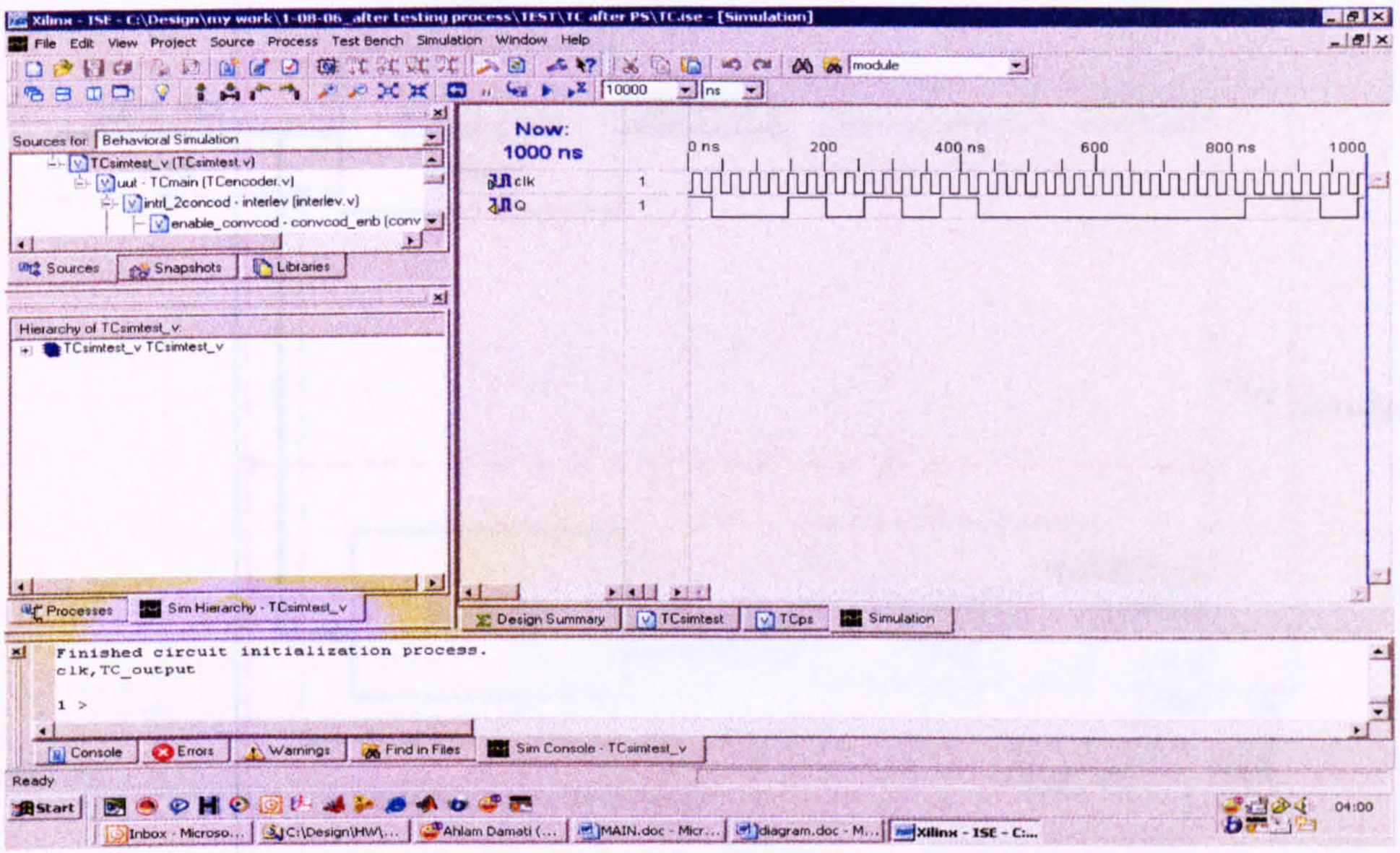


**Figure 6.7: The behavioural test result of the random number generator block**

Figure 6.7 monitors the output of the random number generator block with the clock cycles starting from the 0 ns. The output of the random number generator block is denoted by "s" and the clock cycles are denoted by "clk". From Figure 6.7, the output value, s, started with the following binary sequence 1 0 0 1 0 1 0 1 0 0 0 0 0 0 0 1, which is the initial value of the feedback shift register.

After generating the input data to the proposed design, the data is fed to the second block from Figure 6.5, turbo encoder. Figure 6.8 shows the basic blocks for the turbo encoder subblock as described earlier in Subsection 4.2.1.2.

Figure 6.8 (a) shows the structure of generation turbo codes with a coding ratio equals 2. As can be seen, the turbo encoder consists of two identical convolutional encoders. The output of these encoders is then serialised to form the turbo encoder output. The interleaver is a simple device that rearranges the order of the data bits in a prescribed manner. The delay block is used for synchronisation purposes.

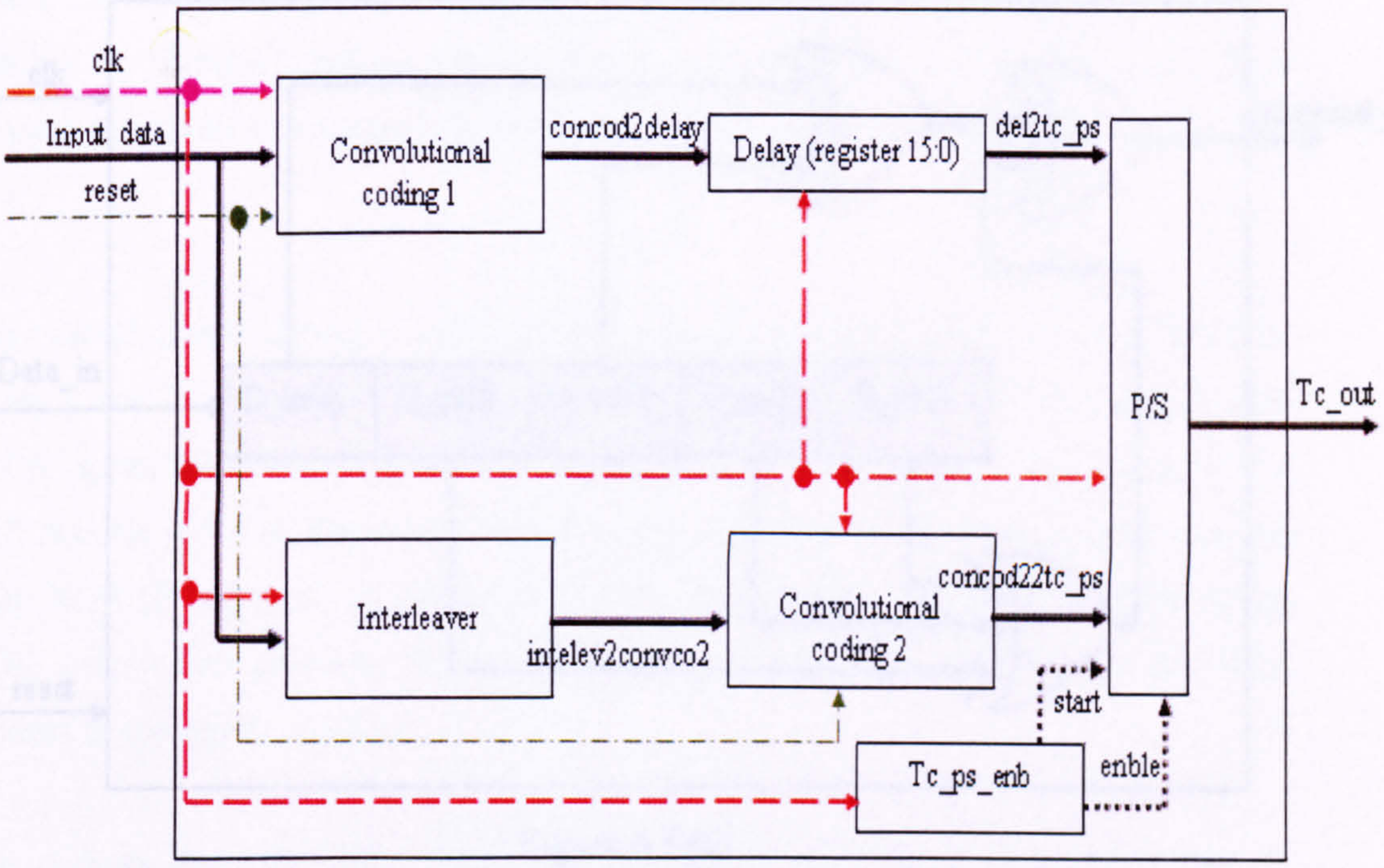


Figure 6.8 (a)

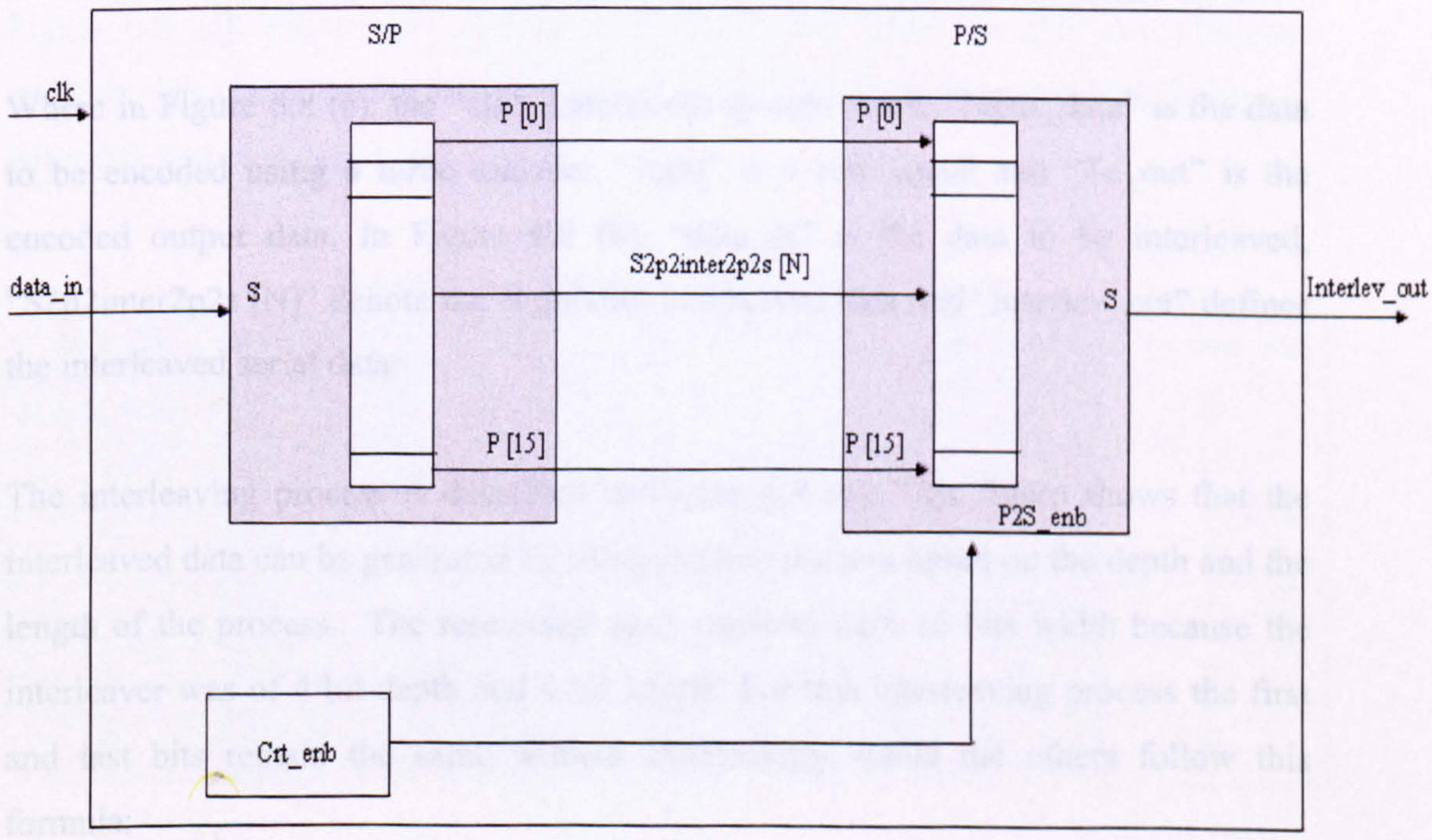


Figure 6.8 (b)

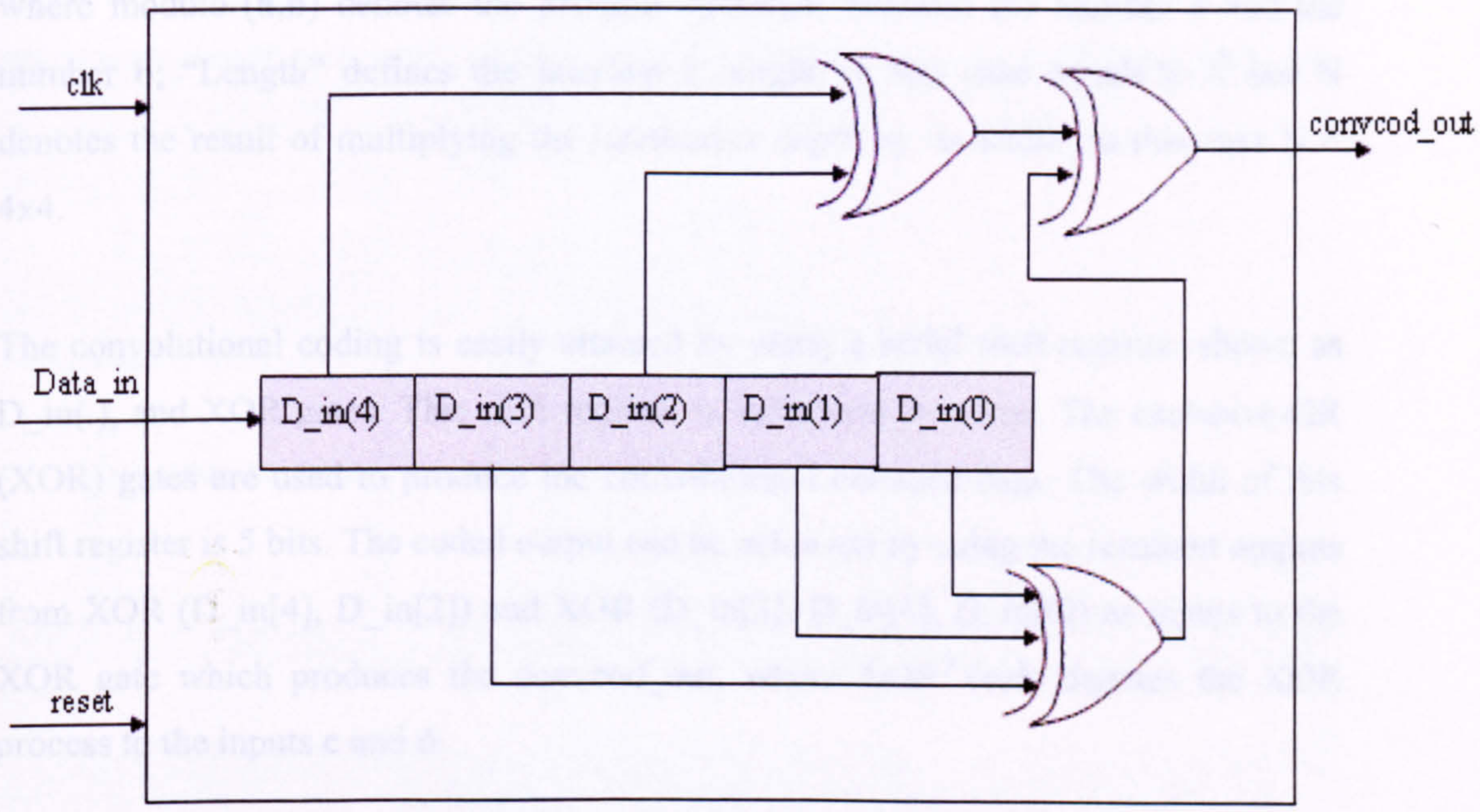


Figure 6.8 (c)

**Figure 6.8: (a) simplifying the turbo encoder into its basic blocks, (b) describing the structure of the interleaver block, and (c) describing the structure of the convolutional encoder block**

Where in Figure 6.8 (a), the "clk" denotes the system clock, "Input_data" is the data to be encoded using a turbo encoder, "reset" is a rest signal and "Tc_out" is the encoded output data. In Figure 6.8 (b), "data_in" is the data to be interleaved, "S2p2inter2p2s [N]" denote the N parallel interleaved data and "interlev_out" defines the interleaved serial data.

The interleaving process is described in Figure 6.8 (b). This figure shows that the interleaved data can be generated by using modulo process based on the depth and the length of the process. The researcher used registers with 16 bits width because the interleaver was of 4 bit depth and 4 bit length. For this interleaving process the first and last bits remain the same without interleaving, while the others follow this formula:

$$S2p2inter2p2s\,[n] = modulo(Length*n, N-1),\ n=1,\ldots,N-2$$

where modulo[8](**a**,**b**) denotes the Modulo operation between the number **a** and the number **b**; "Length" defines the interleaver length, in this case equals to 4 and N denotes the result of multiplying the interleaver depth by its width, in this case N = 4x4.

The convolutional coding is easily attained by using a serial shift register, shown as D_in(.), and XOR gates. This shift register is initialised by zeros. The exclusive-OR (XOR) gates are used to produce the convolutional encoded data. The width of this shift register is 5 bits. The coded output can be achieved by using the resultant outputs from XOR (D_in[4], D_in[2]) and XOR (D_in[3], D_in[1], D_in[0]) as inputs to the XOR gate which produces the convcod_out, where XOR[9] (**c**,**d**) denotes the XOR process to the inputs **c** and **d.**

The outputs from the delay block and the second convolutional encoder, namely "del2tc_ps" and "concod22tc_ps" respectively will be combined together by a P/S block to form the output of the turbo encoder block. According to the description of Figure 6.8 (c), Figure 6.9 shows the encoded data from the first convolutional encoder. The output is denoted by "convcod_out". Starting from the 0 ns, Table 6.2 describes part of the encoded data.

**Table 6.2: Describing the expected encoded data**

| data_in | D_in(4) | D_in(3) | D_in(2) | D_in(1) | D_in(0) | convcod_out |
|---|---|---|---|---|---|---|
| initial value | 0 | 0 | 0 | 0 | 0 | 0 |
| 1 | 1 | 0 | 0 | 0 | 0 | 1 |
| 0 | 0 | 1 | 0 | 0 | 0 | 1 |
| 0 | 0 | 0 | 1 | 0 | 0 | 1 |
| 1 | 1 | 0 | 0 | 1 | 0 | 0 |
| 0 | 0 | 1 | 0 | 0 | 1 | 0 |

Continuously from the 0 ns, and after describing the expected encoded output from the design shown in Figure 6.8 (c), Figure 6.9 shows the encoded data, convcod_out.

---

[8] **Modulo** operation finds the remainder of division of **a** number by **b** and can be expressed by **a** mod **b**.
[9] XOR is a 'stricter' version of the OR gate. Rather than allowing the output to be 1 when either one or both of the inputs are 1, an XOR gate has a 1 output only when only one input is 1.

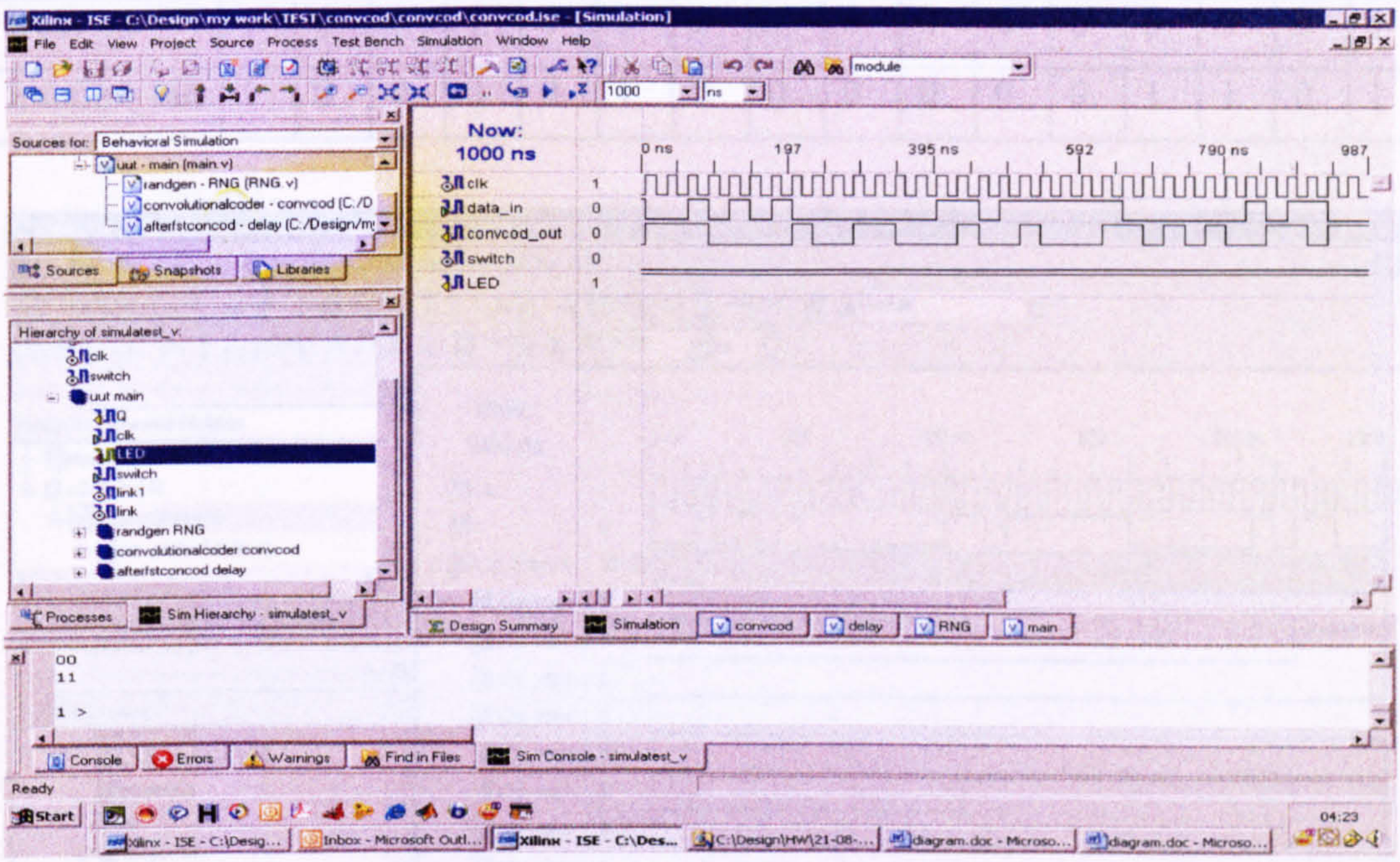


**Figure 6.9: The behavioural test results from the first convolutional encoder**

The same input data is fed the interleaver which is described in Figure 6.9 (b). The interleaving process is follow the modulo formula which described earlier to fill the interleaver output 16 bit register. This process is described in Figure 6.10.

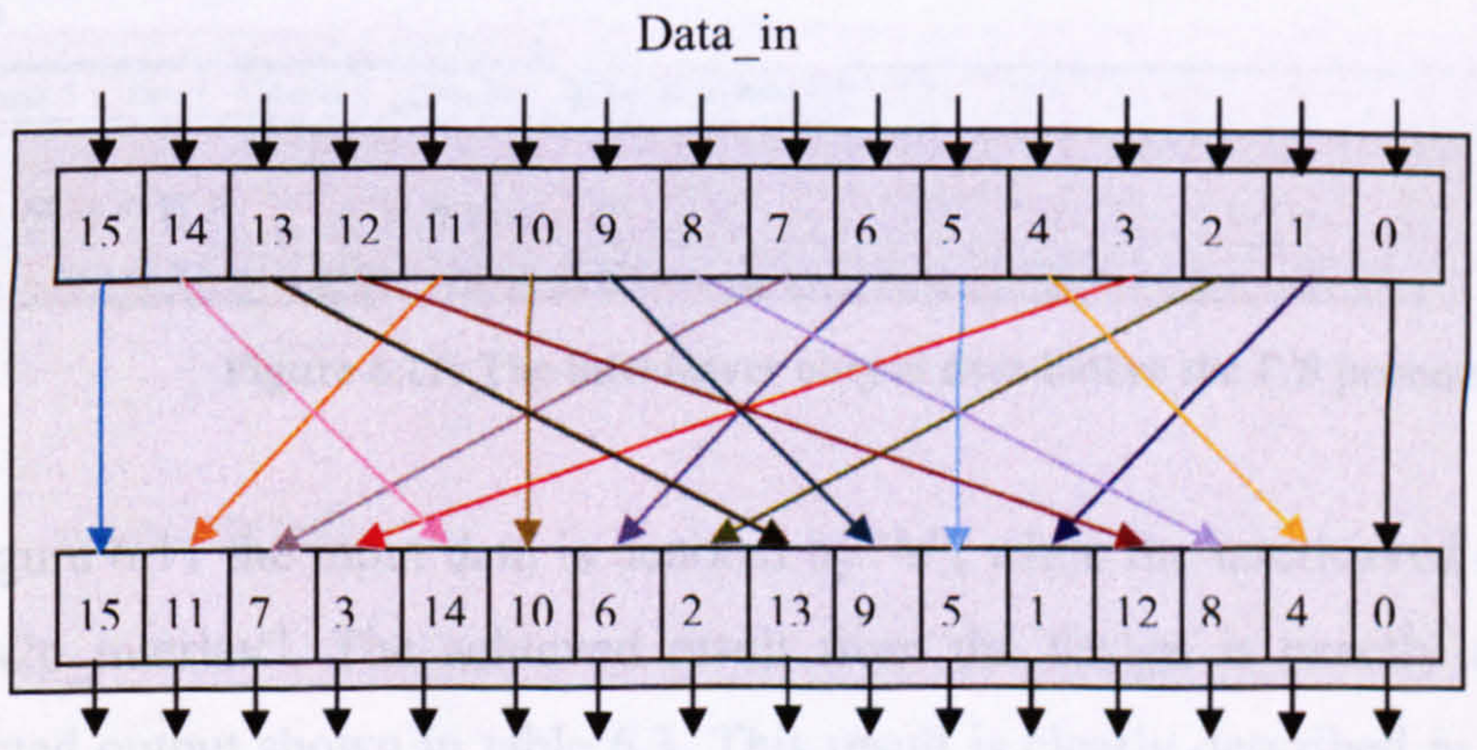


**Figure 6.10: Describing the interleaving process**

According to interleaving process, Table 6.3 describes the expected interleaved output data. This result is shown in Figure 6.11.

**Table 6.3: The expected interleaved output**

| Data_in | 1 | 0 | 0 | 1 | 0 | 1 | 0 | 1 | 0 | 0 | 0 | 0 | 0 | 0 | 0 | 1 |
|---|---|---|---|---|---|---|---|---|---|---|---|---|---|---|---|---|
| Interlev_out | 1 | 0 | 0 | 0 | 0 | 1 | 0 | 0 | 0 | 0 | 0 | 0 | 1 | 1 | 0 | 1 |

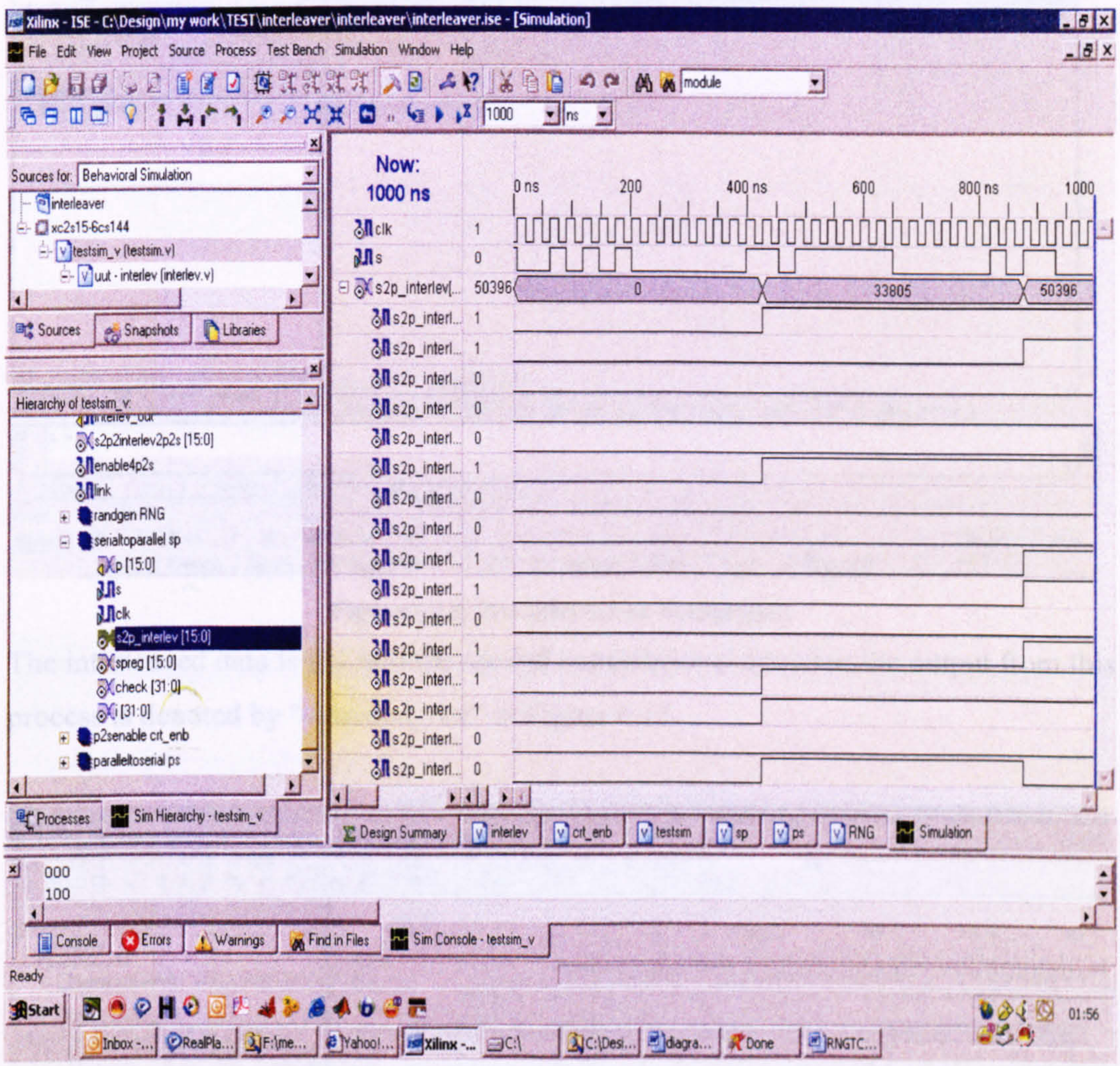


**Figure 6.11: The interleaver output data before the P/S process**

In Figure 6.11 the input data is denoted by "s", while the interleaved data is denoted by "s2p_interlev". The achieved result from the design is exactly as the same as expected output shown in table 6.3. This result is clearly described in Figure 6.12 by monitoring the "interleav_out" port.

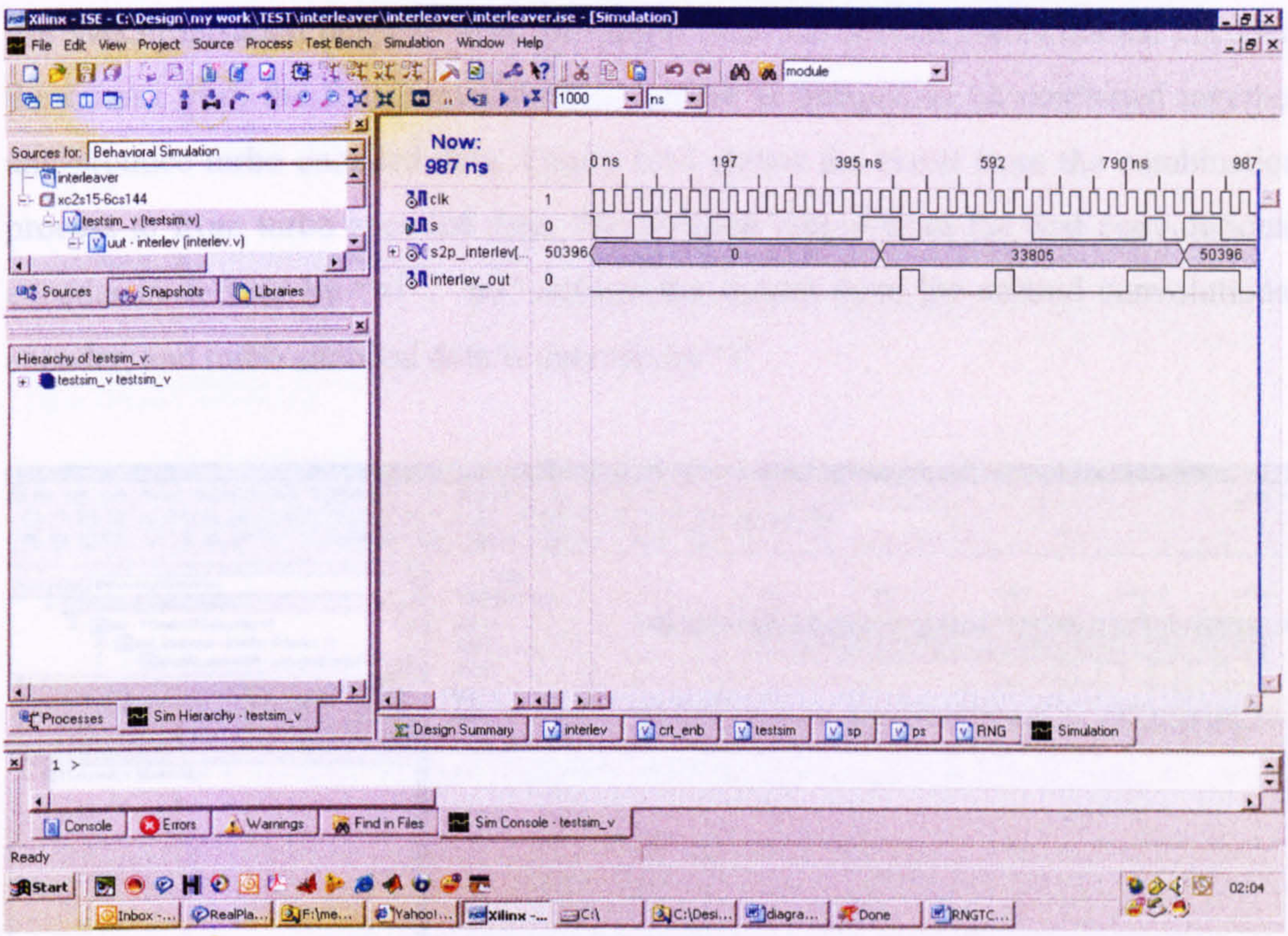


**Figure 6.12: The interleaver output data**

The interleaved data is fed into the second convolutional encoder; the output from this process is denoted by "convcod_out" in Figure 6.13.

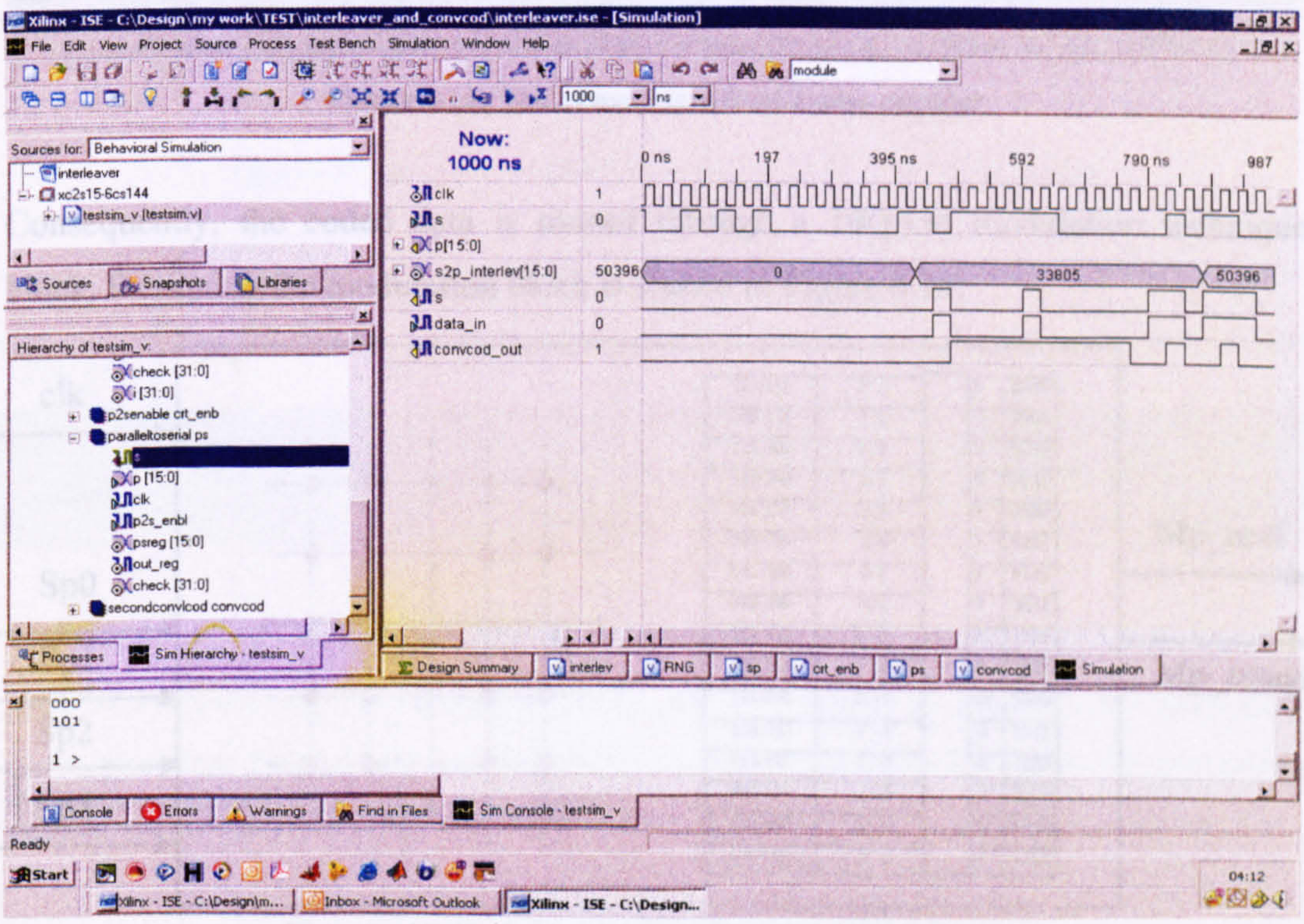


**Figure 6.13: The output of the second convolutional encoder**

For synchronisation purpose with the output from the second convolutional encoder, the output from the first convolutional encoder is delayed to be combined together and produce turbo encoded data. Figure 6.14 shows the result from the combination process to from turbo encoded data. The delayed output from the first convolutional encoder is defined by "p1", "p0" defines the output from the second convolutional encoder, and turbo encoded data is denoted by "s".

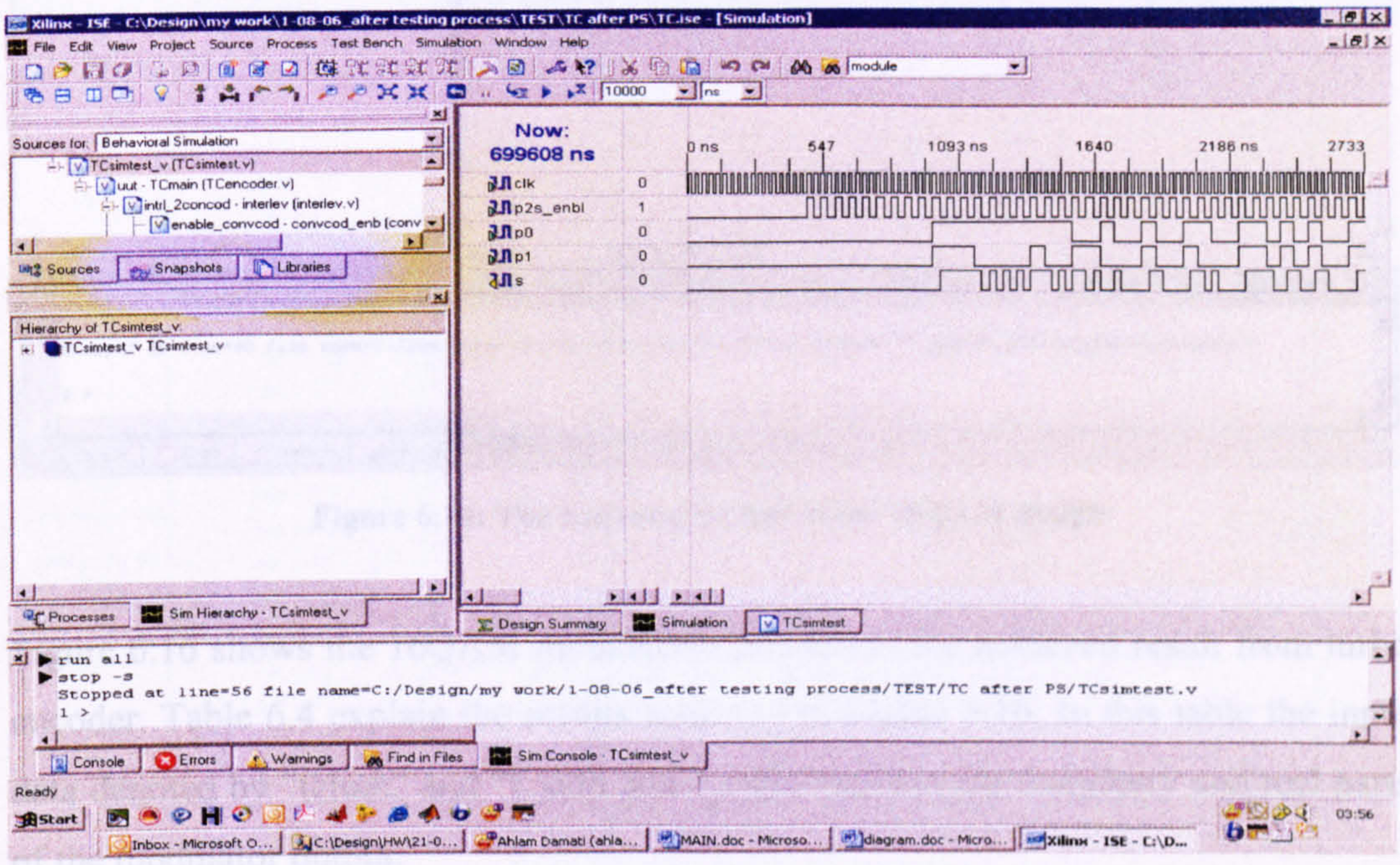


**Figure 6.14: The output data from turbo encoder**

Consequently, the coded data is passed through a 16QAM modulation technique block. Designing the modulation block is shown in Figure 6.15.

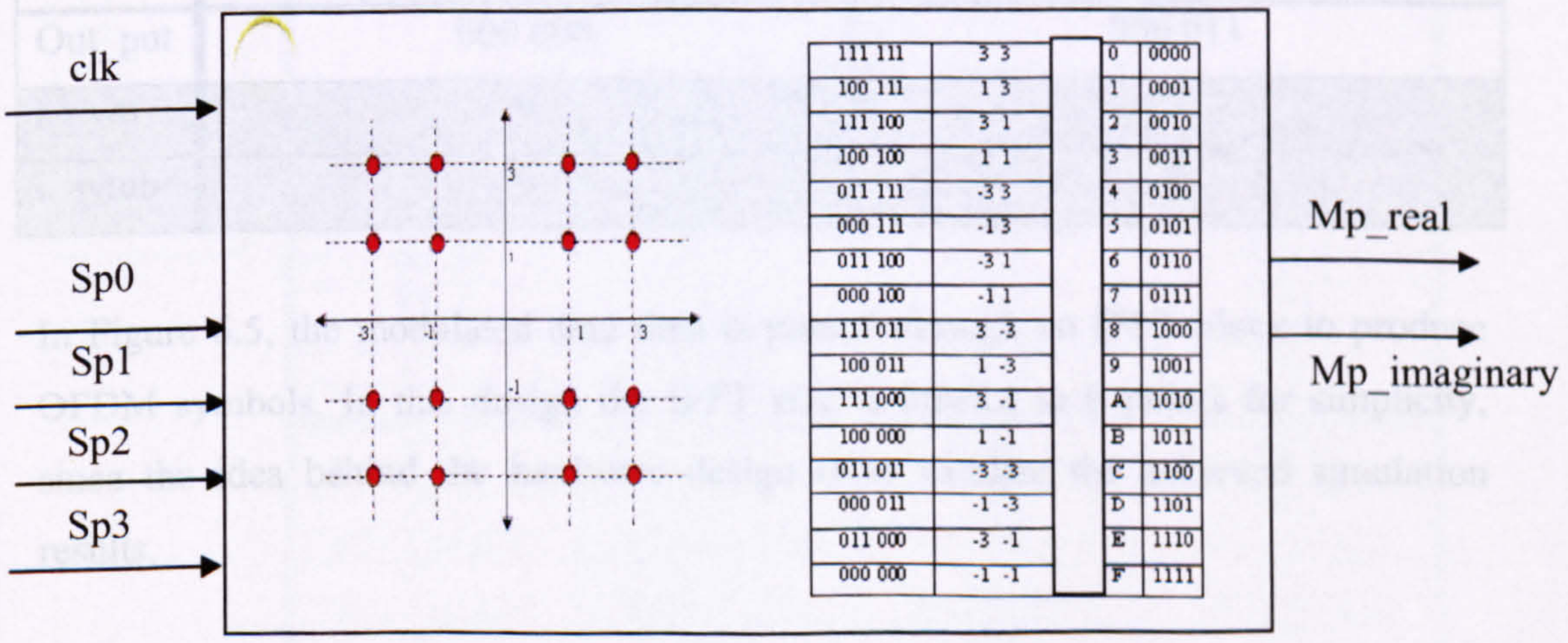


| | | | |
|---|---|---|---|
| 111 111 | 3 3 | 0 | 0000 |
| 100 111 | 1 3 | 1 | 0001 |
| 111 100 | 3 1 | 2 | 0010 |
| 100 100 | 1 1 | 3 | 0011 |
| 011 111 | -3 3 | 4 | 0100 |
| 000 111 | -1 3 | 5 | 0101 |
| 011 100 | -3 1 | 6 | 0110 |
| 000 100 | -1 1 | 7 | 0111 |
| 111 011 | 3 -3 | 8 | 1000 |
| 100 011 | 1 -3 | 9 | 1001 |
| 111 000 | 3 -1 | A | 1010 |
| 100 000 | 1 -1 | B | 1011 |
| 011 011 | -3 -3 | C | 1100 |
| 000 011 | -1 -3 | D | 1101 |
| 011 000 | -3 -1 | E | 1110 |
| 000 000 | -1 -1 | F | 1111 |

**Figure 6.15: Designing a 16QAM modulation technique**

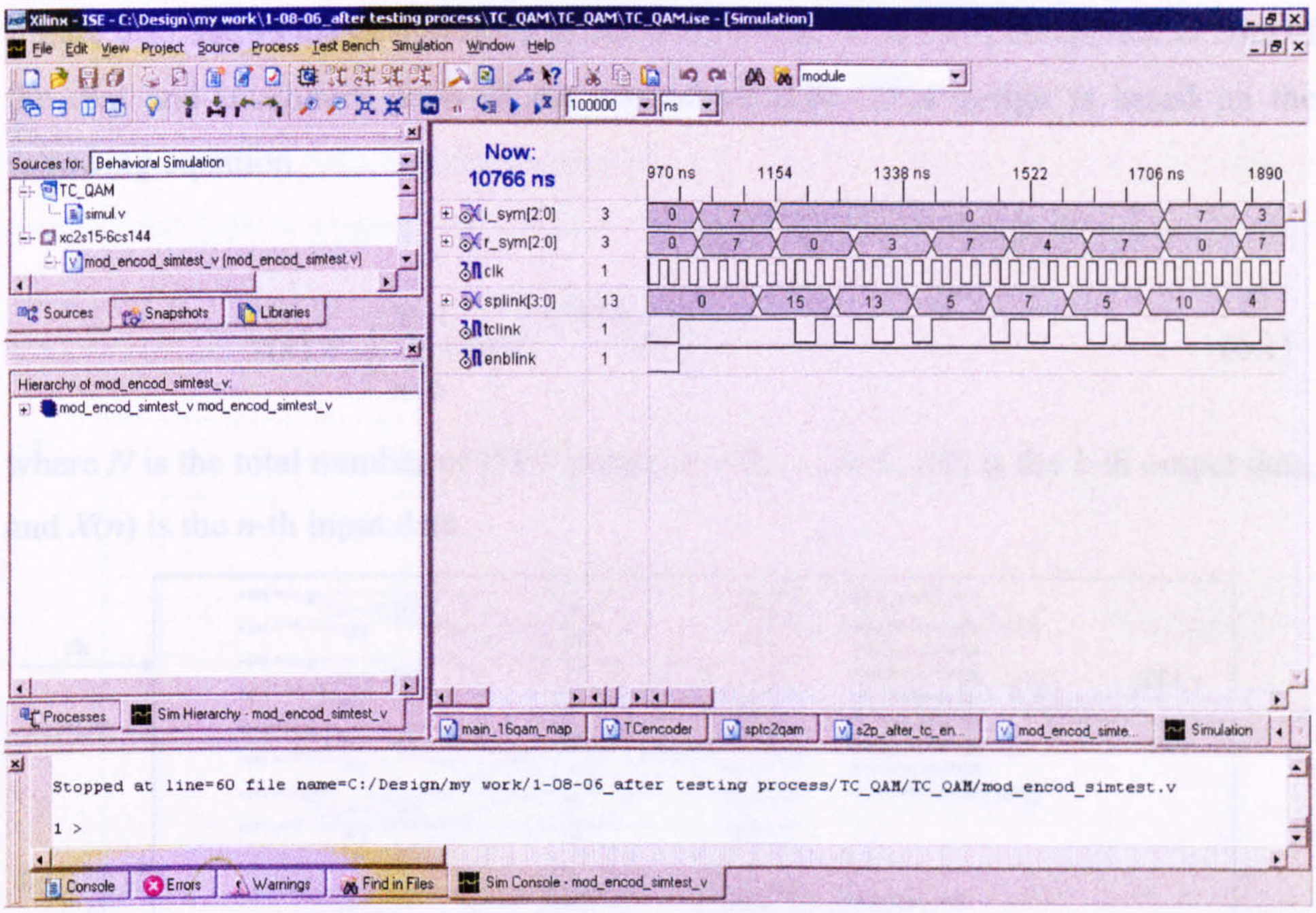


**Figure 6.16: The behavioural test of the 16QAM design**

Figure 6.16 shows the 16QAM modulation process of the achieved result from turbo encoder. Table 6.4 explain the results achieved in Figure 6.16. In this table the input data denoted by "tclink" and "i_sym and r_sym" denotes the imaginary and real parts of the modulator output.

**Table 6.4: The expected data from the 16QAM modulation block**

| tclink | 1 | 1 | 1 | 1 | 1 | 1 | 0 | 1 |
|---|---|---|---|---|---|---|---|---|
| Out_put | 000 000 | | | | 000 011 | | | |
| r_sym | 0 | | | | 3 | | | |
| i_symb | 0 | | | | 0 | | | |

In Figure 6.5, the modulated data then is passed through an IFFT block to produce OFDM symbols. In this design the IFFT size is limited to 8 points for simplicity, since the idea behind the hardware design is to validate the achieved simulation results.

Figure 6.17 shows the design steps of the IFFT block, which will be applied to both of the real and imaginary parts of the modulated data. This design is based on the following equation

$$x(k) = \frac{1}{N}\sum_{n=0}^{N-1} X(n)\left(e^{(-j2\pi nk/N)}\right)^{*} \qquad (6.1)$$

where $N$ is the total number of IFFT points, $k = 0, \ldots, N\text{-}1$, $x(k)$ is the $k$-th output data, and $X(n)$ is the $n$-th input data.

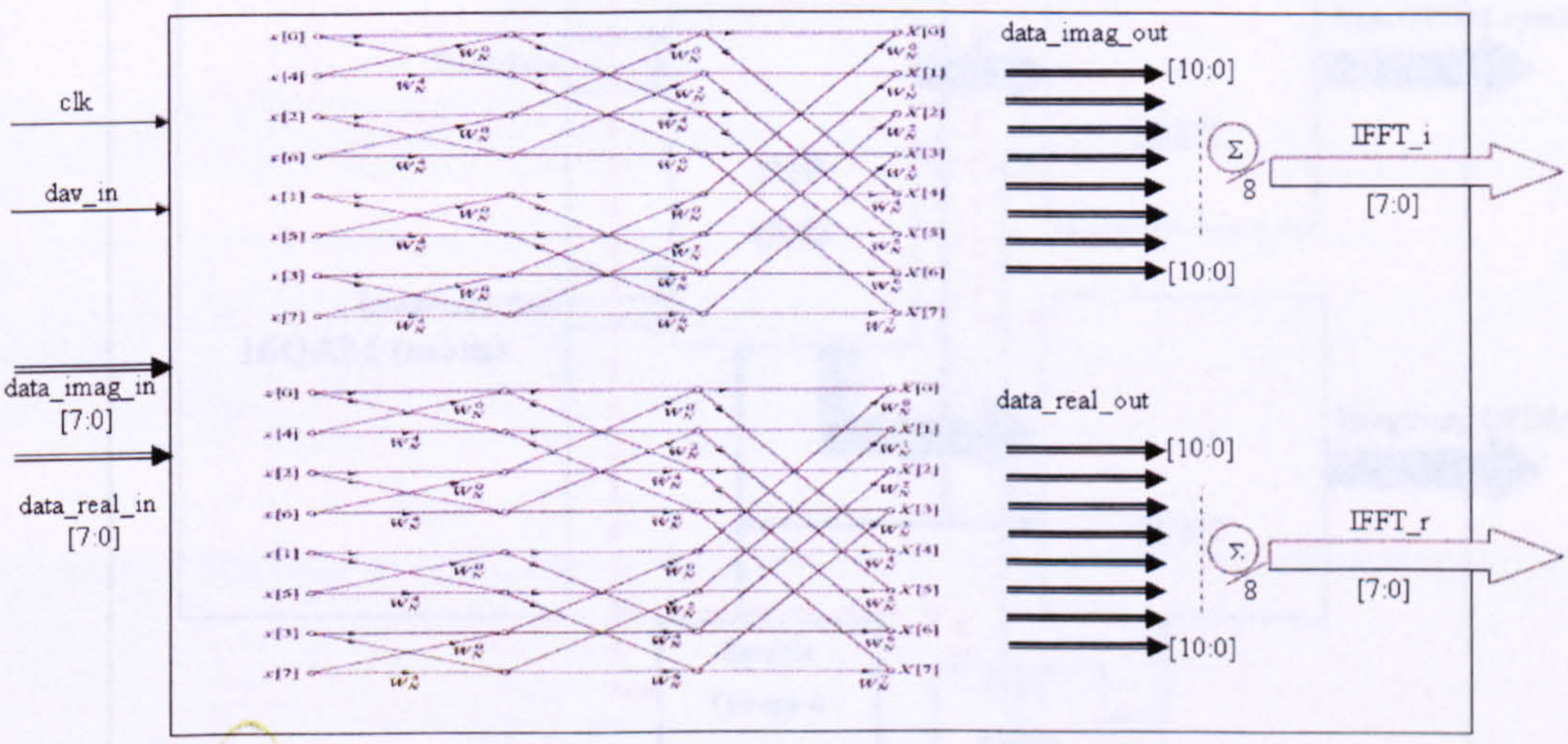


**Figure 6.17: Designing the IFFT block0**

The design of the twiddle factors is described as follows in Table 6.5.

**Table 6.5: Designing the twiddle factors**

| |
|---|
| 0.5 |
| 0.25 |
| 0.125 |
| 0.0625 |
| 0.03125 |
| 0.015625 |
| 0.0078125 |

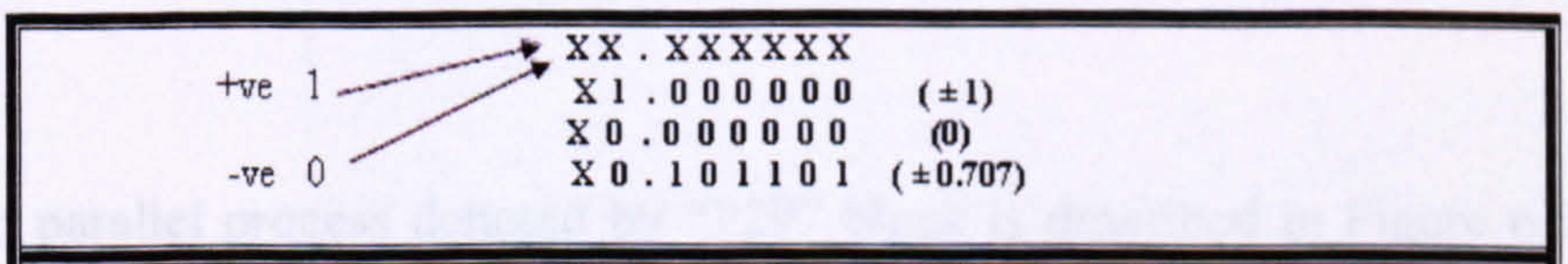


| | | | |
|---|---|---|---|
| $W^{00} = 1$ | $W^{20} = 1$ | $W^{40} = 1$ | $W^{60} = 1$ |
| $W^{01} = 1$ | $W^{21} = j$ | $W^{41} = -1$ | $W^{61} = -j$ |
| $W^{02} = 1$ | $W^{22} = -1$ | $W^{42} = 1$ | $W^{62} = -1$ |
| $W^{03} = 1$ | $W^{23} = -j$ | $W^{43} = -1$ | $W^{63} = j$ |
| $W^{04} = 1$ | $W^{24} = 1$ | $W^{44} = 1$ | $W^{64} = 1$ |
| $W^{05} = 1$ | $W^{25} = j$ | $W^{45} = -1$ | $W^{65} = -j$ |
| $W^{06} = 1$ | $W^{26} = -1$ | $W^{46} = 1$ | $W^{66} = -1$ |
| $W^{07} = 1$ | $W^{27} = -j$ | $W^{47} = -1$ | $W^{67} = j$ |
| $W^{10} = 1$ | $W^{30} = 1$ | $W^{50} = 1$ | $W^{70} = 1$ |
| $W^{11} = 0.707+j0.707$ | $W^{31} = -0.707+j0.707$ | $W^{51} = -0.707-j0.707$ | $W^{71} = 0.707-j0.707$ |
| $W^{12} = j$ | $W^{32} = -j$ | $W^{52} = j$ | $W^{72} = -j$ |
| $W^{13} = -0.707+j0.707$ | $W^{33} = 0.707+j0.707$ | $W^{53} = 0.707-j0.707$ | $W^{73} = -0.707-j0.707$ |
| $W^{14} = -1$ | $W^{34} = -1$ | $W^{54} = -1$ | $W^{74} = -1$ |
| $W^{15} = -0.707-j0.707$ | $W^{35} = 0.707-j0.707$ | $W^{55} = 0.707+j0.707$ | $W^{75} = -0.707+j0.707$ |
| $W^{16} = j$ | $W^{36} = j$ | $W^{56} = -j$ | $W^{76} = j$ |
| $W^{17} = 0.707-j0.707$ | $W^{37} = -0.707-j0.707$ | $W^{57} = -0.707+j0.707$ | $W^{77} = 0.707+j0.707$ |

Figure 6.18 shows the process of generating OFDM Symbols after the IFFT block. The input data generated from the 16QAM block (main); a parallel to parallel block denoted by "P2P" with a 3 bits input and 8 bits output; and the real and imaginary parts of the OFDM symbol described by "Real OFDM symbol and Imaginary OFDM symbol".

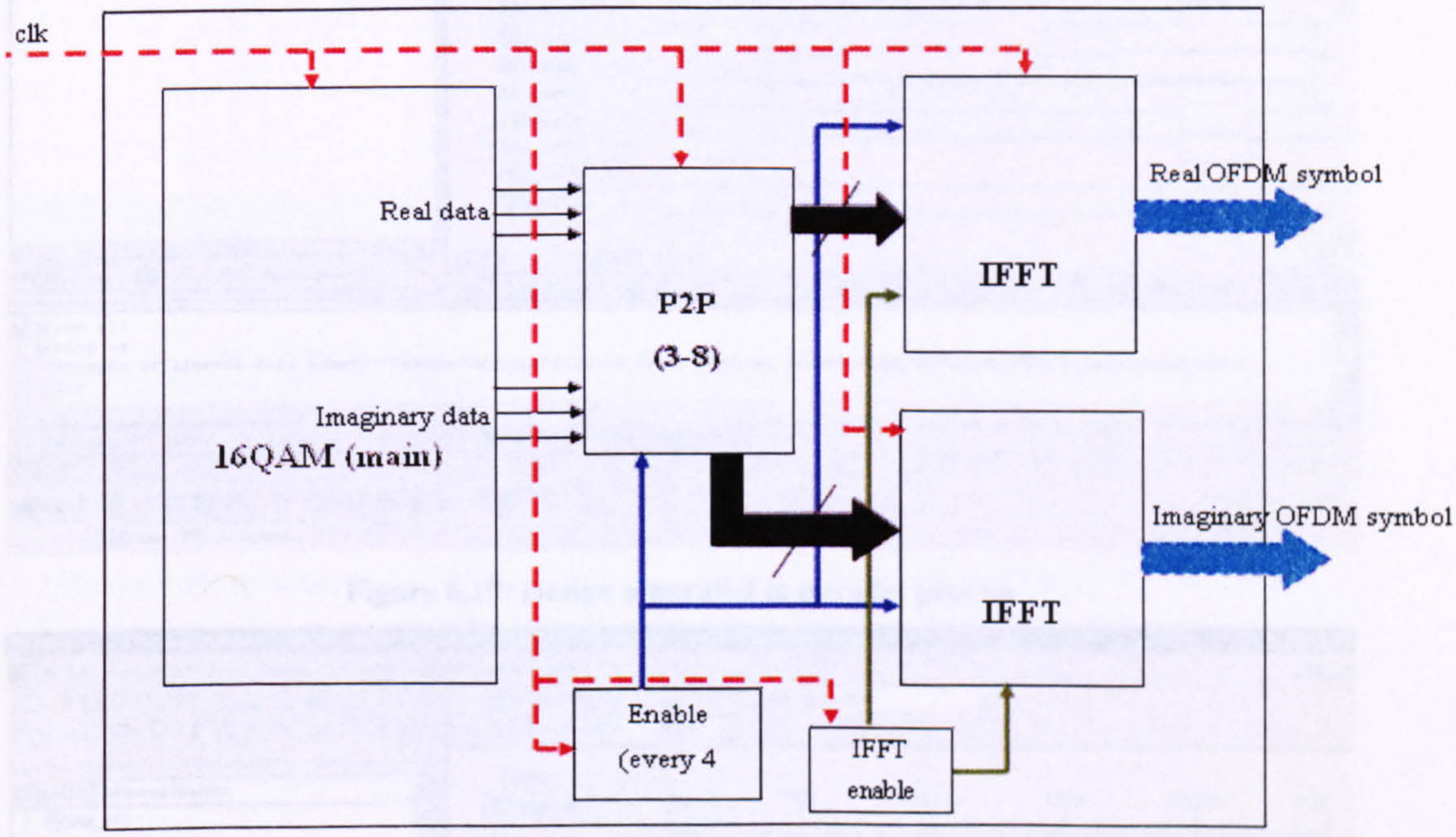


**Figure 6.18: Producing OFDM symbols**

The 16QAM block (main) shown in Figure 6.18 consists of the following concatenation blocks, random number generator, turbo encoder and 16QAM modulation.

The parallel to parallel process denoted by "P2P" block is described in Figure 6.19. The idea behind applying this block is to match output data from the 16QAM block which is in 3 bits width to the size of the IFFT block which is in 8 bits size. The input data is denoted by "p_in", and "p_out" describes the output data. This block accommodates two 16QAM symbols in the first 6 bits while padded the rest two bits by zeros. Figure 6.20, shows the achieved real and imaginary parts of the OFDM symbols. The real part is defined by "OFDM_r", and "OFDM_i" denotes the imaginary part of the OFDM symbol.

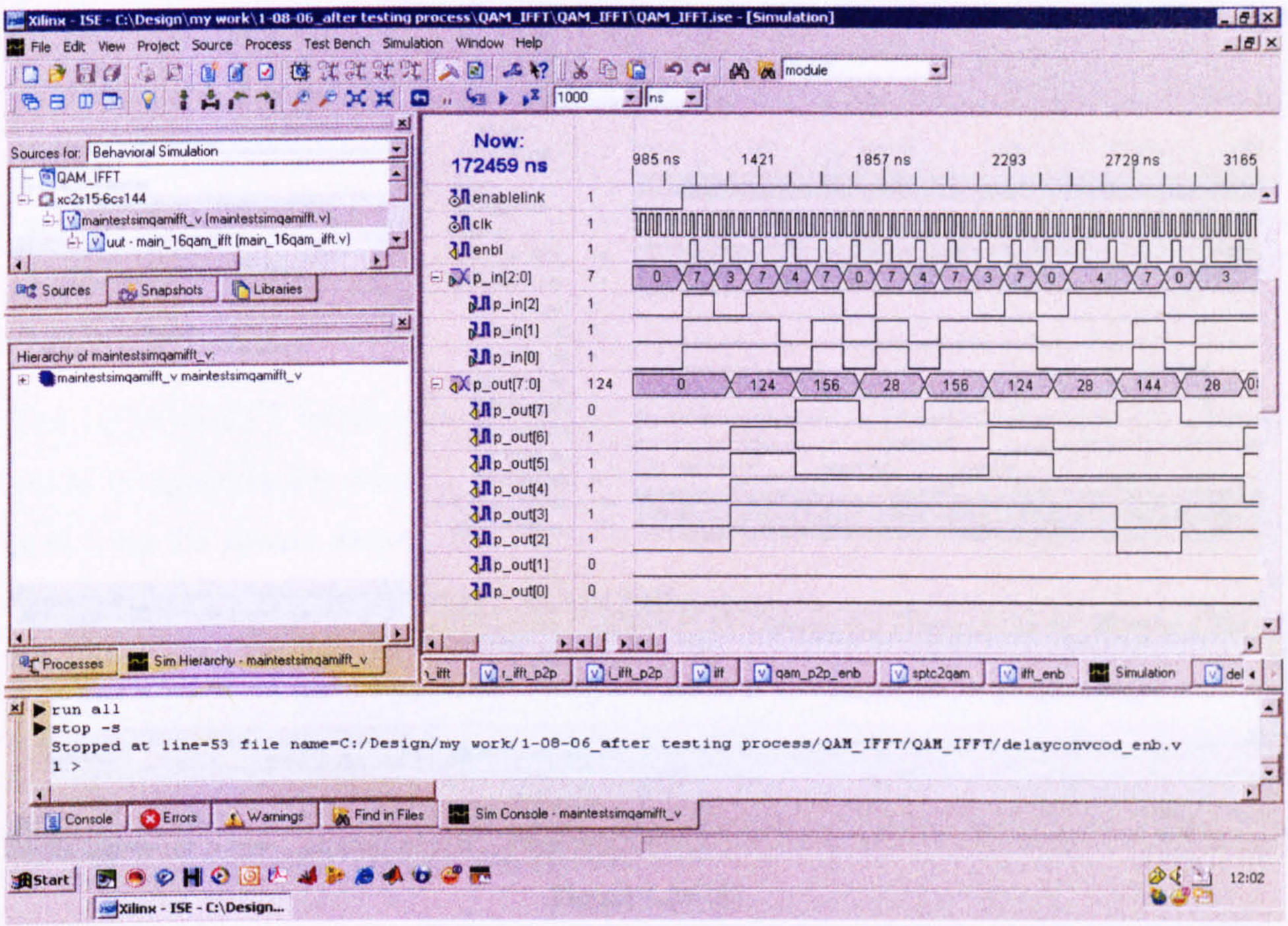


**Figure 6.19: Design a parallel to parallel process**

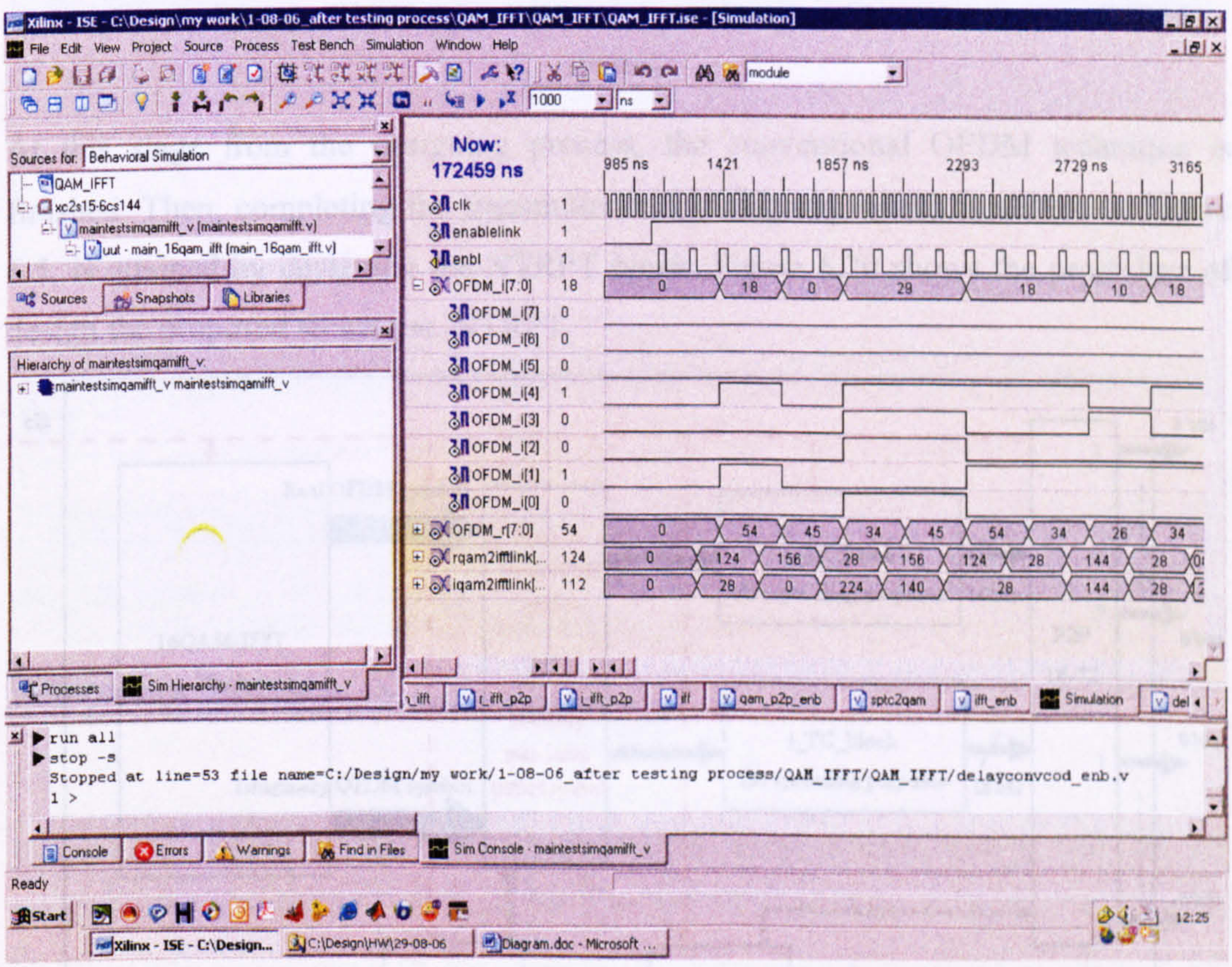


**Figure 6.20 (a)**

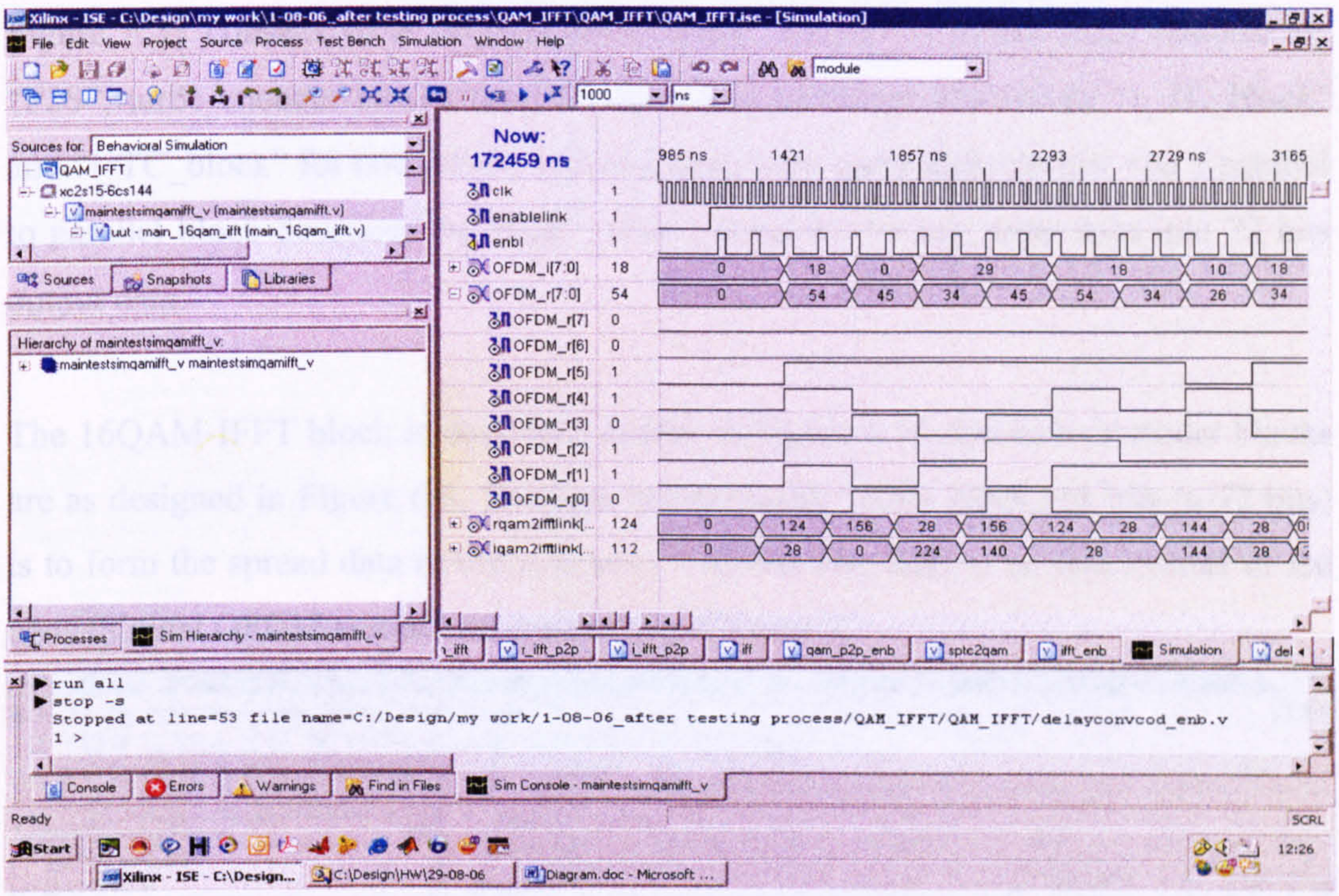


**Figure 6.20 (b)**

**Figure 6.20: Producing the OFDM symbols after IFFT block, (a) describing the data of the imaginary part of the OFDM symbol, (b) describing the data of the real part of the OFDM symbol.**

At this stage from the designing process, the conventional OFDM technique is finished. Then, completing the transmitter block diagram, which is shown in Figure 6.5, is attained by designing the NTRPT block. Figure 6.20 shows the procedure of design the proposed technique, NTRPT.

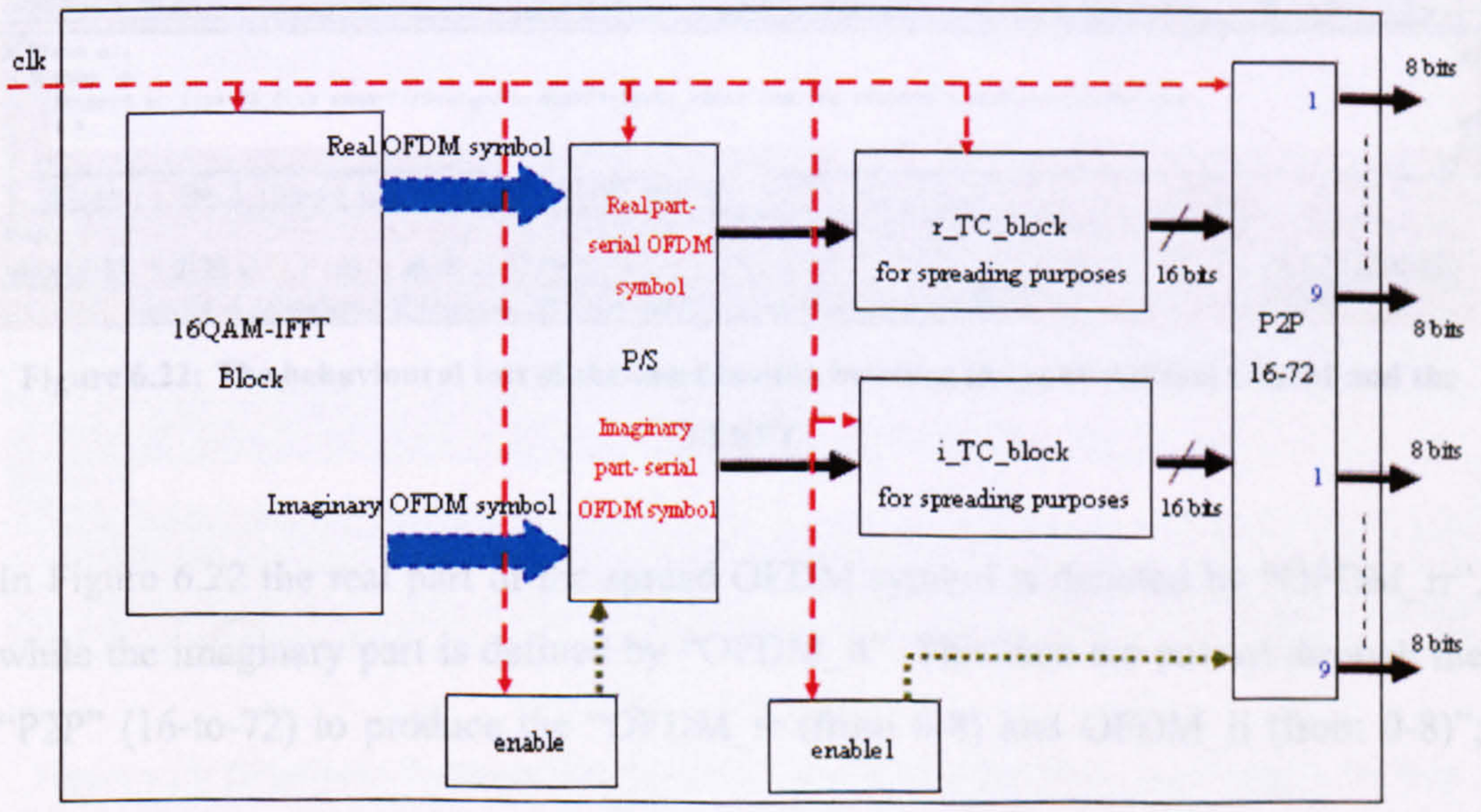


**Figure 6.21: Describing the proposed technique**

Figure 6.21 consists of a 16QAM-IFFT block; parallel to serial block denoted by "P2S"; turbo encoder blocks used for spreading purposes denoted by "r_TC_block" and "i_TC_block" for both of the real and imaginary parts respectively; and a parallel to parallel block described by "P2P", which form the 16 bits input data into 72 bits output data.

The 16QAM-IFFT block is described earlier in Figure 6.18 and turbo encoder blocks are as designed in Figure 6.8. The idea behind using "P2P" block (16 bits-to-72 bits) is to form the spread data in order to search for the best data to be sent instead of the conventional OFDM symbol as described in Chapter 4.

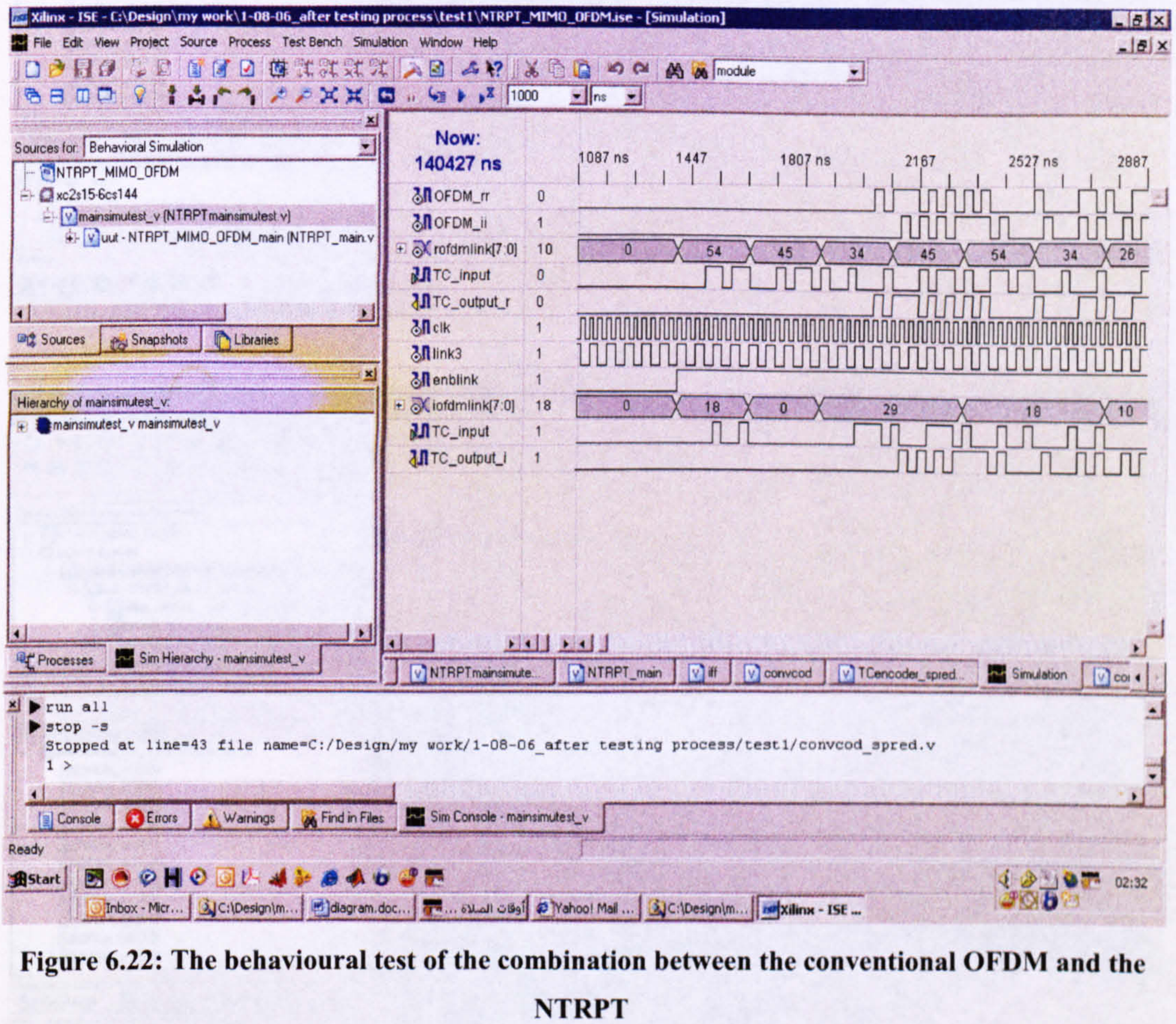


**Figure 6.22: The behavioural test of the combination between the conventional OFDM and the NTRPT**

In Figure 6.22 the real part of the spread OFDM symbol is denoted by "OFDM_rr", while the imaginary part is defined by "OFDM_ii". This data are passed through the "P2P" (16-to-72) to produce the "OFDM_rr (from 0-8) and OFDM_ii (from 0-8)";

which they are described in Figures 6.23 and 6.24; and denote the result of the processed real and imaginary parts of OFDM symbols.

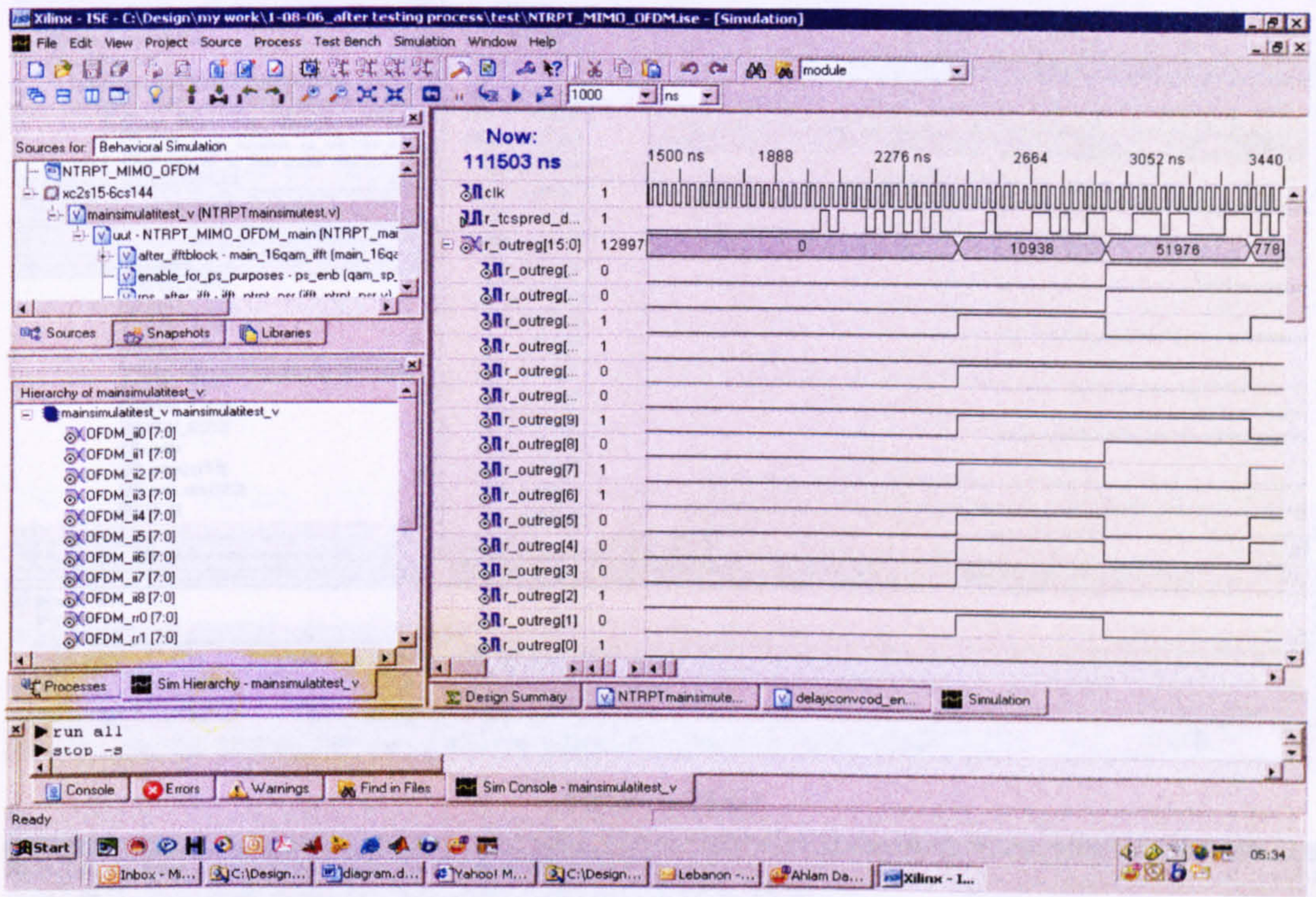


**Figure 6.23 (a)**

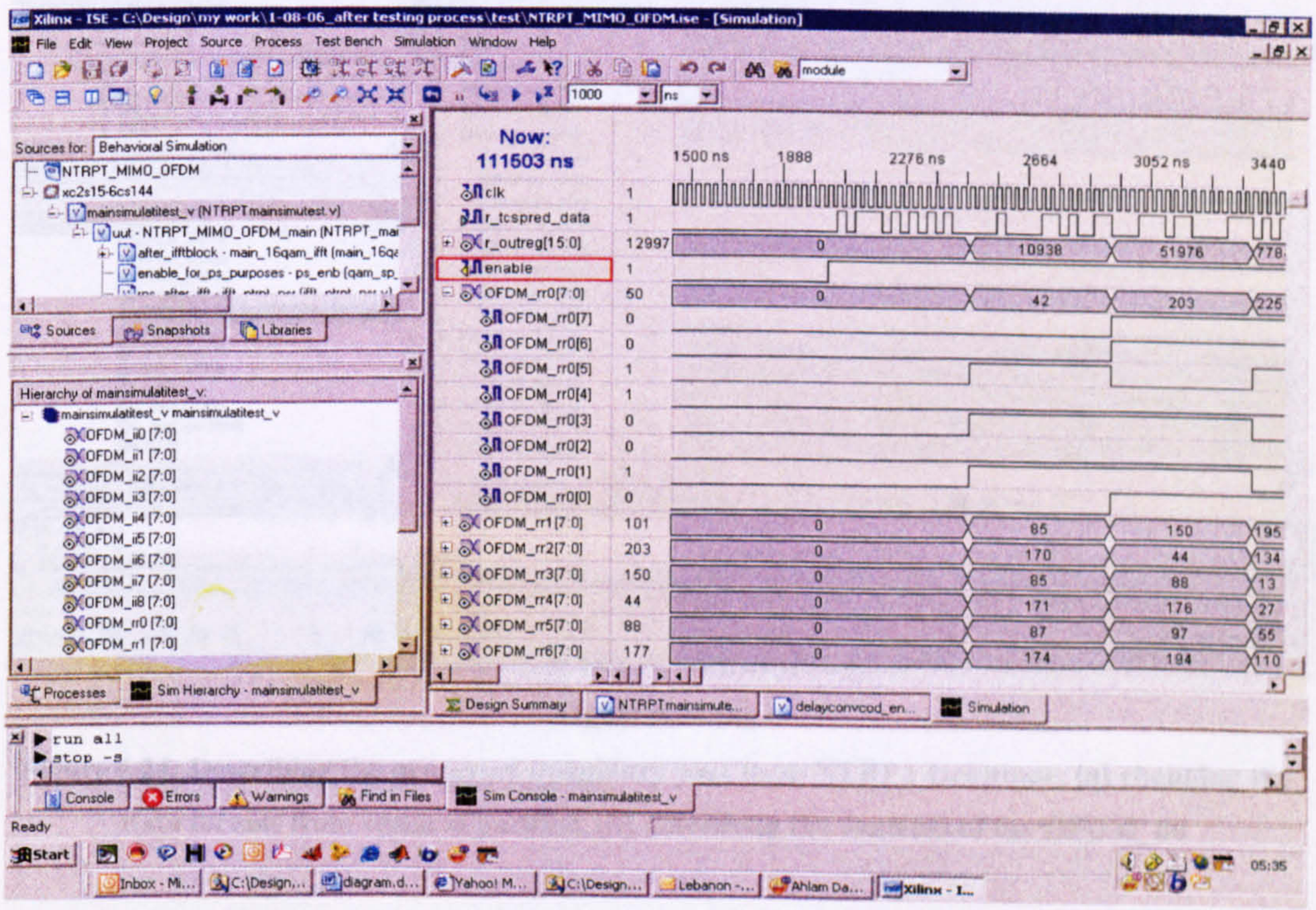


**Figure 6.23 (b)**

**Figure 6.23: Describing the processed real part from NTRPT technique, (a) changing the data format from serial to parallel, (b) describing the contents of the OFDM_rr0**

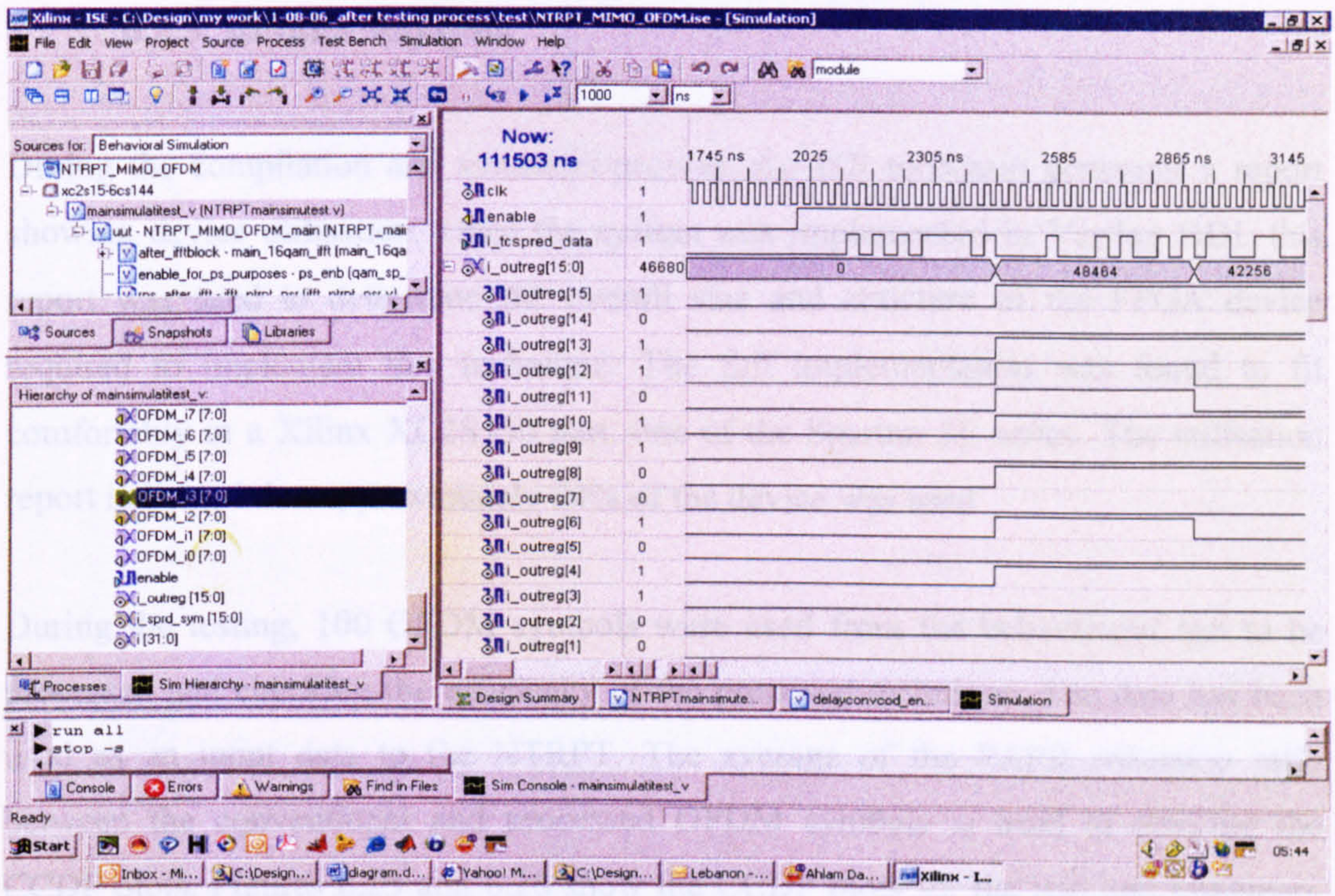


**Figure 6.24 (a)**

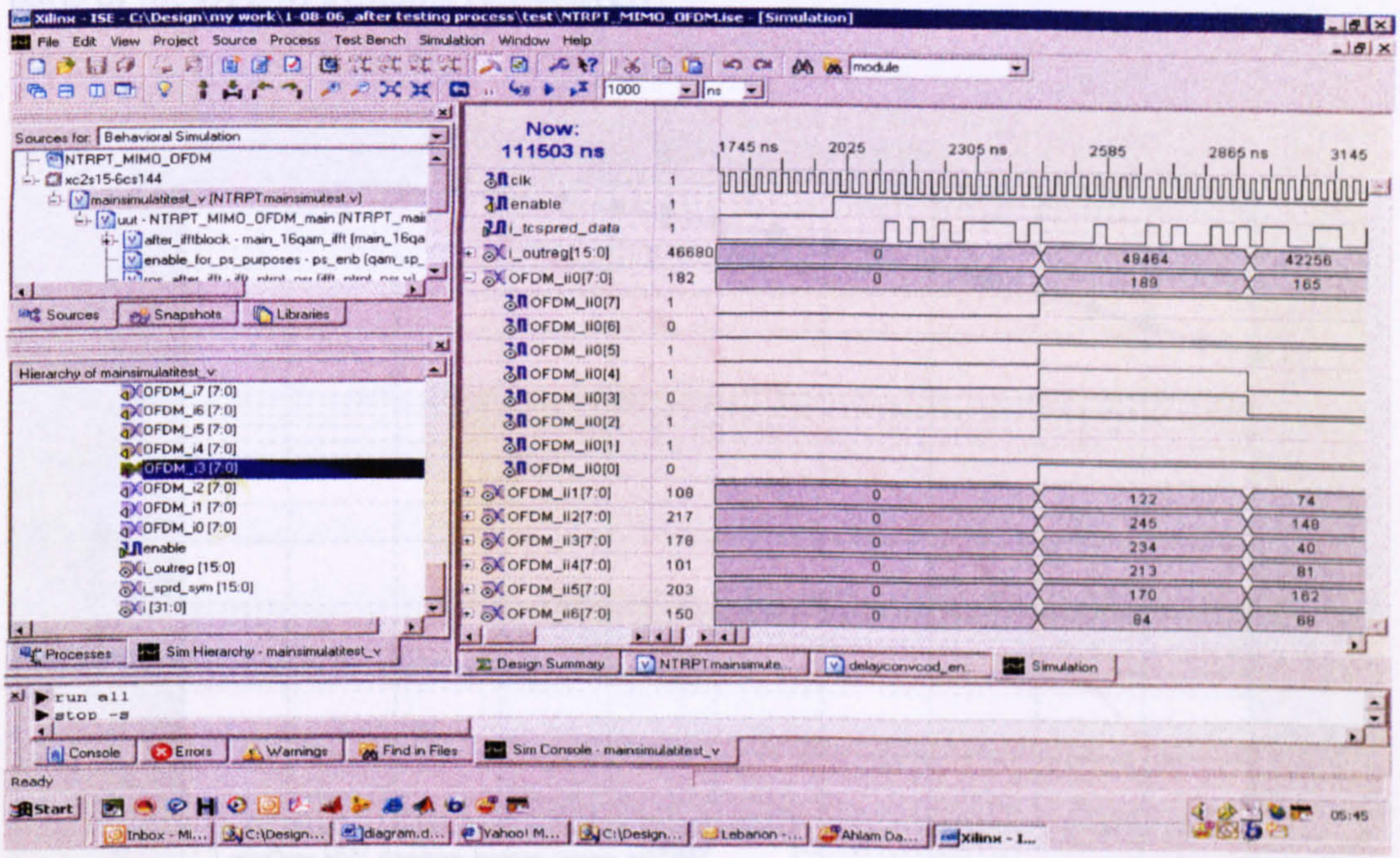


**Figure 6.24 (b)**

**Figure 6.24: Describing the processed imaginary part from NTRPT technique, (a) changing the data format from serial to parallel, (b) describing the contents of the OFDM_ii0**

The achieved results from the behavioural test either from conventional OFDM data or from NTRPT technique are taken to be processed by a MATLAB to be compared with the simulator. This comparison is described in the following subsection.

### 6.2.3. Results Analysis

During the compilation and synthesis process, the ISE toolchain generates a report showing device utilisation. Once the system was implemented in Verilog HDL this report was used to determine the overall size and structure of the FPGA device required to implement this technique. The full implementation was found to fit comfortably in a Xilinx XC2S150 part, one of the Spartan 2E series. The utilisation report indicated that approximately 64% of the device was used.

During the testing, 100 OFDM symbols were used from the behavioural test to be processed and checking the efficiency of the proposed technique. The data has been used as an input data to the NTRPT. The average of the PAPR reduction ratio between the conventional and processed OFDM symbols is used in drawing the CCDF plots. Figures 6.25 and 6.26 show the CCDF plots for the real and imaginary parts of the OFDM symbols respectively.

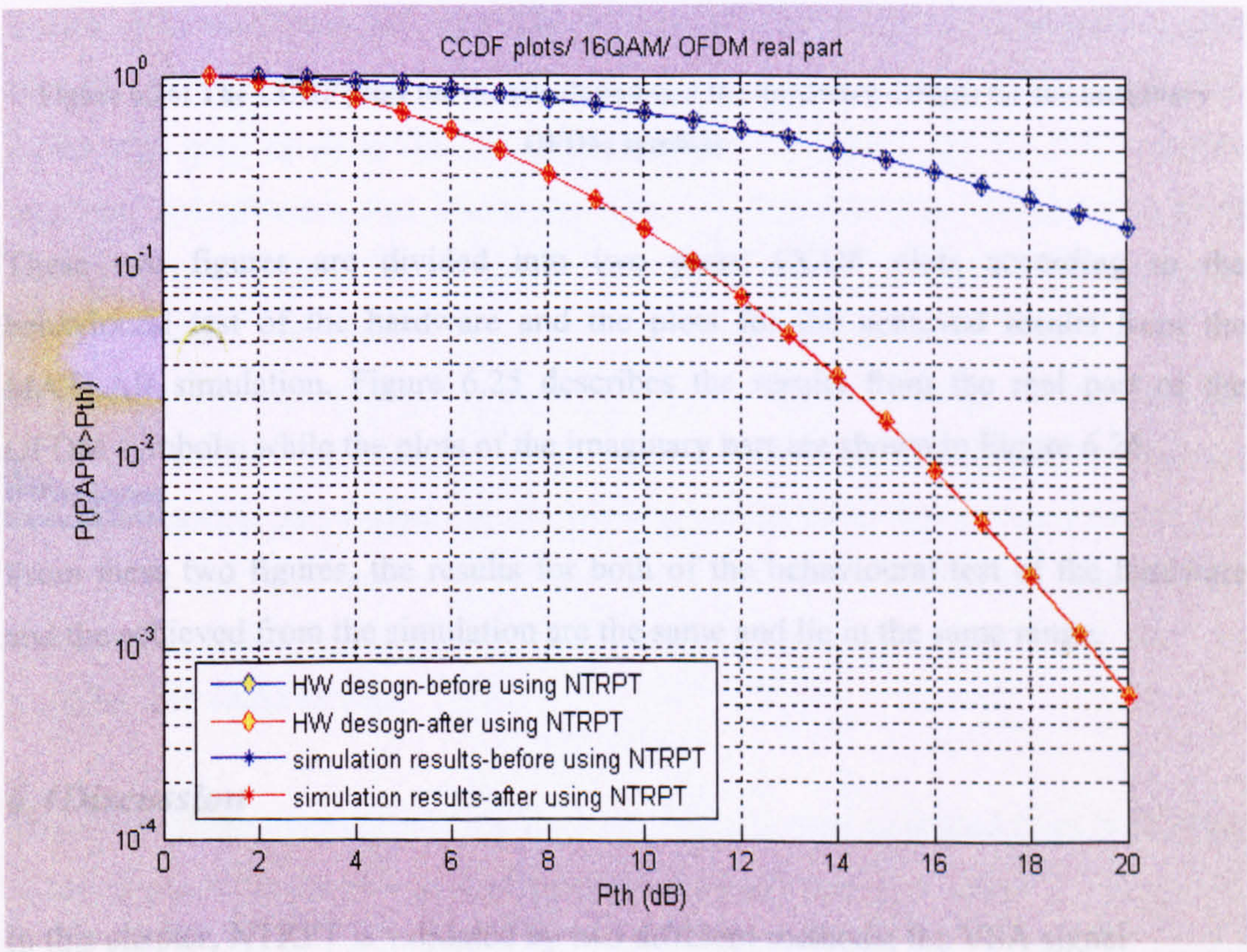


**Figure 6.25: The CCDF plots for the simulation and the hardware designs for the real OFDM symbols**

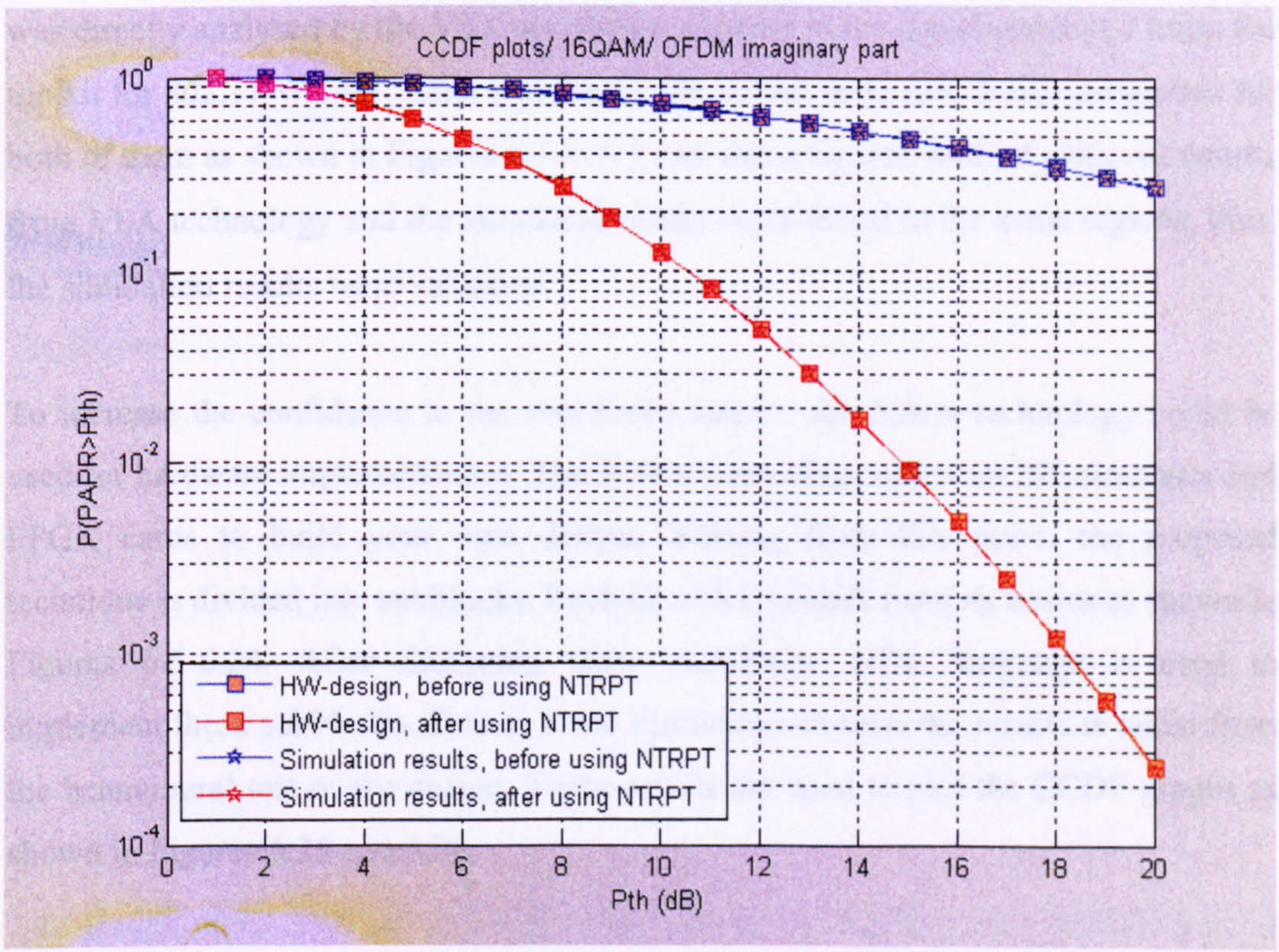


**Figure 6.26: The CCDF plots for the simulation and the hardware designs for the imaginary OFDM symbols**

These two figures are divided into two parts; CCDF plots according to the behavioural test of the hardware and the plots for the achieved results from the MATLAB simulation. Figure 6.25 describes the results from the real part of the OFDM symbols, while the plots of the imaginary part are shown in Figure 6.26.

From these two figures, the results for both of the behavioural test of the hardware and the achieved from the simulation are the same and lie in the same range.

## *6.4Discussion*

In this chapter, NTRPT is validated by two different methods; the VSA signal generator and the behavioural test of a hardware design.

Validation by Agilent technology is achieved since the MATLAB modulated signal was directly analysed by the VSA and then compared to the signal generated using the toolkit for 802.11 WLAN. After that the CCDF values were calculated and plotted for both of them as shown in Figures 6.1-6.4. From these figures, both of achieved results from VSA technology and the simulated results were found in the same regions, thus, the simulation results were validated.

To increase the confidence in the simulation results, the Xilinx technology could be used for hardware implementation. The Xilinx technology offers an ISE simulator and FPGA cards to build your own design. Starting from this point, the proposed technique is divided into subblocks. Each of which is built from its basics as shown in Figures 6.5-6.24. After designing these subblocks, HDL language is used to implement these subblocks. Due to some limitations in time the results is taken from the behavioural test of the design. These results are used to plot the CCDF graphs as shown in Figures 6.25 and 6.26.

During the compilation and synthesis process, the ISE toolchain generates a report showing device utilisation. Once the system was implemented in Verilog HDL this report was used to determine the overall size and structure of the FPGA device required to implement this technique. The full implementation was found to fit comfortably in a Xilinx XC2S150 part, one of the Spartan 2E series. The utilisation report indicated that approximately 64% of the device was used. The Spartan 2E series is a mature, readily available low cost family, showing clearly that the technique can be implemented using low-cost hardware. It is possible to reduce device utilisation still further. In the implementation used during this research, the IFFT block was implemented directly from the flow-graph to expedite development. If necessary, better, space-efficient FPGA implementations of the FFT and IFFT are available and could be used.

From the above achievements, the simulation results were validated from both of the achieved results by the Agilent and the Xilinx technologies.

# Chapter Seven

# 7. Case Studies

## *7.1Introduction*

This chapter will describe the NTRPT for a MIMO-OFDM system from the application's point of view. NTRPT has already been applied to reduce the PAPR of a MIMO-OFDM system in Chapter 5, and the conclusion was reached that this technique can support different types of modulation and coding techniques, as well as offering better PAPR reduction than the conventional techniques currently proposed, such as clipping and PTS techniques.

This chapter is divided into two main parts; firstly, the NTRPT for a MIMO-OFDM-based Digital Video Broadcasting—Handheld (DVB-H) is applied, and secondly, it is applied to the IEEE 802.11n WLAN system. Applying OFDM systems with MIMO technology to these applications will guarantee the very good quality of both of the data and video streams, since these systems show great promising in the area of supporting high data rate transmissions.

Section 7.1 of this chapter gives a brief overview of DVB-H, Section 7.2 will give one of the WLAN IEEE 802.11n, the simulation results will be discussed in Section 7.3, and Section 7.4 will conclude this chapter.

### 7.1.1 Digital Video Broadcasting—Handheld

The DVB Project started research work into the possibility of mobile reception of DVB-T signals as early as 1998, accompanying the introduction of commercial terrestrial digital TV services in Europe. DVB-T shows sufficient flexibility to permit mobile broadcast services. Thus, in early 2002, the DVB community was asked to

provide technical specifications to allow delivery of rich multimedia contents to handheld terminals, a property that was missing in the original DVB-T. This would make it possible to receive TV-type services in a small, handheld device like a mobile phone. This approach requires specific features from the transmission system serving such devices which in turn increases battery usage duration, maintains access to services when receivers leave a given transmission cell and enter a new one, and mitigates of the effect of multipath channels, as well as offering sufficient flexibility and scalability to allow the reception of the services at various speeds while optimising transmitter coverage. The work to define such a system within the DVB Project started in the beginning of the year 2002 by defining a set of commercial requirements for a system supporting handheld devices. The technical work then led to a system called DVB-H, which was published as European Telecommunications Standards Institute (ETSI) Standard EN 302 304 in November 2004 [107].

The DVB-H system is defined based on the existing DVB-T standard for fixed and in-car reception of digital TV. The main additional element in the physical layer is the adopted OFDM for the 4k mode. Also, DVB-H can use all modulation formats, QPSK, 16QAM, and 64QAM with non-hierarchical or hierarchical modes, a capacity which gives additional flexibility for network design. Table 7.1 describes the different options of the DVB-H physical layer parameters [108].

**Table 7.1: The options of the DVB-H physical layer parameters.**

| Parameter | |
|---|---|
| Channel Bandwidth (MHz) | 5,6,7 and 8 |
| FFT sizes | 8k, 4k and 2k |
| Active carriers | 6817, 3409 and 1705 |
| Number of data carriers | 6048, 3024 and 1512 |
| Carrier Spacing (Hz) | 1116, 2232 and 4464 |
| Guard Intervals | 224, 112, 56, 28, 14 and 7 |
| Modulation | QPSK, 16-QAM and 64-QAM |
| Convolutional code rates | 1/2, 2/3, 3/4, 5/6 and 7/8 |

### 7.1.2 Wireless LAN – IEEE 802.11n

The rapidly growing demand for mobile communication and computing has led to intensified interest in increasing the system data rate. Thus, the IEEE announced in

January 2004 that it had formed a new Task Group (TGn) to investigate an new amendment to the WLAN IEEE802.11 standard.

Compared to the previous standards-based 802.11a and 802.11g, which support a throughput up to 54 Mbps, the real potential throughput of this amendment is to reach 540 Mbps, which may lead to a new physical layer structure. That means that it should be up to 100 times faster than 802.11b, as well as offering 802.11n a better operating distance than current networks.

As was mentioned in Chapter 2, MIMO technology uses spatial multiplexing increases data throughput, while exploiting spatial diversity to increase the overall range. Due to these advantages, 802.11n builds upon previous standards by adding MIMO technology.

According to the IEEE 802.11 Working Group Project Timelines, the 802.11n standard is not due for final approval until July 2007 [109].

## *7.2Simulation Results*

In order to verify the mathematically derived result in Chapter 4, a MATLAB simulation program was developed for a uniformly distributed, randomly generated data sequence. Table 7.2 summarises the simulation parameters:

**Table 7.2: The simulation parameters**

| The simulation Parameters | | |
|---|---|---|
| | DVB-H | IEEE 802.11n |
| Channel coding techniques | Convolutional encoder | Turbo encoder |
| Channel coding rate(s) | 1/2 | 1/2 and 1/3 |
| IFFT sizes | 4k | 64 |
| Modulation | QPSK, 16-QAM and 64-QAM | BPSK, QPSK, 16-QAM and 64-QAM |
| Spreading rates | 2 and 3 | 2 and 3 |
| MIMO encoder | STBC and V-BLAST | STBC and V-BLAST |

### 7.2.1 NTRPT for a MIMO-OFDM-based DVB-H

Table 7.3 summarises the simulation results for applying NTRPT to a MIMO-OFDM-based DVB-H. As shown from Table 7.2, different modulation techniques, spreading rates and MIMO encoders are used.

From Table 7.3, it can be seen that the proposed technique maintains a very good PAPR reduction ratio despite using different modulation techniques, MIMO encoders and spreading rates.

Moreover, it shows a slight improvement in the PAPR reduction ratios as a consequence of using different spreading rates. The improvement of the reduction ratio of the PAPR reaches 93.7 % and 81.2 % when the spreading rate equals 3 and 2 respectively.

**Table 7.3: Applying the NTRPT to a MIMO-OFDM-based DVB-H**

| Modulation tech. | MIMO encoding | PAPR before applying NTRPT (dB) | PAPR after applying NTRPT (dB) | | The reduction ratio (%) | | The improvement (%) |
|---|---|---|---|---|---|---|---|
| | | | Spreading rate | | Spreading rate | | |
| | | | 2 | 3 | 2 | 3 | |
| QPSK | STBC | 12.5 | 6.3 | 5.6 | 49.6 | 55.2 | 5.6 |
| | V-BLAST | 12.6 | 2.9 | 2.5 | 77 | 80 | 3 |
| 16QAM | STBC | 11.2 | 2.1 | 1.7 | 81.2 | 93.7 | 12.5 |
| | V-BLAST | 12.6 | 2.7 | 2.4 | 78.5 | 81 | 2.5 |
| 64QAM | STBC | 11.3 | 3.4 | 3 | 70 | 73.5 | 3.5 |
| | V-BLAST | 13.7 | 4.1 | 3.8 | 70 | 72.2 | 2.2 |

### 7.2.2 NTRPT for a MIMO-OFDM-based IEEE 802.11n

Table 7.4 summarises the simulation results when applying NTRPT to a MIMO-OFDM-based IEEE 802.11n. This table shows that the NTRPT gives significant results even with different MIMO-OFDM system structures.

**Table 7.4: Applying the NTRPT to a MIMO-OFDM-based IEEE 802.11n**

| Modulation tech. | Coding rate | MIMO encoding | PAPR before applying the NTRPT (dB) | PAPR after the NTRPT (dB) | | The reduction ratio (%) | | The improvement (%) |
|---|---|---|---|---|---|---|---|---|
| | | | | Spreading rate | | Spreading rate | | |
| | | | | 2 | 3 | 2 | 3 | |
| BPSK | 1/2 | STBC | 12.264 | 2.32 | 1.41 | 81.1 | 88.5 | 7.4 |
| | | V-BLAST | 12.851 | 2.42 | 1.06 | 81.2 | 91.7 | 10.5 |
| | 1/3 | STBC | 10.366 | 2.29 | 1.51 | 77.9 | 85.4 | 7.5 |
| | | V-BLAST | 13.994 | 1.62 | 1.22 | 88.4 | 91.3 | 2.9 |
| QPSK | 1/2 | STBC | 10.394 | 2.09 | 1.87 | 79.9 | 82 | 2.1 |
| | | V-BLAST | 14.397 | 2.57 | 2.11 | 82.1 | 85.3 | 3.2 |
| | 1/3 | STBC | 11.252 | 3.42 | 3.21 | 69.8 | 71.4 | 0.6 |
| | | V-BLAST | 12.824 | 1.54 | 1.01 | 88 | 92.1 | 4.1 |
| 16QAM | 1/2 | STBC | 8.307 | 1.07 | 0.62 | 87.1 | 92.5 | 5.4 |
| | | V-BLAST | 10.601 | 1.55 | 1.13 | 85.4 | 89.3 | 3.9 |
| | 1/3 | STBC | 11.610 | 1.42 | 1.26 | 87.8 | 89.1 | 1.3 |
| | | V-BLAST | 11.980 | 1.41 | 1.21 | 88.2 | 90 | 1.8 |
| 64QAM | 1/2 | STBC | 9.517 | 1.12 | 0.92 | 88.2 | 90.3 | 2.1 |
| | | V-BLAST | 11.728 | 1.74 | 1.43 | 85.2 | 87.8 | 2.6 |
| | 1/3 | STBC | 13.180 | 2.1 | 1.19 | 84.1 | 91 | 5.9 |
| | | V-BLAST | 13.013 | 1.97 | 1.74 | 84.9 | 86.6 | 1.7 |

The PAPR reduction ratios for using STBC as a MIMO encoder varies between 75.6 % and 85.2 % , and between 73.4 % and 84 % when using coding rates 1/2 and 1/3

respectively. Using V-BLAST as a MIMO encoder, the achieved ratios vary between 78.5 % and 86.4 % and between 83.6 % and 86.7 % for using coding rates 1/2 and 1/3 respectively. The results shown in Tables 7.3 and 7.4 lead to the conclusion that NTRPT is suitable for implementation in the two different systems of DVB-H and IEEE 802.11n.

Increasing the NTRPT spreading rate will give a slight improvement in PAPR reduction ratios. Thus, the spreading rate which is equal to 2 is enough for the above improvement.

## *7.3Summary*

In this chapter, the proposed technique was applied to two conventional MIMO-OFDM systems. From the simulation results shown in Table 7.3 and Table 7.4, it can be concluded that NTRPT gives significant PAPR reduction ratios despite using different MIMO-OFDM systems' structures. Thus, NTRPT could be used in furtherance of the main aim of this thesis, which is the improvement of the QoS of Beyond 3G systems in terms of supporting the high quality multimedia applications.

# Chapter Eight

# 8. Conclusions and Future work

The design choice of communication system is largely constrained by the communication channel used. Due to the constructive and destructive combination of the multipath signals during the channel, the received signal can strongly vary as a function of time, frequency and location. The frequency selectivity of channel can be mitigated by OFDM, which essentially splits a wideband frequency selective fading channel into multiple orthogonal narrowband flat fading channels. This process will reduce the equalisation complexity. Together with the robustness and data rate enhancement of MIMO in rich-scattering environments, MIMO-OFDM is seen as a very promising solution for the next generation.

In the next section the research findings are discussed, Section 8.2 describes the research contribution, while the future work is recommended in Section 8.3.

## *8.1Research Findings*

- A MIMO capacity formula-based on the correlation coefficient matrices has been proposed. Depending on this formula, a MIMO channel model was proposed in order to detail the effect of the channel parameters on the system performance. The main features of this model are:

i. As shown in Chapter 3, the achieved capacity formula is divided into two parts: the capacity of parallel independent subchannels and the correlation between the subchannels.

ii. From the proposed model, MOM, the determinant of the correlation matrices is upper-bounded by 1 and lower bounded by 0. Thus, any changes in its

determinant will vary the MIMO channel capacity between its maximum and minimum values. This was shown in Chapter 3.

- A novel technique based on linear coding techniques, NTRPT, which is intended to reduce the PAPR problem, has been proposed for MIMO-OFDM systems. This technique significantly reduces the large values of PAPR compared to the reduction achieved by conventional techniques. A mathematical model simulation and practical validation were performed to validate this technique. As a result, from the mathematical model and the simulation results, the following potential qualities of NTRPT can be established:

i. There is no data loss due to the use of NTRPT to combat PAPR. It also reduces the added complexity formula to the first order. Chapter 4 presents this achievement.

ii. With reference to Chapter 5, NTRPT gives significant PAPR reduction ratios despite using different MIMO-OFDM systems' structures. Thus, it can be used for adaptive MIMO-OFDM systems.

iii. In order to interact with real systems, the proposed technique was implemented in a Xilinx FPGA card to provide the ability to interact with real system. Detailed information is given in Chapter 6.

iv. It is strongly recommended that the turbo encoder is used as a spreading technique in NTRPT, due to its better ability to combat PAPR than convolutional encoders.

- The NTRPT is validated by two different methods; the VSA signal generator and the behavioural test of a hardware design. Validation by Agilent technology is achieved since the MATLAB modulated signal was loaded to be analysed by the VSA and then compared to the signal generated using the toolkit for 802.11 WLAN. After that the CCDF values were calculated and plotted for both of them. By making use of the Xilinx technology, the CCDF plots of behavioural test results are used to

be compared with simulation results. From both of the achieved results by the Agilent and the Xilinx technologies, the simulation results of the proposed technique are validated. Moreover, the proposed technique is feasible to be applied to real time systems.

- After validating the proposed technique, it has been applied into two different case studies, a WLAN IEEE 802.11n and DVB-H. From the simulation results, it can be concluded that the NTRPT gives significant PAPR reduction ratios despite of using different MIMO-OFDM systems' structures. Then, it could be used to improve the QoS of Beyond 3G systems.

## *8.2Research Contributions*

This work's contribution to knowledge consists firstly of the proposition of a MIMO channel model based on the derived MIMO channel capacity formula. This model shows the effect of the correlation coefficients on the system performance, and especially system capacity. Secondly, it describes the proposed model of a novel technique to reduce the effect of PAPR on MIMO-OFDM systems. This technique has advantages over conventional techniques, such as the significant reduction ratios of PAPR and the tackling of the PAPR problem without data loss or an increase of overall system complexity.

With the success of proposing both NTRPT (novel technique to reduce the PAPR problem of MIMO-OFDM systems) and MOM (a MIMO channel to cover all cases from the effect of the correlation coefficients on the MIMO capacity), it is reasonable to conclude that the aim and objectives set forth at the start of this work have been fulfilled.

## *8.3Future work*

The greater success of the proposed technique over conventional techniques direction leads to the following suggestions for further research.

It is highly recommended that future work investigate using other types of either linear or nonlinear coding techniques in NTRPT is considerable. As an example the Low Density Parity Check (LDPC) codes could be used and the achieved results could be compared to what was achieved from using linear encoders. Furthermore, a set of nonlinear encoders could be used to check the capability of PAPR reduction based on nonlinear encoders and the results compared with these from the linear encoder.

The channel model, MOM, could be modified to cover the effect of other channel parameters on the overall MIMO-OFDM systems. In addition, some of the nonlinear detection techniques, such as the Maximum Likelihood Detection technique could be investigated.

In this work, the open-loop MIMO-OFDM scheme is used. For particular environments closed-loop scheme might be feasible and beneficial. Hence, it might be good to list and define a number of closed-loop schemes and evaluate their performance and compare it with those of the open-loop counterparts.

Search for an efficient mathematical algorithm that allow for low-cost hardware of the NTRPT-MIMO-OFDM implementation.

It would be useful to include other SDM receiver algorithms such as MLD and ZF with Successive Interference Cancellation (SIC) besides, finding an upper bound of the error rate performance.

# References

[1] H. Harada and R. Prasad, "Simulation and Software Radio for Mobile Communications", Artech House, May 2002.

[2] R. van Nee and R. Prasad "OFDM wireless multimedia communications", Artech House Boston London, 2000.

[3] L. Hanzo, M. Münster, B. Choi and T. Keller, "*OFDM and MC-CDMA for Broadband Multi-User Communications, WLANs and Broadcasting*", John Wiley & Sons, 05 September, 2003.

[4] K. Patterson, "Generalized Reed-Muller Codes and Power Control in OFDM Modulation," *IEEE Trans. Info. Theory*, vol. 46, no. 1, pp. 104–20, Jan. 2000.

[5] T. Jiang and G. Zhu, "OFDM Peak-to-Average power Ratio reduction by Complement Block Coding Scheme and Its Modified Version," VTC2004-Fall, vol. 1, pp. 448 – 451, 2004.

[6] G. Wunder, "A theoretical framework for peak-to-average power control problem in OFDM transmission", PhD thesis, technical University Berlin, 2004.

[7] S. Han and J. Lee, "An overview of Peak-to-Average Power Ratio reduction techniques for Multicarrier Transmission", *IEEE Wireless Communications*, pp. 56-65. Apr. 2005.

[8] M. Juntti, M. Vehkapera, J. Leinonen, Z. Li and D. Tujkovic, "MIMO MC-CDMA Communications for Future Cellular Systems", IEEE communication magazine, pp. 118-124, Feb. 2005.

[9] J. Hansen and M. Nold, "Analytic calculation of the power delay profile for single room wireless LAN environments", *IEEE Global Telecommunications Conference (GLOBECOM) 2000,* vol. 1, pp. 89-102, 2000.

[10] H. Hashemi, "The Indoor propagation channel", *Proc. of the IEEE,* vol. 81, no. 7, pp. 943-968, Jul. 1993.

[11] T. Schenk, G. Dolmans and I. Modonesi, "Throuput of a MIMO OFDM based WLAN system" in *Proc. Of Symposium IEEE Benelux Chapter on Communications and Vehicular Technology (SCVT2004) 2004,* Belgium, Nov. 2004.

[12] G. Foschini, "Layered space-time architecture for wireless communication in a fading environment when using multiple antennas", *Bell Laboratories Technical Journal,* vol. 1, no. 2, pp. 41-59, 1996.

[13] G. Foschini and M. Gans, "On limits of wireless communications in a fading environment when using multiple antennas", *AT&T-Bell Labs Internal Tech. Memo,* Sept. 1995. *Journal of Wireless Personal Communications*, vol. 6, no. 3, pp. 311-335, March 1998.

[14] L. Zheng and D. N. Tse, "Diversity and multiplexing: a fundamental tradeoff in multiple-antenna channels" *IEEE Transactions on Information Theory,* vol. 49, no. 5, pp. 1073-1096, May 2003.

[15] V. Tarokh, N. Seshadri and A. Calderbank, "Space-Time codes for high data rate wireless communication: performance criterion and code construction", *IEEE Transactions on Information Theory*, vol. 44, no. 3, pp. 744-756, Mar. 1998.

[16] J.-C. Guey, M. Fitz, M. Bell and W. Kuo, "Signal design for transmitter diversity wireless communication systems over Rayleigh fading channels" *IEEE Transaction on Communications,* vol. 47, no. 4, pp. 527-537, Apr. 1999.

[17] M. Gharayi-Alkhansari and A. B. Gershman, "On diversity and coding gains and optimal matrix constellations for space-time block codes", *IEEE Transaction on Signal Processing,* vol. 53, no. 10, part 1, pp. 3703-3717, Oct. 2005.

[18] H. Wang and X.-G. Xia, "Upper bounds of rates of space-time block codes from complex orthogonal designs", in *Proc. of the IEEE International Symposium on Information Theory,* 2002, p. 303, July 2002.

[19] V. Tarokh, H. Jafarkhani and A. Calderbank, "Space-Time block codes from orthogonal design", *IEEE Transactions on Information Theory*, vol. 45, no. 4, pp. 1456-1467, May 1999.

[20] W. Su and X.-G. Xia," Two generalized complex orthogonal space-time block codes of rates 7/11 and 3/5 for 5 and 6 transmit antennas", *IEEE Transactions on Information Theory,* vol. 49, no. 1, Jan. 2003, pp. 313-316.

[21] B. Farahang-Boroujeny and C. Schlegel, "Efficient multicarrier realization of full-rate space-time orthogonal block coded systems", in *Proc. of the International Conference on Communications (ICC) 2003,* vol. 4, pp. 2267-271, May 2003.

[22] S. Sandhu and A. Paularj "Space-Time block codes: a capacity perspective", *IEEE Communications Letter,* vol. 4, no. 12, pp. 384-386, Dec. 2000

[23] O. Tirkkonen, A. Boariu and A. Hottinen, "Minimal non-orthogonality rate 1 space-time block code for 3+ tx", In *Proc. of the International Symposium on Spread Spectrum Techniques and Applications*, pp. 429-432, Sept. 2000.

[24] C. Papadias and G. Foschini, "A space-time coding approach for systems employing four transmit antennas", in *Proc. of the IEEE International Conference on Acoustic, Speech and Signal Processing (ICASSP)2001*, vol. 4, pp. 2481-2484, May 2001.

[25] B. Hassibi and B. Hochwald, "High-rate codes that are linear in space and time", *IEEE Transactions on Information Theory*, vol. 48, no. 7, pp. 1804-1824, July 2002.

[26] S. Alamouti, "A simple transmit diversity technique for wireless communications", *IEEE Journal on Selected Areas in Communications,* vol. 16, no. 8, pp. 1451-1458, Oct. 1998.

[27] M. Jankiraman, "*Space-Time Codes and MIMO systems*", Artech House, Boston, LONDON 2004.

[28] B. Hochwald and S. ten Brink, "Achieving near-capacity on a multiple antenna channel", *IEEE Transaction on Communications,* vol. 51, no. 3, pp. 47-57, March 2003.

[29] M. Sellathurai and S. Haykin, "TURBO-BLAST for high-speed wireless communications", in *Proc. of IEEE Wireless Communications and Networking Conference (WCNC)2000,* vol. 1, pp. 315-320, Sept. 2000.

[30] J. Proakis, *Digital Communications,* Third Edition, New York, McGraw-Hill, 1995, McGraw-Hill Series in Electrical and Computer Engineering.

[31] T. Rappaport, *Wireless Communications, Principles and Practice,* New Jersey, Prentice-Hall, 1996.

[32] R. Chang, "Synthesis of Band-Limited Orthogonal Signals for Multichannel Data Transmission", the Bell Technical Journal, vol. 45, pp. 1775-1796, 1966.

[33] J. Bingham," Multicarrier modulation for data transmission: an idea whose time has come," *IEEE Communications Magazine*, vol. 28, no. 5, pp. 5-14, May 1990.

[34] S. Nanda, R. Walton, J. Ketchum, M. Wallace and S. Howard, "A High-Performance MIMO OFDM Wireless LAN", IEEE communication magazine, pp. 101-109, Feb. 2005.

[35] J-L. Hurel, C. Lerouge, C. Evic and L. Gui, "Mobile network evolution: from 3G onwards", technology white paper, ALCATEL telecommunications review, 4th Quarter 2003/1st Quarter 2004.

[36] H. Nyquist, "Certain topics in telegraph transmission theory", *Transaction on AIEE*, vol. 47, pp. 617-644, 1928.

[37] B. Saltzberg, "Performance of an efficient parallel data transmission system", *IEEE Transaction on Communications,* vol. 15, pp. 805-811, Dec. 1967.

[38] R. Chang and R. Gibby, "A theoretical study of performance of an orthogonal multiplexing data transmission scheme", *IEEE Transaction on Communications*, vol. 16, pp. 529-540, Aug. 1968.

[39] J. Salz and B. Weinstein, "Fourier Transform Communication System" Conference on Computers and Communications, Pine mountain, Georgia. Oct. 1969.

[40] R. Chang, "Orthogonal Frequency Division Multiplex Data transmission system", US Patent no. 3, 488, 445, 1970.

[41] S. Weinstein and P. Ebert, "Data transmission by frequency-division multiplexing using the discrete Fourier transform," *IEEE Transactions on Communication Technology*, vol. 19, pp. 628-634, October 1971.

[42] B. Hirosaki, "An Orthogonally multiplexed QAM system using the Discrete Fourier Transform", *IEEE Transactions on Communications,* vol. 29, pp. 982-989, Jul. 1981.

[43] A. Bahai and B. Saltzberg. *Multi-carrier Digital Communications: Theory and Applications of OFDM.* New York: Kluwer Academic/Plenum Publishers, 1999.

[44] P. Huang and Y. Lee, "Adaptive decision feedback orthogonality restoration filter for windowed OFDM", *IEEE Vehicular Technology Conference (VTC 2001),* vol. 2, pp. 1106 – 1110, Oct. 2001.

[45] A. Ruiz, J. M. Cioffi and S. Kasturia, "Discrete multiple tone modulation with coset coding for the spectrally shaped channel," *IEEE Transactions on Communications*, vol. 40, pp. 1012-1029, June 1992.

[46] G. Giannakis, "Filterbanks for blind channel identification and equalization," *IEEE Signal Processing Letters,* vol. 4, no. 6, pp. 184-187, June 1997.

[47] A. Peled and A. Ruiz, "Frequency domain data transmission using reduced computational complexity algorithms," *Proceedings of the IEEE International Conference on Acoustics, Speech and Signal Processing*, vol. 2, pp. 964-967, April 1980.

[48] S. Haykin, "Communication Systems", 4th edition, JOHN WILEY and Sons, Inc, 2001.

[49] Z. Wang and G. Gainnakis, "Wireless multicarrier communications: where Fourier meets Shannon," *IEEE Signal Processing Magazine*, vol. 17, no.3, pp. 29-48, May 2000.

[50] J.-H. Jong, K. Yang, W. Stark, and G. Haddad, "performance of OFDM systems with Adaptive Nonlinear Amplifiers," *IEEE Military Communications Conference Proceedings (MILCOM 1999)*, vol. 2, pp. 1110-1114, Oct/Nov. 1999.

[51] M. Ingram, "Smart Antenna Research Laboratory", Guillermo Acosta, August, 2000.

[52] A. Jones, T. Wilkinson, and S. Barton, "Block Coding Scheme for Reduction of Peak to Mean Envelope Power Ratio of Multicarrier Transmission Scheme," *Elect. Letters*, vol. 30, no. 22, pp. 2098–99, Dec. 1994.

[53] V. Tarokh and H. Jafarkhani, "On the Computation and Reduction of the Peak-to-Average Power Ratio in Multicarrier Communications," *IEEE Transactions in Communications.*, vol. 48, no. 1, pp. 37–44, 2000.

[54] K. Paterson and V. Tarokh, "On the Existence and Construction of Good Codes with Low Peak-to-Average Power Ratios," *IEEE Transactions on Information Theory*, vol. 46, no. 6, pp. 1974–87, Sept. 2000.

[55] J. Tellado, *Peak to Average Power Reduction for Multicarrier Modulation*, Ph.D. dissertation, Stanford Univ., Sept. 1999

[56] B. Krongold and D. Jones, "PAR Reduction in OFDM via Active Constellation Extension," *IEEE Trans. Broadcast,* vol. 49, no. 3, pp. 258–68, Sept. 2003.

[57] S. Han and J. Lee, "PAPR Reduction of OFDM Signals Using a Reduced Complexity PTS Technique," *IEEE Signal Processing Letters*, vol. 11, no. 11, pp. 887–90, Nov. 2004.

[58] S. Muller and J. Huber, "OFDM with reduced PAPR by optimum combination of partial transmit sequences", *IEEE Electronics Letters*, vol. 33, no. 5, pp. 368-369, Feb. 1997.

[59] S. Chen and C. Zhu, ICI and ISI Analysis and Mitigation for OFDM systems with Insufficient Cyclic Prefix in Time-Varying Channels, IEEE Transactions on Consumer Electronics, Vol. 50, No. 1, p-p 78-83, Feb. 2004.

[60] Y. Baoguo, K. Letaief, R. Cheng, C. Zhigang, "Timing recovery for OFDM transmission", *IEEE Journal on Selected Areas in Communications,* vol. 18, no. 11, pp. 2278-2291, Nov. 2000.

[61] R. Sherratt, S. Linfoot, "Deterministic equalization and results of a DVB-T multipath equalizer for both 16-QAM and 64-QAM operation", *IEEE Transactions* on *Consumer Electronics,* vol. 49, no. 1, pp.21 – 26, Feb. 2003.

[62] B. Muquet, M. de Courville, P. Duhamel, " Subspace-based blind and semi-blind channel estimation for OFDM systems", *IEEE Transactions on Signal Processing*, vol. 50, no. 7, pp. 1699 – 1712, July 2002.

[63] Y. Zhao, J. Leclercq and S. Häggman, "Intercarrier Interference of Compression in OFDM Communication Systems by Using Correlative Coding", *IEEE communications letters*, vol. 2, no. 8, pp 214-216, August 1998.

[64] J. Armstrong, "Analysis of new and existing methods of intercarrier interference due to carrier frequency offset in OFDM", *IEEE transactions on communications*, vol. 47, no. 3, pp 365-369, March 1999.

[65] S. Muller, R. Bauml, R. Fischer, and J. Huber, "OFDM with Reduced Peak-to-Average Power Ratio by Multiple Signal Representation", *Annals of Telecommunications*, vol. 52, no. 1-2, pp. 58-67, Feb. 1997.

[66] D. Wulich, N. Dinur, and A. Glinowiecki, "Level clipped high order OFDM", *IEEE Transactions on Communications*, vol. 48, no. 6, pp. 928-930 June 2000.

[67] K. Fazel and S. Kaiser, "Analysis of Non-linear distortion on MC-CDMA", IEEE International Conference on Communications, vol. 2, pp. 1028-1038, Jun, 1998.

[68] S. Boyd, "Multitone signals with low crest factor", *IEEE Transactions on Circuits and Systems*, vol. 33, no. 10, pp. 1018-1022, Oct. 1986.

[69] B. Popovic, "Synthesis of power efficient multitone signals with at amplitude spectrum" *IEEE Trans Commun*, vol. 39, no. 7, pp. 1031-1033, Jul. 1991.

[70] E. Jones, T. A. Wilkinson, and S. K. Barton, "Block coding scheme for reduction of peak to mean envelope power ratio of multicarrier transmission schemes," *Electronics Letters*, vol. 30, pp. 2098-99, Dec. 1994.

[71] D. Mestdagh, P. Spruyt, and B. Biran, "Analysis of clipping effect in DMT-based ADSL systems," *in Proc IEEE Intl Conf Commun,* 1994.

[72] R. Gross and D. Veeneman, "SNR and spectral properties for a clipped DMT ADSL signal," *in Proc IEEE Intl Conf Commun*, 1994.

[73] R. O'Neill and L. Lopes, "Envelope variations and spectral splatter in clipped multicarrier signals," *in Proc IEEE PIMRC, vol. 1,* (Toronto, Canada), pp. 71-75, Sep 1995

[74] X. Li and L. J. Cimini, "Effects of clipping and filtering on the performance of OFDM," *in Proc IEEE Vehicular Tech Conf*, vol. 3, (Phoenix, AZ), pp. 1634-1638, May 1997.

[75] M. Pauli and H.-P. Kuchenbecker, "Minimization of the intermodulation distortion of a nonlinearly amplified OFDM signal," Wireless Personal Commun, vol. 4, pp. 93-101, Jan 1997.

[76] R. van Nee and A. de Wild, "Reducing the peak-to-average power ratio of OFDM," in Proc IEEE Vehicular Tech Conf, vol. 3, (Ottawa, Canada), pp. 2072-2076, May 1998.

[77] J. Chow, J. Bingham, and M. Flowers, "Mitigating clipping noise in multicarrier systems," *in Proc IEEE Intl Conf Commun,* (Montreal, Canada), pp. 715-719, Jun 1997.

[78] R. van Nee, "OFDM codes for peak-to-average power reduction and error correction," *in Proc IEEE GlobeCom,* vol. 1, (London, UK), pp. 740-744, Nov 1996.

[79] J. Davis and J. Jedwab, "Peak-to-mean power control and error correction for OFDM transmission using Golay sequences and Reed-Muller codes," *Electronics Letters*, vol. 33, pp. 267-268, Feb. 1997.

[80] A. Jones and T. Wilkinson, "Combined coding for error control and increased robustness to system nonlinearities in OFDM," *in Proc IEEE Vehicular Technology Conference*, vol. 2, (Atlanta, GA), pp. 904-908, May 1996.

[81] S. Shepherd, J. Orriss, and S. Barton, "Asymptotic limits in peak envelope power reduction by redundant coding in orthogonal frequency-division multiplex modulation," *IEEE Trans Commun*, vol. 46, pp. 5-10, Jan 1998.

[82] D. Mestdagh and P. Spruyt, "A method to reduce the probability of clipping in DMT-based transceivers," *IEEE Trans Commun*, vol. COM-44, pp. 1234-1238, Oct 1996.

[83] A. Jayalath and C. Tellambura, "Reducing the Peak-to-Average Power Ratio of Orthogonal Frequency Division Multiplexing Signal through Bit or Symbol Interleaving," *Elect. Letters*, vol. 36, no. 13, pp. 1161–63, June 2000.

[84] H. Breiling, S. Müller–Weinfurtner, and J. Huber, "SLM Peak-Power Reduction without Explicit Side Information," *IEEE Commun. Lett.*, vol. 5, no. 6, June 2001, pp. 239–41.

[85] A. Jayalath and C. Athaudage, "On the PAP reduction of OFDM signals using multiple signal representation," *IEEE communications letters*, Vol. 8, no. 7, pp. 425-427, July 2004.

[86] M. Friese, "OFDM signals with low crest-factor", *IEEEGlobal Telecommunications Conference* (GLOBECOM'97), vol. 1, pp. 290 - 294, Nov. 1997.

[87] I. Telatar, "Capacity of multi-antenna gaussian channels", Rm. 2C-174, Lucent Technology, CiteSeer.IST , 1999.

[88] G. Strang, *Linear Algebra and its Applications*, Third Edition, San Diego, Harcourt Brace Jovanovich, Publishers, 1988.

[89] J. Andersen, "Array gain and capacity for known random channels with multiple element arrays at both ends", *IEEE Journal on selected areas in Communications*, vol. 18, no. 11, pp. 2172-2178, Nov. 2000.

[90] C. Shannon, "A mathematical theory of communications", *Bell Systems Technical Journal,* vol. 27, 379-423, 623-656, 1948.

[91] M. Khalighi, K. Raoof and G. Jourdain, "Capacity of wireless communication systems employing antenna arrays, a tutorial study", *Wireless Personal Communications,* vol. 23, pp. 321-352, 2002.

[92] T. Anderson, "An Introduction to Multivariate Statistical Analysis", Second edition, New York, John Wiley & Sons, 1984.

[93] A. Goldsmith, S. Jafar, N. Jindal and S. Vishwanath, " Capacity Limits of MIMO Channels", *IEEE Journal on selected areas in Communications,* vol. 21, no. 5, pp. 684-701, Jun. 2003.

[94] D.-S. Shiu, G. Foschini, M. Gans and J. Kahn, "Fading correlation and its effect on the capacity of multielement antenna systems", *IEEE Transactions on Communications,* vol. 48, no. 3, pp. 502-513, March 2000.

[95] J. Li and E.Y. Zhang, "Analysis of the Spatial Correlation Properties of Wireless MIMO Channel". *In Proceedings of IEEE International Symposium of Communications and Information (ISCIT2005) 2005*, vol. 1, pp. 222-225, Oct. 2005.

[96] K. Yu and B. Ottersten, "Models for MIMO propagation channels: a review", *Wireless Communications and Mobile Computing 2002,* John Wiley & Sons, no. 2, pp. 653-666, 2002.

[97] K. Pederson, J. Andersen, J. Kermoal, and P. Mogensen, "A stochastic multiple-input-multiple-output radio channel model for evaluation", in *Proc. Of the 52nd IEEE VTS Vehicular Technology Conference (VTC) 2000 Fall,* vol. 2, pp. 893-897, 2000.

[98] R. Horn and C. Johnson, *Matrix Analysis,* Cambridge, Cambridge University Press, 1985.

[99] S. Loyka, "Channel capacity of MIMO architecture using the exponential correlation matrix", *IEEE Communications Letters,* vol. 5, no. 9, pp. 369-371, Sept. 2001.

[100] J. Kermoal, L. Schumacher, K. Pedersen, P. Mogensen and F. Frederiksen, "A stochastic MIMO radio channel model with experimental validation", *IEEE Journal on Selected Areas in Communications,* vol. 20, no. 6, pp. 1211-1226, Aug. 2002.

[101] Muck M., de Courville M. and Duhamel P. "A Pseudorandom Postfix OFDM modulator-Semi-blind channel estimation and equalization," IEEE TRANSACTIONS ON SIGNAL PROCESSING, vol. 54, no. 3, pp. 1005- 1017, March 2006.

[102] A. Burr, "Turbo-codes: the ultimate error control codes?" Electronics and Communication Engineering Journal, pp. 1055-165, Aug. 2001.

[103] D. MacKay, "Information Theory, Inference, and Learning Algorithms" Cambridge University Press, 2003.

[104] M. Al-Akaidi, O. Daoud, and S. Linfoot, "A NEW TURBO CODING APPROACH TO REDUCE THE PEAK-TO-AVERAGE POWER RATIO OF A MULTI-ANTENNA-OFDM SYSTEM", *International Journal of Mobile Communications* (IJMC, ISSN: 1470-949X).

[105] M. Al-Akaidi and O. Daoud, "REDUCING THE PEAK-TO-AVERAGE POWER RATIO USING TURBO CODING", *IEE Proceeding Communications.*

[106] O. Daoud, M. Al-Akaidi and J. Ivins, "MIMO-OFDM channel modelling and performance", MESM2006 conference, Egypt, Aug. 2006.

[107] ETSI, Digital video broadcasting (DVB); transmission system for handheld *terminals (DVB-H)*, ETSI EN 302 304 V1.1.1 (2004-11), European Telecommunications Standards Institute.

[108] G. Faria, J. Henriksson, E. Stare and P, Talmola, "DVB-H: Digital Broadcast Services to Handheld Devices", *Proceeding of the IEEE*, vol. 94, no. 1, pp. 194-209, Jan. 2006.

[109] 802.11 Timelines, *IEEE 802.11: Working Group for WLAN standards* (2006-05-31), retrieved on 2006-06-14.

# Appendix A

# Mathematical Appendix

## A.1 Kronecker Product Identities

In this subsection, a proof will be given for the theorem that for any *M*x*N* matrix **A**, *N*x*P* matrix **B**, and *P*x*Q* matrix **C** (D. Harville, 1997),

$$\text{vec}(\mathbf{ABC}) = (\mathbf{C}^T \otimes \mathbf{A})\text{vec}(\mathbf{B}), \tag{A.1}$$

where ⊗ denotes the Kronecker product and vec(.) stands for the vector operation, in which a vector is formed from respective matrix by stacking its columns under each other. To prove (A.1), we need a number of statements. Firstly note that, under the assumption that **A**, **B**, **C**, and **D** have the right dimensions,

$$(\mathbf{AB}) \otimes (\mathbf{CD}) = (\mathbf{A} \otimes \mathbf{C})\,(\mathbf{B} \otimes \mathbf{D}) \tag{A.2}$$

which is simple but tedious to show. Secondly, vec(**A**+**B**) = vec(**A**)+ vec(**B**) and finally, if **a** and **b** are vectors, then vec($\mathbf{ba}^T$) = **a** ⊗ **b**, both of which are obvious.

Now, (A.1) is proved as follows. **B** can be expressed as

$$\mathbf{B} = \sum_{p=1}^{P} \mathbf{b}_p \, \mathbf{u}_p^T \tag{A.3}$$

where $\mathbf{b}_p$ is column $p$ of **B** and up is column $p$ of the identity matrix. Using this property and after changing the order of the 'vec'-operation and the sum, we can rewrite (A.1) as

$$\text{vec}(\mathbf{ABC}) = \text{vec}\left\{\mathbf{A}\left(\sum_p \mathbf{b}_p \mathbf{u}_p^T\right)\mathbf{C}\right\} = \sum_p \text{vec}\,(\mathbf{A}\mathbf{b}_p \mathbf{u}_p^T \mathbf{C}) \tag{A.4}$$

because both $\mathbf{Ab}_p$ and $\mathbf{C}^T\mathbf{u}_p$ are vectors,

$$\sum_p \text{vec}\,(\mathbf{A}\mathbf{b}_p\mathbf{u}_p^T\mathbf{C}) = \sum_p (\mathbf{C}^T\mathbf{u}_p)\otimes(\mathbf{A}\mathbf{b}_p)$$

$$= \sum_p (\mathbf{C}^T \otimes \mathbf{A})(\mathbf{u}_p \otimes \mathbf{b}_p) \qquad \text{(A.5)}$$

To finish the proof, just reverse the previous steps, like:

$$\sum_p (\mathbf{C}^T \otimes \mathbf{A})(\mathbf{u}_p \otimes \mathbf{b}_p) = (\mathbf{C}^T \otimes \mathbf{A})\,\text{vec}\left(\sum_p \mathbf{b}_p\mathbf{u}_p^T\right)$$

$$= (\mathbf{C}^T \otimes \mathbf{A})\,\text{vec}(\mathbf{B}) \qquad \text{(A.6)}$$

# Appendix B

# Digilent D2-FT System board datasheet

## Digilent D2-FT System Board Reference Manual

December 6, 2004

DIGILENT
www.digilentinc.com
246 East Main | Pullman, WA 99163
(509) 334 6306 Voice and Fax

### Overview

The Digilent D2-FT circuit board provides the basis for a complete circuit development platform centered on a Xilinx Spartan 2E FPGA. D2-FT features include:

- A Xilinx XC2S300E FPGA with 300K gates and 350MHz operation (also available with the XC2S400E FPGA);
- 172 user I/Os routed to six standard 40-pin expansion connectors;
- A socket for a JTAG-programmable 18V02 configuration Flash ROM;
- Dual on-board 1.5A power regulators (1.8V and 3.3V);
- An SMD 50MHz oscillator, and a socket for a second oscillator;
- A JTAG programming port;
- A status LED and pushbutton for basic I/O.

The D2-FT has been designed to work with all versions of the Xilinx ISE CAD tools, including the free WebPack tools available at Xilinx web site. (www.xilinx.com) A growing collection of low-cost expansion boards can be used with the D2-FT to add analog and digital I/O capabilities, as well as various data ports like Ethernet and USB. The D2-FT board ships with a power supply and programming cable, so designs can be implemented immediately without the need for any additional hardware.

### Functional Description

The Digilab D2-FT provides a minimal system that can be used to rapidly implement FPGA-based circuits, or to gain exposure to Xilinx CAD tools and Spartan 2E devices. The D2-FT provides only the essential supporting devices for the Spartan 2E FPGA, including clock sources and power supplies. All available I/O signals are routed to standard expansion connectors that mate with 40-pin, 100 mil spaced DIP headers available from any catalog distributor. A pushbutton and LED are also included for basic I/O.

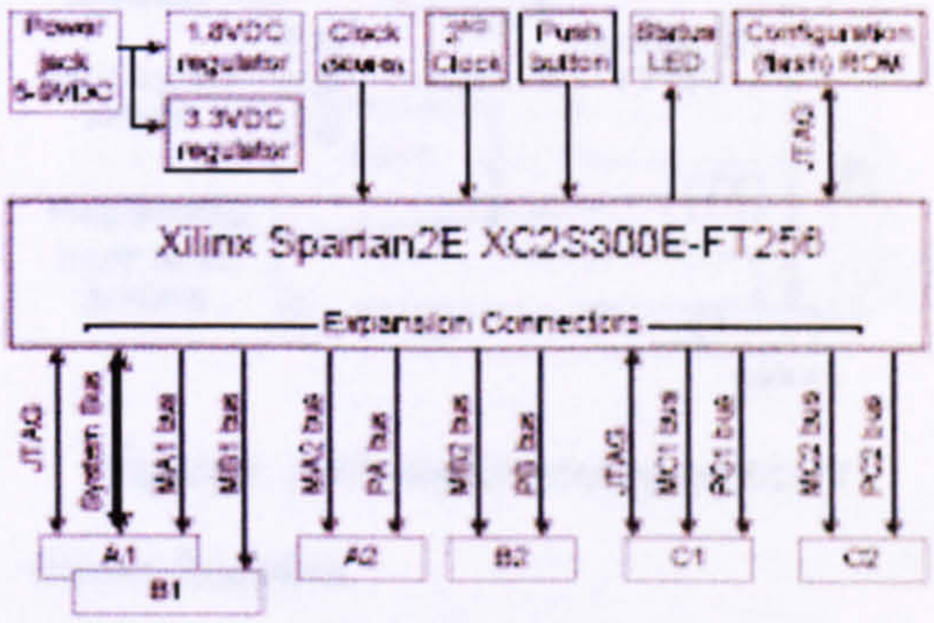


Figure 1. D2-FT Circuit Board Block Diagram

The D2-FT board has been designed to serve primarily as a host for peripheral boards. Each of the six expansion connectors provides the unregulated supply voltage (VU), 3.3V, GND, and 32 I/O signals from the FPGA. Because there are more connector pins than FPGA pins, the A1 and B1 connectors share an 18-pin bus. All other connector positions are driven by individual FPGA signals. JTAG signals are also routed to the A1, B1, and C1 expansion connectors. This allows peripheral boards to drive the scan chain, or to be configured along with the Spartan 2E FPGA.

Application-specific peripheral boards can be created to mate with the D2-FT, or ready-made peripheral boards that offer many standard I/O and data port functions can be obtained from Digilent (for a current listing of available boards, see www.digilentinc.com).

## JTAG Scan Chain and Device Configuration

The Spartan 2E FPGA, the 18V00 ROM on the D2-FT, and any programmable devices on peripheral boards attached to the D2-FT can be programmed via their JTAG ports. The JTAG scan chain is routed to the FPGA, the ROM, and around the board to four connection ports as shown in Figure 2 below. The primary configuration port (Port 1) uses a standard 6-pin JTAG header (J7) that can accommodate Digilent's JTAG3 cable (or cables from Xilinx or other vendors). The other three JTAG programming ports are bi-directional, and they are available on the A1, B1, and C1 expansion connectors. If no peripheral board is present, a buffer on the D2-FT removes the expansion connector from the JTAG chain. If a peripheral board with a JTAG device is attached, the scan chain is driven out the expansion connector so that any JTAG-programmable parts can be configured. If a Digilent port module is connected to one of the three JTAG-enabled expansion connectors, then the port module can drive the JTAG chain to program all devices in the scan chain (port modules include Ethernet, USB, EPP parallel, and serial modules -- see www.digilentinc.com for more information).

The scan chain can be driven from the primary port by powering on the D2-FT, connecting it to a PC with a JTAG programming cable, and running the "auto-detect" feature of the configuration software. The configuration software allows devices in the scan chain to be selectively programmed with any available configuration file. If no programming ROM is loaded in the IC5 socket (or if ROM is present but is not to be included in the scan chain), jumper-shunts must be loaded at JP1 and JP2 in the "Bypass ROM" location to route the JTAG chain around the ROM socket. If an 18V02 (or larger) ROM is loaded in the IC5 socket, it can be included in the scan chain by loading the JP1 and JP2 jumper-shunts in the "Include ROM" positions.

If a programming ROM is present in the IC5 socket, the FPGA will automatically access the ROM for configuration data if jumper shunts are loaded in all three positions of J8 (M2, M1, and M0).

Port modules attached to ports A1, B1, or C1 can drive the scan chain if a jumper-shunt is installed on the primary JTAG header across the TDI and TDO pins. In their default state, Digilent port modules will appear as a JTAG cable to the configuration software. Port modules can disable their JTAG drivers; if more than one JTAG driver is enabled on the scan chain, programming may fail.

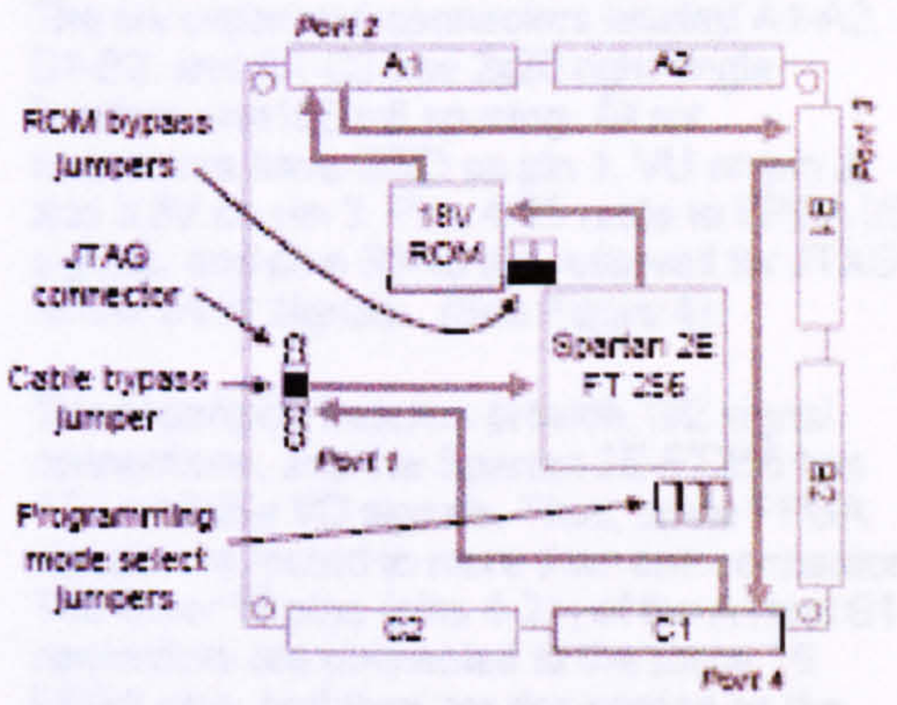


Figure 2. JTAG Signal Routing on D2-FT

## Power Supplies

The D2-FT board uses two LM317 voltage regulators to produce a 1.8VDC supply for the Spartan 2E core, and 3.3VDC supply for the I/O ring. Both regulators have good bypass capacitance, allowing them to supply up to 1.5A of current with less than 50mV of noise (typical). Power can be supplied from a low-cost wall transformer supply. The external supply must use a 2.1mm center-positive connector, and it must produce between 6VDC and 12VDC of unregulated voltage.

The D2-FT uses a four layer PCB, with the inner layers dedicated to VCC and GND planes. Most of the VCC plane is at 3.3V, with an island under the FPGA at 1.8V. The FPGA and the other ICs on the board all have 0.047uF bypass capacitors placed as close as possible to each VCC pin.

Total board current is dependant on FPGA configuration, clock frequency, and external connections. In test circuits with roughly 50K gates routed, a 50MHz clock source, and a single expansion board attached (the DIO5 board), approximately 200mA +/- 30% of supply current is drawn from the 1.8V supply, and approximately 200mA +/- 50% is drawn from the 3.3V supply. These currents are strongly dependent on FPGA and peripheral board configurations.

All FPGA I/O signals use the VCCO voltage derived from the 3.3V supply. If other VCCO voltages are required, the regulator output can be modified by changing R12 according to:

$$VCCO = 1.25(1 + R12/R11).$$

Refer to the LM317 data sheet and D2-FT schematic for further information.

## Oscillators

The D2-FT provides a 50MHz SMD primary oscillator and a socket for a second oscillator. The primary oscillator is connected to the GLK2 input of the Spartan 2E (pin B8), and the secondary oscillator is connected to GCLK3 (pin C8). Both clock inputs can drive the DLL on the Spartan 2E, allowing for internal frequencies up to four times higher than the external clock signals. Any 3.3V oscillator in a half-size DIP package can be loaded into the secondary oscillator socket.

## Pushbutton and LED

A single pushbutton and LED are provided on the board allowing basic status and control functions to be implemented without a peripheral board. As examples, the LED can be illuminated from a signal in the FPGA to verify that configuration has been successful, and the pushbutton can be used to provide a basic reset function independent of other inputs. The circuits are shown in Figure 3.

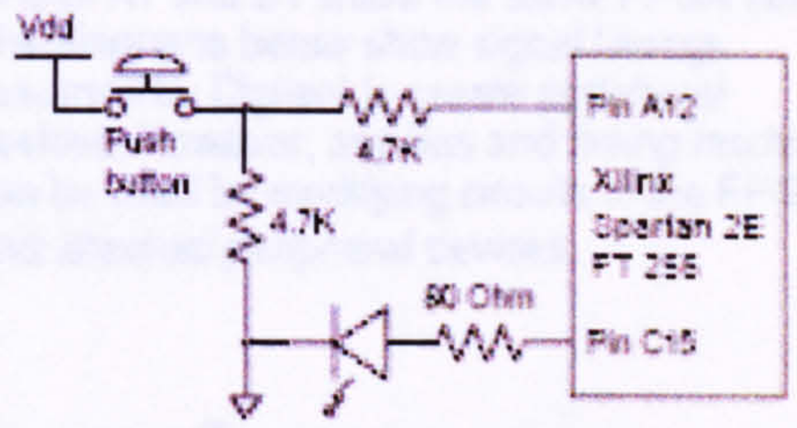


Figure 3. LED and Pushbutton Circuit

## Expansion Connectors

The six expansion connectors labeled A1-A2, B1-B2, and C1-C2 use 2x20 right-angle headers with100 mil spacing. All six connectors have GND on pin 1, VU on pin 2, and 3.3V on pin 3. Pins 4-35 route to FPGA I/O signals, and pins 36-40 are reserved for JTAG and/or clock signals. (See Figure 4)

The expansion headers provide 192 signal connections, and the Spartan 2E-FT256 has 172 available I/O signals. Thus, some FPGA signals are routed to more than one connector. The lower 18 pins (pins 4-21) of the A1and B1 connectors are connected to the same 18 FPGA pins, and they are designated as the "system bus" (a unique chip select signal is routed to each connector). Other than these 18 shared signals, all remaining FPGA signals are routed to individual expansion connector positions.

The lower 18 pins of the A2, B2, and C2 connectors are designated as "peripheral busses", and each of these busses (named PA, PB, and PC) use 18 unique signals. The 14 upper pins of each expansion connector (pins 22-35) have been designated as "module busses". Each connector has a fully populated module bus (named MA1, MA2, MB1, MB2, MC1, and MC2).

## System Bus

The "system bus" is a protocol used by certain expansion boards that mimics a simple 8-bit microprocessor bus. It uses eight data lines, six address lines, a write-enable (WE) strobe that can be used by the peripheral to latch

written data, an output-enable (OE) strobe that can be used by the peripheral to enable read data, a chip select, and a clock to enable synchronous transfers. System bus timings can be used to configure the lower 18 pins of the A1, B1, and C1 connectors (the lower 18 pins of A1 and B1 share the same FPGA pins). The diagrams below show signal timings assumed by Digilent to create peripheral devices. However, any bus and timing models can be used by modifying circuits in the FPGA and attached peripheral devices.

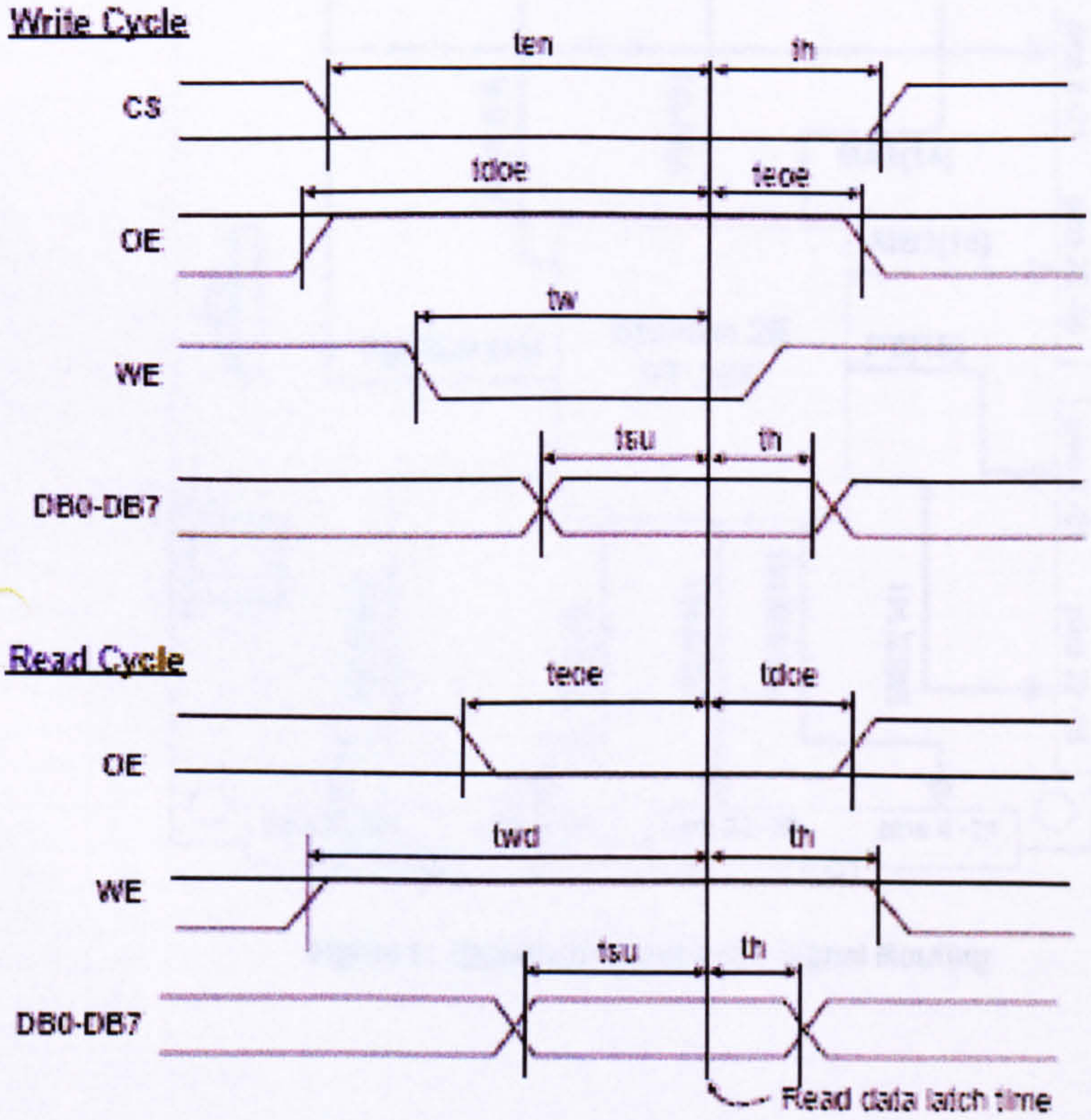


Figure 4. System Bus Timing

| Table 1. System Bus Timing | | |
|---|---|---|
| Symbol | Parameter | Time (typ) |
| ten | Time to enable after CS asserted | 10ns |
| th | Hold time | 1ns |
| tdoe | Time to disable after OE de-asserted | 10ns |
| teoe | Time to enable after OE asserted | 15ns |
| tw | Write strobe time | 10ns |
| tsu | Data setup time | 5ns |
| twd | Write disable time | 0ns |

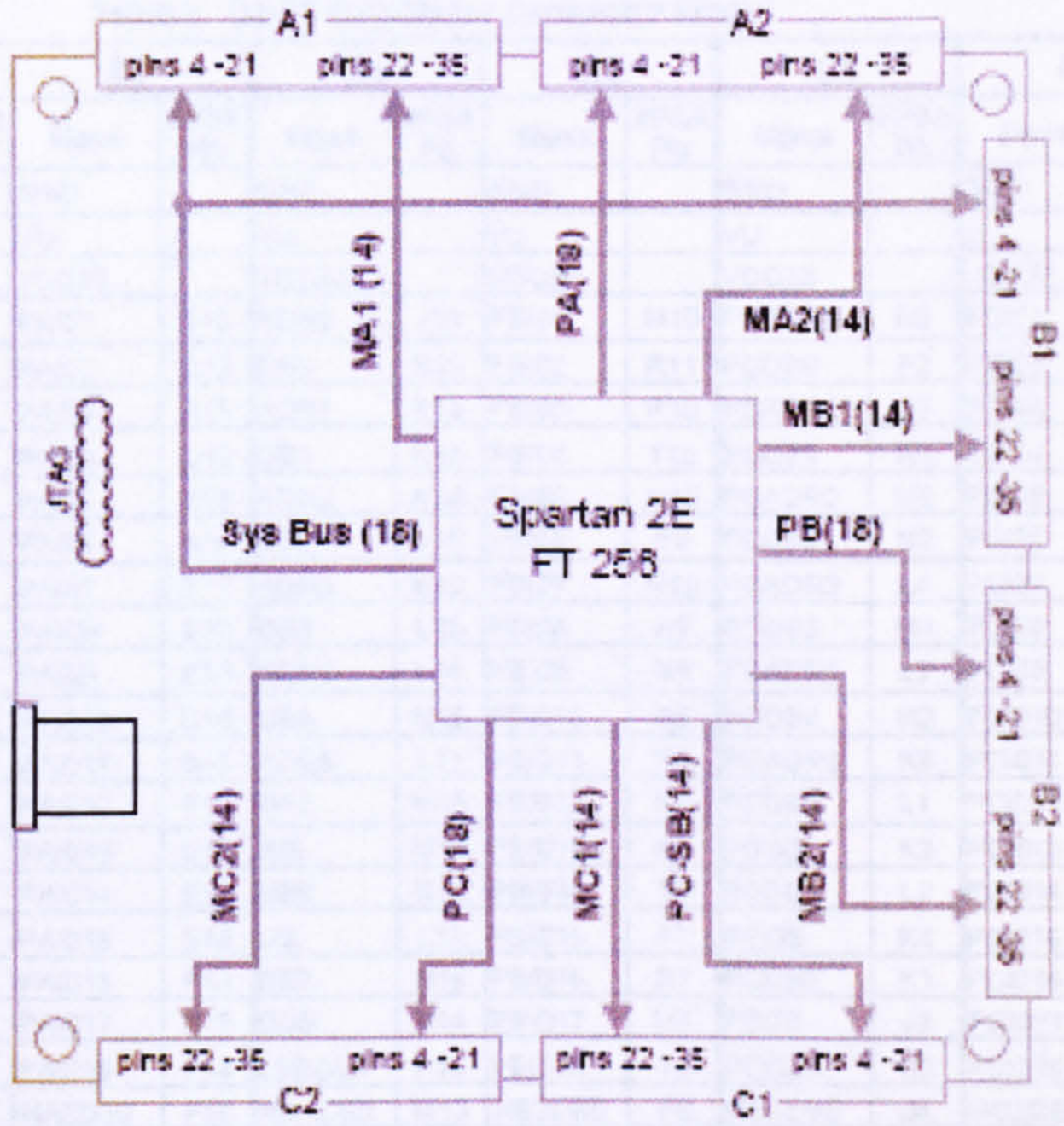


Figure 5. Expansion Connector Signal Routing

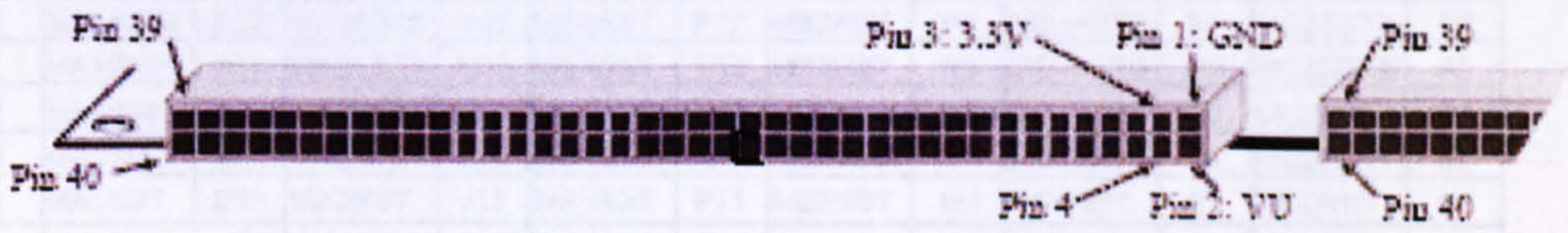


Figure 6. Expansion Connector Pin Locations

Table 2. D2-FT Expansion Connector Pinout

| Pin # | A1 | | A2 | | B1 | | B2 | | C1 | | C2 | |
|---|---|---|---|---|---|---|---|---|---|---|---|---|
| | Signal | FPGA Pin | Signal | FPGA Pin | Signal | FPGA Pin | Signal | FPGA Pin | Signal | FPGA Pin | Signal | FPGA Pin |
| 1 | GND | | GND | | GND | | GND | | GND | | GND | |
| 2 | VU | | VU | | VU | | VU | | VU | | VU | |
| 3 | VCC33 | | VCC33 | | VCC33 | | VCC33 | | VCC33 | | VCC33 | |
| 4 | ADR0 | J14 | PAIO1 | B12 | ADR0 | J14 | PBIO1 | M10 | PCADR0 | N3 | PCIO1 | F2 |
| 5 | DB0 | K16 | PAIO2 | C12 | DB0 | K16 | PBIO2 | R11 | PCDB0 | P2 | PCIO2 | E1 |
| 6 | ADR1 | K13 | PAIO3 | A13 | ADR1 | K13 | PBIO3 | P10 | PCADR1 | L5 | PCIO3 | F4 |
| 7 | DB1 | K15 | PAIO4 | D12 | DB1 | K15 | PBIO4 | T10 | PCDB1 | N1 | PCIO4 | E2 |
| 8 | ADR2 | K14 | PAIO5 | B13 | ADR2 | K14 | PBIO5 | N10 | PCADR2 | M3 | PCIO5 | E3 |
| 9 | DB2 | L16 | PAIO6 | A14 | DB2 | L16 | PBIO6 | P9 | PCDB2 | N2 | PCIO6 | D1 |
| 10 | ADR3 | K12 | PAIO7 | E11 | ADR3 | K12 | PBIO7 | R10 | PCADR3 | L4 | PCIO7 | F5 |
| 11 | DB3 | L15 | PAIO8 | C16 | DB3 | L15 | PBIO8 | N9 | PCDB3 | M1 | PCIO8 | D2 |
| 12 | ADR4 | L14 | PAIO9 | E13 | ADR4 | L14 | PBIO9 | N8 | PCADR4 | L3 | PCIO9 | D3 |
| 13 | DB4 | M16 | PAIO10 | D14 | DB4 | M16 | PBIO10 | R9 | PCDB4 | M2 | PCIO10 | C1 |
| 14 | ADR5 | L13 | PAIO11 | D16 | ADR5 | L13 | PBIO11 | P8 | PCADR5 | K5 | PCIO11 | E4 |
| 15 | DB5 | M15 | PAIO12 | F12 | DB5 | M15 | PBIO12 | R8 | PCDB5 | L1 | PCIO12 | A3 |
| 16 | WE | M14 | PAIO13 | D15 | WE | M14 | PBIO13 | N7 | PCWE | K3 | PCIO13 | C2 |
| 17 | DB6 | N16 | PAIO14 | E14 | DB6 | N16 | PBIO14 | T7 | PCDB6 | L2 | PCIO14 | B3 |
| 18 | OE | L12 | PAIO15 | E16 | OE | L12 | PBIO15 | P7 | PCOE | K4 | PCIO15 | C4 |
| 19 | DB7 | N15 | PAIO16 | F13 | DB7 | N15 | PBIO16 | R7 | PCDB7 | K1 | PCIO16 | A4 |
| 20 | CSA | D8 | PAIO17 | E15 | CSB | N14 | PBIO17 | M7 | PCCS | J3 | PCIO17 | D3 |
| 21 | LSBCLK | P16 | PAIO18 | F14 | LSBCLK | P16 | PBIO18 | T6 | PCCLK | K2 | PCIO18 | B4 |
| 22 | MA1DB0 | D9 | MA2DB0 | F16 | MB1DB0 | M13 | MB2DB0 | P6 | MC1DB0 | J4 | MC2DB0 | C5 |
| 23 | MA1DB1 | A9 | MA2DB1 | G12 | MB1DB1 | T14 | MB2DB1 | R6 | MC1DB1 | J1 | MC2DB1 | A5 |
| 24 | MA1DB2 | C9 | MA2DB2 | F15 | MB1DB2 | N12 | MB2DB2 | N6 | MC1DB2 | J2 | MC2DB2 | B6 |
| 25 | MA1DB3 | B9 | MA2DB3 | G14 | MB1DB3 | R14 | MB2DB3 | T5 | MC1DB3 | H4 | MC2DB3 | B5 |
| 26 | MA1DB4 | D10 | MA2DB4 | G16 | MB1DB4 | P13 | MB2DB4 | P5 | MC1DB4 | H1 | MC2DB4 | C6 |
| 27 | MA1DB5 | A10 | MA2DB5 | G13 | MB1DB5 | T13 | MB2DB5 | R5 | MC1DB5 | H3 | MC2DB5 | A6 |
| 28 | MA1DB6 | C10 | MA2DB6 | G15 | MB1DB6 | M11 | MB2DB6 | M6 | MC1DB6 | H2 | MC2DB6 | D6 |
| 29 | MA1DB7 | B10 | MA2DB7 | H14 | MB1DB7 | R13 | MB2DB7 | T4 | MC1DB7 | G4 | MC2DB7 | B6 |
| 30 | MA1ASTB | E10 | MA2ASTB | H16 | MB1AST | P12 | MB2AST | P4 | MC1ASTB | G1 | MC2ASTB | C7 |
| 31 | MA1DSTB | A11 | MA2DSTB | H13 | MB1DST | T12 | MB2DST | R4 | MC1DSTB | G3 | MC2DSTB | A7 |
| 32 | MA1WRT | C11 | MA2WRT | H15 | MB1WRT | N11 | MB2WRT | N5 | MC1WRT | G2 | MC2WRT | D7 |
| 33 | MA1WAIT | B11 | MA2WAIT | J16 | MB1WAIT | R12 | MB2WAIT | T3 | MC1WAIT | G5 | MC2WAIT | E7 |
| 34 | MA1RST | D11 | MA2RST | J13 | MB1RST | P11 | MB2RST | M4 | MC1RST | F1 | MC2RST | B7 |
| 35 | MA1INT | A12 | MA2INT | J15 | MB1INT | T11 | MB2INT | P1 | MC1INT | F3 | MC2INT | A8 |
| 36 | JTGELA | | | | JTGELB | | | | JTGELC | | | |
| 37 | TMS | | | | TMS | | | | TMS | | | |
| 38 | TCK | | | | TCK | | | | TCK | | | |
| 39 | TDOA | | CLKO | T9 | TDOB | | | | TDOC | | CLK1 | T8 |
| 40 | TDIA | | GND | | TDIB | | | | TDIC | | GND | |

Table 3. D2-FT FPGA Pin Assignments

| | A | B | C | D | E | F | G | H | J | K | L | M | N | P | R | T |
|---|---|---|---|---|---|---|---|---|---|---|---|---|---|---|---|---|
| 1 | GND | TMS | PC-IO10 | PC-IO6 | PC-IO2 | PC-RST | MC1-ASTB | MC1-DB4 | MC1-DB1 | PC-DB7 | PC-DB5 | PC-DB3 | PC-DB1 | MB2-INT | M1 | GND |
| 2 | TCK | GND | PC-IO13 | PC-IO8 | PC-IO4 | PC-IO1 | MC1-WRT | MC1-DB6 | MC1-DB2 | PC-CLK | PC-DB6 | PC-DB4 | PC-DB2 | PC-DB0 | GND | M0 |
| 3 | PC-IO12 | PC-IO14 | VCCI | PC-IO9 | PC-IO5 | MC1-INT | MC1-DSTB | MC1-DB5 | MC1-CS | PC-WE | PC-ADR4 | PC-ADR2 | PC-ADR0 | VCCI | M2 | MB2-WAIT |
| 4 | PC-IO16 | PC-IO18 | PC-IO15 | VCCI | PC-IO11 | PC-IO3 | MC1-DB7 | MC1-DB3 | MC1-DB0 | PC-OE | PC-ADR3 | MB2-RST | VCCI | MB2-ASTB | MB2-DSTB | MB2-DB7 |
| 5 | MC2-DB1 | MC2-DB3 | MC2-DB0 | PC-IO17 | VCCI | PC-IO7 | MC1-WAIT | VCCO | VCCO | PC-ADR5 | PC-ADR1 | VCCI | MB2-WRT | MB2-DB4 | MB2-DB5 | MB2-DB3 |
| 6 | MC2-DB5 | MC2-DB7 | MC2-DB4 | MC2-DB6 | MC2-DB2 | GND | VCCO | VCCO | VCCO | VCCO | GND | MB2-DB6 | MB2-DB2 | MB2-DB0 | MB2-DB1 | PB-IO18 |
| 7 | MC2-DSTB | MC2-RST | MC2-ASTB | MC2-WRT | MC2-WAIT | VCCO | GND | GND | GND | GND | VCCO | PB-IO17 | PB-IO13 | PB-IO15 | PB-IO16 | PB-IO14 |
| 8 | MC2-INT | GCK2 | GCK3 | CSA | VCCO | VCCO | GND | GND | GND | GND | VCCO | VCCO | PB-IO9 | PB-IO11 | PB-IO12 | GCK1 |
| 9 | MA1-DB1 | MA1-DB3 | MA1-DB2 | MA1-DB0 | VCCO | VCCO | GND | GND | GND | GND | VCCO | VCCO | PB-IO6 | PB-IO8 | PB-IO10 | GCK0 |
| 10 | MA1-DB5 | MA1-DB7 | MA1-DB6 | MA1-DB4 | MA1-ASTB | VCCO | GND | GND | GND | GND | VCCO | PB-IO1 | PB-IO5 | PB-IO3 | PB-IO7 | PB-IO4 |
| 11 | MA1-DSTB | MA1-WAIT | MA1-WRT | MA1-RST | PA-IO7 | GND | VCCO | VCCO | VCCO | VCCO | GND | MB1-DB6 | MB1-WRT | MB1-RST | PB-IO2 | MB1-INT |
| 12 | MA1-INT BTN | PA-IO1 | PA-IO2 | PA-IO4 | VCCI | PA-IO12 | MA2-DB1 | VCCO | VCCO | ADR6 | OE | VCCI | MB1-DB2 | MB1-ASTB | MB1-WAIT | MB1-DSTB |
| 13 | PA-IO3 | PA-IO5 | TDI | VCCI | PA-IO9 | PA-IO16 | MA2-DB5 | MA2-DSTB | MA2-RST | ADR1 | ADR5 | MB1-DB0 | VCCI | MB1-DB4 | MB1-DB7 | MB1-DB5 |
| 14 | PA-IO6 | TDO | VCCI | PA-IO10 | PA-IO14 | PA-IO18 | MA2-DB3 | MA2-DB7 | ADR0 | ADR2 | ADR4 | WE | CSB | VCCI | MB1-DB3 | MB1-DB1 |
| 15 | CCLK | GND | LED | PA-IO18 | PA-IO17 | MA2-DB2 | MA2-DB6 | MA2-WRT | MA2-INT | DB1 | DB3 | DB5 | DB7 | OE/RST | GND | CE |
| 16 | GND | DO | PA-IO8 | PA-IO11 | PA-IO15 | MA2-DB0 | MA2-DB4 | MA2-ASTB | MA2-WAIT | DB0 | DB2 | DB4 | DB6 | LDB CLK | CF | GND |